

**On Spinor Condensates as Amplifiers, Sensors and Tunable Quantum
Playgrounds for Studies of Spin**

by

Sabrina Rose Ann Leslie

B.Sc. Hon. (University of British Columbia) 2002

M.A. (University of California, Berkeley) 2005

A dissertation submitted in partial satisfaction of the
requirements for the degree of
Doctor of Philosophy

in

Physics

in the

GRADUATE DIVISION
of the
UNIVERSITY OF CALIFORNIA, BERKELEY

Committee in charge:
Professor Dan M. Stamper-Kurn, Chair
Professor Dmitry Budker
Professor Birgitta Whaley

Fall 2008

The dissertation of Sabrina Rose Ann Leslie is approved:

Chair

Date

Date

Date

University of California, Berkeley

Fall 2008

**On Spinor Condensates as Amplifiers, Sensors and Tunable Quantum
Playgrounds for Studies of Spin**

Copyright 2008

by

Sabrina Rose Ann Leslie

Abstract

On Spinor Condensates as Amplifiers, Sensors and Tunable Quantum Playgrounds
for Studies of Spin

by

Sabrina Rose Ann Leslie

Doctor of Philosophy in Physics

University of California, Berkeley

Professor Dan M. Stamper-Kurn, Chair

Spinor Bose Einstein condensates are employed as nearly quantum-limited sensors. In addition, this magnetic quantum fluid serves as a platform for studies of quantum dynamics. Using a spin sensitive imaging method, its vector magnetization is measured in situ with high spatial and temporal resolution. As a first application toward metrology, ^{87}Rb spinor Bose Einstein condensates are employed as precision magnetic microscopes. The demonstrated field sensitivity of $8.3 \text{ pT/Hz}^{1/2}$ over a measurement area of $120 \mu\text{m}^2$ marks an improvement over the low-frequency field sensitivity of modern SQUID magnetometers. Second, dynamical instabilities in a ^{87}Rb $F = 1$ spinor Bose Einstein condensate are used as a parametric amplifier of quantum spin fluctuations. The performance of this spin amplifier is observed to be nearly quantum-limited at a gain as high as 30 dB. Third, the possibility of preparing spin squeezed states is investigated theoretically, projecting 10 dB and 17 dB of spin squeezing to be attainable in the multi-mode and single-mode regimes. In addition to serving as quantum-limited sensors of spin, spinor condensates provide a compelling opportunity to access the dynamical properties of a magnetic superfluid. For example, the evolution of helical spin textures in $F = 1$ ^{87}Rb Bose condensates is observed to be significantly affected by dipole-dipole interactions, presenting a new experimental arena for studies of dipolar

quantum fluids.

Professor Dan M. Stamper-Kurn
Dissertation Committee Chair

To my parents, Stuart and Frances Leslie, and to my grandparents, Jack and Yetta
Leslie, and Roy and Beryl Brown.

Contents

List of Figures	v
1 Why Study Spinor Condensates?	1
1.1 Motivation for and overview of our experiments	1
1.2 Some perspective: prior work on quantum fluids with spin	3
1.3 The energetic landscape of spinor condensates: a theoretical treatment . . .	5
1.4 The experiments as a team effort	10
1.5 Elements of the experimental apparatus	14
1.5.1 The spin-independent trap	15
1.5.2 Controlling the background magnetic field	17
1.5.3 Applying modulated magnetic fields	19
2 Seeing Spinor Condensates	30
2.1 Dielectric properties of $F = 1$ spinor gases	30
2.1.1 Properties of a spin-1 object	31
2.1.2 Characterizing $F = 1$ spinors by measuring their dielectric tensors .	33
2.1.3 Dielectric properties of magnetic and polar gases	36
2.2 Spin-sensitive phase contrast imaging	37
2.2.1 Measurement principle	38
2.2.2 Imaging system	39
2.3 Larmor precession imaging: extracting the vector magnetization	46
2.3.1 Transverse magnetization measurement principle	46
2.3.2 Longitudinal magnetization measurement principle	47
2.4 Optimizing the imaging settings	52
2.4.1 Considering collective scattering	52
2.4.2 Multi-pulse imaging	53
2.5 On-resonance absorptive imaging	53
3 Spinor Condensates as Spatially Resolved Magnetometers	55
3.1 Spatially resolved magnetometry	55
3.1.1 Existing magnetometers	55
3.1.2 Ultracold atoms for magnetometry	56

3.1.3	Employing a Larmor precessing spinor condensate as a spatially re- solved magnetometer	57
3.2	Magnetic field sensitivity	59
3.2.1	Determining the phase contrast signal detection noise	59
3.2.2	Determining the magnetic field detection noise	62
3.3	Demonstration Experiment	64
3.3.1	Magnetic Microscopy Setup	64
3.3.2	Constructing a Magnetic Field Map	66
3.3.3	Characterizing the magnetic field environment	67
3.3.4	Characterizing a localized magnetic field	70
3.3.5	Limitations to measuring localized fields	72
4	Amplification of Spin Fluctuations in a Spinor Bose Einstein Condensate	75
4.1	Quantum dynamics and the quench of a spinor condensate	76
4.1.1	Instabilities accompanying a quantum phase transition	77
4.2	The spinor condensate as a degenerate parametric amplifier	81
4.2.1	Low-noise amplifiers	81
4.2.2	Mapping the spin mixing interaction to a parametric amplifier . . .	81
4.2.3	The spin-dependent Hamiltonian as a mode-by-mode parametric am- plifier	83
4.3	Spin fluctuation modes in a paramagnetic $F = 1$ spinor condensate	84
4.4	Experimental characterization of the spin-mixing amplifier	87
4.4.1	Initiating the amplifier: the quench into the ferromagnetic regime . .	88
4.4.2	Calibration of the field-induced quadratic Zeeman shift	89
4.4.3	Characterizing the amplifier: the quench to a variable endpoint . . .	91
4.4.4	Spatial magnetization correlations	94
4.4.5	Comparing our observations with a quantum amplification theory . .	99
4.5	Contributions from technical or thermal spin fluctuations	99
4.5.1	Possible role of $F = 2$ atoms	103
4.6	Future investigations	103
4.7	Analysis of the time evolution of populated fluctuation modes	104
5	Spin-squeezing in a Spinor Bose Einstein Condensate	114
5.1	Introduction to spin squeezing in a spinor condensate	114
5.2	Preparing a spin squeezed state in a spinor condensate	117
5.3	Observing squeezed magnetization fluctuations in a spinor condensate . . .	120
5.3.1	Determining the magnetization squeezing spectrum	122
5.3.2	Measuring spin squeezing in a homogeneous multi-mode condensate	124
5.4	A position-space picture of multi-mode squeezing	125
5.4.1	Spatial correlations of squeezed and anti-squeezed spin fluctuations .	126
5.4.2	Position-space modes in an inhomogeneous spin-squeezed condensate	132
5.5	Limitations to spin squeezing in a spinor condensate	134
5.5.1	Limitations to spin squeezing from nonlinearities	135
5.5.2	Numerically determined squeezing spectrum for an inhomogeneous nonlinear condensate	139

5.5.3	Spin-squeezing in the single mode regime	140
5.5.4	Limitations to spin squeezing from atom loss	141
5.6	Generating spin squeezed states for metrology	143
6	Spinor Condensates as Dipolar Quantum Fluids	148
6.1	A puzzling observation	148
6.1.1	Why so puzzling?	149
6.1.2	A possible explanation: dipole-dipole interactions	149
6.2	Evolving helical spin textures in spinor condensates	150
6.2.1	Quantifying short- and long-range magnetic order	153
6.2.2	Manipulating dipole interactions	155
6.2.3	Examining spin correlations	156
A	High-Resolution Magnetometry with a Spinor Bose Einstein Condensate	159
B	Amplification of Fluctuations in a Spinor Bose Einstein Condensate	164
C	Spontaneously Modulated Spin Textures in a Dipolar Spinor Bose-Einstein Condensate	170
D	Transmission spectrum of an optical cavity containing N atoms	175
	Bibliography	184

List of Figures

1.1	The contribution to $c_{2,eff}(k)$ from dipolar interactions is described by $c_{dd}K(k)$, where $K(k)$ is the anisotropic dipole interaction kernel (Eq 1.11) [45]. The dependence of the interaction upon k , taking $\mathbf{k} = k\hat{z}$, is shown for a few precession axis orientations, where the condensate geometry is held fixed. Here $c_{dd} = 0.8 \times 2\pi$ and $c_2 = -8 \times 2\pi$ rad/s.	11
1.2	The geometry of the condensate profile, dictated by the geometry the optical trapping potential, is selected to meet the requirements of a few experimental studies. When the spinor condensate is applied as a magnetic microscope, its density profile along \hat{x} is made to be narrow, enabling robust field measurements along the \hat{z} axis (a). By widening the confinement potential, the evolution of magnetic domain structures in the spinor gas could be examined in two spatial dimensions (b).	16
1.3	The ground state $5 S_{1/2}$, $F = 1, 2$ hyperfine manifolds of ^{87}Rb are shown. The dominant shift in energy of the magnetic hyperfine levels, m_F , is due to the linear Zeeman shift, $\hbar\omega_B = g_F\mu_B B_z$, at low magnetic fields. An applied microwave field, driven at a frequency $\omega_\mu = \omega_R + \delta$, is detuned from the $ F = 1, m_z = 0\rangle$ to $ F = 2, m_z = 0\rangle$ transition by δ . It is used to apply an AC Zeeman shift to the $ F = 1, m_z = 0\rangle$ state, which is quadratic in m_F and the applied microwave field. This applied quadratic shift may be tuned using both the amplitude and detuning and the microwave field.	20
1.4	A schematic describing the implemented microwave source and parts used, as referenced in the text.	25
1.5	Images of the 6.8 GHz marconni antenna designed and used to calibrate applied microwave fields.	26
1.6	The marconi antenna was tuned by adjusting the length of its dipole wire such the spectrum of the reflected power, measured using a directional coupler in the configuration shown, was minimized at the desired operating frequency.	27
1.7	Images of the 6.8 GHz marconni antenna designed and used to calibrate applied microwave fields.	28
1.8	The on-resonance squared Rabi frequency, Ω_R^2 , measured as a function of the control setting for the applied microwave field. The red and green circles correspond to measurements of Ω_R^2 performed twelve days apart.	29

2.1	The phase contrast imaging system is schematically shown, as described in the text.	40
2.2	(a) A mask is placed at the intermediate image plane such that only the pixels on the camera CCD chip which correspond to the condensate's location on the final image are exposed. (b) A series of snapshots of the condensate may be taken in rapid succession, each of which is shifted out of view following its exposure, protected by the mask.	42
2.3	(a) A phase and amplitude test pattern with features as small as $3 \mu\text{m}$ was fabricated to calibrate the imaging system offline. (b) The features on the phase test pattern consisted of trenches fabricated in the glass slide. Their depth was chosen in order to impart a π relative phase shift between the light traversing these regions and the light traversing the entire thickness of the glass. Here, features characterized by a width and periodicity of $3 \mu\text{m}$ are imaged using an optical microscope. The test patterns and their images are courtesy of Thomas P. Purdy.	43
2.4	To characterize the astigmatic character of the imaging system, the contrast of horizontal and vertical features in the test pattern, C_h and C_v , were determined as a function of the position of the first critical lens L_1 . Their ratio, C_h/C_v , corresponds to unity when the imaging system is optimally aligned, and deviates monotonically away from unity as the lens is displaced away from its optimal position. This characterization suggests a $\pm 25 \mu\text{m}$ sensitivity to the placement of L_1	44
2.5	For the aligned imaging system, the measured contrast of the test pattern features diminishes from unity for features larger than $5 \mu\text{m}$ in size to roughly 50% (projected) for features on the order of $2 \mu\text{m}$	45
2.6	An in-situ calibration of the resolution and astigmatism of the imaging system was performed by imaging a small hole punctured in the condensate density profile, whose application by means of a focussed resonant laser beam is schematically shown.	46
2.7	(a) A series of images of the condensate are taken while applying the focussed resonant probe. (b) The depletion of the condensate density at the location of the focus of the probe results in a sharp hole in the condensate with a symmetric Gaussian spatial profile. This image was taken during the alignment of the imaging system; here, a slight misalignment of the imaging system is reflected in the asymmetric cross section of the hole punctured in the condensate.	47
3.1	A sequence of phase contrast images of a Larmor precessing condensate (whose density profile is indicated schematically (a)) is shown following a 50-ms evolution period(b). In this example, the magnetic field environment is dominated by a large field curvature given by $(g_F\mu_B/h)d^2B_z/dz^2 = 80 \text{ kHz/cm}^2$. The relative phase of precession across the condensate varies quadratically with position, z , by roughly 20 rad across its spatial extent (c). For clarity, the magnetic field profile is indicated upon the raw data in (b).	67

- 3.2 A schematic representation of the applied, optically-induced field (a). In the same configuration, a sequence phase contrast images of a Larmor precessing condensate, following a 150 ms integration period, portray the spatial-variation of the accrued phase of precession due to the applied field. For clarity, the Gaussian field profile is indicated upon the raw data. The reduced phase profile $\tilde{\phi}(z)$ provides a quantitative measure of the accrued Larmor phase from which the magnitude of the applied field may be determined. 71
- 3.3 By imposing an inhomogeneous magnetic field characterized by a Gaussian spatial profile for a given integration time, we have locally modified the Larmor precession phase. An instantaneous snapshot of the magnetization profile reveals a local “twist” in \mathbf{M} by an angle about the \hat{z} axis proportional to the magnitude of the applied field. 73
- 4.1 The spectrum of spin excitations $E_s(k)^2$, here normalized by c_2n , has a gap for $q > 2|c_2|n$, in other words $E_s(k)^2 > 0$ and all perturbations about the initial paramagnetic state are stable (a). The gap closes at $q = 2|c_2|n$ as q is lowered (b), and a set of excitation modes become unstable. The unstable modes, for which $E_s(k)^2 < 0$, are characterized by small k in the case of $|c_2|n < q < 2|c_2|n$ (c). As q is lowered further toward $q = 0$, the most unstable modes are characterized by finite k (d). 80
- 4.2 Quantum fluctuations initially symmetric in F_x, N_{yz} are amplified and de-amplified along k -dependent axes given by v_{amp}, v_{sq} in the F_x, N_{yz} plane. 86
- 4.3 The total field-induced quadratic shift due to modulated and static magnetic fields, $q_f(V)$, as a function of the control setting for the applied microwave field, V . Here, $q_\mu(V) = -\Omega_R^2(V)/4\delta$ and $q_B = 70 \text{ Hz/G}^2 B^2$. The circles (squares) correspond to measurements performed at magnetic bias fields $B_z = 190(235) \text{ kHz}$, and microwave field detuning $|\delta| = 35 \text{ kHz}$. The magnitude of the control setting reflects Ω^2 and the sign of the control setting reflects the sign of the microwave field detuning δ 90
- 4.4 The fractional population in $m_z = \pm 1$, measured 110 ms after the quench, as a function of the final quadratic shift, q_f , at the end point of the quench. The squares (circles) correspond to measurements at magnetic bias fields $g_F\mu_B B_z = 190(235) \text{ kHz}$ 91
- 4.5 Representative images of the condensate transverse magnetization density, $\tilde{M}_{x,y}$, for the quench of a paramagnetic condensate to $q_f = 2 \text{ Hz}$. At evolution times $t = 47, 87, 127 \text{ ms}$, four examples of $\tilde{M}_{x,y}$ are shown in order to delineate the stochastic variation in the observed amplified spin fluctuations. 93
- 4.6 The saturated condensate transverse magnetization density as a function of the endpoint of the quench, q_f . For the deep quench, characterized by $0 < q_f < 8 \text{ Hz}$, the transverse magnetization profile is characterized by short-range features, which increase with q_f . As q_f is raised from 8 to 16 Hz, long-range features are observed and the magnetization diminishes. 108

4.7	Snapshots of the amplitude, phase, and spatial correlations of the transverse magnetization of a central region of the condensate, for a range of values of q_f . The amplifier's spatial spectrum, and its tunability with q_f , is characterized using the magnetization correlations.	109
4.8	The temporal evolution of the magnetization correlation function for $q_f = 2$, averaged over 8 repetitions of the experiment. The characteristic feature size remains roughly constant over time.	110
4.9	The power spectrum of the spatial Fourier transform of the condensate magnetization, as described in the text (circles). An approximate theory for a homogeneous condensate of the same average density as the experiment is shown in comparison (line).	110
4.10	The amplitude variance $\langle A_{LP}(\mathbf{r})^2 \rangle$ increases as a function of the peak precession amplitude, $A_{LP,max} = fA$. The simulated amplitude variance averaged over ten repetitions (red circles) agrees with its theoretical value (blue triangles). It is systematically lower if we do not include fluctuations in the photon field (green circles) by an approximately constant offset (green squares). . .	111
4.11	The boost in the measured variance of the precession amplitude which results from taking into account the fluctuations in the photon field, as compared to ignoring these fluctuations, in a numerical simulation. It is found to increase slightly with the average precession amplitude. It reflects the detection noise of our measurement of spin fluctuations and corresponds to photon shot-noise.	112
4.12	The amplitude variance of a fully transversely magnetized cloud, is determined empirically (circles) as well as theoretically (squares). Due to the loss of atoms from the trap, the measured amplitude variance decreased over time.	113
4.13	The time evolution of $G(0)$, with the introduction of a variable hold time, t_s between the purification pulse and magnetic field quench. For the two cases shown ($t_s = 30, 100$ ms), the time evolution for $G(0)$ is in good agreement. . .	113
5.1	Experimental sequence to prepare and observe a magnetization-squeezed state. Quantum fluctuations (a) are amplified and de-amplified along k -dependent axes (dotted lines given by v_{amp}, v_{sq}) in the F_x, N_{yz} plane (b). A magnetization-squeezed state is prepared by rotating the de-amplified fluctuations onto the F_x -axis (c,R1). In order to measure the squeezed fluctuations, they must be re-amplified into view. A second rotation (c,R2) is performed, and then the amplifier is reactivated. After a re-amplification period equal to the initial squeezing period, the fluctuations are again quantum-limited (d). After further amplification they are macroscopic and measurable(e).	118

5.2	The time evolution of the transverse magnetization $ F_{x,k} ^2$ throughout the aforementioned experimental sequence normalized by the initial quantum-limited fluctuations (solid line). In addition, one would probe the evolution of quantum fluctuations throughout the re-amplification stage (dotted line). Following re-amplification, the measured ratio of squeezed fluctuations <i>vs.</i> quantum fluctuations (S_{meas}) would correspond to the achieved degree of squeezing (S_{sq}). Experimental parameters are taken to be $q_{amp}/h = 4$ Hz, $q_{rot}/h = 50$ Hz, $t_{amp} = 40$ ms, $t_{rot} = 4.4$ ms, $k = \pi/10\mu\text{m}^{-1}$. For reference, the steps of the outlined experimental sequence are schematically shown below, described by Fig. 5.1.	123
5.3	The squeezing spectrum, corresponding to the degree of squeezing per mode k , is shown in the linear homogeneous case (a). Maximum squeezing is observed for the mode k for which the applied rotation angle ($\theta_{appl} \approx q_{rot}t_{rot}$), matches the optimal rotation angle, $\theta(k)$, shown in (b). Experimental parameters are taken to be $q_{amp}/h = 4$ Hz, $t_{amp} = 40$ ms, $q_{rot}/h = 2$ kHz, $q_{rot}t_{rot} = \pi/2$	125
5.4	For a single mode, the amplification and de-amplification axes are shown with respect to F_x and N_{yz} and ϕ_R, ϕ_I , which are oriented at 45 degrees with respect to one another.	128
5.5	Spatial distribution of amplified spin fluctuations, $G_{11}(\mathbf{r} , t = 6\tau)$ (dashed line); squeezed spin fluctuations, $G_{22}(\mathbf{r} , t = 6\tau)$ (red line); and $U(\mathbf{r} , t = 6\tau)$ (grey line). Position is normalized by the spin healing length, $\tau = 1/(c_2n)$ and $q = 1.5c_2n$	131
5.6	The position-space distribution of the maximum gain mode, set by $\gamma_0(r)$, is shown to be localized at the center of the trap.	135
5.7	A description of the spin-mixing interaction which takes into account the depletion of the pump results in the saturation of spin-squeezing. The depleted pump results in a reduced amplifier gain, thus both the amplification and squeezing of spin fluctuations reach saturation. The variance of the squeezed fluctuations ($ \phi_I ^2$) is reduced from $\vartheta(N)$ to $\vartheta(1)$ after an optimal evolution time on the order of the saturation time. Experimental parameters correspond to $ c_2 n/\hbar = 2\pi(8 \text{ Hz})$	138
5.8	A description of the spin-mixing amplifier which fully accounts for the depletion of the pump results in the saturation of spin-squeezing after a shorter evolution period. In this case, the variance of the squeezed fluctuations is reduced from $\vartheta(N)$ to $\vartheta(\sqrt{N})$. Experimental parameters correspond to $N = 10^4$ atoms, $ c_2 n/\hbar = 2\pi(8 \text{ Hz})$	140
5.9	The squeezing spectrum for an inhomogeneous nonlinear condensate is shown for reasonable experimental parameters (similar to the amplifier demonstration experiment) for the multi-mode case.	141

5.10	Examples of the RF and microwave pulses described in the text are schematically shown with respect to the ground state $5 S_{1/2}$, $F = 1, 2$ hyperfine manifolds of ^{87}Rb . The RF pulse serves to rotate the $F = 1$ condensate order parameter, a three-component vector composed of atoms in the three magnetic Zeeman sublevels, $ F = 1, m_F\rangle$. The frequency of the RF pulse is given by the Zeeman splitting between the sublevels, $\omega_B = g_F \mu_B B_z$, and its magnitude and phase determines the desired rotation. In addition, a two-photon microwave pulse is shown which is used to transfer population between the $ F = 1, m = 0\rangle$ and $ F = 1, m = 1\rangle$ levels. It is chosen to be detuned with respect to the $ F = 1, m_z = 0\rangle$ to $ F = 2, m_z = 0\rangle$ hyperfine transition.	146
6.1	(Right) A sequence of phase contrast images characterizing the Larmor precession of a uniformly transversely magnetized condensate (a) and a helical spin texture imposed upon the condensate (b). (Left) An instantaneous snapshot of the condensate spin depicts its homogeneous or helical spatial profile.	152
6.2	Long-range helical textures evolved into a finely modulated transverse magnetization profile $\tilde{M}_{x,y}$. Shown here, due to a slight astigmatism in the optical trap alignment, this pattern of magnetized domains was observed to nucleate most often at one end of the condensate.	153
6.3	The power spectrum of the spatial Fourier transform of the vector magnetization $\tilde{\mathbf{M}}(k_x, k_z)$. The spectral weight of the initial spin helix is concentrated in a central region of k -space, reflecting its long-range order (a). Following the dissolution of the spin helix into a finely modulated magnetization pattern, the spectral weight of short-range features, characterized by modulation frequencies $\sim 2\pi/10 \mu\text{m}^{-1}$, is apparent [10].	154
6.4	The short- and long-range magnetic order of the evolving spin texture are found to increase and decrease respectively, at a rate which depends upon the initial pitch of the helix (inset) [10].	155
6.5	The evolution of the short-range order acquired by the condensate magnetization is characterized with and without the application of dipole-cancellation pulses. The initial helix pitch was $\lambda = 80 \mu\text{m}$ [10].	157
6.6	Correlations in the spatial correlation function of the condensate magnetization reveal magnetic order characterized by a spatial periodicity of roughly $10 \mu\text{m}$	158

Acknowledgments

Thank you to everyone whose support and good company have made these explorations stimulating and rewarding. Thank you to my advisor, Dan Stamper-Kurn, for his guidance and his example. Thank you to my research team, Jay Deep Sau, Jennie Guzman, and Mukund Vengalatorre, for their comradeship and dedicated team work. Thanks to my friends Andrea Tao, Dan Butter, Naomi Ginsberg and Erin Quealy for their considerable support. Thanks to Tom Purdy for being an expert at electronics; to Tony Oetl for being an expert on microwave fields; to Kater Murch for helping me keep a steady supply of dewars filled with LN_2 at critical times; and to Lorraine Sadler and James Higbie for their mentorship and dedication to our spinor condensate apparatus. Thanks to Ken Brown and Neil Shenvi for their mentorship and teamwork in my introduction to research at Berkeley. Thanks to Dima Budker and Birgitta Whaley for reading my thesis and for their support; to Irfan Siddiqi for teaching me how to teach physics through his example; and to the Stamper-Kurn research group, Daniel Tatum, and the Physics Department staff for their help. Thanks to Friedhelm Serwane and Julia Hartmann for showing me California and to Sharon Jue and Allie for showing me the Berkeley Hills; to Dori Aspuru-Takata and Alan Aspuru-Guzik for their constant positive outlook; to Lianne Beltran and Tony Dutoi for being in Karlsruhe when a conference took me there; and to Quelani Penland for performing the Bach Double Concerto with me, providing a release from labwork. Thank you to my undergraduate mentors, Jess Brewer, Mark Halpern and Douglas Scott, and to my high school physics teacher, Mr. Millet, for inspiring my studies in physics from an early age. Thank you to my oboe teacher Beth Orson; to my sisters, Alexandra and Simone Leslie; and to my parents and grandparents, for their support and understanding.

Chapter 1

Why Study Spinor Condensates?

To embark upon this exploration of the salient features and potential applications of spinor Bose Einstein condensates, we begin with an overview of our experiments. To gain perspective on this work, we briefly survey prior research on quantum fluids with spin and outline the basic theory of spinor Bose gases – the energetic landscape which our experiments serve to investigate. To access the rich array of magnetic phenomena at our disposal, we must first surmount a number of technical hurdles; here, we document the principal additions to our experimental apparatus which have made these explorations possible.

1.1 Motivation for and overview of our experiments

The spinor Bose Einstein condensate offers the experimentalist the opportunity to grapple with fundamental questions about quantum dynamics in the most tangible of ways: to image the dynamics of a macroscopic quantum system directly. Emerging from such experimental explorations are a deepened theoretical understanding and sophisticated level of control over these systems which may be directed toward their application as quantum-limited measurement devices. Permeating this work are the themes of quantum dynamics and quantum-limited measurements, whose central questions and formalism lie at the intersection of the fields of quantum optics and condensed matter physics.

The unique opportunity to probe out of equilibrium dynamics in spinor condensates is afforded by the long timescales and long-range spatial features which characterize the spin dynamics of interest. In our experiments, we focus on two studies of quantum dynamics using $F = 1$ ^{87}Rb Bose Einstein condensates. First, we take advantage of the dynamical

instabilities which accompany a quantum phase transition between two phases of the spinor condensate to study the amplification of quantum fluctuations. In describing the dynamics which follow the rapid quench of the spinor condensate across this transition, we interpret the observed macroscopic magnetization pattern, first presented in Ref. [1], as an amplified version of the noise seeding its formation. By mapping the spin-dependent Hamiltonian which describes our system onto a parametric amplifier of spin fluctuations, we have been able to compare our experimental findings with the predictions of a quantum amplification theory at a quantitative level. Our experimental characterization of the “spinor condensate amplifier” indicates that in future studies of quantum magnetism, we may employ $F = 1$ ^{87}Rb spinor condensates as tunable, low-noise amplifiers of magnetization [2].

Studies of dipolar interactions in atomic systems, which are relevant to materials science and underly the complex many-body phases exhibited by a range of condensed matter systems, have previously focussed on atomic gases with high magnetic moments such as ^{52}Cr [3] or polar molecules [4]. In a second study of quantum dynamics, we study the evolution of spin textures in $F = 1$ ^{87}Rb Bose condensates. We find, much to our surprise, that a long-wavelength spin helix dissolves spontaneously into short-range spatially modulated patterns of spin domains [10]. Following extensive experimental tests, we are able to attribute the observed dissolution of helical spin textures to be a consequence of the dipole-dipole interactions inherent to the magnetized spinor gas. In this way, our characterization of $F = 1$ ^{87}Rb Bose condensates as dipolar magnetic fluids serves as a gateway toward a rich landscape of studies of quantum magnetism, featuring short- and long-range interactions of separately controlled magnitudes. By manipulating its spin-dependent Hamiltonian to simulate other condensed matter systems [5], spinor condensates may be employed in the future to gain insight on the magnetic phenomena displayed by magnetic thin films [6], ferrofluids [7], strongly correlated electronic systems [8], and frustrated quantum magnets [9].

And what would our explorations of quantum magnetism be without a sophisticated tool-kit suitable for performing quantum measurements? In this spirit, we make use of our understanding and control of the spinor condensate to develop sensitive spinor-condensate-based measurement devices. One such device corresponds to a spatially-resolved magnetometer. Following the ground work presented in Ref. [11], extensive experimental activity lead to our demonstration of spinor condensate magnetometry with a low-frequency field sensitivity, surpassing that of modern SQUID magnetometers for small measurement

areas ($\lesssim 150 \mu\text{m}^2$).

To broaden our set of spinor-condensate based tools, we consider the possibility of preparing spin squeezed states in these systems, which may serve as sub-shot-noise magnetic field sensors. We outline an experimental scheme to prepare spin squeezed condensates, finding that we may achieve roughly 17 dB of spin squeezing in the single mode regime and 10 dB of spin squeezing in the multi mode regime, for reasonable experimental parameters [13].

1.2 Some perspective: prior work on quantum fluids with spin

The first experimental realization of a multi-component superfluid of ^3He atoms, reported in 1949 [15], lead to a fascinating series of experiments on quantum fluids with spin. Nearly fifty years later, the creation of multi-component Bose Einstein condensates of dilute alkali vapors has provided an opportunity to investigate the equilibrium properties and dynamics of magnetic quantum fluids in a novel physical system. Spinor Bose Einstein condensates have the advantage of being described by a mathematically tractable theory, due to their weak interactions. Since their realization in dilute alkali vapors, they have served as a prototype system in the development of our understanding of quantum fluids with spin.

Focussing on the bulk properties of these systems, the past decade of research on multi-component condensates has developed the pathway to our own spatially-resolved studies of these systems. The first multi-component Bose condensate of alkali atoms was realized using two distinct magnetically trapped states of ^{87}Rb at JILA in 1996, following the group's creation of the first Bose Einstein condensate of alkali atoms in 1995 [16]. Pioneering experiments on quantum dynamics of spinor gases, one of the themes of the work presented in this dissertation, were subsequently performed by the same research group.

Spinor condensates of $F = 1$ ^{23}Na atoms, characterized by three spin components, were first studied by the Ketterle group at MIT. By employing a spin-independent optical trap to confine the condensate, and in so doing, liberating its spin degree of freedom [17], the MIT research team was able to determine the equilibrium properties of the spinor gas [18]. Phase separation and spin transport in the spinor gas were subsequently characterized

by this team of researchers [19, 20].

More recently, experiments characterizing the temporal evolution of the population in each spin component of $F = 1$ and $F = 2$ ^{87}Rb Bose condensates have been performed by a few research groups to discern their bulk properties and ground state character. Interestingly, while the ground state character of $F = 1$ ^{23}Na and $F = 2$ ^{87}Rb condensates is antiferromagnetic [22, 23], that of $F = 1$ ^{87}Rb condensates is ferromagnetic [21, 24, 25, 26]. To spatially separate each spin state, allowing its population to be determined, a magnetic field gradient pulse was applied; subsequently the gas was allowed to expand and was imaged. The inherent poor spatial resolution and destructive nature of this “Stern-Gerlach method of separations” limited these findings to describing the bulk properties of the system.

Spatially-resolved studies of spin dynamics in $F = 1$ ^{87}Rb spinor condensates have widened the experimental characterization of these systems to include the observation of topological defects and spatially inhomogeneous spin structures [1]. The multi-component order parameter of the spinor Bose condensate gives rise to a variety of topological defects, including spin vortices, spin textures and skyrmions, predicted by a flurry of theoretical work following its experimental realization [27, 28, 29, 30, 31]. Further, due to the dynamical instabilities characterizing small fluctuations about a given coherent state, most studies of the dynamics of spinor condensates, which are inherently multi-mode systems, are inevitably probing the evolution of spatially inhomogeneous spin structures [32, 33, 34, 35]. An exception to this rule are experiments carried out in the single mode regime, imposed by a tightly confining potential [24, 26], which may be described theoretically using a single-mode treatment [25, 36].

Spinor condensates have recently received attention as prototype systems for studies of quantum magnetism in solids, a field of research traditionally explored by condensed matter physicists [37, 38]. By virtue of the variety of tunable interaction strengths characterizing these systems, such as local spin-dependent contact interactions and long-range dipolar interactions, and the “purity” of these experimental samples in comparison with real materials, spinor condensates offer many advantages towards studies of quantum magnetism [39]. Implemented in optical lattice potentials, spinor gases provide a means to “simulate” the phase diagrams predicted by many-body Hamiltonians. Conceivably, spinor Bose condensates may also enable the first experimental realization of a magnetic supersolid, an idea under current experimental and theoretical investigation. In addition, controllable

arrays of multi-component quantum gases have been proposed as quantum-limited sensors of miniature magnetic structures [12] or as prototype systems for developing new materials. Recently, spinor condensates have served as a platform for theoretical studies of quantum entanglement and in the future, may be applied as components of a quantum computer [40].

1.3 The energetic landscape of spinor condensates: a theoretical treatment

In setting the stage for our experimental characterization of the dynamics of $F = 1$ spinor condensates, we begin with a description of their underlying energetics. In this treatment, we represent an $F = 1$ Bose condensate by a three-component spinor, reflecting its three magnetic Zeeman sublevels $m_z = +1, 0, -1$ [27]. In our experiments, the \hat{z} quantization axis corresponds to the orientation of the applied magnetic field, $\mathbf{B} = B\hat{z}$. The relevant energy scales for the homogeneous spinor condensate are described by the second-quantized Hamiltonian, [18, 27, 41, 42]:

$$\begin{aligned} H &= H_{kin} + H_Z + H_{Int} + H_{dip} \\ H_{kin} &= \int d\mathbf{r} \phi_m^\dagger(\mathbf{r}) \left[-\frac{\hbar^2}{2m} \nabla^2 \right] \phi_m(\mathbf{r}) \\ H_Z &= \int d\mathbf{r} (g_F \mu_B B \hat{F}_z(\mathbf{r}) + q \hat{F}_z(\mathbf{r})^2) \\ H_{int} &= \frac{1}{2} \int d\mathbf{r} c_0 \phi_m^\dagger \phi_{m'}^\dagger \phi_{m'} \phi_m + \frac{1}{2} \int d\mathbf{r} c_2 \hat{\mathbf{F}}(\mathbf{r}) \cdot \hat{\mathbf{F}}(\mathbf{r}) \end{aligned} \quad (1.1)$$

where $m_z = +1, 0, -1$ label the z -projection of the condensate spin. Here, $\phi_0(\phi_0^\dagger)$, $\phi_+(\phi_+^\dagger)$, $\phi_-(\phi_-^\dagger)$ are the destruction (creation) operators for condensate atoms in the $m_z = 0, 1, -1$ states respectively; the condensate spin, $\hat{\mathbf{F}}(\mathbf{r})$, may be expressed as,

$$\hat{F}_m(\mathbf{r}) = \sum_{m,n} \hat{\phi}(\mathbf{r})_m^\dagger J_{m,n} \hat{\phi}(\mathbf{r})_n; \quad (1.2)$$

and $J_{mn,i}$ correspond to the standard spin-one matrices,

$$J_x = \frac{1}{\sqrt{2}} \begin{pmatrix} 0 & 1 & 0 \\ 1 & 0 & 1 \\ 0 & 1 & 0 \end{pmatrix}; J_y = \frac{1}{\sqrt{2}} \begin{pmatrix} 0 & -i & 0 \\ i & 0 & -i \\ 0 & i & 0 \end{pmatrix}; J_z = \frac{1}{\sqrt{2}} \begin{pmatrix} 1 & 0 & 0 \\ 0 & 0 & 0 \\ 0 & 0 & -1 \end{pmatrix}. \quad (1.3)$$

Field-induced energy shifts

The interaction of the condensate spin with a homogeneous magnetic field, $\mathbf{B} = B\hat{z}$, is described by

$$H_Z = \int d\mathbf{r} (g_F \mu_B B \hat{F}_z(\mathbf{r}) + q \hat{F}_z(\mathbf{r})^2), \quad (1.4)$$

including the linear and quadratic Zeeman energy [43]. When the applied field is spatially homogeneous, it is convenient to view the evolution of the system in the *rotating frame*, the frame rotating about the \hat{z} axis at the Larmor frequency, $\omega_L = g_F \mu_B B / \hbar$. In this frame, linear Zeeman shift is identically zero. The field-induced energy shift which is quadratic in B , however, remains nonzero. For an $F = 1$ gas of ^{87}Rb atoms, an applied magnetic field induces a quadratic energy shift corresponding to $q/\hbar = 70B^2 \text{ Hz/G}^2$. We can see that when the quadratic Zeeman shift is very large, *e.g.* at high magnetic fields, the $m_z = \pm 1$ states will be significantly raised in energy with respect to the $m_z = 0$ state; thus, the quadratic Zeeman shift favors an *unmagnetized* condensate. In our experiments, the magnitude of the induced quadratic Zeeman shift is controlled using the magnitude of the applied bias field, in addition to the magnitude of an applied AC magnetic field, to discussed in Section 1.6.

Contact interactions in spinor Bose gases

Low-energy collisions in spinor Bose condensates lead to spin-dependent contact interactions, which are key to their behavior at low magnetic fields. In the dilute Bose gases that we consider, we may focus on two-body collisions, neglecting higher order collisions which are suppressed by the low density of the gas. Due to the low temperature of the gas, we need only consider low-energy collisions described by s-wave scattering.

Due the symmetry requirements imposed by Bose statistics, the total angular momentum of two colliding $F = 1$ ^{87}Rb atoms in the condensate is given by either $f=0$ or $f=2$, where $\mathbf{f} = \mathbf{F}_1 + \mathbf{F}_2$. As presented in Ref. [27, 41], s-wave scattering may be modeled by a hard-sphere potential, characterized by an effective scattering length, a_f . Here a_f takes distinct values for the $f = 0$ and $f = 2$ collision channels. The contact interaction resulting from the s-wave collisions in the spinor gas may be described using the interaction potential,

$$U(\mathbf{r} - \mathbf{r}') = \sum_{f=0,2} \frac{4\pi\hbar^2 a_f}{m} \delta(\mathbf{r} - \mathbf{r}') \hat{P}_f \quad (1.5)$$

where P_f is the projection operator defined with respect to the total angular momentum f state. The interaction Hamiltonian is then given by [43],

$$\begin{aligned} H_{Int} &= \frac{1}{2} \int d\mathbf{r} \, c_0 \phi_m^\dagger \phi_{m'}^\dagger \phi_{m'} \phi_m + \frac{1}{2} \int d\mathbf{r} \, c_2 \hat{\mathbf{F}}(\mathbf{r}) \cdot \hat{\mathbf{F}}(\mathbf{r}) \\ c_0 &= \frac{4\pi\hbar^2}{3m} (2a_2 + a_0) \\ c_2 &= \frac{4\pi\hbar^2}{3m} (a_2 - a_0). \end{aligned} \quad (1.6)$$

The contribution to the spinor condensate Hamiltonian due to contact interactions is given by a sum of two terms. The interaction strength of the first, spin-independent term is characterized by c_0 ; the interaction strength of the second, spin-dependent term is characterized by c_2 and we see that it is symmetric with respect to rotations about \hat{z} .

For a spinor gas of ^{87}Rb atoms, both a_2 and a_0 are positive; thus collisions characterized by $f = 0$ and $f = 2$ are described by repulsive interactions. The difference in scattering lengths between the two collision channels is small and negative, *i.e.*, $\Delta a = (a_2 - a_0) < 0$ and $c_2 < 0$. This has a clear consequence for the energetics of the spinor Bose gas: the spin-dependent contact interaction will be minimized when $\langle \mathbf{F}^2 \rangle$ is large. This is made transparent by its mean-field value $\sim c_2 \langle \mathbf{F}^2 \rangle$. Thus, spin-dependent contact interactions favor the condensate to be in a uniformly *magnetized* state.

Physically, we may interpret the total angular momentum $f=0$ ($f=2$) collisions to correspond to collisions in which the incoming spins are anti-aligned (aligned). Since $a_0 > a_2$, it is slightly more costly for the atoms to be anti-aligned *vs.* aligned with respect to one another. This tends to favor the spin of the atoms to co-align over the spatial extent of the gas, a phenomenon referred to as the *ferromagnetic character* of a spinor Bose gas.

Despite their magnitude being small, the spin-dependent contact interactions break the degeneracy between the magnetic Zeeman sublevels and are therefore critical in determining the observed magnetic phenomena in spinor gases. For example, for the values of a_2 and a_0 reported in Ref. [44], and taking a condensate density $n = 2.1 \times 10^{14}/\text{cm}^3$, we find $\Delta a = -1.4 \, a_B$, and $c_2 n / \hbar = -7.6 \, \text{Hz}$. For the same density, the spin-independent mean-field interaction strength is given by $c_0 n / \hbar = 1.6 \, \text{kHz}$, corresponding to the condensate chemical potential. The spin dynamics of the system are consequently characterized by longer timescales and long range spatial features, in comparison to the evolution of features in the condensate density profile.

Dipole-dipole interactions in spinor Bose gases

In a spinor Bose gas, the magnetic dipole interactions are characterized by an interaction strength which is comparable in magnitude to the aforementioned spin-dependent contact interactions. Dipolar interactions may therefore influence the spin dynamics and ground state character of the spinor Bose gas. In our experiments, we take advantage of an imaging technique which relies upon the Larmor precession of the condensate magnetization. Thus in considering the role of magnetic dipolar interactions in our experiments, we consider the precession-averaged dipole-dipole interaction energy.

The dipole-dipole interaction energy due to two magnetic dipoles, characterized by dipole moments \wp_1 and \wp_2 and located at positions \mathbf{r}_1 and \mathbf{r}_2 , is characterized by

$$U_{dip} = \frac{\mu_0}{4\pi} \left(\frac{\wp_1 \cdot \wp_2 - 3(\wp_1 \cdot \hat{\mathcal{R}})(\wp_2 \cdot \hat{\mathcal{R}})}{\mathcal{R}^3} \right) \quad (1.7)$$

where $\hat{\mathcal{R}} = (\mathbf{r}_1 - \mathbf{r}_2)/|\mathbf{r}_1 - \mathbf{r}_2|$ is the unit vector pointing between \mathbf{r}_1 and \mathbf{r}_2 . We consider the dipoles to be Larmor precessing about the $\hat{\mathbf{D}}$ axis (typically corresponding to \hat{z} in our experiments) and without loss of generality, define a right-handed coordinate system, formed by $\hat{x}, \hat{y}, \hat{D}$, in which to study the above interaction. First, \hat{x} is chosen to correspond to a unit vector in the plane of $\hat{\mathcal{R}}$ and $\hat{\mathbf{D}}$, satisfying $\hat{x} \cdot \hat{\mathbf{D}} = 0$. Next, \hat{y} is determined by $\hat{y} \equiv \hat{D} \times \hat{x}$ and satisfies $\hat{\mathcal{R}} \cdot \hat{y} = 0$. The interaction energy then becomes,

$$U_{dip} = \frac{\mu_0}{4\pi} \left(\frac{\wp_{1D}\wp_{2D} + \wp_{1x}\wp_{2x} + \wp_{1y}\wp_{2y} - 3(\wp_{1D}\cos\theta + \wp_{1x}\sin\theta)(\wp_{2D}\cos\theta + \wp_{2x}\sin\theta)}{\mathcal{R}^3} \right), \quad (1.8)$$

where $\hat{\mathcal{R}} \cdot \hat{D} = \cos(\theta)$. As a given magnetic dipole \wp undergoes Larmor precession about the $\hat{\mathbf{D}}$ axis, \wp_x, \wp_y vary sinusoidally in time and are characterized by a temporal average, $\langle \wp_x \rangle = 0$, $\langle \wp_y \rangle = 0$ whereas \wp_D and $\wp_1 \cdot \wp_2$ remain invariant. By symmetry we expect

$$\langle \wp_{1x}\wp_{2x} \rangle = \langle \wp_{1y}\wp_{2y} \rangle \quad (1.9)$$

$$= (\wp_1 \cdot \wp_2 - \wp_{1D}\wp_{2D})/2 \quad (1.10)$$

and using these observations, the Larmor-precession averaged interaction simplifies to,

$$\bar{U}_{dip} = \frac{\mu_0}{4\pi} \left(\frac{1 - 3\cos^2(\theta)}{2\mathcal{R}^3} (3\wp_{1D}\wp_{2D} - \wp_1 \cdot \wp_2) \right). \quad (1.11)$$

The dipole-dipole interaction energy which characterizes a spinor gas may be similarly defined using its magnetization density, taking $\hat{\phi}(\mathbf{r}_i) = \hat{\mathbf{F}}(\mathbf{r}_i)$. The total energetic contribution due to dipolar interactions in the condensate is then described as [45],

$$\begin{aligned}\bar{U}_{dip} &= c_{dd} \int d\mathbf{r}_1 d\mathbf{r}_2 K(\mathbf{r}_1, \mathbf{r}_2) (3F_{1D}F_{2D} - \mathbf{F}_1 \cdot \mathbf{F}_2) / 2 \\ K(\mathbf{r}_1, \mathbf{r}_2) &= \frac{1 - 3\cos^2(\theta)}{\mathcal{R}^3} \\ c_{dd} &= \mu_0(g_F\mu_B)^2/4\pi\end{aligned}\tag{1.12}$$

where we have separated the prefactor c_{dd} , reflecting the strength of the interaction, and the anisotropic kernel $K(\mathbf{r}_1, \mathbf{r}_2)$, reflecting the system geometry.

Having determined the precession-averaged form of the dipolar interactions relevant to our experiments, we ask, what are its salient features? The role of dipolar interactions in the spinor gas is in general quite subtle. In a given experiment, it depends significantly upon the sample geometry, dimensionality, and orientation with respect to the magnetic field. To put the dipolar and aforementioned contact interactions on the same footing, it is insightful to define an effective interaction strength which takes both interactions into account. Including both the spin-dependent contact interaction and dipole-dipole interaction, one may define an effective spin-dependent interaction,

$$\begin{aligned}H_{int,spin} &\equiv \int d\mathbf{r} c_2 n(\mathbf{r}) \hat{\mathbf{F}}(\mathbf{r})^2 + H_{dip} \\ &= \int d\mathbf{r}_1 d\mathbf{r}_2 c_{2,eff}(\mathbf{r}_1, \mathbf{r}_2) \hat{\mathbf{F}}_1 \cdot \hat{\mathbf{F}}_2 + 3 \int d\mathbf{r}_1 d\mathbf{r}_2 c_{dd} K(\mathbf{r}_1, \mathbf{r}_2) \hat{F}_{1D} \hat{F}_{2D} / 2 \\ c_{2,eff}(\mathbf{r}_1, \mathbf{r}_2) &= c_2 \delta(\mathbf{r}_1 - \mathbf{r}_2) - c_{dd} K(\mathbf{r}_1, \mathbf{r}_2) / 2\end{aligned}\tag{1.13}$$

Physically, the dipole interactions effectively renormalize c_2 in a manner specific to the system geometry. We elucidate this behavior by considering a homogeneous condensate in three-dimensions, in which case it is natural to express c_2 as a function of a mode's wavevector k . We find,

$$\begin{aligned}c_{2,eff}(k, \chi, \eta) &= c_2 - c_{dd} K(k, \chi, \eta) / 2 \\ K(k, \chi, \eta) &= -\frac{4\pi}{3} (1 - 3\sin^2 \chi \cos^2 \eta).\end{aligned}\tag{1.14}$$

where \mathbf{k} is taken to be $\mathbf{k} = k\hat{z}$; χ and η correspond to the polar angles describing the orientation of the precession axis \hat{D} with respect to the condensate axis, \hat{z} , as shown in Fig. 1.1. In our experiments, the magnetic field is typically oriented along \hat{z} , corresponding

to the case $\chi = \pi/2, \eta = 0$. Since $c_2 < 0$, the magnitude of $c_{2,eff}$ is increased when $\eta = 0$, corresponding to the case when the precession axis is aligned to the wavevector \mathbf{k} ; in contrast, the magnitude of $c_{2,eff}$ is lowered when the mode \mathbf{k} of interest is transverse to the precession axis ($\eta = \pi/2$).

In our experiments, the condensate may be considered as two-dimensional with respect to spin dynamics. For ease of presentation, $K(k, \chi, \eta)$ is simply shown in Fig. 1.1 [45]. We are typically interested in wavevectors characterized by $k < 0.6 \mu\text{m}^{-1}$, corresponding to spatial features in the condensate magnetization profile larger than roughly $5 \mu\text{m}$ in size. Taking the precession axis to be aligned to the condensate axis (\hat{z}), we observe that as k approaches zero, $c_{dd}K(k)$ decreases in magnitude and eventually becomes negative. Thus, for small k , the dipole interactions serve to increase the magnitude of $c_{2,eff}$; for large k , we observe the opposite behavior. When the precession axis is transverse to the wavevector of interest, the role of the dipole interactions for small and large k modes is reversed. It is interesting to note that in the case of large k , the dipolar interactions renormalize c_2 in a similar way in two- and three-dimensions, whereas in the case of small k , they behave differently. We see that varying the orientation of the precession axis relative to the condensate axis provides an experimental means to study the influence of dipole-dipole interactions upon the behavior of the spinor condensate.

By modifying the spin-dependent contact interactions, the dipole-dipole interactions influence the behavior of the spinor condensate in each of our experiments. In our study of the amplification of spin fluctuations atop an $m = 0$ condensate, the form of $c_{2,eff}$ affects the gain by which the initial spin fluctuations are amplified, in addition to the characteristic lengthscale of the saturated pattern of transversely magnetized domains (to be discussed in Ch. 4). In our study of helical spin textures imprinted upon a transversely magnetized gas, the dissolution of long-range features into highly-corrugated spatial patterns in the condensate magnetization is attributed to dipole-dipole interactions (to be discussed in Ch. 6).

1.4 The experiments as a team effort

With a rich landscape of physics on the horizon to explore, we must first overcome a number of technical hurdles. A detailed account of the construction and operation of the majority of our experimental apparatus is provided by References [11, 14], to which we

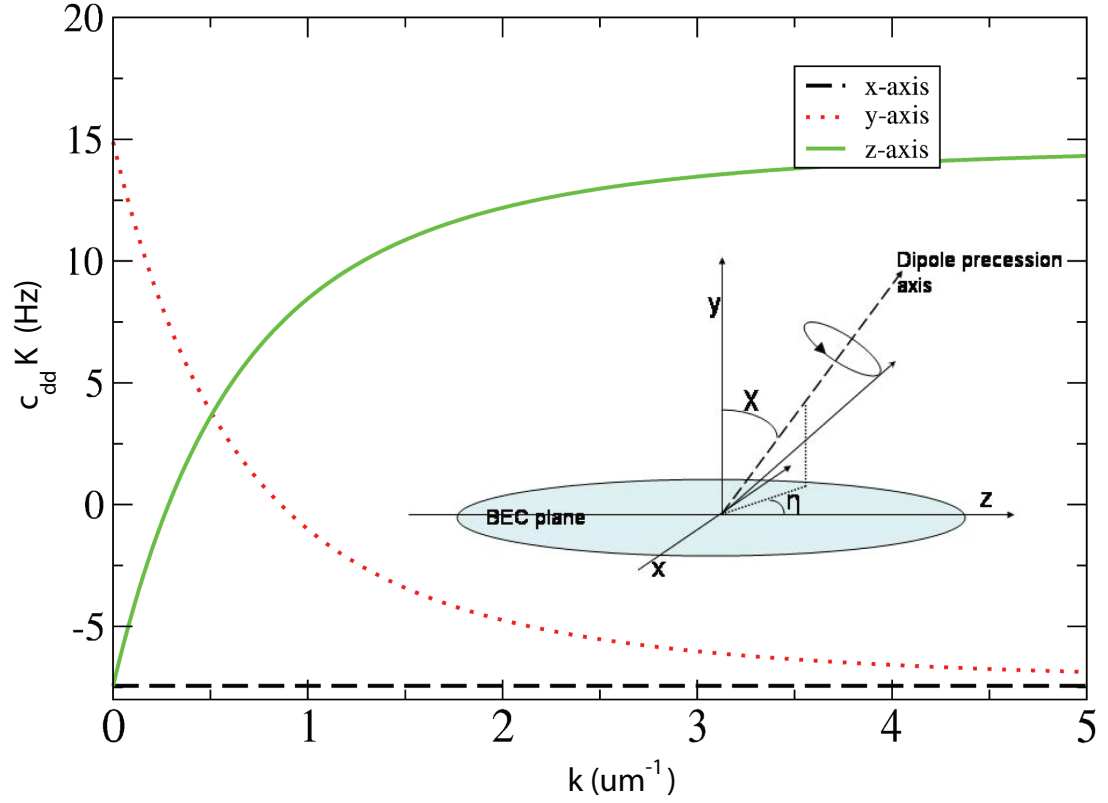


Figure 1.1: The contribution to $c_{2,eff}(k)$ from dipolar interactions is described by $c_{dd}K(k)$, where $K(k)$ is the anisotropic dipole interaction kernel (Eq 1.11) [45]. The dependence of the interaction upon k , taking $\mathbf{k} = k\hat{z}$, is shown for a few precession axis orientations, where the condensate geometry is held fixed. Here $c_{dd} = 0.8 \times 2\pi$ and $c_2 = -8 \times 2\pi$ rad/s.

shall direct the reader throughout this work. More recent additions to our experimental apparatus, such as the implementation of microwave fields (Sec 1.6) are presented here in detail. Our improved level of control over the background magnetic field in our apparatus (Sec 1.5.2) in addition to the specific optical trap geometries used to perform the discussed experiments (Sec 1.5.1) are summarized.

To characterize the spinor gas optically, we use an in situ phase contrast imaging technique which relies upon its dielectric properties. Developments in both the design and alignment of the imaging system (Sec 2.2.2) and the imaging techniques and data analysis (Sec 2.3) are discussed; in particular, our characterization of both the longitudinal and transverse magnetization of a spinor Bose gas is outlined in detail. Taking the improvements made to our imaging methodology into account, a current assessment of our detection noise floor is presented (Sec 3.2.1).

A brief chronology of our work

The experimental work presented in this thesis represents the outcome of a collaborative endeavor carried out by four team players including myself, fellow graduate student Jennie Guzman, post-doctoral fellow Mukund Vengalattore, and Professor Dan Stamper-Kurn. The lines of inquiry that we pursued and the apparatus that we used for our experiments relied significantly upon the dissertation work of James Higbie and Lorraine Sadler (Ref. [11, 14]).

Following Ref.[11], which introduced the concept behind and first demonstration of the spinor condensate magnetometer, this dissertation begins by describing the experimental work performed from December 2005 to July 2006, leading to a photon shot-noise-limited demonstration of this device Ref.[12]. I contributed to both the experimental work and the data analysis over the course of this experiment. My primary responsibility in the preliminary stage of our data analysis was to assess the phase detection noise characteristic of our background magnetic field measurements. In addition, to accompany our implementation of a spin-echo sequence in the Fall of 2005, I designed, built and implemented a polarization-stabilization unit for the laser beam which was used to optically-induce a local magnetic field. Synchronized with the π pulse implemented in the spin-echo sequence, this unit reversed the polarization of the laser beam from σ^+ to σ^- ; this enabled the continued application of the optically-induced field while the effect of spatial inhomogeneities in

the background field was reversed. The polarization of the laser beam was manipulated using an electro optic modulator, controlled by electronic feedback circuitry. However, following the construction of this device, our improved level of control over background field inhomogeneities rendered it unnecessary to use a spin-echo sequence in the experiments.

Following our demonstration of the spinor condensate magnetometer, our experimental work followed two lines of inquiry, the first of which included an exploration of the salient features predicted for the spin-mixing amplifier. The technical noise floor of our experimental apparatus at the time included spin-flip noise sources (corresponding to Larmor frequencies up to roughly 200 kHz), contaminating the performance of the spin-mixing amplifier. Following extensive efforts to characterize and reduce this noise floor, we eventually decided to perform our experiments at higher bias fields, using an independent microwave field induced quadratic shift to vary the total quadratic shift. I calibrated and implemented the microwave source in January 2007 (Sec 1.6); the experimental characterization of the spin-mixing amplifier was carried out by myself and Jennie Guzman. I was responsible for the analysis of our findings in addition to developing our theoretical understanding of the system.

Supporting our efforts to compare our experimental characterization of the spin-mixing amplifier to a quantum amplification theory has been a flurry of theoretical work. In particular, Jay Deep Sau, a fellow graduate student in the group of Marvin L. Cohen, has contributed significantly to this effort. Following the insights that we gained on the amplification of spin fluctuations in the spinor gas, we theoretically considered how to harness this parametric amplifier to generate spin squeezed states, an endeavor that has seen significant contributions from myself, Jay and Dan.

A second research direction evolved from a peculiar observation made during our preparation for the quantum quench experiment (Ref. [1]), which required a homogeneous magnetic field environment. To measure and cancel the inhomogeneities present in the magnetic field environment, we would routinely characterize the precession of a transversely magnetized cloud, using the spatial-inhomogeneity of the accrued precession phase to determine the spatial-inhomogeneity of the background magnetic field. Surprisingly, following roughly 200 ms of precession in fairly homogeneous environment ($\Delta B < 12 \mu\text{G}$), we observed the condensate magnetization to dissolve into short-range magnetic structures. Returning to this puzzling observation, we systematically studied the evolution of helical textures in a spinor gas. In the Spring of 2007 we implemented a new imaging system in the

apparatus, which was characterized by Mukund. Wondering whether the observed corrugated magnetic structures reflected a ground state for the spinor gas, we performed a slow evaporation of an initially incoherent gas and indeed observed it to condense into a spatially corrugated magnetic structure. While all the team players contributed significantly to the demanding experimental work involved, not the least of which was the perpetual resuscitation of our sensitive experimental apparatus, the analysis of the data for the publications emerging from these experiments was performed by Mukund.

In parallel to running our experiments in the basement, we have been designing and assembling the components for a new experimental apparatus over the past few years, gearing up toward studies of spinor gases in optical lattices. My contributions to this effort include the design and collection of components for the vacuum system (Summer 2005); the design of specialized in-vacuum components which were fabricated by in-house machinists (Fall 2005); and, in collaboration with Jennie, the assembly and testing of a preliminary capillary-based oven and ^{87}Rb Zeeman slower (early 2006). In addition, I designed and collected the optical components for the dual species (Rb, Li) MOT, optical trap, and diagnostic imaging systems for the new experiment (Spring 2007). Much of this work has been modified, over time, to accommodate a widened set of goals. The new apparatus will soon replace the current one, with Jennie and a new team at its helm; thus, its operational form will be documented in her thesis.

A few contributions of mine to the apparatus described in Refs [11, 14], including the optical trap's intensity stabilization unit and a new repump laser, are documented elsewhere. A theoretical treatment pertinent to the cavity experiment QED next door to our lab is included in Appendix D. This work characterizes the transmission spectrum of an optical cavity, taking into account the effects of atomic motion, as a tool for counting atoms in a cavity.

1.5 Elements of the experimental apparatus

To the extent that the construction and operation of our spinor-condensate apparatus is described in detail in Ref. [11, 14], we focus on the significant changes made to the experiment since their publication. Briefly, we discuss the geometry of the optical traps used in the series of experiments presented in Chapters 3, 4 and 6 (Sec 1.5.1); we describe our improved control over the background magnetic field in the apparatus and the

procedures we used to achieve this control (Sec 1.5.2); and we present the calibration and implementation of microwave fields in our experiments (Sec 1.6).

1.5.1 The spin-independent trap

The optical dipole trap used to confine the atoms is provided by the focus of a linearly polarized, single mode laser beam tuned to approximately 830 nm. The spatial intensity profile of the laser beam, separately controlled in the x, y directions by means of beam-shaping optics, induces a spatially-varying AC stark shift which serves as an attractive potential for the atoms. For a description of the optical components used in shaping the optical trap, the techniques used in its alignment, and the measurement of its characteristic trapping frequencies, the reader is directed to Ref. [11, 14]. In conjunction with its experimental characterization, a theoretical description of the trapping potential is also provided.

In our demonstration of the spinor condensate magnetometer presented in Chapter 3, we made use an optical dipole trap characterized by trap frequencies $(\omega_x, \omega_y, \omega_z) = 2\pi \times (165, 440, 4.4) \text{ s}^{-1}$. A condensate containing 1.4×10^6 atoms was characterized by Thomas Fermi radii $(r_x, r_y, r_z) = (5.2, 2.0, 196) \text{ }\mu\text{m}$ (Fig 1.2(a)). In particular, tight confinement of the condensate along the imaging (\hat{y}) axis enforced the spinor condensate to be effectively two-dimensional with respect to its spin degree of freedom. By imaging the spinor gas along the \hat{y} axis, we are discarding information about its magnetization profile along this direction, assuming it to be homogeneous.

In employing the condensate as a magnetic microscope, the \hat{x} dimension of the condensate profile was purposefully made to be narrow. Since our characterization of the background magnetic field was less sensitive to inhomogeneous features along the \hat{x} axis than the \hat{z} axis, our ability to control field inhomogeneities in the \hat{x} direction was comparatively less robust. To obtain quantitative measurements of an applied magnetic field, we integrated over the narrow (\hat{x}) dimension of the condensate, yielding a low-noise measurement of the field profile along the \hat{z} direction (to be discussed in Chapter 3). Enforcing a relatively tight confinement of the condensate in the \hat{x} dimension had the additional advantage of suppressing the nucleation of undesirable short-range spin excitations. As we have since observed, magnetic field inhomogeneities, which were controlled along the narrow \hat{x} dimension of the condensate to a lesser degree, can lead to short-range spatially modulated

spin structures. While this behavior may be suppressed using techniques analogous to NMR (to be discussed in Chapter 6), the trap geometry employed in the demonstration of the spinor condensate magnetometer simplified its presentation.

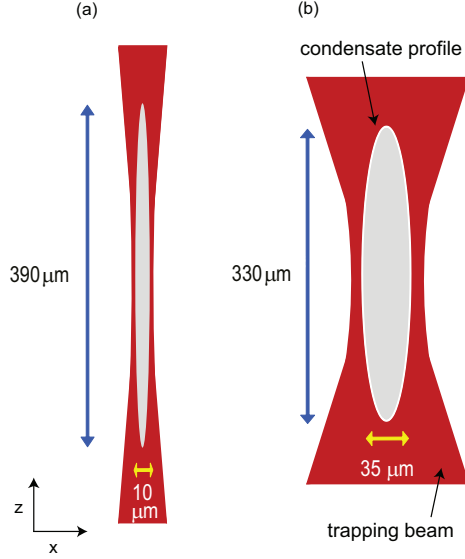


Figure 1.2: The geometry of the condensate profile, dictated by the geometry the optical trapping potential, is selected to meet the requirements of a few experimental studies. When the spinor condensate is applied as a magnetic microscope, its density profile along \hat{x} is made to be narrow, enabling robust field measurements along the \hat{z} axis (a). By widening the confinement potential, the evolution of magnetic domain structures in the spinor gas could be examined in two spatial dimensions (b).

In our characterization of the spinor condensate as an amplifier of spin fluctuations (to be discussed in Chapter 4), and as a playground for studying the evolution of spin textures (to be discussed in Chapter 6), the optically-trapped condensates were characterized by a larger diameter along the \hat{x} axis. By widening the confinement potential, the evolution of magnetic domain structures could be examined in two spatial dimensions. Further, the dynamical instabilities underlying the formation of these structures were influenced by the trap geometry. The same trap was used for both experiments, characterized by trap frequencies $(\omega_x, \omega_y, \omega_z) = 2\pi \times (39, 440, 4.2)\text{ s}^{-1}$. The Thomas Fermi radii describing these condensates, which typically contained 2×10^6 atoms, corresponded to $(r_x, r_y, r_z) = (17.6, 1.6, 165)\text{ }\mu\text{m}$ (Fig 1.2(b)).

As a future outlook for studies of spinor gases, it would be interesting to investigate the behavior of these systems as a function of the aspect ratio of the condensate density

profile. In particular, probing the dynamics of an isotropic spinor condensate (potentially produced using a high-power laser in a cross-dipole trap configuration) would enable a more straight-forward comparison with theory. By tuning the trap geometry, one can vary the dynamical instabilities in the spinor gas. In addition, one can vary the effect of dipole-dipole interactions in the spinor gas. For example, in a single-mode, three-dimensional system, such as the spherical node of an optical lattice potential, the effect of dipole-dipole interactions is geometrically averaged to zero.

1.5.2 Controlling the background magnetic field

Our studies of spinor condensates require precise control over the magnitude, orientation, and spatial variation of the background magnetic field. The characterization and control of the bias magnetic field used in our experiments is described by Ref. [11, 14]. The bias field was produced using three pairs of coils, each of which was arranged in a Helmholtz configuration outside the vacuum system. Both the magnitude and orientation of the applied magnetic field were calibrated as a function of the current in each pair of bias coils, to the level of a few mG. The magnetic field reproducibility, upon multiple repetitions of the experiment, was similarly at the level of a few mG.

Due to the imperfect geometry of the bias coils and contributions to the magnetic field from various components of the experimental apparatus, the magnetic field at the location of the condensate was spatially inhomogeneous. With the use of suitable gradient and curvature coils, the residual inhomogeneities in the background magnetic field could be controlled. In our experiments, the magnetic bias field was typically given by $\mathbf{B} = B\hat{z}$. The magnetic field gradients along the \hat{x} and \hat{z} directions, given by dB_z/dz and dB_z/dx , were controlled using two pairs of coils located outside the vacuum chamber. Each pair of coils was arranged in an anti-Helmholtz configuration, the first of which, denoted as the “axial gradient coils”, was aligned to the \hat{z} axis; the second of which, denoted as the “transverse gradient coils”, was aligned to the \hat{x} axis. In addition, the magnetic field curvature along the \hat{z} axis was controlled by running a small current through a \hat{z} -oriented pair of coils, located inside the vacuum chamber. During the initial stage of the experimental sequence in which a cold gas of magnetically trapped atoms was produced, this same pair of coils served as the “curvature coils” for the magnetic trap [11, 14].

To enable sensitive magnetic field measurements and to follow the temporal evo-

lution of the spinor condensate out to long evolution times, we required a homogeneous background magnetic field whose spatial variation was less than a few μG across the spatial extent of the condensate. Without this level of control, the field sensitivity of the magnetometer was limited by inhomogeneities in the background magnetic field. In addition, dynamics in the spinor gas were found to be sensitive to field inhomogeneities. Prior to performing a given experiment, several hours were typically dedicated to obtaining a homogeneous background magnetic field,

To spatially resolve the background magnetic field in two dimensions, we imaged the Larmor precession of the condensate magnetization (to be discussed in Section 2.3). The condensate was initially prepared in a uniformly magnetized state, e.g. $\mathbf{M}(x, z) = M\hat{x}$, oriented transverse to the bias magnetic field, $B\hat{z}$. At a given location in the condensate, the condensate spin precesses according to the magnitude of the local magnetic field. The local phase of precession, accrued following a given evolution period, is proportional to the local value of the magnetic field. By constructing a spatial map of the relative phase of precession $\delta\phi_{LP}(\mathbf{r})$, accrued at different locations in the condensate, we were able to determine the spatial variation of the background magnetic field, i.e., $\delta B(\mathbf{r}) = (\hbar/g_F\mu_B)(\delta\phi(\mathbf{r})/t)$. This corresponds to the principle of operation of the spinor condensate magnetometer, to be discussed in more detail Section 3.1.3.

Following a given evolution period, the contribution to the background field from a \hat{z} -oriented magnetic field gradient was measured using,

$$\frac{dB_z}{dz} = \frac{\hbar}{g_F\mu_B t} \frac{d\phi_z}{dz}, \quad (1.15)$$

where the phase gradient $d\phi_z/dz$ was determined from a polynomial fit to $\phi(\mathbf{r})$, averaged in the x direction over a central region of the condensate. The control current for the axial gradient coils was adjusted to compensate for the measured field gradient. By gradually increasing the evolution time, t , more sensitive measurements of dB_z/dz were made. At long evolution times (up to 350 ms), the current was adjusted at the level of 0.1 mA, such that the field variation along the \hat{z} direction was reduced to the level of $|\Delta B_z| = |dB_z/dz|\Delta z < 3 \mu G$. For typical experiment conditions, $|dB_z/dz|$ was reduced to a level of 0.1 mG/cm; however prior to achieving this level of control, measurements of other contributions to the field inhomogeneities had to be characterized.

In addition to the contribution to the background magnetic field from a \hat{z} -oriented field gradient, the contribution from a \hat{x} -oriented field gradient was also measured and re-

duced. However, due to the narrow x -dimension of the condensate, this measurement was performed with a different bias field configuration; instead, a bias field directed along \hat{x} , provided by the same Helmholtz coils, was used. This was motivated by the observation that since magnetic field is curl-free in free space, $|dB_z/dx| = |dB_x/dz|$. In this configuration, the inhomogeneity of the accrued Larmor phase, measured along the advantageously larger z dimension of the condensate, could be used to sense dB_x/dz . Using the above procedure, the measured gradient dB_x/dz was determined; next, by adjusting the control current for the transverse gradient coils, it was systematically reduced. Ideally the transverse gradient coils would be oriented along the \hat{x} axis, but due to the constraints imposed by the vacuum chamber, they were oriented at roughly 30 degrees to this axis. In practise, the control currents for the axial and transverse coils were adjusted in iteration, using the above procedures.

To observe the homogeneous Larmor precession of the condensate magnetization following evolution periods greater than roughly 200 ms, small adjustments to the control currents for both the axial and transverse gradient coils were made with the bias field orientation held fixed; for our experiments, $B = B\hat{z}$. Contributions to dB_z/dz were compensated for by measuring and reducing $d\phi_z/dz$, as discussed. Somewhat less trivially, contributions to dB_z/dx were compensated for by enforcing the spatially homogeneous precession of the gas. For instance, when the control current for the transverse gradient coils was tuned away from its optimal value (corresponding to $|dB_z/dx| < 0.3$ mG/cm), the condensation magnetization pattern was found to dissolve into small-scale magnetic domains following long evolution periods ($t > 200$ ms), to be discussed in Chapter 6. The final control current settings for the axial and transverse gradient coils were on the order of 1-3 A; the measured magnetic field gradients were reduced to the level of $|dB_z/dz|, |dB_z/dx| < 0.1 - 0.3$ mG/cm.

In addition, the contribution to the background \hat{z} -oriented magnetic field curvature could be separately controlled using a small current directed through “curvature coils” of the magnetic trap. Typically on the order of 0.3 A, this control current enabled the magnetic field curvature to be reduced to a level of $d^2B_z/dz^2 < 10 - 20$ mG/cm².

1.5.3 Applying modulated magnetic fields

Noise sources in the magnetic field environment, characterized by RF frequencies up to roughly 140 kHz, prevented the study spin dynamics at very small magnetic fields.

In order to study spin dynamics which were unaffected by spurious sources of spin-flips, our experiments were performed at higher magnetic fields, $g_F \mu_B B / h > 140$ kHz ($B > 200$ mG). However, the field-induced quadratic shift, $q_B / h = 70$ Hz/G² B^2 , quickly becomes comparable to the relevant spin-dependent energy scales as the magnetic field is raised; for example, $q_B / h = c_2 n / h \approx 8$ Hz for $B \approx 460$ mG. In order to study the behavior of the spinor condensate at low quadratic shift, one requires an additional control of its magnitude which is independent of the bias magnetic field.

This control was achieved by introducing a modulated magnetic field, provided by a linearly polarized microwave field, detuned from the $|F = 1, m_z = 0\rangle$ to $|F = 2, m_z = 0\rangle$ hyperfine transition. The applied microwave field induced an AC quadratic Zeeman shift, which was either positive or negative in sign, depending upon its detuning from resonance.

Microwave field induced AC Zeeman shift

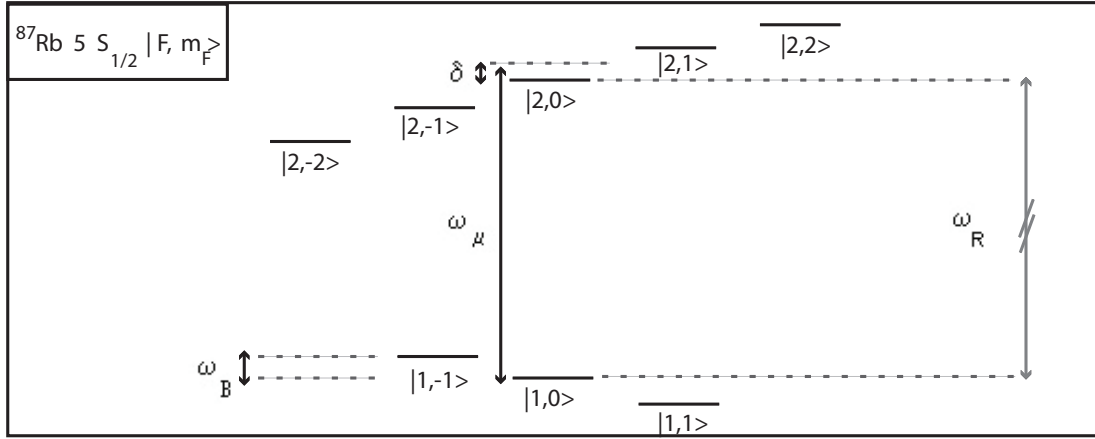


Figure 1.3: The ground state $5 S_{1/2}$, $F = 1, 2$ hyperfine manifolds of ^{87}Rb are shown. The dominant shift in energy of the magnetic hyperfine levels, m_F , is due to the linear Zeeman shift, $h\omega_B = g_F \mu_B B_z$, at low magnetic fields. An applied microwave field, driven at a frequency $\omega_\mu = \omega_R + \delta$, is detuned from the $|F = 1, m_z = 0\rangle$ to $|F = 2, m_z = 0\rangle$ transition by δ . It is used to apply an AC Zeeman shift to the $|F = 1, m_z = 0\rangle$ state, which is quadratic in m_F and the applied microwave field. This applied quadratic shift may be tuned using both the amplitude and detuning and the microwave field.

An applied magnetic field, modulated at a frequency ω_μ , and detuned from the $|F = 1, m_z = 0\rangle$ to $|F' = 2, m'_z = 0\rangle$ hyperfine transition by a frequency δ , couples the

$F = 1$ and $F' = 2$ ground state manifolds (Fig. 1.3). Here, we are interested in making use of the AC Zeeman shift of a ground state $|F = 1, m_i\rangle$ resulting from its coupling to the states $|F' = 2, m'\rangle$ by means of the applied field $\vec{B}_\mu(t) = \vec{B}_\mu e^{i\omega_\mu t}$. The resulting AC Zeeman shift is given by,

$$\varepsilon_Z = \sum_m \frac{|V_{m',m_i}|^2}{\omega_\mu - \omega_{m',m_i}}, \quad (1.16)$$

where $V = -\vec{\mu} \cdot \vec{B}_\mu = g_F \mu_B (F_z B_{\mu,z} + F_+ B_{\mu,-} + F_- B_{\mu,+})$, and we have decomposed the field \vec{B}_μ and spin \vec{F} vectors with respect to a standard spherical basis set labeled by m_z the \hat{z} -projection of the condensate spin, \mathbf{F} . The energetic shift can be written as,

$$\varepsilon_Z = (g_F \mu_B)^2 \sum_{m'} \frac{|B_{\mu,z} \langle m' | F_z | m_i \rangle + B_{\mu,+} \langle m' | F_- | m_i \rangle + B_{\mu,-} \langle m' | F_+ | m_i \rangle|^2}{\omega_\mu - \omega_{m',m_i}}. \quad (1.17)$$

Given the initial state $|F = 1, m_i\rangle$, then only one coupling element to a given state in the upper ground state manifold, $|F' = 2, m'\rangle$, among the coupling elements $\langle m' | F_z | m_i \rangle$ and $\langle m' | S_\pm | m_i \rangle$, is nonzero. Thus it is convenient to express ε_Z as,

$$\begin{aligned} \varepsilon_Z = & (g_F \mu_B)^2 \left(\frac{|B_{\mu,z}|^2 |\langle F = 1, m_i = k | F_z | F' = 2, m' = k \rangle|^2}{\delta_{F=1, m_i=k; F'=2, m'=k}} \right) \\ & + (g_F \mu_B)^2 \left(\frac{|B_{\mu,+}|^2 |\langle F = 1, m_i = k | F_- | F' = 2, m' = k + 1 \rangle|^2}{\delta_{F=1, m_i=k; F'=2, m'=k+1}} \right) \\ & + (g_F \mu_B)^2 \left(\frac{|B_{\mu,-}|^2 |\langle F = 1, m_i = k | F_+ | F' = 2, m' = k - 1 \rangle|^2}{\delta_{F=1, m_i=k; F'=2, m'=k-1}} \right), \end{aligned} \quad (1.18)$$

where the above field-dependent detunings are in general given by,

$$\begin{aligned} \delta_{F=1, m_F; F'=2, m_{F'}} & \equiv \omega_\mu - \omega_{m_{F'}, m_F} \\ & = (\omega_R + \delta) - (\omega_R + g_{F'} \mu_B m_{F'} B - g_F \mu_B m_F B) \\ & = \delta - (g_{F'} \mu_B m_{F'} B - g_F \mu_B m_F B) \\ & \equiv \delta - \omega_{B, m_F, m_{F'}}, \end{aligned} \quad (1.19)$$

and $g_{2,1} = \pm 1/2$, $\mu_B = 1.4$ MHz/G, and $\omega_{B, m_F, m_{F'}}$ corresponds to the linear Zeeman splitting between $m_F, m_{F'}$ due to the static magnetic field $B\hat{z}$. The coupling elements can be calculated using

$$\langle F, m_F | F_q | F', m_{F'} \rangle = \langle F || F_q || F' \rangle \left((-1)^{F'-1+m_F} \sqrt{2F+1} \begin{pmatrix} F' & 1 & F \\ m_{F'} & q & -m_F \end{pmatrix} \right) \quad (1.20)$$

where an expanded form of the standard short-hand notation, $\langle F || F_q || F' \rangle$, is available in most atomic physics textbooks. At this point we have fully specified the form of the applied AC Zeeman shift, $\varepsilon_Z(B_\mu, \delta, m_i)$.

Microwave field induced quadratic shift

We are interested in extracting the *quadratic* energy shift relevant to our experimental study of the $F = 1$ manifold, which results from the field-induced AC Zeeman shift. To do so, we decompose $\varepsilon_Z(B_\mu, \delta, m_i)$ as,

$$\begin{aligned}\varepsilon_Z(B_\mu, \delta, m_F) &= a(B_\mu, \delta) + b(B_\mu, \delta)m_F + c(B_\mu, \delta)m_F^2 \\ a(B_\mu, \delta) &= \varepsilon_Z(B_\mu, \delta, 0) \\ b(B_\mu, \delta) &= (\varepsilon_Z(B_\mu, \delta, 1) - \varepsilon_Z(B_\mu, \delta, -1))/2 \\ c(B_\mu, \delta) &= (\varepsilon_Z(B_\mu, \delta, 1) + \varepsilon_Z(B_\mu, \delta, -1))/2 - \varepsilon_Z(B_\mu, \delta, 0)\end{aligned}\tag{1.21}$$

where the field-induced linear and quadratic shifts corresponds to $b(B_\mu, \delta)$ and $c(B_\mu, \delta)$ respectively.

Including the effect of the applied static magnetic field, a ground state level $|F = 1, m_F\rangle$ is shifted in energy by,

$$\varepsilon_{tot}(B_\mu, \delta, m_F, B) = a(B_\mu, \delta) + (b(B_\mu, \delta) + g_F\mu_B B)m_F + (c(B_\mu, \delta) + q_B)m_F^2,\tag{1.22}$$

thus defining an effective linear and quadratic shift. We can re-express this energy shift in a form which connects directly to the physical quantities of interest in our experiment,

$$\varepsilon_{tot}(B_\mu, \delta, m_F, B) = const + \hbar\omega_{Larmor}(B_\mu, \delta, B)m_F + q_{eff}(B_\mu, \delta, B)m_F^2.\tag{1.23}$$

Introducing a microwave field results in a linear energy shift, which modifies the Larmor precession frequency very slightly. For typical parameters of our experiment, $b(B_\mu, \delta)/h \leq 1$ Hz whereas $g_F\mu_B B/h \approx 250$ kHz. In addition, it introduces a quadratic energy shift. For a $F = 1$ gas of ^{87}Rb atoms, the effective induced quadratic shift is described by,

$$\begin{aligned}q_{eff} &\equiv q_\mu + q_B \\ q_\mu &= c(B_\mu, \delta) \\ q_B/h &= 70\text{Hz/G}^2 B^2.\end{aligned}\tag{1.24}$$

In the experiment, we typically use q_μ to tune q_{eff} over the range $-2c_2n \leq q_{eff} \gg 2c_2n$. Typically, $\omega_{Larmor} \geq 2\pi \times (230 \text{ kHz})$ and $q_B/h \geq 8 \text{ Hz}$.

Choice of parameters for the applied quadratic shift

In the experiment, the microwave waveguide was oriented at 30° with respect to the \hat{x} axis. The applied AC magnetic field is given by $\vec{B} = B \cos(30^\circ)\hat{z} + B \sin(30^\circ)\hat{x}$. Its spherical components are therefore given by $B_\pm = B_x \pm iB_y = B \sin(30^\circ)$. Ideally we would choose \vec{B} to be polarized along \hat{z} so $B_\pm = 0$, but the available viewport to which we could attach the microwave waveguide was off-axis.

The value for δ was chosen to be sufficiently far from resonance to avoid populating the $F' = 2, m_{F'}$ levels, to apply a q_{eff} of the desired magnitude, and to avoid field-dependent resonances. For the experiments discussed in this thesis, we chose δ such that $\delta \ll \omega_{B, m_F, m_{F'}}$; for example, $\delta = 2\pi \times (35 \text{ kHz})$ and $g_1 \mu_B B / h = 230 \text{ kHz}$. To a good approximation, the applied field simply shifted the energy of the $|F = 1, m = 0\rangle$ state. The resulting fractional population of the $|F' = 2, m = 0, \pm 1\rangle$ states was less than one part in 10^4 for typical parameters, and was neglected. The coupling to the $|F' = 2, m = \pm 1\rangle$ states, suppressed by $\delta / \sqrt{3} \omega_{B, m_F, m_{F'}}$ was also assumed to play a negligible role. These assumptions were tested empirically, the results of which are presented in Section 4.4.2.

Under these approximations and operating conditions, the AC field-induced quadratic shift simplifies to,

$$q_\mu = -\frac{\hbar \Omega_R^2}{4 \delta}, \quad (1.25)$$

where $\Omega_R = g_F \mu_B |B_\mu| / \hbar$. The calibration of q_μ is discussed in the upcoming sections. To give the reader a sense of reasonable parameters, with an available microwave power of $P_\mu < 10 \text{ Watts}$, we were able to apply an AC magnetic field with an amplitude $|B_\mu| < 14.3 \text{ mG}$ ($\Omega_R < 2\pi \times (9.9 \text{ kHz})$). For $\delta_\mu = 2\pi \times (35 \text{ kHz})$, this corresponded to $q_\mu / h < 700 \text{ Hz}$. In the reported studies of spin dynamics in Chapter 4, however, we applied $q_\mu / h < 20 \text{ Hz}$.

Microwave source and implementation

The implemented microwave source which was used to apply a modulated magnetic field to the condensate is illustrated in Figure 1.4. A frequency source (IFR) referenced to a Rb atomic clock provides an output of 13 dBm at $\omega_{IFR} = (\omega_R / 2 - \Delta)$; the frequencies ω_R and Δ are defined by Figure 1.4. The output passes through a TTL-controlled switch (Minicircuits, rated up to 5 GHz). It is then doubled by a frequency doubler/amplifier (Marki microwave, DA-0210K) which provides an output of 17 dBm at $\omega_{doubler} = (\omega_R - 2\Delta)$. This provides the local oscillator input (L) to a mixer (Minicircuits) and acts as the carrier

signal. Depending on the required output of the mixer, the type of mixer and attenuation to its input (L) were adjusted. The modulation input (I) is provided by a function generator (SRS DS340) which adds sidebands to the carrier at frequencies $\omega_R - 2\Delta \pm \omega_{SRS}$. The SRS drive frequency and Δ therefore determine the detuning, δ , of the applied microwave field, ω_μ . The experiment parameters for the spin-mixing amplifier experiment (Ch.4) included $\Delta = 2\pi \times (20 \text{ MHz})$, $\omega_{IFR} = 2\pi \times (3.407341305 \text{ GHz})$, and $\omega_{SRS} = 2\pi \times (19965202 \text{ Hz})$ ($\delta = 2\pi \times (-35 \text{ kHz})$), or $\omega_{SRS} = 2\pi \times (20035202 \text{ Hz})$ ($\delta = 2\pi \times (35 \text{ kHz})$).

The linewidth of the $|F = 1, m_z = 0\rangle$ to $|F = 2, m_z = 0\rangle$ hyperfine transition is small; thus, by choosing both $\Delta \gg 1 \text{ kHz}$, $\delta \gg 1 \text{ kHz}$ the carrier and red-detuned sideband have a negligible effect upon the atoms, and the sideband closest to resonance is used to address the atoms. Its frequency is given by $\omega_\mu = \omega_R - 2\Delta + \omega_{SRS} \equiv \omega_R + \delta$. The output of the mixer (R) is sent to a 40 dB amplifier with a maximum total output of 20 Watts. The output of the amplifier connects to a circulator/isolator (ATM Advanced Technical Materials P/N ATc4-8, Freq 4-8 GHz) followed by a stub-tuner (Maury Microwave, model 1819D). This is attached to the μ -wave waveguide (ATM Advanced Technical Materials WG P/N 137-201B-2, Freq 5.85-8.2 GHz) which is taped directly to a viewport of the chamber.

The circulator/isolator protects the amplifier from back-reflections. We chose to use a circulator which has three ports, an input (1), an output (2), and a re-circulation port (3) which probes the reflected power, P_{ref} . By measuring this reflected power while adjusting the stub tuner, one can minimize it and in so doing impedance match the waveguide to the chamber. After adjusting the stub tuner, we placed a 50 ohm terminator on the third port of the circulator so that it acts as an isolator, sending the reflected power to ground. We used the regular 2 Watt 50 Ohm terminators from Minicircuits. The reflected power was typically 10^{-4} times the input power.

The microwave cables used to connect the output of the amplifier to the isolator, stub-tuner and waveguide were provided by the company Huber Suhner. Their losses were lower than the cables provided by Pasternack (by roughly 2 dB). One cable part number we used was ST18/SMAm/SMAm/36 Order No. 84002061. An essential calibration tool is a directional coupler (Pasternack PE2210-02). This part has three ports, an input, an output, and a directional probe which probes the input, $P_{probe} = P_{in} - 20 \text{ dB}$. If connected in reverse, it can be used to probe reflected power.

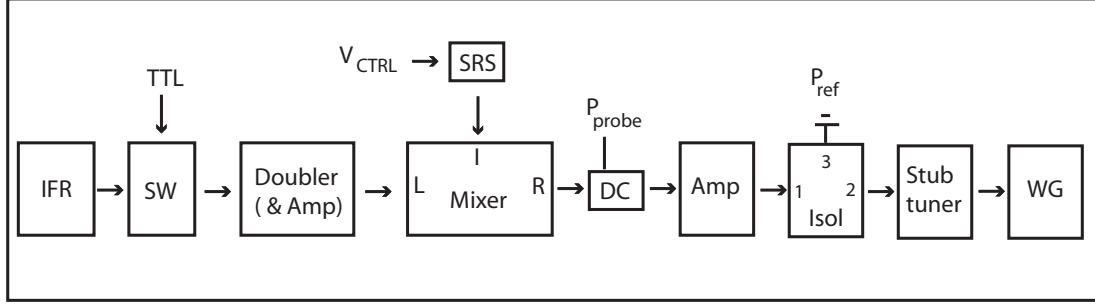


Figure 1.4: A schematic describing the implemented microwave source and parts used, as referenced in the text.

Calibration of the microwaves: field measurements

Prior to implementing the microwave source in the experiment, an applied microwave field was calibrated using a test vacuum chamber. This enabled us to determine whether the simple approach of taping the waveguide to a viewport of the chamber would provide a sufficiently large microwave field at the location of the atoms.

The applied microwave field was calibrated using Marconi antennae. A Marconi antenna designed to broadcast or sense a field of wavelength λ consists a ground plane, made with a copper disk of diameter λ (or larger), and a half-dipole, made using a wire of length $\lambda/4$, which is centered on the plane and normal to it. The antenna emits a dipolar radiation pattern, produced by charge oscillating on the wire, whose mirror image is located below the ground plane.

A thin copper disk, with thickness four thousandths of an inch, and a diameter of 8 cm was used for the ground plane (Fig. 1.5). An SMA connector was braised onto the copper disk from below, and an approximately 1 cm long wire was soldered to the connector, above the ground plane. Cleaning the ground plane with acid (HNO_3), such that no oxidation remained upon it (turning the copper pink) was important in optimizing the response of the antenna.

The length of the dipole wire was tuned empirically such that the antenna broadcast at the desired frequency. This was accomplished by measuring the reflected power spectrum. The length of the wire was adjusted so as to minimize the reflected power at the desired frequency. As illustrated in Fig. 1.6, the reflected power was measured using the directional coupler (DC), connected in reverse, such that the reflected rather than input power was probed. A typical response curve of a homebuilt Marconi antenna tuned to

6.8 GHz marconi antenna

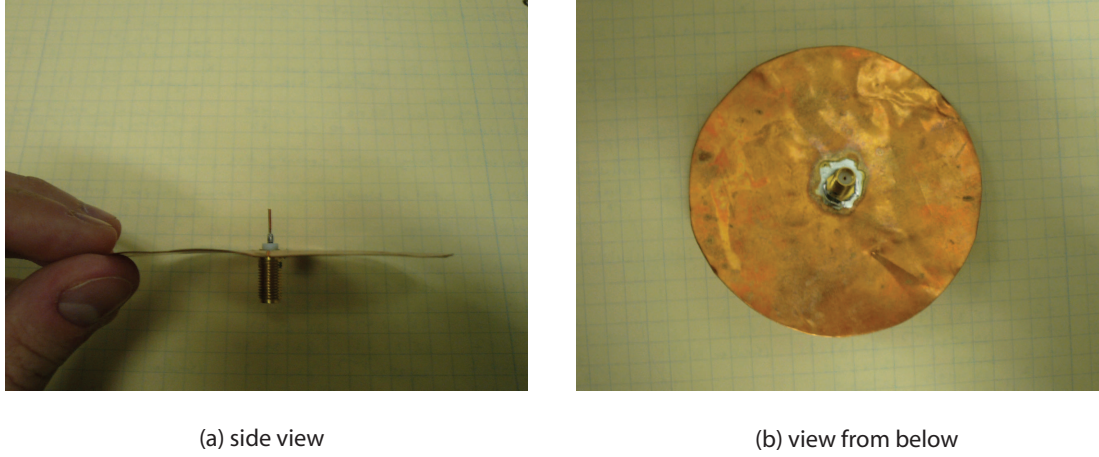


Figure 1.5: Images of the 6.8 GHz marconi antenna designed and used to calibrate applied microwave fields.

approximately 6.8 GHz is shown in Fig. 1.6. A broad dip in the reflected power spectrum is centered around the resonance frequency of the antenna. In practise, one continues to shorten the wire until that resonance matches with the desired frequency.

To calibrate one pickup antenna, a second identical antenna was made which served as a known quantitative field source, co-aligned with the first antenna. The oscillating electric field radiated by the source antenna was measured by the pickup antenna as a function of their separation. Specifically, the power measured on a spectrum analyzer, using the pickup antenna, is given by $P_m = V_{rms}^2/50\Omega = ((1/2)E_\mu(\lambda/4))^2/50\Omega$, where V_{rms} refers to the potential across the dipole wire. This is a probe of the magnitude of the electric field sensed by that antenna, E_μ . The sensed magnetic field is then given by $B_\mu = 10^4 E_\mu/c$ G. Once the pickup antenna was calibrated, it could be used to measure an applied modulated magnetic field from an arbitrary source.

The aforementioned waveguide was centered and taped onto the viewport of a vacuum chamber similar to the one in the experiment, and impedance matched to its environment using the stub tuner. The calibrated pickup antenna was placed at the center of the chamber. For an input power to the waveguide of one Watt, a 3-6 mG field was measured at the center of the chamber, depending upon the configuration of the measurement. The steel chamber served to guide the applied field. In comparison, an antenna placed an equivalent distance away (approximately 12 cm) from a waveguide which broadcast into

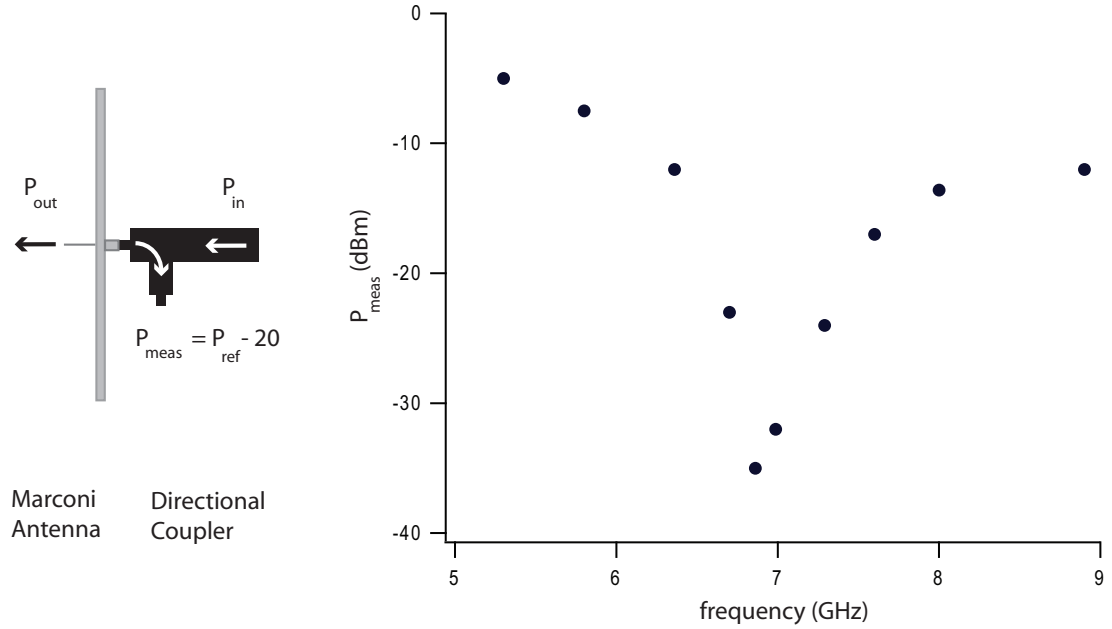


Figure 1.6: The marconi antenna was tuned by adjusting the length of its dipole wire such the spectrum of the reflected power, measured using a directional coupler in the configuration shown, was minimized at the desired operating frequency.

free space, detected a field suppressed by approximately 10 dB.

Calibration of the microwave drive field with the atoms

To calibrate the applied quadratic shift at a given detuning, it was necessary to confirm independently the magnitude of the applied microwave field. To do so, a thermal gas of optically trapped $|F = 1, m_z = 0\rangle$ atoms was irradiated by a microwave field resonant with the $|F = 1, m_z = 0\rangle$ to $|F = 2, m_z = 0\rangle$ hyperfine transition. As a result, population was transferred from the $|F = 1, m_z = 0\rangle$ state to the $|F = 2, m_z = 0\rangle$ state. The population in the $|F = 2, m_z = 0\rangle$ state after a given irradiation period was determined from an on-resonance time-of-flight image (using a Stern Gerlach technique described in Sec 2.5) taken without the use of a repump beam so as to be insensitive to $F = 1$ atoms. The population of $|F = 2, m_z = 0\rangle$ atoms oscillated at a frequency given by the on-resonance Rabi frequency, Ω_R , proportional to the magnitude of the modulated magnetic field, B_μ .

First, the modulation frequency resonant with the transition, ω_R , was measured by irradiating the atoms at low power for a short time period, t_μ , and determining the population of $|F = 2, m_z = 0\rangle$ atoms as a function of the frequency of the applied microwave

field. This *Rabi pedestal*, whose center determines ω_R , was measured at low power ($\Omega_R = 2\pi \times (170 \text{ Hz})$) for $t_\mu = 1.2 \text{ ms}$, at a bias magnetic field of $g_f \mu_B B_z / h = 230 \text{ kHz}$. We observed its center to be offset from the IFR setting taken from Ref. [46] ($\omega_R/2 = 2\pi \times 3.417341305452145(45)$) by roughly 200 Hz.

The on-resonance Rabi frequency, Ω_R , was determined by measuring the population in $|F = 2, m_z = 0\rangle$ as a function of the irradiation period t_μ , with the frequency of the irradiation field tuned to the empirically-determined resonance, $\omega_\mu = \omega_R$. For an initial population of 6.6×10^6 atoms in $|F = 1, m_z = 0\rangle$, a few Rabi oscillations at $\Omega_R = 2\pi \times (630 \text{ Hz})$ are shown in Fig. 1.7, measured at the same experiment conditions. As a function of the input power to the waveguide, P_μ , we calibrated the Rabi frequency, $\Omega_R = 2\pi \times 3.1 \text{ kHz/W}^2 P_\mu^2$. This corresponds to a modulated magnetic field of magnitude 4.4 mG for 1 Watt of power, which is in remarkable agreement with the rough initial measurement of the applied field with the Marconi antenna.

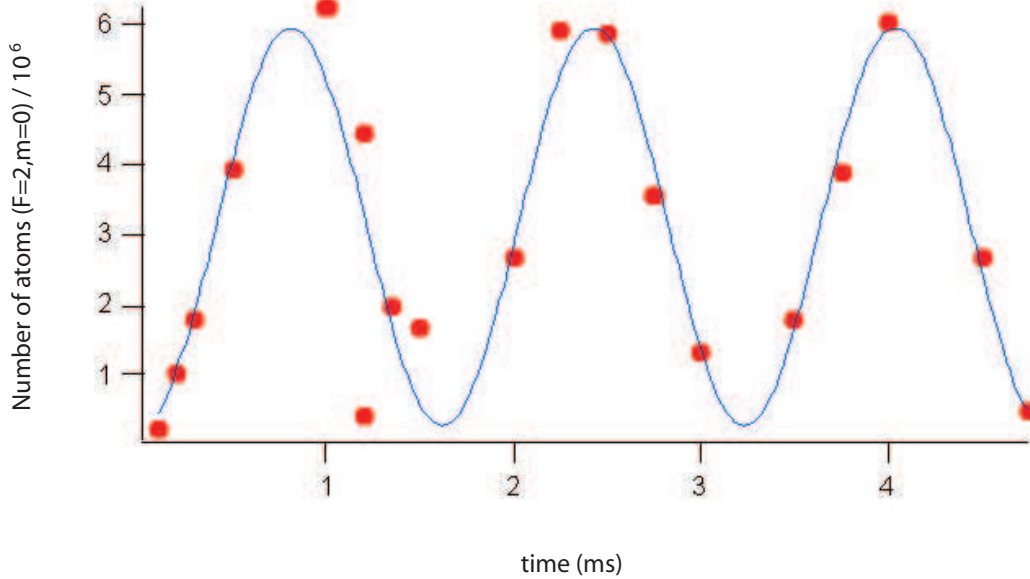


Figure 1.7: Images of the 6.8 GHz marconni antenna designed and used to calibrate applied microwave fields.

In running the experiment, the measured value of Ω_R^2 for the same input power would vary by up to 25 percent over a one week period, presumably due to a slight change in the position of the waveguide and the relevant impedance matching. In order to determine precisely the microwave-induced quadratic shift, $q_\mu = \Omega_R^2/\delta$, Ω_R was routinely calibrated

as a function of its control setting within one to two days of taking data.

In Figure 1.8, the on-resonance Rabi frequency Ω_R is shown as a function of its control setting – a computer-controlled analog voltage, used as the external amplitude control for the function generator. As described, the output of the SRS was used as the input to a mixer. Thus, the amplitude of the resulting sideband, which served as the frequency source for the relevant microwave field, reflects the characteristic nonlinear response curve of a mixer. The output power of the microwave amplifier, measured using a spectrum analyzer, exhibited the same dependence upon the control setting as the squared Rabi frequency Ω_R^2 , measured using the atoms.

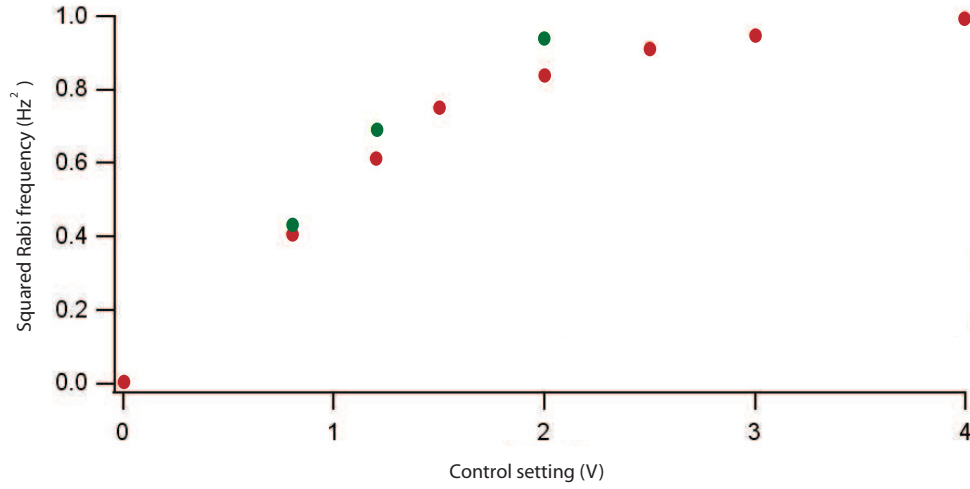


Figure 1.8: The on-resonance squared Rabi frequency, Ω_R^2 , measured as a function of the control setting for the applied microwave field. The red and green circles correspond to measurements of Ω_R^2 performed twelve days apart.

An additional calibration of q_μ which makes use of the phase transition of the spinor condensate, and the empirical tests supporting our choice of operating parameters Ω_R, δ , are presented in the context of that experiment, in Section 4.4.2.

Chapter 2

Seeing Spinor Condensates

To investigate the rich array of physics associated with the $F = 1$ spinor Bose condensate, we characterize the spinor order parameter optically, using an in situ phase contrast imaging technique which relies upon the dielectric properties of the spinor gas. To motivate our imaging technique, we show that by measuring the dielectric susceptibility tensor of a $F = 1$ spinor we may completely characterize its key properties, including its scalar density, vector magnetization, and tensor quadrupole moment. Our imaging technique enables the direct observation of features of the spinor order parameter, such as spin textures, with high spatial resolution. The implementation and characterization of a new $2\text{ }\mu\text{m}$ -resolution imaging system is presented, in addition to the experimental techniques and data analysis which enable the characterization of both the longitudinal and transverse magnetization of a spinor Bose gas.

2.1 Dielectric properties of $F = 1$ spinor gases

Having laid out the compelling energetic landscape of spinor Bose condensates and established the experimental controls to facilitate its exploration, our next task is to devise measurements suitable to its direct characterization. In our experiments, we characterize the spinor order parameter optically, using an in situ phase contrast imaging technique which relies upon the dielectric properties of the spinor gas. This enables the direct observation of features of the spinor order parameter, such as spin textures, with high spatial resolution.

By fully characterizing the dielectric tensor of an $F = 1$ spinor gas, one may obtain a complete description of the three-component spinor order parameter, ψ_i . This

follows from the fact that both the dielectric susceptibility tensor χ_{ab} and the one-body density matrix $m_{ab} = \psi_a^\dagger \psi_b$, which characterize an $F = 1$ spinor gas, correspond to rank two tensors, each constructed by the product of two angular momentum one objects. A direct mapping between two second-rank tensors may be obtained by decomposing each in terms of its irreducible components with angular momentum 0, 1, and 2. For example, by experimentally characterizing the components of dielectric susceptibility tensor, χ_{ab} , one may determine m_{ab} using known proportionality constants.

The properties of an $F = 1$ spinor order parameter, ψ_a , may be gleaned from the irreducible tensor components ρ, S_a, N_{ab} of its one-body density matrix with angular momentum 0, 1, and 2, where

$$\begin{aligned}\rho &= \sum_j m_{jj} = \psi^\dagger \cdot \psi, \\ S_a &= -i\varepsilon_{abc} m_{bc} = -i(\psi^\dagger \times \psi)_a, \\ N_{ab} &= \frac{1}{2}(m_{ab} + m_{ba}) - \frac{\rho}{3}\delta_{ab},\end{aligned}\tag{2.1}$$

and ε_{abc} is the totally antisymmetric unit tensor. Here ρ, S_a , and N_{ab} correspond to the scalar number density, vector spin density, and second-rank nematicity (or quadrupole moment) of the spinor. These three properties uniquely define a given $F = 1$ spinor. We shall return to them often throughout this discussion and in the analysis of the presented experimental studies.

2.1.1 Properties of a spin-1 object

To develop an understanding of the properties of $F = 1$ spinors it is helpful to begin by considering two families of states, denoted as magnetic and polar. Following our introduction of these families of states, we will examine their spin and nematic character in relation to the measurable properties of their characteristic dielectric susceptibility tensors.

A magnetic state is one which may be expressed by a rotation of the \hat{z} unit vector,

expressed as

$$\begin{aligned}\xi_{Mag} &= e^{i\theta} U_{rot}(\alpha, \beta, \tau) \begin{pmatrix} 1 \\ 0 \\ 0 \end{pmatrix} \\ &= e^{i(\theta-\tau)} \begin{pmatrix} e^{-i\alpha} \cos^2 \beta/2 \\ \sqrt{2} \cos \beta/2 \sin \beta/2 \\ e^{i\alpha} \sin^2 \beta/2 \end{pmatrix};\end{aligned}\tag{2.2}$$

it is described by Euler rotation angles α, β , and τ , and an overall phase θ [27]. Here we express ξ_{Mag} in terms of the standard spherical basis. The spin S_a of a magnetic state may be interpreted simply as a unit vector,

$$\vec{S} = \cos \beta \hat{z} + \sin \beta (\cos \alpha \hat{x} + \sin \alpha \hat{y})\tag{2.3}$$

oriented at an angle β with respect to \hat{z} and an angle α in the xy plane. The configurations of magnetic states, ξ_{Mag} , are labeled by three Euler rotation angles, and obey the symmetry requirements imposed by the SO(3) symmetry group. Here SO(3) corresponds to the group of rotations in three-dimensions. In our experiments, we will encounter states of the form ξ_{Mag} when the spin-dependent Hamiltonian is tuned such that $|\langle F \rangle| = 1$ is energetically favorable; these states are characterized by a macroscopic magnetization. Reminiscent of co-aligned spins in a solid state magnet, the family of states ξ_{Mag} is denoted as magnetic.

A second family of states, denoted as polar, may be determined from the rotation of an unmagnetized but fully coherent state given by,

$$\begin{aligned}\xi_{Pol} &= e^{i\theta} U_{rot}(\alpha, \beta, \tau) \begin{pmatrix} 0 \\ 1 \\ 0 \end{pmatrix} \\ &= e^{i\theta} \begin{pmatrix} -\frac{1}{\sqrt{2}} e^{-i\alpha} \sin \beta \\ \cos \beta \\ \frac{1}{\sqrt{2}} e^{i\alpha} \sin \beta \end{pmatrix}.\end{aligned}\tag{2.4}$$

A polar state is unmagnetized since $\langle S_a \rangle = 0$; therefore, a polar state may not be described by a vector orientation. Instead, a polar state is characterized by its alignment axis, given by the angles α, β . The alignment of a given spinor is characterized by N_{ab} , its quadrupole moment, or nematicity.

In the expression for ξ_{Pol} , we note no dependence upon the Euler angle τ ; thus, the family of polar states is characterized by a different symmetry group than above. Its symmetry group contains rotations of the alignment axis of the spinor, described by the angles α, β , and is given by $U(1) \times S^2$, where S^2 corresponds to the surface of a unit sphere describing those rotations. Physically, the properties of a polar state which govern its interaction with light depend only upon its *alignment* rather than its orientation. This behavior is common to nematic liquid crystals, whose optical properties depend only upon the alignment of the long axis of each constituent polymer. In contrast, the polymer orientation along its long axis has no effect upon its dielectric susceptibility [47].

2.1.2 Characterizing $F = 1$ spinors by measuring their dielectric tensors

As a starting point for devising optimal state-specific measurement schemes, it is interesting to consider the dielectric properties of magnetic and polar gases. Following the formalism presented by Ref. [48], the dielectric susceptibility tensor describing a spinor gas may be expressed in terms of the irreducible tensor components of its one-body density matrix m_{ab} and appropriate proportionality constants; specifically,

$$\chi_{bc} = C_0 \langle \rho \rangle - iC_1 \varepsilon_{abc} \langle S_c \rangle + C_2 \langle N_{bc} \rangle, \quad (2.5)$$

where the constants C_i are determined from physical parameters describing the measurement and the spinor gas.

In our experiments, we are interested in optically characterizing the susceptibility dielectric tensor of a spinor gas. In a single measurement, we direct an optical probe along one axis, denoted as the \hat{y} axis, and measure the outgoing light. The electric field of the probe beam, \mathbf{E}_{in} is transverse to the propagation axis; thus the measured outgoing probe, \mathbf{E}_{out} may only carry information about the transverse components of χ_{ab} . Thus, while χ_{jk} is described by a 3×3 matrix, a single optical measurement is sensitive to a 2×2 section of this matrix, denoted as $\tilde{\chi}_{ij}$. For example, we may characterize the response of the spinor gas dielectric susceptibility to \hat{x}, \hat{z} -linearly polarized light, propagating along the \hat{y} axis, by measuring the outgoing electric field,

$$\mathbf{E}_{out,i} = \text{Exp}[-ik \int n_{ij}(y) dy] \cdot \mathbf{E}_{in,j} \quad (2.6)$$

$$n_{ij} = \sqrt{\delta_{ij} + \tilde{\chi}_{ij}}; \quad (2.7)$$

here, n_{ij} is the refractive index tensor of the sample, determined from its dielectric susceptibility. In our experiments, the probe frequency is tuned far from the atomic resonance so that, to a good approximation, the outgoing probe simply acquires a phase shift due to its interaction with the spinor gas. Assuming the condensate acts as a thin lens,

$$\mathbf{E}_{out,i} = e^{-ik \int dy \sqrt{\delta_{ij} + \tilde{\chi}_{ij}}} \mathbf{E}_{in,j} \quad (2.8)$$

$$\approx e^{-ik(2r_y)(\delta_{ij} + \tilde{\chi}_{ij}/2)} \mathbf{E}_{in,j} \quad (2.9)$$

and the probe acquires a position-dependent phase shift, which we may describe by

$$\mathbf{E}_{out,i} = e^{-i\phi_{ij}} \mathbf{E}_{in,j} \quad (2.10)$$

$$\phi_{ij} = \phi_0(\delta_{ij} + \tilde{\chi}_{ij}/2).$$

Here, the overall phase acquired by the probe corresponds to $\phi_0 = 2kr_y$ where r_y is the condensate Thomas Fermi radius along the \hat{y} axis. An additional, state-dependent phase given by $\phi_0\tilde{\chi}_{ij}/2$ depends upon the orientation and alignment of the atomic ensemble. Along the imaging (\hat{y}) axis, the condensate radius r_y is smaller than the spin healing length. Consequently, spin excitations along this direction are too energetically costly to be sustained, and we assume the spinor condensate is effectively two-dimensional with respect to its spin degree of freedom. By imaging the spinor gas along the \hat{y} axis, we are discarding information about its magnetization profile along this direction, assuming it to be homogeneous.

To characterize the dielectric properties of a spinor gas, one may therefore measure the phase shift of the light as it traverses the condensate. For this characterization to be complete, one must probe the sample along multiple axes. A neat aspect of working with spinor gases (as compared to solid state samples, for example) is that this characterization may be accomplished, in practise, using a single fixed imaging system. Rather than rotate the imaging axis by ninety degrees, one may hold the imaging axis fixed and rotate the spinor wavefunction by ninety degrees. We make use of this principle, for example, in characterizing both the transverse and longitudinal magnetization of the spinor gas (to be discussed in Sec 2.3.2).

The dielectric susceptibility tensor of a given $F = 1$ ^{87}Rb spinor condensate describes its interaction with the probe. Assuming the probe is tuned close to the D1 transition of ^{87}Rb , and following the formalism presented in Ref. [48], the dielectric susceptibility tensor of the $F = 1$ ^{87}Rb spinor gases probed in our experiments may be expressed as,

$$\begin{aligned}
\tilde{\chi}_{ij} &= \left(\sigma_0 \frac{n\gamma}{2} \frac{\lambda}{2\pi} \right) \left(\frac{1}{\delta} \tilde{\chi}_{F'_2} + \frac{-1}{800 - \delta} \tilde{\chi}_{F'_1} \right) \\
\tilde{\chi}_{F'_2} &= \frac{5}{18} \rho \begin{pmatrix} 1 & 0 \\ 0 & 1 \end{pmatrix} + \frac{-5}{24} \begin{pmatrix} S_{11} & S_{12} \\ S_{21} & S_{22} \end{pmatrix} + \frac{1}{12} \begin{pmatrix} N_{11} & N_{12} \\ N_{21} & N_{22} \end{pmatrix} \\
\tilde{\chi}_{F'_1} &= \frac{1}{18} \rho \begin{pmatrix} 1 & 0 \\ 0 & 1 \end{pmatrix} + \frac{1}{24} \begin{pmatrix} S_{11} & S_{12} \\ S_{21} & S_{22} \end{pmatrix} + \frac{-1}{12} \begin{pmatrix} N_{11} & N_{12} \\ N_{21} & N_{22} \end{pmatrix}
\end{aligned} \tag{2.11}$$

where δ corresponds to the probe detuning below the $F = 1 \rightarrow F' = 2$ transition measured in MHz; $-800 + \delta$ is then the probe detuning below the $F = 1 \rightarrow F' = 1$ transition; λ is the probe wavelength; $\sigma_0 = 3\lambda^2/2\pi$ is the resonant cross section; and γ is the natural linewidth of the transition. The coefficients used in the construction of $\tilde{\chi}_{F'_2}$ and $\tilde{\chi}_{F'_1}$ are determined from the state-dependent interaction strengths of the probe with the atomic sample, as outlined by Ref. [48]. In general they depend upon the probe polarization. In the expression for $\tilde{\chi}_{ij}$ given in Eq 2.11, the 2×2 components of m_{ij} , denoted as \tilde{S}_{ij} and \tilde{N}_{ij} are given with respect to a Cartesian basis.

To determine the dielectric susceptibility tensor characterizing the interaction of a given spinor with linearly polarized light, we must express ψ_i and m_{ij} with respect to the Cartesian basis ψ_x, ψ_y, ψ_z . Frequently, as in the above definitions of magnetic and polar states, ψ_i is expressed in terms of the spherical basis ψ_+, ψ_0, ψ_- . For clarity, we outline the construction of $\tilde{\chi}_{ij}$, making use of the standard basis transformation $\psi_x = (\psi_+ - \psi_-)/\sqrt{2}$, $\psi_y = i(\psi_+ + \psi_-)/\sqrt{2}$, $\psi_z = \psi_0$. Given ψ^s in the spherical basis, we may determine ψ^c in the Cartesian basis from

$$\begin{aligned}
\psi^c &= U\psi^s, \\
U &= \begin{pmatrix} 1/\sqrt{2} & 0 & -1/\sqrt{2} \\ i/\sqrt{2} & 0 & i/\sqrt{2} \\ 0 & 1 & 0 \end{pmatrix},
\end{aligned} \tag{2.12}$$

where we have deliberately chosen the 1,2 elements of U to correspond to the Cartesian components transverse to the imaging axis. Using the convention of Eq 2.12 the 1,2 components of χ_{ij} interact with the components of \mathbf{E} transverse to the probe axis. The irreducible components of the one-body density matrix $m_{ij}^c = \psi_i^{\dagger,c} \psi_j^c$ (Eq 2.1) are then used to construct $\tilde{\chi}_{ij}$ in Eq 2.11. Thus determined, the dielectric susceptibility (Eq 2.11) describes the outgoing electric field in response to an incoming linearly polarized field.

In our experiments we make use of a circularly polarized probe. To express $\tilde{\chi}_{ij}$ in terms of σ^+, σ^- polarization basis, we simply apply the transformation,

$$\begin{aligned}\tilde{\chi}_{circ} &= \tilde{U} \cdot \tilde{\chi}_{pol} \cdot \tilde{U}^\dagger \\ \tilde{U} &= \begin{pmatrix} 1/\sqrt{2} & -i/\sqrt{2} \\ -1/\sqrt{2} & -i/\sqrt{2} \end{pmatrix}\end{aligned}\tag{2.13}$$

which we will adopt throughout the remainder of this discussion.

2.1.3 Dielectric properties of magnetic and polar gases

To develop an intuition for the measurable dielectric properties of a general $F = 1$ state (Eq. 2.11), we begin by considering the magnetic and polar families of states $\xi_f(\alpha, \beta), \xi_p(\alpha, \beta)$ given by Eq. 2.2, 2.4. In this context, the angle β is defined with respect to the probe axis (\hat{y}) and α describes a rotation in the x, z plane. To proceed, we consider the contributions to χ_{ij} which depend upon the spin state of interest. Specifically, \tilde{S}_{ij} and \tilde{N}_{ij} for the magnetic and polar states are given by

$$\begin{aligned}\tilde{S}_{Mag} &= \begin{pmatrix} \cos \beta & 0 \\ 0 & -\cos \beta \end{pmatrix} \\ \tilde{S}_{Pol} &= \overleftrightarrow{0} \\ \tilde{N}_{Mag} &= \begin{pmatrix} \frac{1}{24}(1 + 3 \cos 2\beta) & -\frac{1}{4} \sin^2 \beta (\cos 2\Phi + i \sin 2\Phi) \\ -\frac{1}{4} \sin^2 \beta (\cos 2\alpha - i \sin 2\alpha) & \frac{1}{24}(1 + 3 \cos 2\beta) \end{pmatrix} \\ \tilde{N}_{Pol} &= -2\tilde{N}_{Mag},\end{aligned}\tag{2.14}$$

where we have made use of the σ^+, σ^- polarization basis.

Measurable properties of the dielectric tensor clearly distinguish between polar and magnetic states. For example, the dependence of χ_{ij} upon the orientation β of a magnetic state is reflected by the contribution of its spin, \tilde{S}_f . In contrast, the dielectric properties of a polar state are weakly dependent upon its orientation; since the polar state is unmagnetized, $\tilde{S}_p = 0$, and this dependence is attributed to its quadrupole moment \tilde{N}_{ij} .

It becomes the task of the experimentalist to craft optical measurements of the dielectric properties of a spinor gas to extract its magnetic and nematic properties. By performing a measurement sensitive to $\tilde{\chi}_{++}$ and $\tilde{\chi}_{--}$, for example, one may characterize

the vector spin of a magnetic state. This may be accomplished by probing the phase shift acquired by a circularly polarized probe, to be discussed. The nematic properties of a spinor gas may also be characterized with suitable optical measurements. These may best be performed using linearly polarized light; in this case, the diagonal components of χ are due solely to N_{ij} . For example, when employing \hat{x}, \hat{z} -polarized light, measurements of $\tilde{\chi}_{xx}$, $\tilde{\chi}_{zz}$ are made with twice the signal strength for the polar *vs.* magnetic states.

2.2 Spin-sensitive phase contrast imaging

In our experiments, we make use of the phase contrast imaging technique [49] to determine simultaneously the phase shift acquired by light passing through all positions in the condensate. Specifically, we measure the phase shift acquired by a σ^+ polarized probe, detuned from the D1 atomic resonance, due to its interaction with the atomic spin. Our imaging settings are selected such that a given measurement provides instantaneous snapshot of the \hat{y} -projection of the condensate magnetization profile, $F_y(\mathbf{r})$ [50].

Employing an off-resonance or dispersive measurement technique offers many advantages. In contrast to absorptive measurements, which must frequently be performed at low-densities following the expansion of the gas, dispersive measurements may be performed in-situ, with high spatial resolution. Further, by employing an approximately non-destructive measurement, we may perform repeated measurements of the same sample; this is in contrast to resonant absorptive measurements which significantly heat the atomic ensemble.

The capability of performing multiple measurements of the same atomic sample serves as a gateway to studies of spin dynamics and to the development of novel measurement tools. First, by performing repeated measurements over appreciable timescales, we may characterize of the time evolution of the spinor gas. Second, by taking multiple snapshots of the condensate in rapid succession, we may extend our characterization of the spinor gas to include more degrees of freedom. For example, as we shall see in Sec. 2.3, by taking a rapid sequence of images of a Larmor precessing gas, we may characterize the amplitude and phase of the transverse magnetization \mathbf{F}_\perp , rather than simply measure its projection along the probe axis, F_y . While dispersive measurements have been implemented in prior studies of Bose condensates (Ref.[51], for example), our ability to characterize the vector magnetization profile of a spinor Bose gas is a novel experimental tool.

2.2.1 Measurement principle

The phase contrast imaging technique relies upon the interference of the light scattered by a refractive object, such as a spinor gas, with a known reference, corresponding to the original light source advanced by a constant phase. In imaging a refractive object using this technique, the scattered and unscattered light propagate along the same physical path (Fig. 2.1); thus, this interference method is robust against common-mode vibrations in the imaging optics. To advance exclusively the phase of the unscattered light by ϕ_{pd} , a thin dielectric (phase dot) is placed at the location of an intermediate focus, prior to the image. At this location, the scattered light, which has acquired an additional angular spread due to its interaction with the refractive medium, is much larger than the phase dot; to a good approximation, it may be considered as unaffected by the phase dot. The scattered and unscattered fields, \mathbf{E}_{scatt} and $\mathbf{E}_{unscatt}$ are recombined at the image plane according to,

$$\begin{aligned}\mathbf{E}_{out} &= \mathbf{E}_{unscatt} + \mathbf{E}_{scatt} \\ &= (e^{i(\phi_0 + \phi_{pd})} \mathbf{E}_0) + (e^{i\phi_0(\delta_{ij} + \chi_{ij}/2)} \cdot \mathbf{E}_0 - e^{i\phi_0} \mathbf{E}_0),\end{aligned}\tag{2.15}$$

where $\phi_0 = k2r_y$ is an overall phase acquired by the ingoing probe \mathbf{E}_0 (defined in Eq. 2.10); the dielectric susceptibility χ_{ij} characterizes the state-dependent phase shift imposed by the atomic sample; and ϕ_{pd} is the phase imposed by the phase dot. Taking $\phi_{pd} = \pi/2$, assuming the atom-imposed phase shift to be small such that $e^{i\phi_0\chi_{ij}/2} \simeq (\delta_{ij} + i\phi_0\chi_{ij}/2)$, and applying σ^+ polarized probe represented as $(1, 0)^\dagger$, the outgoing probe may be described by,

$$\mathbf{E}_{out}/|\mathbf{E}_0|e^{i\phi_0} = i \begin{pmatrix} 1 \\ 0 \end{pmatrix} + e^{i\phi_0\chi_{ij}/2} \cdot \begin{pmatrix} 1 \\ 0 \end{pmatrix} - \begin{pmatrix} 1 \\ 0 \end{pmatrix}\tag{2.16}$$

$$\simeq i(\delta_{ij} + \frac{\phi_0\chi_{ij}}{2}) \cdot \begin{pmatrix} 1 \\ 0 \end{pmatrix}\tag{2.17}$$

The probe-normalized intensity is given by,

$$|\mathbf{E}_{out} \cdot \mathbf{E}_{out}^\dagger|/|E_0|^2 \simeq 1 + \phi_0 \langle \chi_{11} \rangle + \frac{\phi_0^2}{4} (\langle \chi_{11} \chi_{11}^\dagger \rangle + \langle \chi_{21} \chi_{21}^\dagger \rangle).\tag{2.18}$$

Neglecting the contributions to χ_{11}, χ_{21} from the quadrupole tensor \tilde{N}_{ij} which are suppressed by numerical prefactors (Eq. 2.11), $\langle \chi_{11} \rangle$ may be expressed as,

$$\phi_0 \langle \chi_{11} \rangle \simeq \left(\sigma_0 \frac{2\tilde{n}\gamma}{2} \right) \left(\left(\frac{5}{18} \frac{1}{\delta} - \frac{1}{18} \frac{1}{800 - \delta} \right) + \left(-\frac{5}{24} \frac{1}{\delta} - \frac{1}{24} \frac{1}{800 - \delta} \right) \langle F_y \rangle \right)\tag{2.19}$$

where \tilde{n} is the condensate column density. Under these approximations, the probe-normalized intensity may be conveniently expressed as,

$$|E_{out}|^2/|E_0|^2 \simeq 1 + 2\tilde{n}\sigma_0 \frac{\gamma}{2\delta} (c_0 + c_1 \langle F_y \rangle + c_2 \langle F_y^2 \rangle), \quad (2.20)$$

where the detuning-dependent constants are then given by,

$$\begin{aligned} c_0 &= \delta \left(\frac{5}{18} \frac{1}{\delta} - \frac{1}{18} \frac{1}{800 - \delta} \right) \\ c_1 &= \delta \left(-\frac{5}{24} \frac{1}{\delta} - \frac{1}{24} \frac{1}{800 - \delta} \right). \end{aligned} \quad (2.21)$$

Our recent phase contrast imaging settings include $\lambda = 795$ nm, $\delta = 500$ MHz (below the $F = 1 \rightarrow F' = 2$ D1 transition), and $\gamma/2 = 3$ MHz; in this case, $c_0 = 0.18$ and $c_1 = -0.28$. The central region of the condensate for the optical trap geometry used in our demonstration of spinor condensate magnetometry (Ch.3), for example, is described by $\tilde{n} = 850$ atoms/ μm^2 and $r_y = 2.4$ μm . Taking these condensate parameters, the phase contrast signal includes a density-dependent offset of magnitude $\left(\sigma_0 \frac{2\tilde{n}\gamma}{2}\right) c_0 \simeq 0.28$ and a contribution proportional to $\langle F_y \rangle$ with a maximum magnitude given by $\left(\sigma_0 \frac{2\tilde{n}\gamma}{2}\right) c_1 \simeq 0.43$.

2.2.2 Imaging system

To spatially-resolve spin textures in spinor condensates, such as the dipole-interaction induced features discussed in Chapter 6, we require an imaging system with a spatial resolution on the order of 2 μm . Tests of our imaging system, performed concurrently with our experimental work in early 2007, revealed that our ability to resolve these features was limited by spherical aberrations. Thus in the Spring of 2007 the imaging system presented in Ref. [11],[14] was replaced with a new system shown in Fig. 2.1. To determine our spatial resolution and enable an aberration-free characterization of 2 μm sized features in the spinor gas, we characterized the new system both off-line, using a fabricated phase contrast test pattern, and in-situ, by imaging small features in the condensate density profile.

The spatial resolution of the imaging system shown in Fig. 2.1 is determined by the angular spread of the rays captured by the first composite lens, characterized by a 117 mm effective focal length (f_{L1}) and a 2 inch diameter (D_{L1}). To reduce spherical aberrations in the imaging system, the composite lens is formed by a meniscus lens ($f_{M1} = 125$ mm) followed by an achromatic lens ($f_{A1} = 140$ mm). The meniscus lens serves to bend the incoming light rays radially inwards, directing the rays closer to the center of the achromatic

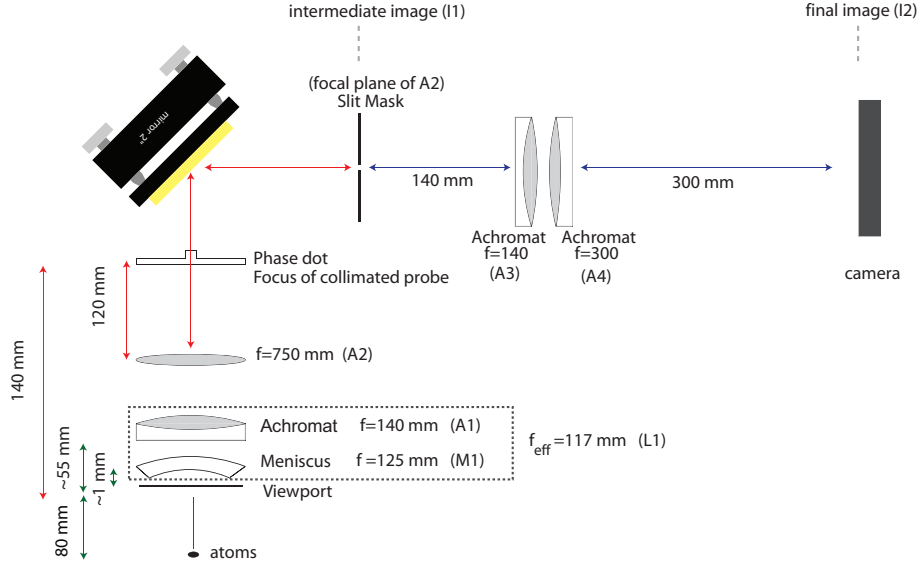


Figure 2.1: The phase contrast imaging system is schematically shown, as described in the text.

lens, and bringing its performance closer to ideal. In particular, the spherical aberrations due to the same achromatic lens are significantly reduced with the introduction of the meniscus lens. The effective numerical aperture ($N.A.$) is then improved since the angular spread of rays captured by the composite lens (θ) is increased, lowering the diffraction-limited spatial resolution σ_{DL} . The ideal performance of our imaging system is described by,

$$\tan \theta = D_{L1}/2f_{L1} = 0.18 \quad (2.22)$$

$$N.A. = \sin \theta \simeq 0.18$$

$$\sigma_{DL} = \frac{1.22\lambda}{2N.A.} = 2.7\mu m,$$

where σ_{DL} corresponds to the distance to the first minimum of the Airy pattern corresponding to the image of a point source. An alternative measure of the spatial resolution of an imaging system corresponds to the FWHM of the Gaussian fit to the aforementioned Airy pattern; here this is given by $2.2\mu m$.

Following the first composite lens, the remainder of the imaging system closely

resembles the system presented in Ref. [11, 14], which we overview briefly. An achromatic lens ($f_{A2} = 750$ mm) is chosen to establish the magnification of the intermediate image (I1) of the condensate, given by $M = f_{A1}/f_{L1} = 6.4$. Prior to the plane of the intermediate image, the collimated probe (corresponding to light which has not been scattered by the atoms) is focussed at the location of the phase dot. At the intermediate image plane, a mask is placed which exposes only the pixels on the camera CCD chip which correspond to the condensate's location on the final image. Shown schematically in Fig 2.2(a), the mask is formed from the space between the edges of two parallel razor blades, aligned to the \hat{z} axis of the condensate image, separated by a distance slightly greater than the imaged x -dimension of the condensate ($\sim M_1 \times 40 \mu\text{m} \sim 256 \mu\text{m}$).

Following the plane of the intermediate image, an additional pair of lenses of focal lengths $f_{A3} = 140$ mm and $f_{A4} = 300$ mm is placed to form a second magnification stage (characterized by $M_2 = 2.1$). The final magnification of the image at the location of the camera is given by $M = M_1 \times M_2 = 13.7$ such that 1 pixel on the camera CCD chip ($13 \mu\text{m}$ in size) corresponds to roughly $1 \mu\text{m}$ on the condensate. Using the rapid-frame-transfer capability of the camera, once a 40×512 pixel region of the camera CCD chip is exposed, it may be shifted (at a rate of $1 \mu\text{s}/\text{pixel}$) into the unexposed region. This frame transfer capability, dubbed kinetics imaging, enables a series of snapshots of the condensate to be taken in rapid succession, at a rate of roughly 20 kHz or $50 \mu\text{s}/\text{frame}$ (Fig. 2.2(b)). We take advantage of kinetics imaging in characterizing the Larmor precession of the condensate magnetization, to be discussed. For details on the data read-out underlying kinetics imaging, we refer the reader to Ref. [11].

Off-line calibration of the imaging system

Prior to its implementation in the experiment, we calibrated the first stage of our imaging system off-line by imaging suitable phase and amplitude test patterns fabricated for this purpose (Fig. 2.3). The meniscus and achromatic lenses M_1, A_1, A_2 were arranged according to Fig. 2.1 and were first aligned using a He-Ne laser centered upon the optics. First, the tilt of the second achromatic lens (A_2) was adjusted such that the back-reflections of its surfaces were co-aligned; its displacement with respect to the probe axis was corrected by overlapping the position of the co-linear back-reflections with respect to the original beam. Second, the first achromatic lens (A_1) was added to the optical path and aligned in

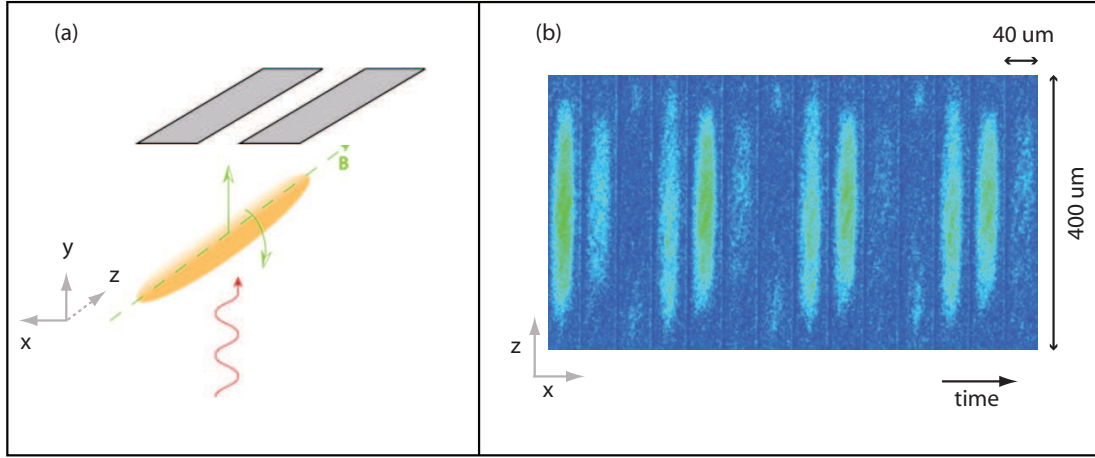


Figure 2.2: (a) A mask is placed at the intermediate image plane such that only the pixels on the camera CCD chip which correspond to the condensate's location on the final image are exposed. (b) A series of snapshots of the condensate may be taken in rapid succession, each of which is shifted out of view following its exposure, protected by the mask.

the same manner. Third, the meniscus lens (M_1) was aligned to A_1 to form a composite lens (L_1), mounted in the same housing. The pair of lenses M_1 and A_1 were separated by 55 mm, specified by the manufacturer (Melles Griot). To optimize the position of L_1 following this coarse alignment, images of amplitude and phase test-patterns were characterized while translating L_1 along the probe axis. For this characterization, a 795 nm probe was used.

Very briefly, the phase and amplitude test patterns were fabricated from $1'' \times 1'' \times 3$ mm fused silica optical flats according to a mask shown in Fig. 2.3(a). The fabrication was performed by Thomas P. Purdy using lithographic techniques to be outlined in Ref. [52]. The phase test pattern consisted of a series of recessed horizontal and vertical bars as small as $3 \mu\text{m}$ in length and periodicity, each characterized by a depth of slightly over 800 nm. A representative series of horizontal trenches with a $3 \mu\text{m}$ width and periodicity are shown in Fig. 2.3(b). Light passing through the recessed regions is advanced in phase by roughly π relative to the light traversing the glass, with a refractive index given by $n \sim 1.45$. Thus, by placing the phase dot at the intermediate focus, a destructive interference pattern was observed with spatial features given by the phase test pattern. A separate amplitude test pattern was fabricated on the same substrate by depositing a thin coating of chromium, opaque with respect to the probe. Both the phase and amplitude test patterns were imaged in characterizing the imaging system and gave similar results.

Characterizing the imaged test pattern as a function of the position and alignment

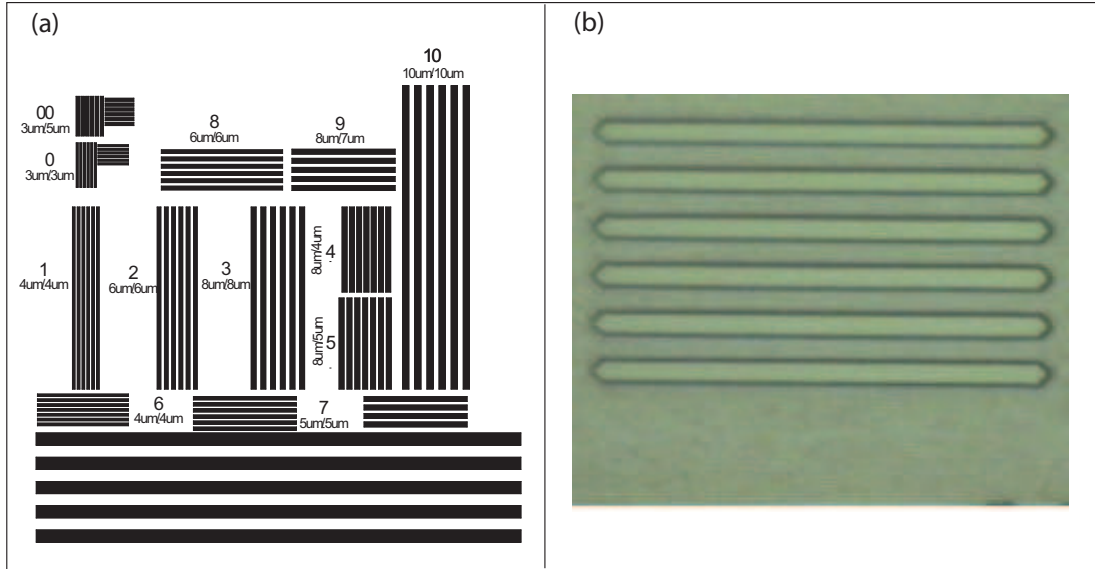


Figure 2.3: (a) A phase and amplitude test pattern with features as small as $3 \mu\text{m}$ was fabricated to calibrate the imaging system offline. (b) The features on the phase test pattern consisted of trenches fabricated in the glass slide. Their depth was chosen in order to impart a π relative phase shift between the light traversing these regions and the light traversing the entire thickness of the glass. Here, features characterized by a width and periodicity of $3 \mu\text{m}$ are imaged using an optical microscope. The test patterns and their images are courtesy of Thomas P. Purdy.

of the lenses enabled the optimization the focus and astigmatic character of the imaging system, following small adjustments to the initial alignment. To optimize the focus and minimize the astigmatism, the measured contrast of the repeated horizontal and vertical features, C_h and C_v , were separately determined for small displacements of the lens L_1 along and transverse to the probe axis. For example, the image of the horizontal bars was fit to a sinusoidal waveform characterized by minimum and maximum signal strengths A_{min} , A_{max} , yielding a measured contrast $C_h = |A_{max,h} - A_{min,h}| / (A_{min,h} + A_{max,h})$. The astigmatic character of the imaging system corresponded to the deviation of the ratio C_h/C_v from unity as a function of the translation of L_1 and was corrected with fine adjustments to the tilt of L_1 (Fig. 2.4). Following several iterations of measuring C_h, C_v as a function of the translation of L_1 and adjusting its tilt to bring their ratio close to unity, a final position and alignment for L_1 were determined. For these settings, the measured contrast as a function of the feature size is shown in Fig. 2.5, projecting 50 % contrast for features approximately $2 \mu\text{m}$ in size. This off-line characterization of the imaging system indicates that the lens L_1

must be aligned to within $\pm 25 \mu\text{m}$ of its optimal position to avoid an astigmatic focus (2.4). A 8" viewport identical to the one used in the experiment was inserted along the imaging path to discern its effect upon the observed resolution and astigmatism; its effect was found to be negligible in comparison to the effects bounded by the above alignment criteria.

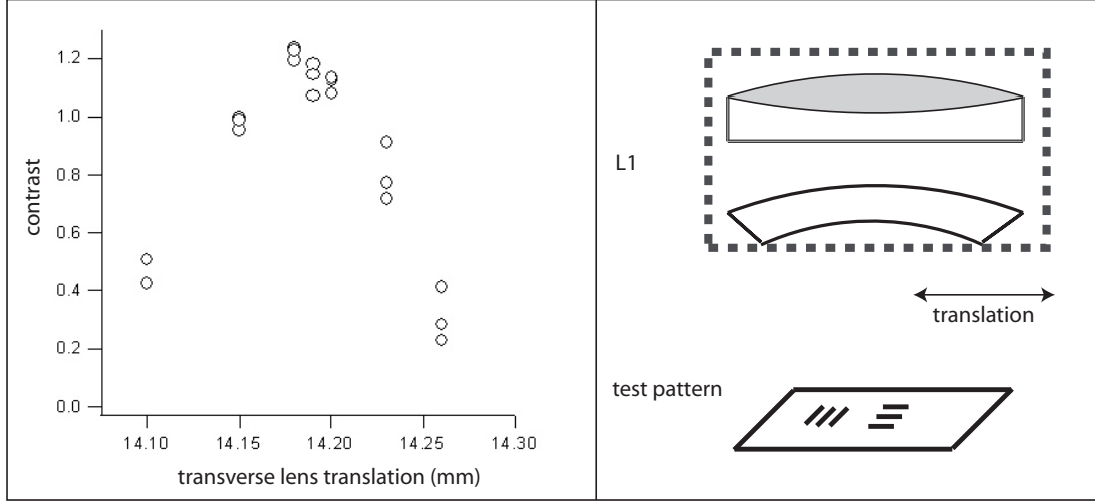


Figure 2.4: To characterize the astigmatic character of the imaging system, the contrast of horizontal and vertical features in the test pattern, C_h and C_v , were determined as a function of the position of the first critical lens L_1 . Their ratio, C_h/C_v , corresponds to unity when the imaging system is optimally aligned, and deviates monotonically away from unity as the lens is displaced away from its optimal position. This characterization suggests a $\pm 25 \mu\text{m}$ sensitivity to the placement of L_1 .

In-situ calibration of the imaging system

Following its calibration off-line, the imaging system was implemented in the experiment. The same alignment procedure was carefully applied, using the back-reflections of a He-Ne laser beam co-linear with the D1 imaging probe (which had previously been aligned to the center of the condensate). To enable a sensitive characterization of the imaging system in-situ, a small circular feature in the condensate density profile was used. To apply this feature, as shown schematically by Fig. 2.6, a resonant laser beam was focussed to a $\sim 15 \mu\text{m}$ circular spot size at the location of the intermediate image plane (I1). A thin pellicle beam splitter placed at that location served to reflect the beam, such that it propagated along the imaging probe path toward the condensate. At the location of the condensate, the beam was de-magnified by M_1 to a final size of $2.3 \mu\text{m}$.

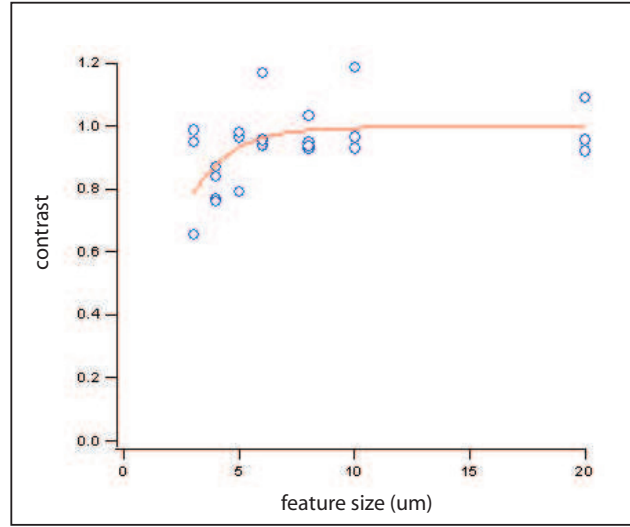


Figure 2.5: For the aligned imaging system, the measured contrast of the test pattern features diminishes from unity for features larger than $5\text{ }\mu\text{m}$ in size to roughly 50% (projected) for features on the order of $2\text{ }\mu\text{m}$.

By scattering atoms at the location of its focus and puncturing a small hole in the condensate density profile, the resonant beam was used to create the small feature needed in confirming, in-situ, the resolution and astigmatism of the imaging system. As shown in Fig. 2.7(a) a series of images of the condensate, taken at a rate of $200\text{ }\mu\text{s}/\text{frame}$ (during each of which the resonant (D1) probe was applied for $100\text{ }\mu\text{s}$) reflect the gradual depletion of atoms from its focus. Following their normalization by the imaging probe, the data reveal the evolution of the hole punctured in the condensate (Fig. 2.7)(b). Using a two-dimensional Gaussian fit to the punctured hole following a short exposure, the resolution and astigmatism of the imaging system were determined. First, the feature contrast and feature size, measured using the amplitude and average width of a Gaussian fit function, were determined as a function of the resonant probe intensity. As the resonant probe intensity was lowered, the condensate hole size (FWHM) diminished asymptotically toward roughly $2\text{ }\mu\text{m}$. The feature contrast was roughly 50 % for a $\sim 2\text{ }\mu\text{m}$ feature in the final alignment. The aspect ratio of the hole, determined from the ratio of the x and z widths, was measured to be 1.05 ± 0.06 within a $50\text{ }\mu\text{m}$ window of the optimal position of $L1$, thus placing a bound upon the astigmatic character of the imaging system.

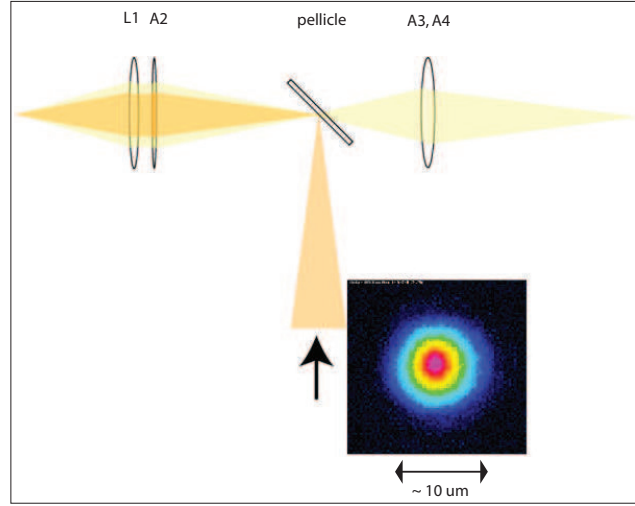


Figure 2.6: An in-situ calibration of the resolution and astigmatism of the imaging system was performed by imaging a small hole punctured in the condensate density profile, whose application by means of a focussed resonant laser beam is schematically shown.

2.3 Larmor precession imaging: extracting the vector magnetization

By taking a series of phase contrast images of the condensate in rapid succession, we may extend our characterization of the condensate magnetization from a single projective measurement of F_y , to a complete description of the vector magnetization, \mathbf{F} . To do so, we determine the transverse and longitudinal magnetization of the condensate magnetization, F_\perp and F_L , using two consecutive measurements.

2.3.1 Transverse magnetization measurement principle

In our experiments, a bias magnetic field is directed along the long axis of the condensate, described by $\mathbf{B} = B\hat{z}$. The condensate magnetization oriented transverse to \mathbf{B} undergoes Larmor precession about the \hat{z} axis; consequently, its projection along the probe axis, F_y varies sinusoidally. The measured phase contrast signal at each location in the condensate, described by Eq 2.20, oscillates with a characteristic amplitude proportional to the local transverse magnetization density. By simultaneously observing the sinusoidal variation of the phase contrast signal at each point in the condensate, the relative phase of each signal may be determined, corresponding to the relative orientation of the condensate

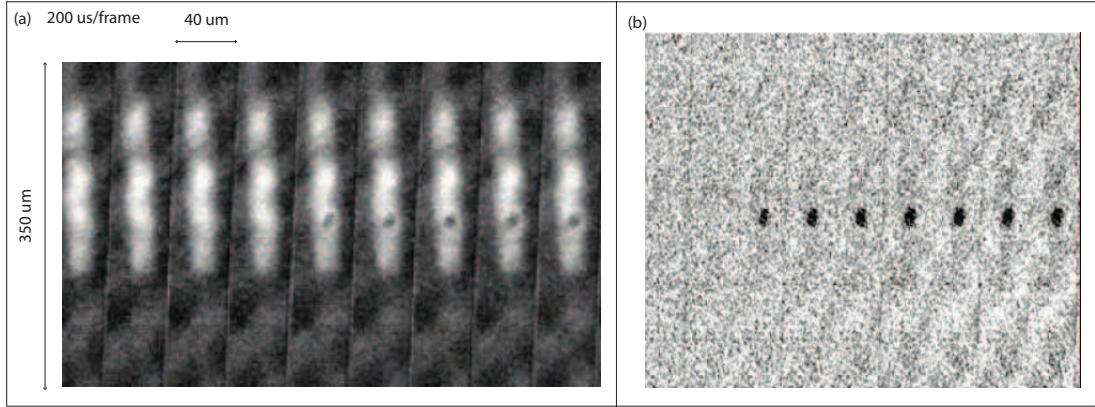


Figure 2.7: (a) A series of images of the condensate are taken while applying the focussed resonant probe. (b) The depletion of the condensate density at the location of the focus of the probe results in a sharp hole in the condensate with a symmetric Gaussian spatial profile. This image was taken during the alignment of the imaging system; here, a slight misalignment of the imaging system is reflected in the asymmetric cross section of the hole punctured in the condensate.

magnetization in the transverse (xy) plane. Specifically, from the analysis of the sequence of snapshots of the Larmor precession gas, the transverse magnetization density is determined (Sec. 2.3.2). It is described by the complex field $\mathbf{F}_\perp(r) = A(r)e^{i\phi(\mathbf{r})}$, where $A(\mathbf{r})$ and $\phi(\mathbf{r})$ describe its amplitude and orientation in the transverse plane, respectively. A representative sequence of phase contrast images demonstrating the Larmor precession of a homogeneous transversely magnetized cloud is shown in Fig. 2.2(b).

2.3.2 Longitudinal magnetization measurement principle

To characterize completely the vector magnetization of the condensate, both the transverse and longitudinal components of \mathbf{F} must be determined. To accomplish this, a second sequence of snapshots is taken following the first, between which the condensate magnetization is rotated by an angle of $\pi/2$ about the \hat{y} axis using a resonant RF pulse. Following the rotation, the longitudinal (\hat{z}) component of \mathbf{F} is oriented in the transverse (xy) plane and precesses about the bias field. It is determined by considering the sinusoidally varying phase contrast signal in a second sequence of phase contrast images, taken following the rotation.

The measurement of the transverse and longitudinal components of the vector magnetization relies upon determining the amplitude and phase of the sinusoidally varying

phase contrast signal in both sequences of frames. Using the first sequence of frames, the amplitude and phase describing $\mathbf{F}_\perp(r)$ are determined to be $A^{(1)}(\mathbf{r}), \phi^{(1)}(\mathbf{r})$. Next the $\pi/2$ pulse is applied to rotate \mathbf{F} about \hat{y} . At the instant of the application of the pulse, due to its slight delay following the first measurement, we assume the phase of F_\perp to have advanced by δ_1 . At this instant, the transverse components of \mathbf{F} are given by

$$\begin{aligned} F_x(r) &= A^{(1)}(r) \cos(\phi^{(1)}(r) + \delta^{(1)}) \\ F_y(r) &= A^{(1)}(r) \sin(\phi^{(1)}(r) + \delta^{(1)}). \end{aligned} \quad (2.23)$$

Following its rotation by $\pi/2$ about the \hat{y} axis, the vector magnetization to be described by,

$$\begin{aligned} \mathbf{F}_{rot} &= \begin{pmatrix} 0 & 0 & 1 \\ 0 & 1 & 0 \\ -1 & 0 & 0 \end{pmatrix} \cdot \begin{pmatrix} F_x \\ F_y \\ F_z \end{pmatrix} \\ &= \begin{pmatrix} F_z \\ F_y \\ -F_x \end{pmatrix}. \end{aligned} \quad (2.24)$$

The second sequence of frames reflect the Larmor precession of the magnetization transverse to the bias field following the rotation, given by \mathbf{F}_{rot} . From the determination of the amplitude and phase of precession of \mathbf{F}_{rot} , we may therefore determine the components F_z, F_y of \mathbf{F} . The second sequence of frames are analyzed in the analogous fashion to the first, assigning an amplitude and phase to F_{rot} where $\mathbf{F}_{rot}(\mathbf{r}) = A^{(2)}(\mathbf{r})e^{i\phi^{(2)}(\mathbf{r})}$. We may project backward to the instant of the pulse, assuming a small delay between the application of the pulse and the second sequence of measurements, to obtain

$$\begin{aligned} F_z(\mathbf{r}) &= A^{(2)}(\mathbf{r}) \cos(\phi^{(2)}(\mathbf{r}) + \delta^{(2)}) \\ F_y(\mathbf{r}) &= A^{(2)}(r) \sin(\phi^{(2)}(\mathbf{r}) + \delta^{(2)}) \end{aligned} \quad (2.25)$$

where $\delta^{(2)}$ is a small phase shift attributed to the delay. Since the series of measurements were performed on much shorter timescale (~ 1 ms) than that associated with spin dynamics (10-100 ms) in the spinor gas, we assume the two measurements of $F_y(\mathbf{r})$ to be equivalent; thus,

$$A^{(1)}(r) \sin(\phi^{(1)}(r) + \delta^{(1)}) = A^{(2)}(r) \sin(\phi^{(2)}(r) + \delta^{(2)}), \quad (2.26)$$

enabling the determination of the unknown phase delays δ_1, δ_2 . One solution for the components of the vector magnetization (up to an overall phase) is given by,

$$\begin{aligned} F_x &= A^{(1)}(\mathbf{r}) \cos(\phi^{(1)}(\mathbf{r})) \\ F_y &= A^{(1)}(\mathbf{r}) \sin(\phi^{(1)}(\mathbf{r})) \\ F_z &= A^{(2)}(\mathbf{r}) \cos(\phi^{(2)}(\mathbf{r}) - \delta) \end{aligned} \quad (2.27)$$

where the small phase shift δ may be determined by a least-squares optimization of the constraint,

$$A^{(1)}(\mathbf{r}) \sin(\phi^{(1)}(\mathbf{r})) = A^{(2)}(\mathbf{r}) \sin(\phi^{(2)}(\mathbf{r}) + \delta). \quad (2.28)$$

Our assumption that δ is constant reflects the fact that the $\pi/2$ pulse is approximately instantaneous with respect to the imaging sequence.

Optimal amplitude and phase determination

The amplitude and phase of the transverse magnetization density are determined from the pixel-by-pixel analysis of the sinusoidally varying phase contrast signal, measured over N_f consecutive images. We may assume that a given pixel in the series of N_f frames corresponds to the same condensate region since the duration of the imaging sequence is much shorter than the characteristic timescales for the motion of the condensate. For each $1 \mu\text{m}$ sized region of the condensate, we may therefore obtain a time sequence of N_f signals, $\{y_n(\mathbf{r})\}$, sampled at roughly 20 kHz. This sampling rate, corresponding to $50 \mu\text{s}/\text{frame}$, is limited by the $1 \mu\text{s}/\text{pixel}$ transfer rate of the camera and the $40\text{-}50 \mu\text{m}$ condensate width (where $M \simeq 1 \text{ pixel}/\mu\text{m}$). Assuming each phase contrast data series $\{y_n(r)\}$ to be described by a sinusoidally varying signal, and taking into account the contribution of photon shot-noise to our detection, we model the data by $\tilde{y}_n(r)$, where

$$\tilde{y}_n(r) = A(r) \cos(2\pi f n + \phi(r)) + w_n, \quad (2.29)$$

and $n = 0..N_f - 1$, the frequency f is assumed to be known, and $w_n = G(0, \sigma_{ps}^2)$ is a white Gaussian noise source. The added detection noise, characterized by a variance σ_{ps}^2 , is in practise dominated by photon shot-noise for our imaging settings (to be discussed in Sec. 3.2.1). Throughout this treatment, we assume that we have subtracted the constant offset to each phase contrast data series $y_n(\mathbf{r})$, enforcing $\langle y_n(\mathbf{r}) \rangle = 0$.

A linear least squares algorithm is applied to each location of the condensate to estimate the amplitude and relative phase of the sinusoidally varying signal, given by $A(\mathbf{r})$ and $\phi(\mathbf{r})$. Following Eq. 2.29,

$$\tilde{y}_n(\mathbf{r}) = A(\mathbf{r}) (\cos(2\pi f n) \cos(\phi(\mathbf{r})) - \sin(2\pi f n) \sin(\phi(\mathbf{r}))) + w_n \quad (2.30)$$

which may be expressed as a matrix equation,

$$\tilde{\mathbf{y}}(\mathbf{r}) = \mathbf{M} \cdot \Phi(\mathbf{r}) + \mathbf{w}; \quad (2.31)$$

$$\Phi(\mathbf{r}) = A(\mathbf{r}) \begin{pmatrix} \cos(\phi(\mathbf{r})) \\ \sin(\phi(\mathbf{r})) \end{pmatrix},$$

$$\mathbf{M} = \begin{pmatrix} \cos(2\pi f 0) & -\sin(2\pi f 0) \\ \cos(2\pi f 1) & -\sin(2\pi f 1) \\ \vdots & \vdots \\ \cos(2\pi f n) & -\sin(2\pi f n) \\ \vdots & \vdots \\ \cos(2\pi f (N_f - 1)) & -\sin(2\pi f (N_f - 1)) \end{pmatrix}. \quad (2.32)$$

Assuming the model $\tilde{\mathbf{y}}(\mathbf{r})$ to describe the data $\mathbf{y}(\mathbf{r})$, the optimal values for the amplitude and phase of the sinusoidal signal are determined from,

$$\mathbf{M}^T \cdot (\mathbf{y}(\mathbf{r}) - \mathbf{w}) = \mathbf{M}^T \cdot \mathbf{M} \cdot \Phi(\mathbf{r}) \quad (2.33)$$

$$\Phi(\mathbf{r}) = (\mathbf{M}^T \mathbf{M})^{-1} \cdot \mathbf{M}^T \cdot \tilde{\mathbf{y}}(\mathbf{r}).$$

Here we have expressed $\Phi(\mathbf{r})$ in terms of known quantities $\mathbf{M}, \mathbf{y}(\mathbf{r})$, thus determining the desired quantities

$$A(\mathbf{r}) = \sqrt{\cos(\phi(\mathbf{r}))^2 + \sin(\phi(\mathbf{r}))^2}, \quad (2.34)$$

$$\phi(\mathbf{r}) = \arctan(-\sin(\phi(\mathbf{r})) / \cos(\phi(\mathbf{r}))).$$

Under the assumptions that the frequency f is well known, the data series is sufficient in length to ensure $\langle y_n \rangle = 0$ and characterized by a signal to noise ratio s , and the decay of the signal is negligible, the linear least squares algorithm is characterized by a phase error,

$$\sigma_\phi = \frac{1}{s} \frac{N_f - 1}{N_f(2N_f + 1)}, \quad (2.35)$$

corresponding to the Cramer-Rao bound for phase estimation.

In analyzing a given data series, f is found prior to determining the aforementioned amplitude and phase profiles. In determining f , the condensate is divided into several 10 μm sized regions, over which the phase contrast signal is averaged, yielding several data series $\bar{y}_n(r)$ with a higher signal to noise ratio. By taking the Fourier transform of each data series and creating a histogram of the resulting values for f , the most likely value for f is determined and used in remainder of the analysis.

In our experiments, the sampling rate ($f_s \sim 20$ kHz) is typically much smaller than the Larmor frequency determined by the bias field ($f_L = g_F \mu_B B / h$). The observed signal oscillation frequency, f , in fact corresponds to the difference frequency (or beat note) between f_L and the nearest integer multiple of f_s . Typically f ranges from 2-5 kHz in order to sample optimally the sinusoidally varying signal in 11-15 frames. The aliased Larmor frequency can be treated as constant since, for typical operating conditions, the bias field varies by less than 5 μG across the extent of the condensate. In other words, the relative phase of precession accrued during the ~ 1 ms imaging sequence is negligible in comparison to the phase accrued during the preceding evolution period $\phi(\mathbf{r})$, which we are interested in measuring.

Thus far we have neglected the decay of the phase contrast signal over the sequence of N_f measurements. In practise, the atoms may be scattered by the imaging probe, depleting the condensate throughout the imaging sequence (to be discussed in Sec 2.4). The condensate depletion is modeled by an exponential decay of the phase contrast signal, which may be taken into account in the aforementioned amplitude and phase estimation procedures. Specifically, Eq. 2.33 is modified to become,

$$\Phi(\mathbf{r}) = (\mathbf{M}^T \cdot \mathbf{D} \cdot \mathbf{D} \cdot \mathbf{M})^{-1} \cdot \mathbf{M}^T \cdot D \cdot \tilde{\mathbf{y}}(\mathbf{r}) \quad (2.36)$$

where $\mathbf{D}_{nm} = e^{-n/\tau} \delta_{mn}$ is a diagonal $n \times n$ matrix parameterized by a decay constant τ , empirically determined to reflect the probe-induced depletion of the condensate. For typical imaging settings the condensate was depleted by roughly 50 % throughout the imaging sequence.

The linear least squares phase and amplitude estimation may be extended to take into account systematic effects such as the spatial profile of the imaging probe, which correlates the noise source with the measured transverse magnetization. Far more effective than this extension to our data analysis, however, was to reduce the probe intensity until these

correlations had a negligible effect upon the phase detection noise. This was made possible by optimizing our imaging settings and by employing a multi-pulse imaging technique, to be discussed.

2.4 Optimizing the imaging settings

Our dispersive imaging technique employs an off-resonance probe so as to be “non-destructive” with respect to the atomic state, enabling the study of spin dynamics through repeated measurements of the same sample. An off-resonance probe, however, may scatter atoms into a number of final states, at a rate proportional to the probe intensity.

As presented in Ref.[11], calculations based upon linear Raman scattering rates predicted that a probe fluence of up to $3400 \text{ photons}/\mu\text{m}^2$ per frame could be used to perform sensitive phase measurements. However, in using a probe fluence of this magnitude to image the condensate, we observed light-induced loss rates which greatly exceeded the expected loss rates due to linear scattering. The discrepancy between the observed and above calculated loss rates was attributed to collective light scattering, denoted as superradiant scattering, of the probe by the condensate.

2.4.1 Considering collective scattering

In our experiment, superradiant Raman scattering of atoms into the $F = 2$ hyperfine states depletes the population of probed $F = 1$ atoms. Both the probe-induced loss rate and the magnitude of the measured precession signal depend upon the probe detuning. To optimize the probe detuning and fluence with respect to the final phase sensitivity, we empirically determined the amplitude of the precession signal as well as the probe-induced losses at a number of settings. Following a generalization of the calculation presented in Ref. [11], we considered several candidate probe frequencies. With respect to the $F = 1 \rightarrow F' = 2$ (D1) transition, we employed probe frequencies characterized by $\delta_{D1} = -500$ and 200 MHz , the latter of which yielded a smaller phase contrast signal. With respect to the $F = 1 \rightarrow F' = 2$ (D2) transition, we employed probe frequencies characterized by $\delta_{D2} = -400, -700, -110, -200 \text{ MHz}$, whose main disadvantages were high probe-induced loss rates. In agreement with our estimates, the optimal probe frequency corresponded to a detuning of $\delta = -500 \text{ MHz}$ with respect to the $F = 1 \rightarrow F' = 2$ hyperfine transition and was employed throughout the discussed experiments. A probe fluence of

750 photons/ μm^2 , applied using a 4-pulse sequence per image, was used in our demonstration of the spinor condensate magnetometer. In our characterization of the amplification of spin fluctuations (Ch. 4) and the evolution of spin textures (Ch. 6) in the spinor gas, for which our phase detection noise was less critical, we typically used a probe fluence of roughly 100-120 photons/ μm^2 by applying a single light pulse per image.

2.4.2 Multi-pulse imaging

In our phase contrast imaging sequence, probe-induced losses were primarily due to superradiant Raman scattering of atoms into the $F = 2$ hyperfine states. To reduce the probe-induced scattering rate, the probe intensity was lowered while maintaining a high probe fluence. This was accomplished by obtaining each frame in the imaging sequence by integrating N pulses of light characterized by an intensity I/N in lieu of one pulse characterized by an intensity I . As mentioned previously, in our characterization of the spinor condensate magnetometer, four pulses were spaced by the Larmor period of roughly $T_L = 10 \mu\text{s}$ and characterized by a duration of $2.2 \mu\text{s} < T_L/4$. In addition, to disrupt the coherent superradiant Raman scattering of condensate atoms into the $F = 2$ state, we applied light close to the $F = 2 \rightarrow F' = 3$ (D2) transition during the imaging sequence ($\delta_{D2} = -30 \text{ MHz}$).

2.5 On-resonance absorptive imaging

In addition to our dispersive high-resolution imaging system, we employ resonant low-magnification ($M=2.1$) imaging techniques to characterize bulk properties of the spinor gas. For a detailed characterization of our “time-of-flight” and “Stern-Gerlach” imaging systems the reader is directed to Ref.[14, 11]. Briefly, using the time-of-flight imaging technique, the condensate is released from the trap and allowed to expand as it falls. With independent measurements of the optical trap frequencies, determining the condensate size following an appreciable expansion provides a direct measurement of the temperature of the gas. By characterizing its absorption of a resonant probe following its expansion, the condensate density, or total number of atoms, may be determined.

When the expansion occurs in the presence of a pulsed magnetic field gradient, the $m_z = \pm 1, 0$ magnetic sublevels of the $F = 1$ gas may be separated, since a differential force is applied between them. The relative populations in the spatially separated sublevels

are determined from their absorption of a resonant probe. Typically, using these absorptive techniques we image the gas following a 34 ms time-of-flight.

Chapter 3

Spinor Condensates as Spatially Resolved Magnetometers

We implement ^{87}Rb spinor Bose-Einstein condensates as precision magnetic microscopes with high spatial-resolution. Following the ground work presented in Ref. [11] in December 2005, several months of ensuing experimental activity lead to our demonstration of spinor condensate magnetometry in July 2006 with a sensitivity of $8.3 \text{ pT/Hz}^{1/2}$ over a measurement area of $120 \text{ }\mu\text{m}^2$ [12]. This experimental demonstration marks an improvement over the low-frequency field sensitivity of modern SQUID magnetometers, and we outline the experimental route to this achievement. We begin this discussion with the dominant contributions to our final field detection noise and the strategies employed in its reduction. We assess the performance of the spinor condensate magnetometer under two operating conditions: as a sensor of a long-range inhomogeneous background field and as a sensor of a localized applied magnetic field.

3.1 Spatially resolved magnetometry

3.1.1 Existing magnetometers

Sensitive magnetic field measurements serve as the cornerstone for a range of scientific studies, from tests of fundamental symmetries to the characterization of biological samples. In atomic systems, for example, precision magnetometers are employed in the search for the violation of parity and time reversal invariance [53]. Sensitive field measure-

ments are also important in the characterization of condensed matter [54] and biological systems [55]. For a number of these applications, magnetometers operating at low frequencies (< 10 Hz) with high spatial resolution are particularly useful.

Spatially resolved magnetometry may be accomplished with an array of magnetic microscopes suitable to a wide range of operating conditions, extending from room temperature settings to cryogenic or ultra-high vacuum environments. The state of the art in spatially resolved magnetometry includes devices such as superconducting quantum interference devices (SQUIDS), scanning Hall probe microscopes, magnetic force microscopes, and magneto-optical imaging techniques [56].

Among micron-scale magnetic microscopes, SQUID magnetometers currently provide the most sensitive measurements of magnetic fields. A SQUID magnetometer determines the magnetic field indirectly from its measurement of the magnetic flux. For a measurement area of $100 \mu\text{m}^2$, the SQUID's field sensitivity has been demonstrated to be as low as $30 \text{ pT/Hz}^{1/2}$ [57]. It is the $1/f$ flicker noise of these devices that limits their sensitivity at low measurement frequencies [58]. Another drawback in their employment is the potential for their flux calibration to vary when it is coupled to an unsteady measurement environment.

Atomic magnetometers have the advantage of providing magnetic field measurements which depend only upon fundamental physical constants. Atomic magnetometry which makes use of the Larmor precession of spin-polarized atoms has previously been demonstrated using hot atomic vapors. With a measurement volume of 0.3 cm^3 , a field sensitivity as low as $0.15 \text{ fT/Hz}^{1/2}$ has been attained [59]. However, the thermal diffusion of atoms in the hot atomic vapor limits the spatial resolution of vapor-cell magnetometers to 1 mm.

3.1.2 Ultracold atoms for magnetometry

In this work we take advantage of ultracold atoms to develop sensitive atomic magnetometers with high spatial resolution. Ultracold atoms, characterized by negligible Doppler broadening and long coherence times [60, 50, 61], represent potential sensing media which may be applied to a range of precision measurements. Their low temperature and high density may be considered as excellent ingredients toward their potential application as spatially resolved precision sensors. Despite these attractive properties, however, few

precision measurements have been made with ultracold gases. Thus far, Bose Einstein condensates have been employed in measurements of the Casimir-Polder force [62]; the photon recoil momentum in dispersive media [63]; and \hbar/m and the fine constant structure α [64]. The application of ultracold gases toward metrology has been limited as a result of collisional frequency shifts proportional to the density of the atomic sample being probed [65, 66].

The spinor Bose condensate is an example of an ultracold atomic system which may be applied toward metrology without additional uncertainties imposed by density-dependent mean-field shifts. In this Chapter, we discuss how spinor condensates may be employed as spatially-resolved magnetometers which are free of such mean-field shifts. The potential role of dipole-dipole interactions in the spinor gas, which depend upon the geometry of the sample and orientation of the applied magnetic fields, may be suppressed using techniques analogous to those employed in NMR (Sec. 6.2.2). To operate a spinor condensate as a magnetometer, one measures the local accrued phase of Larmor precession of the condensate magnetization. Due to the rotational invariance of inter-particle interactions in a spinor gas, Larmor precession is unaffected by density-dependent mean field shifts (Eq 1.6) [27, 41]; hence, so is the sensitivity of the spinor condensate magnetometer.

3.1.3 Employing a Larmor precessing spinor condensate as a spatially resolved magnetometer

To spatially resolve an applied magnetic field in two dimensions, we image the Larmor precession of a $F = 1$ Bose Einstein condensate with high spatial resolution. The condensate is prepared in a uniformly magnetized state, e.g. $\mathbf{M}(x, z) = M\hat{x}$, oriented transverse to the applied magnetic field, whose \hat{z} -projection is given by $B(x, z)$. At a given location in the condensate, the spins precess according to the magnitude of the local magnetic field $B(x_0, z_0)$. The local phase of precession accrued over a given integration time is given by $\phi_L(x_0, z_0) = \omega_L(x_0, z_0)t$, where $\omega_L(x_0, z_0) = g\mu_B B(x_0, z_0)/\hbar$ is the Larmor frequency. By imaging the Larmor precession of the condensate using our magnetization sensitive technique (Ch. 2), we construct a spatial map of the relative phase of precession accrued at different locations in the condensate. From this spatially-resolved image of the precession phase, we then determine $B(x_0, z_0)$, the applied magnetic field.

What limits the field sensitivity of a spinor condensate magnetometer? The field

sensitivity, $\delta B = (\hbar/g_F\mu_B)(\delta\phi/t)$, is set by the minimum uncertainty in the measurement of the Larmor precession phase, $\delta\phi$. This phase uncertainty is fundamentally limited by atomic shot-noise, or projection noise. Specifically, for a coherent spin state, the uncertainty in the accrued Larmor phase results from the projection noise in measuring N_a atoms, yielding $\delta\phi = 1/\sqrt{N_a}$.

In addition to the phase uncertainty, the field uncertainty is limited by the integration time. Over a measurement area A , we take the number of atoms to be given by $N_a = \tilde{n}A$, where \tilde{n} is the two-dimensional column density. Assuming a series of field measurements is made over a total measurement time T , at a duty cycle D , and taking the integration time per measurement to be τ , the field sensitivity is given by,

$$\delta B = \frac{\hbar}{g\mu_B} \frac{\delta\phi}{\sqrt{\tau DT}}. \quad (3.1)$$

In our experiment, the phase detection noise, $\delta\phi$, is limited by photon shot-noise rather than atom shot-noise. A discussion of the expected phase uncertainty is presented in Section 3.2 for reasonable experiment parameters.

The above expression for the field sensitivity takes into account two implementation-dependent limitations of a given magnetometer including the duty cycle, D , and the total integration time T . For a single-shot measurement, the integration time is given by τ , the coherence time. In our current experiment, the single-shot integration time is limited by three body collisions which result in the loss of atoms from the trap, and has been measured to range between 250 ms and 1000 ms, depending on the trap geometry used. The present duty cycle is limited to $D = .003$, but may be increased to $D = 1$ in a future implementation by taking advantage of previously demonstrated all-optical BEC production techniques [67].

For the spinor condensate magnetometer operating in the atom shot-noise detection limit, $\delta\phi = 1/\sqrt{\tilde{n}A}$ and the field sensitivity improves as the measurement area as $1/\sqrt{A}$. For small measurement areas, this leads to an improvement in sensitivity in comparison with SQUID magnetometers (Fig. 1, Appendix A). Since a SQUID magnetometer is sensitive to flux, its minimal detectable δB in the simplest case scales as $1/A$. Sophisticated SQUID magnetometers are characterized by a range of scaling relations in A , from $A^{-3/4}$, in the case of a fixed SQUID sensor coupled to a variable pickup loop, and $A^{-5/8}$ in the case of a quantum-limited SQUID used in the direct sensing, low noise energy, operating mode [68].

3.2 Magnetic field sensitivity

In operating the spinor condensate magnetometer, one measures an inhomogeneous magnetic field by directly imaging the local accrued phase of precession of the condensate transverse magnetization, following a given integration period. Contributions to the uncertainty in the measured phase of precession are due to fluctuations in condensate magnetization and fluctuations in the light field used to image the condensate magnetization. In this section, we estimate these contributions to the phase detection noise, which we identify as atom and photon shot-noise respectively.

3.2.1 Determining the phase contrast signal detection noise

To determine the phase detection noise, we begin by considering the fluctuations in the measured signal. At each location in a given phase contrast image of the condensate, the measured signal is proportional to the number of photons which reached a corresponding location on the camera. Fluctuations in the measured signal result from fluctuations in the number of incoming photons and the number of atoms probed at each location in the image.

In this treatment we assume these fluctuations are described by Poissonian statistics. That is, the number of atoms and photons per pixel are described by Poissonian distributions characterized by an average number of atoms and photons per pixel given by λ and ξ respectively.

The measured phase contrast signal per pixel, as presented in Ch. 2, is given by

$$S = N_p(1 + c_0\langle N_a \rangle + c_1\langle M_y \rangle), \quad (3.2)$$

where N_p and N_a correspond to the number of photons and atoms per pixel, c_0 and c_1 are constants determined by the imaging settings and condensate parameters, and M_y is the \hat{y} -projection of the condensate magnetization. As before, \hat{y} corresponds to the imaging axis.

To determine the expected fluctuations, ΔS , in the measured signal about its average value $\langle S \rangle$, we determine the distribution of possible signal values and their respective probabilities. This distribution is derived from the Poissonian statistics governing the number of photons, number of atoms, and \hat{y} -projection of the magnetization measured at each pixel.

A given atomic state $|\Psi\rangle$, composed of N_a atoms distributed among the magnetic

sublevels $|+\rangle, |-\rangle$, and $|0\rangle$ with probabilities determined by amplitudes α, β, γ , is described by,

$$\begin{aligned} |\Psi\rangle &= (\alpha|+\rangle + \beta|0\rangle + \gamma|-\rangle)^{N_a} \\ &= \sum_{i,j,k} \sqrt{\frac{N_a!}{i!j!k!}} \delta_{N_a, i+j+k} \alpha^i \beta^j \gamma^k |+\rangle^i |0\rangle^j |-\rangle^k, \end{aligned} \quad (3.3)$$

such that there are i, j, k atoms in sublevels $|+\rangle, |0\rangle, |-\rangle$; the number of atoms is given by $N_a = i + j + k$; and the \hat{y} -projection of the magnetization is given by $M_y = i - k$. For a given atomic state, the phase contrast signal $S(N_p, N_a, \Psi_{i,j,k,N_a})$ is measured with probability $P(N_p)P(i, j, k, N_a)$, where

$$\begin{aligned} S &= N_p(1 + c_0(i + j + k) + c_1(i - k)) \\ P(i, j, k, N_a) &= \frac{N_a!}{i!j!k!} \delta_{N_a, i+j+k} |\alpha|^{2i} |\beta|^{2j} |\gamma|^{2k} e^{-\xi} \frac{\xi^{N_a}}{N_a!} \\ &= \frac{1}{i!j!k!} |\alpha|^{2i} |\beta|^{2j} |\gamma|^{2k} e^{-\xi} \xi^{i+j+k} \\ P(N_p) &= e^{-\lambda} \frac{\lambda^{N_p}}{N_p!}. \end{aligned} \quad (3.4)$$

The expected fluctuations in the signal, ΔS , about its average value $\langle S \rangle$, may therefore be determined from,

$$\begin{aligned} \langle S \rangle &= \sum_{i,j,k,N_a,N_p} P(N_p)P(i, j, k, N_a) S(N_p, N_a, \Psi_{i,j,k,N_a}) \\ \langle S^2 \rangle &= \sum_{i,j,k,N_a,N_p} P(N_p)P(i, j, k, N_a) S^2(N_p, N_a, \Psi_{i,j,k,N_a}) \\ \Delta S &= \sqrt{\langle S^2 \rangle - \langle S \rangle^2}. \end{aligned} \quad (3.5)$$

We can identify separate contributions to the signal detection noise ΔS from atomic shot-noise and photon shot-noise, associated with fluctuations in the atom and photon fields, respectively.

Atom shot-noise

We determine the contribution to the signal detection noise from fluctuations in the atomic field by holding the number of photons per pixel fixed. Taking $N_p = \xi$,

$$\Delta^2 S = \xi^2 \lambda (c_0^2 + c_1^2 (|\alpha|^2 + |\gamma|^2) + 2c_0 c_1 (|\alpha|^2 - |\gamma|^2)) \quad (3.6)$$

$$\equiv \Delta^2 S_a. \quad (3.7)$$

and we denote ΔS_a as the atomic shot-noise contribution to the signal detection noise. It is a sum of three terms that we can individually understand: since $S/\xi = 1 + c_0 N_a + c_1 M_y$, we expect to find $\Delta^2 S/\xi^2 = c_0^2 \Delta^2 N_a + c_1^2 \Delta^2 M_y + 2c_0 c_1 (\langle N_a M_y \rangle - \langle N_a \rangle \langle M_y \rangle)$.

The first term, given by $\xi^2 c_0^2 \lambda$, reflects fluctuations in the atom number. The second term, $\xi^2 c_1^2 \lambda (|\alpha|^2 + |\gamma|^2)$, reflects projection noise in the magnetization. The third term reflects correlations between these two related quantities.

Photon shot-noise

Similarly, we can determine the contribution to the signal detection noise from photon shot-noise, $\Delta^2 S_p$, by considering a fixed atomic field. This yields,

$$\Delta^2 S_p = \xi (1 + \lambda (c_0 + c_1 (|\alpha|^2 - |\gamma|^2))^2). \quad (3.8)$$

In our experiment, the detection noise floor is dominated by photon shot-noise.

Total signal detection noise

The signal detection noise, $\Delta^2 S$, is given by,

$$\begin{aligned} \Delta^2 S &= \xi(\xi + 1) \lambda (c_0^2 + c_1^2 (|\alpha|^2 + |\gamma|^2) + 2c_0 c_1 (|\alpha|^2 - |\gamma|^2)) + \xi (1 + \lambda (c_0 + c_1 (|\alpha|^2 - |\gamma|^2)))^2 \\ &= \xi(\xi + 1) \frac{\Delta^2 S_a}{\xi^2} + \Delta^2 S_p. \end{aligned}$$

It is nearly the case that $\Delta^2 S = \Delta^2 S_a + \Delta^2 S_p$, with the exception that in the former term, ξ^2 is replaced by $\xi(\xi + 1)$. In our experiments, ξ is large (> 100) and $\xi(\xi + 1) \sim \xi^2$; thus, to a good approximation, the atomic and photon shot-noise may be added in quadrature to determine the signal detection noise.

3.2.2 Determining the magnetic field detection noise

In the determination of the phase of a sinusoidally varying signal, the phase uncertainty is given by,

$$\Delta\phi = \sqrt{\frac{2}{N_m} \frac{\Delta S}{A_L}}, \quad (3.9)$$

where ΔS reflects the signal detection noise, A_L corresponds to amplitude of the signal oscillation; and N_f reflects the number of signal measurements.

A sequence of N_f phase contrast images of a Larmor precessing condensate may be considered, pixel-by-pixel, as a series of sinusoidally varying signals. At a given pixel, the oscillating phase contrast signal is described by,

$$S/N_p = (1 + \Lambda + A_L \cos(\omega_L t + \phi)), \quad (3.10)$$

where, in connection with Eq.3.2, Λ is a constant offset given by $\Lambda = c_0 \langle N_a \rangle$ and A_L is the signal oscillation amplitude, which for a transversely magnetized condensate is given by $A_L = c_1$. A quantitative analysis of the phase noise is presented in the following Section.

In our experiment, a given phase contrast image is normalized by the probe field. The probe field corresponds to a separate image taken without atoms present, to determine the number of photons per pixel. In the limit that the signal detection noise is dominated by photon shot-noise, the phase uncertainty of the normalized image is given by,

$$\begin{aligned} \Delta\phi &\sim \sqrt{\frac{2}{N_f} \frac{\Delta S_p}{\xi A_L}} \\ &= \sqrt{\frac{2}{N_f} \frac{\sqrt{\xi}(1 + \Lambda)}{\xi A_L}}. \end{aligned} \quad (3.11)$$

To determine our phase detection noise, we take into account our phase contrast imaging settings and condensate parameters, presented in Chapter 2. A phase contrast image is taken using circularly polarized light detuned by $\delta = 2\pi \times (500 \text{ MHz})$ below the $F = 1 \rightarrow F' = 2$ (D1) transition of ^{87}Rb . In our experiment, the normalized phase contrast signal is approximately given by,

$$\tilde{S}(x, z) = 1 + 2\tilde{n}(x, z)\sigma_0(\gamma/2\delta)(\tilde{c}_0 + \tilde{c}_1 \langle M_y \rangle), \quad (3.12)$$

where $\sigma_0 = 3\lambda^2/2\pi$ is the resonant cross section and γ is the natural linewidth of the transition. As presented in Ch. 2, \tilde{c}_0 and \tilde{c}_1 are detuning-dependent constants which reflect the refractive properties of the spinor gas. For the selected imaging settings, $\tilde{c}_0 = .12$ and $\tilde{c}_1 = .27$, which describe its isotropic polarizability and optical activity, respectively. We neglect contributions to the phase contrast signal from linear birefringence, which are proportional to $\langle F_y^2 \rangle$.

Phase detection noise

For our imaging settings, the phase detection noise is dominated by photon shot-noise (Eq. 3.11). Evaluated at a pixel at position \mathbf{r} , $\delta\phi_p$ is given by

$$\delta\phi_p(\mathbf{r}) = \sqrt{\frac{2}{eN_fN_p} \frac{\sqrt{1 + \tilde{n}(\mathbf{r})\sigma_0\frac{\gamma}{2\delta}\tilde{c}_0}}{\tilde{n}\sigma_0\frac{\gamma}{2\delta}\tilde{c}_1}}, \quad (3.13)$$

where in our experiment $N_p = 750$ corresponds to the number of photons per pixel per frame and $N_f = 20$ corresponds to the number of frames used. One pixel corresponds to an area of $1 \mu\text{m} \times 1 \mu\text{m}$ in the condensate. The total probe fluence per pixel is given by $750/\mu\text{m}^2$, and is collected using the multi-pulse imaging technique described in Section 2.4.2. The detector efficiency is taken to be $e = .33$.

In our experiment, $N_a = 1.4 \times 10^6$ and the condensate is described by a Thomas-Fermi profile with characteristic radii $(r_x, r_y, r_z) = (5.6, 2.4, 211) \mu\text{m}$. The column density profile, $\tilde{n}(x, z)$, is determined by integrating the condensate density profile, $n(x, y, z)$ along the imaging (\hat{y}) axis, where

$$\begin{aligned} n(x, y, z) &= \frac{15}{8\pi} \frac{N_a}{r_x r_y r_z} \left(1 - \frac{x^2}{r_x^2} - \frac{y^2}{r_y^2} - \frac{z^2}{r_z^2} \right) \\ \tilde{n}(x, z) &= \frac{5}{2\pi} \frac{N_a}{r_x r_z} \left(1 - \frac{x^2}{r_x^2} - \frac{z^2}{r_z^2} \right)^{3/2}. \end{aligned} \quad (3.14)$$

For a $1 \mu\text{m}^2$ measurement area at the condensate center, $\tilde{n}_0 = 937 \text{ atoms}/\mu\text{m}^2$ and the phase detection noise corresponds to $\delta\phi = 47 \text{ mrad}/\mu\text{m}^2$. In our demonstration of the spinor condensate magnetometer, we typically make use of a central condensate region $5 \times 24 \mu\text{m}^2$ in size. Over this measurement area, $\langle \tilde{n} \rangle = .9 \tilde{n}_0$ and the phase uncertainty is given by $\delta\phi_p = 4.8 \text{ mrad}$.

Thus far, we have ignored the reduction in the atom number throughout the operation of the magnetometer due to atom loss. In our experiment, Larmor precession was observed following an integration time given by $\tau = 250$ ms. Assuming the atom loss is described by exponential decay characterized by a rate constant given by $1/\tau$ ms⁻¹, the latter phase noise estimate is increased to $\delta\phi_p = 7.9$ mrad.

The contribution to the phase detection noise due to atomic shot-noise was roughly $\delta\phi_a = 4.1$ mrad for the same conditions. The total phase detection noise is therefore expected to be on the order of $\delta\phi = 8.9$ mrad, in good agreement with the measured phase noise in our experiment (Sec. 3.3.3).

Field detection noise

The estimated phase detection noise translates directly to an expected magnetic field detection noise per measurement given by,

$$\delta B = \frac{\hbar}{g_F \mu_B} \frac{\delta\phi}{\tau}. \quad (3.15)$$

Taking $\delta\phi = 10$ mrad, an integration time $\tau = 250$ ms, and $g_F \mu_B = 700$ kHz/G, the field uncertainty is given by 9 nG. This corresponds to the single-shot sensitivity of a spinor condensate magnetometer described by the above parameters (using a $120 \mu\text{m}^2$ measurement area). Repeated measurements of the applied field would enable the field uncertainty, δB , to be reduced further (ideally according to $1/\sqrt{T}$, as described by Eq. 3.1).

3.3 Demonstration Experiment

3.3.1 Magnetic Microscopy Setup

In our demonstration of the spinor condensate magnetometer, we make use of optically trapped condensates of ⁸⁷Rb atoms, initially prepared in the $m_z = -1$ state as described in Section 1.5.1. In this experiment, the optical dipole trap is characterized by trap frequencies $(\omega_x, \omega_y, \omega_z) = 2\pi \times (165, 440, 4.4)$ s⁻¹, and the condensate is characterized by Thomas Fermi radii $(r_x, r_y, r_z) = (5.6, 2.4, 211)$ μm . Along the imaging (\hat{y}) axis, the condensate radius r_y is smaller than the spin healing length. Consequently, spin excitations along this direction are too energetically costly to be sustained, and we assume the spinor

condensate is effectively two-dimensional with respect to its spin degree of freedom. By imaging the spinor gas along the \hat{y} axis, we are discarding information about its magnetization profile along this direction, assuming it to be homogeneous.

In this demonstration experiment, we operate the spinor condensate as a two-dimensional sensor of an applied magnetic field. With this application in mind, we consider the condensate simply as gas of Larmor precessing atoms. In particular, for the trap geometry and field orientation chosen for this experiment, we may assume the role of dipole-dipole interactions to be negligible (as discussed in Section 1.5.1). In general, one may employ techniques analogous to those used in NMR to suppress the role of dipole-dipole interactions in the system during its operation as a spatially resolved magnetometer (Sec. 6.2.2).

Prior to the measurement of an applied magnetic field, inhomogeneous features in the background field were deliberately canceled with the use of electromagnets designed for this purpose. Our procedure for characterizing and reducing the ambient field inhomogeneities is discussed in Section 1.5.2. In the magnetometry experiment, the background field was measured to be homogeneous over the spatial extent of the condensate to a level of $\Delta B < 6 \mu\text{G}$. The background field included the homogeneous bias field, $\mathbf{B} = B_{\text{bias}}\hat{z}$, necessary to induce Larmor precession. For this experiment, $B_{\text{bias}} = 165(7) \text{ mG}$, corresponding to a Larmor precession frequency of $\omega_L = 2\pi \times (115 \text{ kHz})$.

In the operation of the spinor condensate magnetometer, the initial condition corresponds to a uniformly transversely magnetized condensate. In our experiment, the transversely magnetized state was prepared by rotating the condensate magnetization, initially longitudinally magnetized along $-\hat{z}$, to be transverse to the magnetic field by applying a $\pi/2$ pulse. The $\pi/2$ pulse was applied using an RF generator (SRS DS340), whose output was characterized by a sinusoidal waveform with drive frequency $f_{RF} = 117 \text{ kHz}$ and N_{osc} full cycles. The number of cycles set the pulse bandwidth and was chosen to accommodate shot-to-shot variations in the bias magnetic field, ΔB_z . Typically $\Delta B_z = \pm g_F \mu_B (10 \text{ kHz})$, and $N_{osc} = 10$. The pulse bandwidth, then given by $\Delta f_{RF} = f_{RF}/N_{osc} \approx 12 \text{ kHz}$, was sufficiently large to accommodate shot-to-shot variations in the field. The RF pulse was broadcast using one of the gradient coils of the magnetic trap, conveniently oriented along the \hat{y} axis (as described by Ref. [11]).

The reproducibility of the $\pi/2$ pulse in the preparation of a transversely magnetized state was assessed using both in-situ and time-of-flight imaging techniques. Following a variable evolution period, we verified that the measured contrast and offset of the oscillating

phase contrast signal correspond to the expected signal strengths for a Larmor precessing condensate. In addition, we applied the Stern-Gerlach technique of spatially separating the magnetic Zeeman levels m_z to determine and verify their relative populations (Sec. 2.5). For a transversely magnetized state, the ratio of populations of $m_z = (-1, 0, 1)$ atoms corresponds to 1 : 2 : 1.

3.3.2 Constructing a Magnetic Field Map

We construct two-dimensional maps of the magnetic field from the described pixel-by-pixel determination of the Larmor precession phase $\phi(x_0, z_0)$ at each point in the condensate. As presented in Section 2.3.2, our method of determining the Larmor phase takes into account the decay of condensate number caused by off-resonant scattering of the imaging probe.

The magnetometry experiment was performed prior to the replacement of our imaging system discussed in Chapter 2. Consequently, the measured two-dimensional phase map suffered from imaging aberrations, particularly in the narrow (\hat{x}) dimension of the condensate. To obtain robust field measurements, the corresponding measured field profile $B(x, z)$ was integrated over this (\hat{x}) direction. In determining the sensitivity of the magnetometer, we characterized repeated measurements of the reduced field profile, $\tilde{B}(z)$.

The one-dimensional field profile, $\tilde{B}(z)$, was determined by making use of the form of the aberration incurred by the imaging system. For each z coordinate in the condensate, the aberration profile $I_z(x)$ was determined from the average of several frames. For a uniformly precessing condensate, the average phase contrast signal (taken over several frames) is proportional to the convolution of the condensate density profile with $I_z(x)$, thus enabling its determination. By making use of the aberration profile, $I_z(x)$, the peak phase contrast signal per frame was determined at each coordinate z , $\tilde{S}(z)$. By applying the same analysis procedures to the reduced phase contrast images $\tilde{S}(z)$, one-dimensional phase profiles $\tilde{\phi}(z)$, and their related field profiles, $\tilde{B}(z)$, were obtained.

A representative sequence of phase contrast images of a Larmor precessing condensate and its corresponding phase profile $\tilde{\phi}(z)$, are shown in Fig. 3.1. The sequence of phase contrast images of a Larmor precessing condensate, taken following a 50-ms evolution period in a curvature-dominated field environment, delineates its approximately quadratic spatial profile. This profile is also reflected in the corresponding one-dimensional Larmor phase

$\tilde{\phi}(z)$. For clarity, the form of the inhomogeneous field profile $\tilde{B}(z)$ is shown in juxtaposition with the phase contrast data.

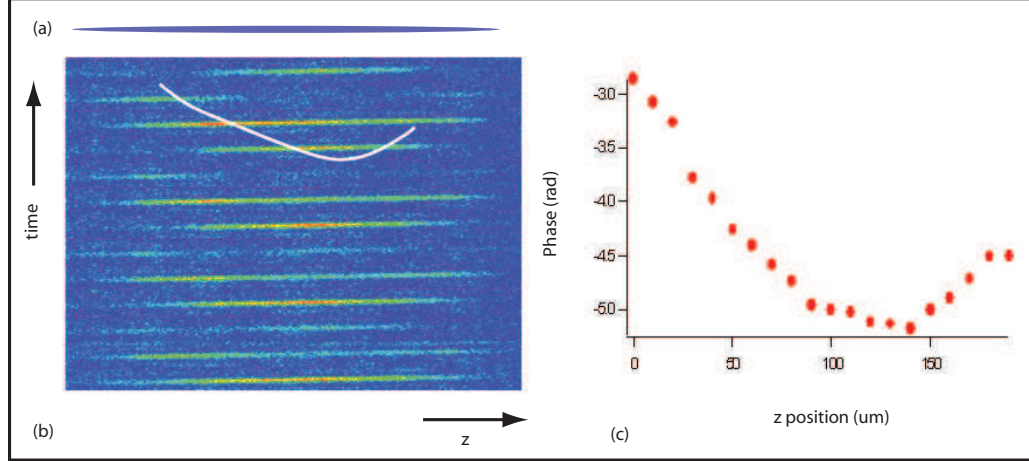


Figure 3.1: A sequence of phase contrast images of a Larmor precessing condensate (whose density profile is indicated schematically (a)) is shown following a 50-ms evolution period (b). In this example, the magnetic field environment is dominated by a large field curvature given by $(g_F\mu_B/h)d^2B_z/dz^2 = 80$ kHz/cm². The relative phase of precession across the condensate varies quadratically with position, z , by roughly 20 rad across its spatial extent (c). For clarity, the magnetic field profile is indicated upon the raw data in (b).

3.3.3 Characterizing the magnetic field environment

In the first testing condition of the spinor condensate magnetometer, it was used to characterize the background magnetic field present in the apparatus. Prior this characterization, the dominant contributions to the field inhomogeneities were measured and canceled, as described in Section 1.5.2. Specifically, contributions to field inhomogeneities by stray field gradients and curvatures corresponding to $\frac{dB_z}{dz}$, $\frac{dB_x}{dz}$ and $\frac{d^2B_z}{dz^2}$ were measured and canceled. In this experiment, the field inhomogeneities were reduced to magnitudes: $|\frac{dB_z}{dz}|, |\frac{dB_x}{dz}| < 0.1 - 0.3$ mG/cm and $|\frac{d^2B_z}{dz^2}| < 10 - 20$ mG/cm². The total magnetic field inhomogeneity was reduced to roughly $\Delta B < 6$ μ G over the spatial extent of the condensate.

In the operation of the magnetometer, following the cancelation of these inhomogeneities, the remaining field background $\tilde{B}(z)$ was fit to a third-order polynomial $B_p(z) = c_0 + c_1z + c_2z^2 + c_3z^3$, which characterized its long-range features. Field variations from fourth order terms and higher terms were negligible (estimated to be smaller than 1 fT in magnitude). From shot to shot, the background field varied. The residuals

from the third order polynomial fit, $R(z) = \tilde{B}(z) - B_p(z)$, were used to characterize the noise floor of the magnetometer. Specifically, the spatial root Allen variance of $R(z)$ over the active measurement region corresponded to the quoted field detection noise, δB .

Demonstrated magnetometer sensitivity

The field detection noise determined during the first testing condition of the spinor condensate magnetometer – as a sensor of the nearly homogeneous field background – is in good agreement with the shot-noise estimate presented in Section 3.2.2. For a $5.3 \times 24 \mu\text{m}^2$ measurement area, the single-shot rms phase sensitivity was determined to be 10 mrad, corresponding to a single-shot field sensitivity of 0.9 pT. The x -dimension of the measurement area corresponds to the $5.3 \mu\text{m}$ length over which the aberrated signal was effectively averaged in the \hat{x} direction.

Repeated measurements of the magnetic field background with a duty cycle of $D = 3 \times 10^{-3}$ yielded a corresponding field sensitivity of $8.3 \text{ pT/Hz}^{1/2}$. This already marks an improvement over the sensitivity of existing SQUID magnetometers at low measurement frequencies ($< 10 \text{ Hz}$). The duty cycle of our experiment could be improved up to $D = 1$ by taking advantage of demonstrated all-optical BEC production techniques [69, 57], in which case our single-shot field sensitivity would translate to a field sensitivity of $0.5 \text{ pT/Hz}^{1/2}$.

The magnetic field detection noise for some regions of the condensate, typically larger than $20 \mu\text{m}^2$, was found to exceed the above average shot-noise estimate by roughly 10 to 20 percent (Fig. 3 Appendix A). The corresponding increase in phase noise detected in these regions was correlated with the local intensity profile of the probe beam. As we saw in Section 1.5.3, although in another context, an applied AC Stark shift may also modify the precession frequency of an atomic spin by a small amount. In this context, the circularly polarized imaging probe optically induces an AC Stark shift; this results in a probe-induced shift of the Larmor precession frequency on the order of 1 mHz. For comparison, a 6-mHz shift in the Larmor frequency would lead to an additional Larmor phase of 10 mrad to be accrued over 250 ms. We observe the Larmor phase to be slightly altered by the application of the probe; this is reflected by a position-dependent increase in the phase detection noise, correlated to the probe intensity profile. In a future implementation, by using a linearly polarized probe and by spatially filtering the probe intensity profile so as to make it homogeneous, this probe-induced frequency shift may be reduced. Due to a residual

effect of alignment-to-orientation conversion it may not be eliminated completely [70].

Strategies employed for reducing the field detection noise

In our experiment, the magnetic field detection noise is limited by the photon shot-noise in the optical characterization of the Larmor phase. To minimize the photon shot-noise, one may naively suggest to increase the probe fluence indefinitely. Increasing the probe fluence, however, also results in increasing the atomic shot-noise since atoms will be increasingly scattered by the probe into other states. In our experiment, the probe fluence and frequency were chosen to simultaneously minimize these losses and optimize the phase detection noise. Our empirical determination of these optimal settings is presented in Section 2.4.1.

Two additional strategies were employed in this experiment to minimize probe-induced losses, allowing the probe fluence to be raised to $750 \text{ photons}/\mu\text{m}^2$ per frame. As discussed in Section 2.4.1, probe-induced losses were primarily due to superradiant Raman scattering of atoms into the $F = 2$ hyperfine states. First, to reduce the probe-induced scattering rate, the probe intensity was lowered while maintaining a high probe fluence. This was accomplished by obtaining each frame in the imaging sequence by integrating four pulses of light characterized by an intensity $I/4$ in lieu of one pulse characterized by an intensity I . The four pulses were spaced by the Larmor period of roughly $T_L = 10 \mu\text{s}$ and characterized by a duration of $2.2 \mu\text{s} < T_L/4$. Second, to disrupt the coherent superradiant Raman scattering of condensate atoms into the $F = 2$ state, we applied light close to the $F = 2 \rightarrow F' = 3$ (D2) transition during the imaging sequence ($\delta_{D2} = -30 \text{ MHz}$).

More pertinent to the measurement of a localized field than to the measurement of the inhomogeneous background, an additional strategy was employed during the field measurement to monitor the condensate motion. As a result of small vibrations in the environment of the experiment, we observed small center-of-mass oscillations of the condensate along the z axis, characterized by the trap frequency $\omega_z = 4.4 \text{ Hz}$. These oscillations served to blur spatial features of the measured magnetic field over a lengthscale comparable to the displacement of the condensate during the integration period. We were unable to completely remove the observed condensate oscillations. However, by monitoring these oscillations we were able to discard measurements for which the condensate was displaced by an amount comparable to the spatial-extent of the applied field. Prior to the Larmor precession imag-

ing sequence, we took four additional phase contrast images, spaced by a quarter period of the axial trap oscillation, $(2\pi/4\omega_z)$. A measurement was discarded when the maximum displacement of the condensate center of mass with respect to its average position over the four frames was comparable to the spatial-extent of the applied field.

3.3.4 Characterizing a localized magnetic field

Demonstrating the sensitivity of the condensate magnetometer required the application of a known, localized magnetic field, and its quantitative characterization. We simulated applying a localized magnetic field *optically* by taking advantage of the spin-dependence of the AC Stark shift. Following Refs [11, 71], an AC Stark shift induced by an applied laser beam was manipulated to emulate a linear Zeeman shift.

In our experiment, the optically-induced AC Stark shift was applied using a circularly-polarized ($\hat{\sigma}$) laser beam characterized by a wavelength $\lambda = 790$ nm. Neglecting the hyperfine structure, the resulting AC Stark shift imparted upon the $|J = 1/2, m_J = \pm 1/2\rangle$ state, given by $\Delta E_{J=1/2, m_J=\pm 1/2}$, may be interpreted as a linear Zeeman shift due to an effective magnetic field of magnitude [11],

$$\begin{aligned} B_{sim} &= \frac{1}{gJ\mu_B} \frac{\Delta E_{J=1/2, m_J=1/2} - \Delta E_{J=1/2, m_J=-1/2}}{2} \\ &= \frac{\hbar\gamma^2}{8\mu_B gJ} \frac{I}{I_{sat}} \frac{1}{\delta}, \end{aligned} \quad (3.16)$$

where I is the beam intensity; $I_{sat} = 1.67$ mW/cm²; the detuning, $\delta = -2\pi \times 4.8$ THz, is given with respect to the $F = 1 \rightarrow F' = 2$ (D1) transition; and $\gamma = 6$ MHz corresponds to its natural linewidth.

The applied laser beam was aligned at an angle of 60 degrees with respect to the bias field (\hat{z}) and focussed at the condensate center, in the x, z plane. At the location of its focus, the beam intensity profile is described by $I(\mathbf{r}) = I_0 G(\mathbf{r})$ where $G(\mathbf{r})$ is a normalized two-dimensional Gaussian distribution with characteristic $1/e^2$ radii given by x_0, y_0 . The focus of the laser beam (x_0, y_0) was adjusted using two pairs of cylindrical lenses (Section 1.5.1), enabling the characterization of the applied field as a function of its spatial extent. The application of the laser beam resulted in an position-dependent precession phase to be accrued following a given integration period t , given by

$$\delta\phi(\mathbf{r}) = \left(\frac{g_F\mu_B}{\hbar} \right) \left(\frac{B_{sim}(\mathbf{r})}{t} \right) \cos(60^\circ). \quad (3.17)$$

where B_{sim} is the magnitude of the applied field, whose calibration is presented in Ref. [11]. The orientation of the applied laser beam with respect to the condensate \hat{z} axis is shown schematically in Fig. 3.2(a). The sequence of phase contrast images of a Larmor precessing condensate, taken following a 150-ms evolution period in the presence of an optically induced field $B_{sim}(\mathbf{r})$, delineates its Gaussian spatial profile. This profile is also reflected in the corresponding one-dimensional Larmor phase $\tilde{\phi}(z)$.

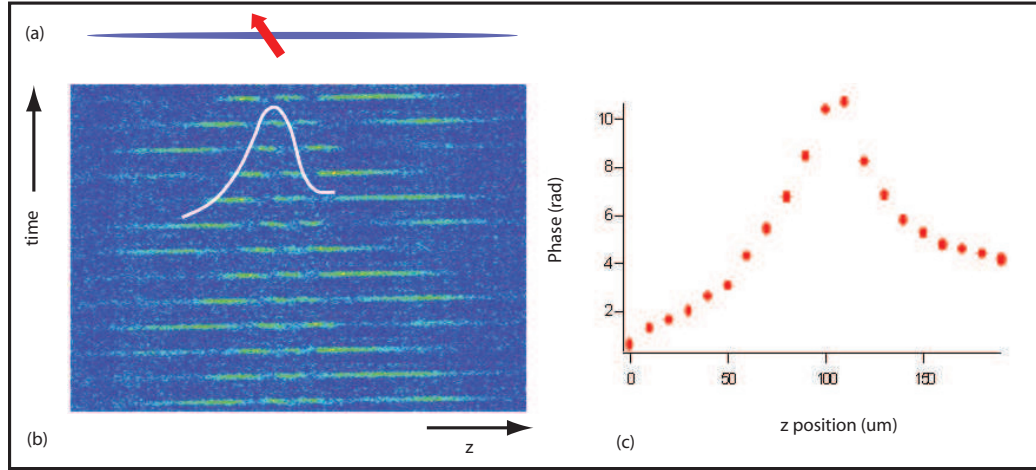


Figure 3.2: A schematic representation of the applied, optically-induced field (a). In the same configuration, a sequence phase contrast images of a Larmor precessing condensate, following a 150 ms integration period, portray the spatial-variation of the accrued phase of precession due to the applied field. For clarity, the Gaussian field profile is indicated upon the raw data. The reduced phase profile $\tilde{\phi}(z)$ provides a quantitative measure of the accrued Larmor phase from which the magnitude of the applied field may be determined.

Demonstrated measurement of an applied field

In the characterization of a spatially-localized applied magnetic field, both the background field and the localized field were measured for each run of the experiment. The background field was determined using the aforementioned third-order polynomial fit, $B_p(z)$, applied to the regions of the condensate far from the localized field (typically using a 70-100 μm regions on each side of the condensate). The profile of the localized field was then determined from the residuals of this polynomial fit, $R(z)$, when applied to the region of the localized field (typically using a 30-50 μm central region of the condensate).

The strength of the applied field was determined from the peak value of a Gaussian fit to $R(z)$ and measured for several powers, P of the applied laser beam. This enabled a

calibration of the applied field with the laser beam power, presented in Ref. [11]. Shown in Fig.3 of Appendix A are measurements of localized magnetic fields ranging from 20 to 150 pT in magnitude following a 250-ms integration period, simulated by a laser beam whose focus is characterized by radii $x_0 = 5.3 \mu\text{m}$, $z_0 = 24 \mu\text{m}$. The field detection noise is reflected by the error bars of the field measurements presented in this Figure. Using a $120\text{-}\mu\text{m}^2$ measurement area under the Gaussian field profile, the single-shot field detection noise corresponded to roughly 0.9 pT. We measured a similar field sensitivity for applied fields up to $B_{sim} = 60$ pT. The systematic errors associated with the measurements were therefore negligible in comparison with their variance. For $B_{sim} > 60$ pT, the field sensitivity appears to deteriorate slightly with the beam power, pointing to systematic effects possibly associated with atomic motion and the spatially-varying field strength.

3.3.5 Limitations to measuring localized fields

Limitations to the field sensitivity of the spinor condensate magnetometer were first outlined in Ref. [11]. In addition to preliminary estimates for the field detection noise, potentially limiting systematic effects due to atomic motion, the self-field of the condensate, the role of dipole interactions, and the applied quadratic shift were presented. The reader is referred to Ref. [11] for the supporting calculations. The discussed limitation to field uncertainty imposed by inhomogeneities in the background field could be overcome by implementing a spin-echo sequence. However, by developing better control over the field inhomogeneities in our experiment, their contribution to the field uncertainty was suppressed. The field detection noise was dominated by photon shot-noise, and, offering negligible benefit, the proposed spin-echo sequence in Ref. [11] was no longer pursued. In this Section, we will focus upon the experimental tests of the limitations of the magnetometer which followed these initial projections.

In our characterization of the spinor condensate magnetometer, we have experimentally investigated the limitation imposed by atomic motion upon its field sensitivity. Thus far, we have considered the spinor Bose condensate as a stationary sensor of applied magnetic fields. In reality, the spinor gas consists of atoms which are free to move. Taking into account both the quantum and classical effects of atomic motion, the phase sensitivity of our optical detection scheme is systematically altered.

From the perspective of quantum mechanics, a spinor condensate which has ac-

quired a position-dependent Larmor phase – which we may consider as a position-dependent rotation in its transverse magnetization, \mathbf{M} – is penalized by the kinetic energy associated with this rotation. For example, by imposing a homogeneous magnetic field $B\hat{z}$ of a characteristic length σ for a given integration time t , we have advanced the Larmor phase by $\delta\phi = \hbar g_F \mu_B B t$ over a region of length σ . An instantaneous snapshot of the magnetization profile would reveal a local “twist” in \mathbf{M} by an angle of $\delta\phi$ rad about the \hat{z} axis. This twist has a kinetic energy cost $\sim \hbar^2/m\sigma^2$, assuming $\delta\phi \gtrsim 1$; and as a result, it will “unwind”. This effect may be described as quantum diffusive motion of the atomic fluid and corresponds to the quantum limit of thermal diffusion observed in NMR experiments [72].

Quantum diffusive motion following the application of a localized magnetic field on a lengthscale σ effectively limits the spatial resolution of the magnetometer. For integration times larger than the time scale of the diffusive motion ($t > m\sigma^2/\hbar$), the diffusion of atoms throughout the integration period averages the accrued Larmor phase over a region $> \sigma$. The corresponding reduction in field sensitivity may be considered as a consequence of the lowered integration time for a field measurement performed at a given point in space. In our experiment, the 250 ms integration time exceeds the diffusion timescale for features in the applied field larger than $10\ \mu\text{m}$ in size.

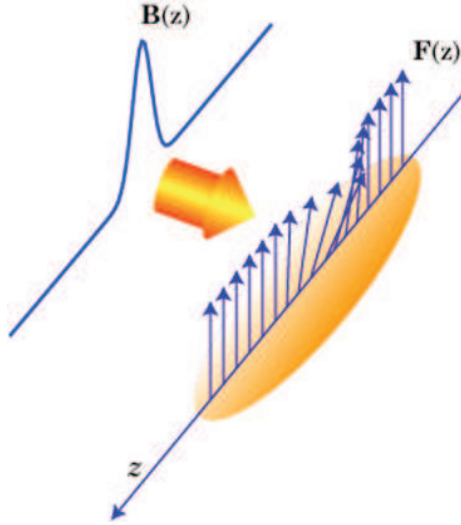


Figure 3.3: By imposing an inhomogeneous magnetic field characterized by a Gaussian spatial profile for a given integration time, we have locally modified the Larmor precession phase. An instantaneous snapshot of the magnetization profile reveals a local “twist” in \mathbf{M} by an angle about the \hat{z} axis proportional to the magnitude of the applied field.

Experimentally, we characterize quantum diffusion in the spinor condensate magnetometer and determine the limitation it imposes upon its field sensitivity to applied localized fields. To do so, we deliberately apply a field localized to $\sigma < 10 \mu\text{m}$ and study its evolution (Fig. 3.3). For this study, we make use of the optically-induced field imposed by a laser beam characterized by a $5.4\text{-}\mu\text{m}$ beam waist. The field-inducing beam is applied for $5 \text{ ms} \ll m\sigma^2/\hbar$. Following this “field measurement”, the condensate is allowed to evolve for a given time t , after which its magnetization profile is probed. The observed time evolution of the Gaussian phase profile is shown in Fig. 4 of Appendix A. At $t = 0$ its characteristic lengthscale is $5 \mu\text{m}$, in correspondence with the applied laser beam, and as time progresses, its width increases and its peak value is reduced (Fig. 4 (b),(c) Appendix A). The observed time evolution is well described by the theory for a non-interacting spinor gas in a localized field (depicted on Fig. 4 (b)(c)).

The limitation to the field sensitivity of the spinor condensate magnetometer imposed by atomic motion may be circumvented by employing an atomic ensemble whose constituent atoms are fixed in position. For example, by making use of an array of $1 \mu\text{m}$ -sized optically-trapped condensates, one would recover a spatial resolution limited by the periodicity of the optical lattice. The lattice implementation of the spinor condensate magnetometer may be limited in its sensitivity by spatial inhomogeneities of the trapping potential.

In conclusion, we have demonstrated near to atom-shot-noise limited performance of a spatially resolved spinor-condensate-based magnetometer. With a few technical improvements, atom-shot-noise-limited magnetometry will be in reach. A future outlook for this work is the prospect of spatially resolved studies of spin-squeezed states. An alternative approach to spatially resolved spin squeezing, making use of atomic interactions inherent to a ^{87}Rb spinor Bose condensate, is presented in Chapter 5.

Chapter 4

Amplification of Spin Fluctuations in a Spinor Bose Einstein Condensate

We implement ^{87}Rb spinor Bose-Einstein condensates as nearly quantum-limited amplifiers of spin fluctuations with high spatial resolution. In so doing, we re-interpret the observation of spontaneous ferromagnetism in the quantum quench of a spinor condensate (Ref. [1]) as the operation of the spinor condensate as a tunable amplifier of spin fluctuations. With this perspective, the spectrum of excitations in a spinor condensate defines the spectrum of a mode-by-mode parametric amplifier. We present a formalism to describe the spin-or condensate amplifier, enabling a quantitative comparison of the observed magnetization dynamics to a quantum amplification theory. In our experimental characterization of this spin amplifier, we demonstrate nearly quantum-limited performance at a gain as high as 30 dB [2]. In particular, we are motivated to understand the types of spin fluctuations that are being amplified in this $F = 1$ spinor gas and to explore its potential application as a quantum measurement device.

4.1 Quantum dynamics and the quench of a spinor condensate

The spinor Bose Einstein condensate offers the experimentalist the opportunity to grapple with fundamental questions about quantum dynamics in the most tangible of ways: to image directly the quantum dynamics of a macroscopic quantum system. The unique opportunity to probe out of equilibrium dynamics in the spinor condensate is afforded by the long timescales and long-range spatial features which characterize the spin dynamics of interest. Here we focus on the dynamics which accompany a quantum phase transition between two phases of the spinor condensate, which we characterize with high spatial and temporal resolution.

In studying the dynamics associated with a given phase transition, one can gain access to a rich array of physics realized in a range of physical systems. The physics of phase transitions between disordered and ordered phases – for example, how equilibrium phases, or out of equilibrium dynamics are affected by interactions, quantum and thermal fluctuations and the proximity to the transition – is a subject of general interest and one which is made accessible with studies of spinor condensates.

In the quantum phase transition of a spinor condensate that we consider here, the energetically-favorable state of the system is rapidly tuned from an unmagnetized phase to a ferromagnetic phase by quenching the quadratic Zeeman shift, q , induced by the applied magnetic field. Initially prepared in the unmagnetized phase, the system is forced to find its ferromagnetic ground state following the quench and does so locally, due to the conservation of magnetization. The phenomenology of the resulting symmetry-broken domain structure has been characterized in prior work by directly imaging the formation of transversely magnetized domains, following the quench [1]. In more recent work, by tuning the spectrum of instabilities associated with the transition and comparing our observations to a complete quantitative analysis of the system, we investigate whether we are indeed observing dynamics which are fully described by a quantum theory [2].

We can gain a great deal of insight in describing the dynamics surrounding the phase transition by interpreting the observed macroscopic magnetization pattern as an amplified version of the initial seeding fluctuations. We accomplish this goal in the next sections by showing that the spin-dependent Hamiltonian for the system may be rigorously mapped onto that of a parametric amplifier. Here we begin by introducing the spin-dependent

interaction and the resulting spectrum of instabilities which lead to the growth of any perturbations about the initial state.

In addition to describing the amplification process, we are motivated by the question of what is amplified when the spinor condensate is quenched into the ferromagnetic parameter regime. For example, can we provide a physical interpretation for the spin fluctuations which are amplified and further, can we quantitatively determine whether they are quantum-limited in magnitude? To what extent are we peering directly at quantum fluctuations which have been amplified, in a noiseless fashion, to a macroscopic level?

4.1.1 Instabilities accompanying a quantum phase transition

Descriptions of the dynamics of initially paramagnetic spinor condensates [42, 73, 74, 75, 33, 76] have focused upon the competing spin-dependent energy scales, the quadratic Zeeman energy and the spin-dependent contact interaction. The latter has the mean-field energy given by $c_2 n \langle \mathbf{F} \rangle^2$, which favors a ferromagnetic state when $c_2 < 0$. The quadratic Zeeman energy $q \langle F_z^2 \rangle$, on the other hand, favors a paramagnetic state and dominates when q is large. The competing terms give rise to a phase transition at a critical value of $q = q_0$ between the paramagnetic and ferromagnetic regimes, where $q_0 = 2|c_2|n$.

To develop a basic understanding of the ensuing dynamics when q is rapidly lowered from $q = \infty$ to $q = q_f < q_0$, we begin by considering how small perturbations about the initial $m_z = 0$ coherent state evolve. In a homogeneous system, it is natural to work in a momentum (k) basis. Thus we are interested in determining the response of the system to a small modulation of the m -component of the spinor wavefunction, $\phi_{m,k}$.

In particular, we are interested in determining whether a given perturbation to the condensate will be stable or unstable, *i.e.*, whether it will evolve by simply accruing a phase over time, or by becoming exponentially amplified or de-amplified. This distinction is dictated by the properties of the spectrum of excitations for the condensate, which we now determine.

Motivated to treat the regime in which fluctuations about the initial state are small, let's take the condensate wavefunction to be $\Psi_k = \Psi_{0,k} + \phi_k$, where $\Psi_{0,k}$ describes the initial coherent state, and ϕ_k corresponds to a perturbation about that state. In this regime, where a mean-field treatment is applicable, we can make use of the Gross-Pitaevski approximation, as in much of the theoretical work on spinor condensate dynamics [42, 73, 74,

75, ?, 33, 76, 77, 32, 78] and assign a vector order parameter for the condensate, $\Psi_{k,m} = \sqrt{n} \psi_{k,m}$. In our case, $\psi_{k,\pm} = \phi_{k,\pm}$ and $\psi_{k,0} = \phi_{k,0} + \phi_{k,0}$. We determine the spin-dependent energy density, keeping terms up to first order in $\phi_{k,m}$, using Equations 1.1 and 1.13:

$$\begin{aligned} E_{spin,k}/n &= \langle \Psi_k | H_{kin} + H_Z + H_{int,spin} | \Psi_k \rangle \\ &= (\varepsilon_k + \tilde{c}_2(k)n + q)(|\phi_{k,+}|^2 + |\phi_{k,-}|^2) \\ &\quad + \tilde{c}_2(k)n(\phi_{k,+}^* \phi_{-k,-}^* + \phi_{k,+} \phi_{-k,-}), \end{aligned} \quad (4.1)$$

where ε_k is the kinetic energy, $\varepsilon_k = k^2/2m$ taking $\hbar = 1$, $\tilde{c}_2(k)$ describes the effective spin-dependent contact interactions (defined in Sec 1.3), and q is the total field-induced quadratic Zeeman shift. The linearized spin-dependent Hamiltonian $H_{spin,k}$, in an analogous form to the linearized spin-dependent energy density (Eq. 4.1), is given by

$$H_{spin,k} = \sum_{m=\pm} \phi_{k,m}^\dagger (\varepsilon_k + \tilde{c}_2(k)n + q) \phi_{k,m} + \tilde{c}_2(k)n (\phi_{k,+}^\dagger \phi_{-k,-}^\dagger + \phi_{k,+} \phi_{-k,-}). \quad (4.2)$$

The evolution of the spin fluctuations is described by their equations of motion,

$$\partial_t \hat{\Psi}_{\mathbf{k}} = (i(\varepsilon_k + q + \tilde{c}_2(k)n) \sigma_{\mathbf{z}} + \tilde{c}_2(k)n \sigma_{\mathbf{y}}) \hat{\Psi}_{\mathbf{k}} \quad (4.3)$$

where $\sigma_{\mathbf{i}}$ are the standard spin 1/2 matrices, and we take

$$\hat{\Psi}_{\mathbf{k}} = \begin{pmatrix} \phi_{k,+} \\ \phi_{-k,-}^\dagger \end{pmatrix}. \quad (4.4)$$

The salient features of the resulting spin dynamics are brought into view with the decomposition of $\hat{\Psi}_{\mathbf{k}}(t)$ into its normal modes and frequencies ω_k (which are derived for the position-space modes in Ref. [45]),

$$\begin{aligned} \hat{\Psi}_{\mathbf{k}} &= \sum_{\nu=\pm} \hat{c}_\nu e^{i\nu\omega_k t} \Phi(\mathbf{k}, \nu) \\ \omega_k &= \sqrt{(\varepsilon_k + q + \tilde{c}_2 n)(\varepsilon_k + q)} \\ \Phi(\mathbf{k}, \nu) &= \begin{pmatrix} u_{+,k,\nu} \\ u_{-,k,\nu} \end{pmatrix} \\ u_{+,k,\nu} &= \nu \omega_k^{-1} \sqrt{\varepsilon_k + q} \\ u_{-,k,\nu} &= 1/\sqrt{\varepsilon_k + q}. \end{aligned} \quad (4.5)$$

These normal modes correspond to two polarizations of spin excitation modes, denoted as magnons or spin waves. They are characterized by sinusoidally modulated densities of $m = \pm 1$ atoms at spatial modulation frequencies, k . Whether each of these modes evolves in a stable or unstable manner depends upon whether ω_k is real or imaginary. If ω_k is real, the pair of normal modes characterized by k evolve as stationary modes, by simply accumulating a phase factor proportional to $e^{i\omega_k t}$. If ω_k is imaginary, one normal mode is amplified and the other is de-amplified by roughly $e^{|\omega_k|t}$, and we refer to these modes as unstable.

Above and below the transition, the properties of the spin excitations are made evident by considering the squared spin excitation spectrum (Fig. 4.1),

$$\begin{aligned} E_s(k)^2 &= \omega_k^2 \\ &= (\varepsilon_k + q + \tilde{c}_2)(\varepsilon_k + q) \end{aligned} \tag{4.6}$$

as a function of q , the endpoint of the quench, as presented in Ref. [42]. For $q > 2|\tilde{c}_2|n$, $\omega_k^2 > 0$ and ω_k is real. The paramagnetic condensate is stable, and there exists a gap to all spin excitations (Fig. 4.1a). For $q \leq 2|\tilde{c}_2|n$, the gap closes (Fig. 4.1b) for a set of modes characterized by $E_{s,k}^2 < 0$, and these modes become unstable. The unstable regime is divided into two qualitatively different regions. For $|\tilde{c}_2|n \leq q \leq 2|\tilde{c}_2|n$, the spectrum of instabilities is broad and “white” with respect to the spatial-frequency k of the instability (Fig. 4.1c). Modes characterized by small k are amplified with the largest gain. In this regime, initial quantum fluctuations atop the paramagnetic state are amplified into a macroscopic pattern of domains characterized by long-range spatial correlations. For $0 \leq q \leq |\tilde{c}_2|n$ the spectrum of instabilities is k -dependent, or colored. Modes characterized by non-zero k , $|k_{opt}| = \sqrt{(2m/\hbar)(|\tilde{c}_2|n - q)}$, are amplified with maximal gain. In this regime, initial magnetization fluctuations are amplified into a pattern of domains characterized by short-range spatial features, whose characteristic lengthscale decreases as q is lowered (Fig. 4.1d). As we will discuss in the following sections, the spin-dependent Hamiltonian (Eq. 4.2) takes two qualitatively different forms depending upon the value of q relative to the transition, q_0 . For $q > q_0$ it takes the form of a stable harmonic oscillator with respect to all modes k , and condensate excitations evolve by accruing a k -dependent phase. For $q < q_0$, there exist both stable and unstable modes. For the stable modes, the Hamiltonian again takes the form of a stable harmonic oscillator. For the unstable modes, it takes the form of an unstable harmonic oscillator, and a class of excitations are exponentially amplified or

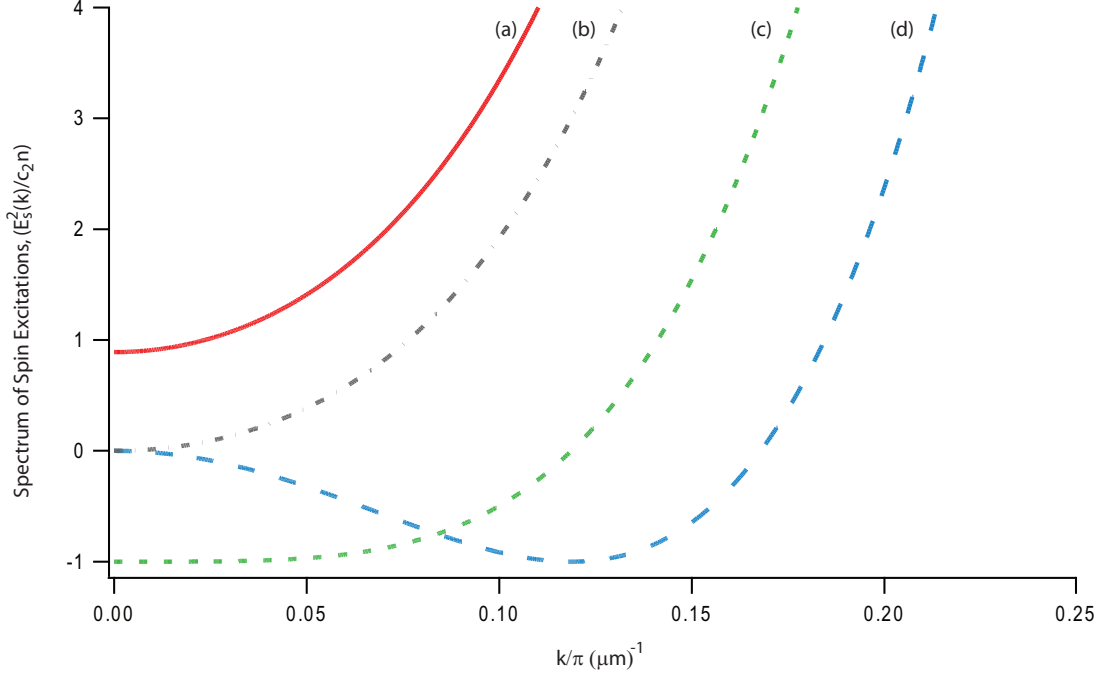


Figure 4.1: The spectrum of spin excitations $E_s(k)^2$, here normalized by c_2n , has a gap for $q > 2|c_2|n$, in other words $E_s(k)^2 > 0$ and all perturbations about the initial paramagnetic state are stable (a). The gap closes at $q = 2|c_2|n$ as q is lowered (b), and a set of excitation modes become unstable. The unstable modes, for which $E_s(k)^2 < 0$, are characterized by small k in the case of $|c_2|n < q < 2|c_2|n$ (c). As q is lowered further toward $q = 0$, the most unstable modes are characterized by finite k (d).

de-amplified according to a k -dependent gain profile.

In the latter case, the spectrum of excitations in the spinor condensate defines the spectrum of a mode-by-mode amplification process, in which fluctuations atop the initial paramagnetic condensate grow to form a macroscopic magnetization pattern. This definition motivates re-interpreting the *observation* of spontaneous ferromagnetism in a spinor condensate as the *operation* of the spinor condensate as a tunable amplifier of spin fluctuations. With the latter approach – which offers a clear formalism and connections to quantum optics – we seek to understand the types of spin fluctuations that are being amplified, to compare the observed dynamics to a quantum amplification theory at a quantitative level, and to explore the potential use of the system as a quantum measurement device with applications toward metrology.

4.2 The spinor condensate as a degenerate parametric amplifier

4.2.1 Low-noise amplifiers

Recently there has been a great deal of interest in observing “macroscopic quantum systems.” At the heart of this bold endeavor is the very device that takes the “quantum world” to the “macroscopic world”: the amplifier.

The development of low-noise amplifiers has enabled the observation of nonclassical phenomena in a range of physical systems. In solid state systems, for example, one can use low-noise Josephson-parametric amplifiers to probe nonclassical electromagnetic fields [79]. In opto-mechanical systems, one can continuously monitor the quantum zero-point fluctuations of a mechanical resonator. In these systems, developing the quantum-limited amplifiers and detectors necessary to do so is the focus of current work [80, 81]. Quantum-limited detection is also a subject of current research in the context of achieving single-spin resolution in NMR [82], or in detecting gravitational waves [83].

Quantum limited amplification can also be turned on its head, and used as a means for generating sub-shot-noise, or squeezed, quantum states. In solid state systems, for example, low-noise phase-sensitive amplification has lead to the preparation of squeezed states, such as squeezed microwave sources.

In this work, we study the use of dynamical instabilities in a quenched spinor condensate as a mode-by-mode parametric amplifier of magnetization fluctuations. As we will see in Ch. 5, quantum-limited amplification in spinor condensates could also be used to prepare of spin squeezed states, with applications toward spatially-resolved magnetometry.

4.2.2 Mapping the spin mixing interaction to a parametric amplifier

To describe the aforementioned spin-dependent Hamiltonian (Eq. 4.2) as a parametric amplifier of spin fluctuations, we will make use of a change of basis. This change of basis is motivated by first considering the spin mixing interaction in the spinor condensate. A standard description of spin-mixing in a spinor condensate begins by introducing the microscopic collision process in which two $m_z = 0$ particles are converted into a $m_z = +1$ and $m_z = -1$ particle, and the converse process [43]. In a homogeneous condensate (ignoring kinetic energy), this process is described by the interaction term, expressed in second-

quantized notation as,

$$H_{sm,k} = \tilde{c}_2(k)n(\phi_{0,k}\phi_{0,k}\phi_{+,k}^\dagger\phi_{-,k}^\dagger + \phi_{0,k}^\dagger\phi_{0,k}^\dagger\phi_{+,k}\phi_{-,k}), \quad (4.7)$$

where $\phi_{0,k}(\phi_{0,k}^\dagger)$, $\phi_{+,k}(\phi_{+,k}^\dagger)$, $\phi_{-,k}(\phi_{-,k}^\dagger)$ are the destruction (creation) operators for condensate atoms in the $m_z = 0, 1, -1$ states respectively, with momentum k . As before, we have assumed the initial population of the initial coherent state ϕ_0 is large and have made the approximation $\phi_0 = \phi_0^\dagger = \sqrt{n}$. The population generated by spin-mixing collisions in ϕ_+ , ϕ_- is taken to be small in comparison.

The spin-mixing interaction, when expressed in a different basis, takes the form of two degenerate parametric amplifiers. This basis corresponds to the zero-eigenvalue modes of F_x, F_y, F_z , whose annihilation operators are defined as,

$$\begin{aligned} \phi_{x,k} &= i\sqrt{i}\frac{(\phi_{+,k} - \phi_{-,k})}{\sqrt{2}} \\ \phi_{y,k} &= \sqrt{i}\frac{(\phi_{+,k} + \phi_{-,k})}{\sqrt{2}} \\ \phi_{z,k} &= \phi_{0,k}. \end{aligned} \quad (4.8)$$

We will make use of this complete and orthogonal “polar basis set” in the remainder of this discussion. Re-expressed in this polar basis, the spin mixing interaction takes a form of two mode-by-mode degenerate parametric amplifiers, given by,

$$H_{sm,k} = -\frac{i}{2}\tilde{c}_2(k)n((\phi_{x,k}^2 - \phi_{x,k}^{\dagger 2}) + (\phi_{y,k}^2 - \phi_{y,k}^{\dagger 2})). \quad (4.9)$$

A standard treatment of a degenerate parametric amplifier is provided in Ref.[84], Ch. 5.1.1. Its characteristic Hamiltonian is given by,

$$H_{param} = -\frac{i}{2}\omega((\phi^2 - \phi^{\dagger 2})). \quad (4.10)$$

and the quadratures of ϕ , corresponding to its real and imaginary parts, are given by,

$$\begin{aligned} X_1 &= (\phi + \phi^\dagger)/2 \\ X_2 &= (\phi - \phi^\dagger)/2i. \end{aligned} \quad (4.11)$$

The parametric amplifier serves to amplify one quadrature and attenuate the other by a gain given by ω :

$$\begin{aligned} X_1(t) &= e^{\omega t}X_1(0) \\ X_2(t) &= e^{-\omega t}X_2(0). \end{aligned} \quad (4.12)$$

Under the operation of a parametric amplifier, time evolution of the modes is given by $\phi(t) = \phi(0) \cosh(\omega t) + \phi^\dagger(0) \sinh(\omega t)$.

The spin mixing interaction, which takes the form of two generate parametric amplifiers, serves to generate pairs of particles in the initially unpopulated ϕ_x, ϕ_y modes, made clear by the exclusive presence of quadratic terms in ϕ_x, ϕ_y in the interaction. In analogy to quantum optics, the population of the ϕ_x, ϕ_y modes is initially zero and grows approximately exponentially by processes of spontaneous and stimulated emission, as discussed in Section 4.7.

4.2.3 The spin-dependent Hamiltonian as a mode-by-mode parametric amplifier

To identify the spinor condensate as a parametric amplifier of spin fluctuations, we re-introduce the spin-dependent Hamiltonian (Eq. 4.2) for the homogeneous spinor condensate:

$$H_s = \sum_k (\varepsilon_k + q + \tilde{c}_2(k)n(\phi_{x,k}^\dagger \phi_{x,-k} + \phi_{y,k}^\dagger \phi_{y,-k}) - \frac{i\tilde{c}_2(k)n}{2}((\phi_{x,-k}^2 - \phi_{x,k}^{\dagger 2}) + (\phi_{y,-k}^2 - \phi_{y,k}^{\dagger 2})), \quad (4.13)$$

expressed in the aforementioned polar basis. Since we can treat each k mode independently and ϕ_x, ϕ_y enter H_s independently, it is sufficient to study the single-mode Hamiltonian of the form,

$$H_k = (\varepsilon_k + q + \tilde{c}_2(k)n)(\phi_k^\dagger \phi_{-k}) - \frac{i\tilde{c}_2(k)n}{2}(\phi_{-k}^2 - \phi_k^{\dagger 2}). \quad (4.14)$$

We show that this Hamiltonian can take the form of a stable or unstable harmonic oscillator by using a basis of modes a_k, a_k^+ related to original modes ϕ_k, ϕ_k^\dagger by a Bogoliubov transformation,

$$\begin{aligned} \phi_k^\dagger &= a_k^\dagger \cosh(\gamma_k) + ia_k \sinh(\gamma_k) \\ \phi_k &= a_k \cosh(\gamma_k) - ia_k^\dagger \sinh(\gamma_k). \end{aligned} \quad (4.15)$$

We find that H_k takes the form of an unstable harmonic oscillator (or parametric amplifier) when we choose $\gamma_k = \gamma_{k,amp}$ such that,

$$\tanh(2\gamma_{k,amp}) \equiv (\varepsilon_k + q + \tilde{c}_2(k)n)/\tilde{c}_2(k)n \quad (4.16)$$

$$H_k = -\frac{i\omega_k}{2}(a_k^2 - a_k^{\dagger 2}) \quad (4.17)$$

$$\omega_k^2 = -(\varepsilon_k + q + \tilde{c}_2(k))(\varepsilon_k + q), \quad (4.18)$$

where ω_k corresponds to the dispersion relation for the spinor condensate. The time evolution of the modes is given by $a_k(t) = a_k(0) \cosh(\omega_k t) + a_k^\dagger(0) \sinh(\omega_k t)$. Thus the spin-dependent Hamiltonian, when appropriately tuned, can be described by a sum of independent degenerate parametric amplifiers,

$$H_s = \sum_k \left(-\frac{i\omega_k}{2}((a_{-k}^2 - a_k^{\dagger 2}) + (b_{-k}^2 - b_k^{\dagger 2})) \right) \quad (4.19)$$

where b_k, b_k^\dagger are formed from $\phi_{k,y}, \phi_{k,y}^\dagger$ in the analogous way. We can interpret a_k, b_k as two polarizations of spin excitation modes. Here $\tanh(2\gamma_k) = |\tilde{c}_2(k)|n$ may be interpreted as the excess population of $m = \pm 1$ atoms in the modulation of the spinor wavefunction corresponding to a spin excitation modes (or spin waves).

Additionally, we can tune q above the transition ($q > q_0$) such that the spinor condensate Hamiltonian takes the form of a stable harmonic oscillator. In this case, we choose $\gamma_k = \gamma_{k,rot}$ such that,

$$\tanh(2\gamma_{k,rot}) \equiv \tilde{c}_2(k)n/(\varepsilon_k + q + \tilde{c}_2(k)n) \quad (4.20)$$

$$H_k = \omega_k(a_k^\dagger a_k + b_k^\dagger b_k)$$

$$\omega_k^2 = (\varepsilon_k + q + \tilde{c}_2(k))(\varepsilon_k + q).$$

In this regime, $q \gg q_0 \equiv \tilde{c}_2 n$, and there exists a gap to any spin excitations. The stationary eigenmodes of H accrue a k -dependent phase given by $\omega_k t$, and evolve as $a_k(t) = a_k(0) \cos(\omega_k t) + a_k^\dagger(0) \sin(\omega_k t)$.

4.3 Spin fluctuation modes in a paramagnetic $F = 1$ spinor condensate

Thus far, we have shown that the system Hamiltonian takes the form of a sum of degenerate parametric amplifiers when expressed in terms of the complex modes a_k, a_k^\dagger and

b_k, b_k^\dagger , which are not Hermitian operators and do not correspond to observable quantities. In contrast, the fluctuations in the transverse magnetization of the spinor, given by $F_{x,k}$ and $F_{y,k}$ (components of the spin vector), and fluctuations in the alignment of the spinor, created by $N_{xz,k}^\dagger$ and $N_{yz,k}^\dagger$ (components of the spin quadrupole tensor) are observable [48]. The properties of $F = 1$ spinors and their fluctuation operators are discussed in Section 2.1.1.

The operators which describe fluctuations atop the paramagnetic state, $\phi_{z,k}$ (to be defined with respect to a general coherent state in Section 5.6), may be expressed in their second-quantized form as:

$$F_{x,k} = (-i\sqrt{i}/\sqrt{2})(\phi_{z,k}^\dagger \phi_{y,k} + i\phi_{y,k}^\dagger \phi_{z,k}) \quad (4.21)$$

$$F_{y,k} = (-i\sqrt{i}/\sqrt{2})(\phi_{z,k}^\dagger \phi_{x,k} + i\phi_{x,k}^\dagger \phi_{z,k}) \quad (4.22)$$

$$N_{xz,k} = (-\sqrt{i}/\sqrt{2})(\phi_{z,k}^\dagger \phi_{x,k} - i\phi_{x,k}^\dagger \phi_{z,k}) \quad (4.23)$$

$$N_{yz,k} = (-i\sqrt{i})/\sqrt{2}(\phi_{z,k}^\dagger \phi_{y,k} - i\phi_{y,k}^\dagger \phi_{z,k}). \quad (4.24)$$

We are interested in the fluctuations atop a coherent state populated by a large number of atoms. We therefore consider a classical coherent state, $\phi_{z,k}^\dagger = \phi_{z,k} = \sqrt{n}$, and consider fluctuation operators in the linear regime, which are given by,

$$F_{x,k} = (-i\sqrt{i}\sqrt{n}/\sqrt{2})(\phi_{y,k} + i\phi_{y,k}^\dagger) \quad (4.25)$$

$$F_{y,k} = (-i\sqrt{i}\sqrt{n}/\sqrt{2})(\phi_{x,k} + i\phi_{x,k}^\dagger) \quad (4.26)$$

$$N_{xz,k} = (-\sqrt{i}\sqrt{n}/\sqrt{2})(\phi_{x,k} - i\phi_{x,k}^\dagger) \quad (4.27)$$

$$N_{yz,k} = (-i\sqrt{i}\sqrt{n})/\sqrt{2}(\phi_{y,k} - i\phi_{y,k}^\dagger). \quad (4.28)$$

Using the commutation relations $[\phi_{i,k}, \phi_{j,k'}^\dagger] = \delta_{ij}\delta_{kk'}$, we find that the above fluctuation operators obey canonical commutation relations,

$$[F_{x,k}, N_{yz,k'}] = -in\delta_{k,k'} \quad (4.29)$$

$$[F_{y,k}, N_{xz,k'}] = in\delta_{k,k'} \quad (4.30)$$

where we again take $\hbar = 1$. The two polarizations of fluctuations are separable; thus we can focus on one polarization, such as $\phi_{y,k}$. We therefore focus on the fluctuation operators $F_{x,k}$ and $N_{yz,k}$. Under the parametric amplifier these fluctuations evolve as,

$$\begin{pmatrix} F_{x,k} \\ N_{yz,k} \end{pmatrix}_t = \begin{pmatrix} \cosh(t/\tau_k) & -e^{-2\gamma_{amp,k}} \sinh(t/\tau_k) \\ -e^{2\gamma_{amp,k}} \sinh(t/\tau_k) & \cosh(t/\tau_k) \end{pmatrix} \begin{pmatrix} F_{x,k} \\ N_{yz,k} \end{pmatrix}_{t=0} \quad (4.31)$$

where $\gamma_{amp,k}$ and $\tau_k = 1/\omega_{amp,k}$ are given by Eq. 4.17-4.18 and depend upon $q = q_{amp} \ll q_c$. In the (F_x, N_{yz}) plane, spin fluctuations will grow along the “amplification axis” given by $\mathbf{v}_{amp} = (-e^{-2\gamma_{amp,k}}, 1)$ and shrink along the “squeezing axis” $\mathbf{v}_{sq} = (e^{-2\gamma_{amp,k}}, 1)$ (Fig. 4.2). This is made clear by the decomposition,

$$M_{amp}(t) = e^{t_{amp}/\tau_l} \mathbf{v}_{amp} \tilde{\mathbf{v}}_{amp}^\dagger + e^{t_{amp}/\tau_l} \mathbf{v}_{sq} \tilde{\mathbf{v}}_{sq}^\dagger \quad (4.32)$$

where $\tilde{\mathbf{v}}_{amp}^\dagger$ and $\tilde{\mathbf{v}}_{sq}^\dagger$ form the dual basis to \mathbf{v}_{amp} and \mathbf{v}_{sq} respectively. In practise, the spectral gain profile $|\omega_k|$ is maximum for a wavevector k satisfying $\epsilon_k + q + \tilde{c}_2(k)n = 0$ and hence $\gamma_{amp,k} = 0$. Thus the “amplification/squeezing axes” of the maximum-gain mode k are oriented at $\pm\pi/4$ with respect to the F_x, N_{yz} axes.

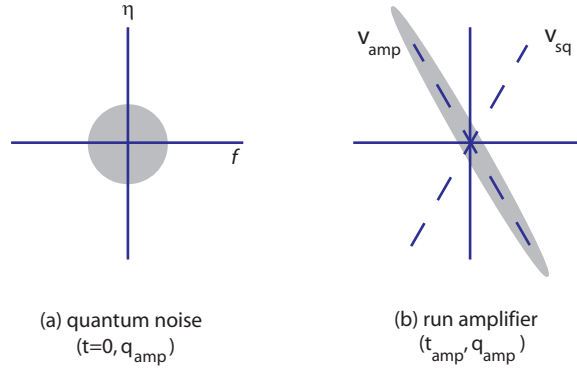


Figure 4.2: Quantum fluctuations initially symmetric in F_x, N_{yz} are amplified and de-amplified along k -dependent axes given by v_{amp}, v_{sq} in the F_x, N_{yz} plane.

Briefly, we outline the calculation of the time evolution of F_x, N_{yz} , which we determine from the time evolution of ϕ_k ,

$$\begin{pmatrix} \phi_k(t) \\ \phi_k^\dagger(t) \end{pmatrix} = M_{amp,k} \begin{pmatrix} \phi_k(0) \\ \phi_k^\dagger(0) \end{pmatrix}. \quad (4.33)$$

We make use of the following relations, where $X_{1,k}, X_{2,k}$ correspond to the real and imaginary parts of the unstable (Bogoliubov) modes a_k given by Eq.4.15, and ω_k corresponds to the aforementioned spin excitation spectrum:

$$\begin{pmatrix} X_{1,k}(t) \\ X_{2,k}(t) \end{pmatrix} = \begin{pmatrix} e^{\omega_k t} & 0 \\ 0 & e^{-\omega_k t} \end{pmatrix} \begin{pmatrix} X_{1,k}(0) \\ X_{2,k}(0) \end{pmatrix} \equiv A_3 \begin{pmatrix} X_{1,k}(0) \\ X_{2,k}(0) \end{pmatrix} \quad (4.34)$$

$$\begin{pmatrix} X_{1,k} \\ X_{2,k} \end{pmatrix} = \begin{pmatrix} 1/2 & 1/2 \\ 1/2i & -1/2i \end{pmatrix} \begin{pmatrix} a_k \\ a_k^\dagger \end{pmatrix} \equiv A_2 \begin{pmatrix} a_k \\ a_k^\dagger \end{pmatrix} \quad (4.35)$$

$$\begin{pmatrix} \phi_k \\ \phi_k^\dagger \end{pmatrix} = \begin{pmatrix} \cosh(\gamma_k) & -i \sinh(\gamma_k) \\ i \sinh(\gamma_k) & \cosh(\gamma_k) \end{pmatrix} \begin{pmatrix} a_k \\ a_k^\dagger \end{pmatrix} \equiv A_1 \begin{pmatrix} a_k \\ a_k^\dagger \end{pmatrix}. \quad (4.36)$$

We construct M_{amp} from

$$\begin{pmatrix} \phi_k(t) \\ \phi_k^\dagger(t) \end{pmatrix} = A_1 A_2^{-1} A_3 A_2 A_1^{-1} \begin{pmatrix} \phi_k(0) \\ \phi_k^\dagger(0) \end{pmatrix} \equiv M_{amp} \begin{pmatrix} \phi_k(0) \\ \phi_k^\dagger(0) \end{pmatrix}. \quad (4.37)$$

Finally, we determine $F_x(t), N_{yz}(t)$ from $\phi_k(t), \phi_k^\dagger(t)$ using Eq. 4.27,4.28, for example. In principle, by determining $\phi_k(t), \phi_k^\dagger(t)$, we have in fact specified all aspects of the evolution of the system under the stated approximations.

4.4 Experimental characterization of the spin-mixing amplifier

In a manner similar to prior experimental studies of low-noise amplifiers in other physical systems [79, 85, for example], we have pursued characterizing the “spin-mixing amplifier”, an amplifier of spin fluctuations. To do so, we have effectively seeded the amplifier with broadband noise, and characterized the spectrum of its output.

Our first goal in this characterization was to measure the spectrum of the spin-mixing amplifier and determine whether it is in agreement with a quantum amplification theory. To activate the amplifier, we rapidly quenched the field-induced quadratic Zeeman shift to a range of final values (Section 4.4.1). The quadratic Zeeman shift was induced by

a combination of magnetic and microwave fields, which were carefully calibrated (Section 4.4.2). Following the quench, we characterized the evolution of the transverse magnetization (Sections 4.4.3). By varying the induced quadratic Zeeman shift, we demonstrated that the characteristic lengthscale of the observed magnetization pattern and underlying spectrum of instabilities is tunable. In particular, we examined its spatial correlations as a function of the final quadratic Zeeman shift (Sections 4.4.4). We found the experimentally probed spectrum to compare well with a theoretical model that accounts for the inhomogeneous condensate density and for magnetic dipole interactions, with some discrepancies [45].

To enable a quantitative comparison between the observed structure formation and a quantum amplification theory, we measured precisely the temporal evolution of transverse magnetization acquired by the condensate following the quench. The observed transverse magnetization, interpreted as amplified spin fluctuations, was measured at various stages of amplification, up to a gain of 30 dB in the magnetization variance.

Further, we investigated possible contributions from spin fluctuations other than quantum fluctuations, such as thermal or technical noise, in the experiment (Section 4.5). To extend our understanding of the system, we have suggested future tests of the spin-mixing amplifier, in particular, to empirically determine the role of dipolar interactions and to reduce our uncertainty in the gain of the amplifier (Section 4.6).

4.4.1 Initiating the amplifier: the quench into the ferromagnetic regime

The paramagnetic optically-trapped condensates which serve as the initial condition in this study are prepared in a similar manner to previous work [1]. As described in Section 1.5.1, condensates of $N_0 = 2.0 \times 10^6$ ^{87}Rb atoms are prepared, with peak densities of $n = 2.6(1) \times 10^{14} \text{ cm}^{-3}$ and kinetic temperatures of $\simeq 50 \text{ nK}$. They are trapped in a linearly polarized optical dipole trap characterized by trap frequencies $(\omega_x, \omega_y, \omega_z) = 2\pi \times (39, 440, 4.2) \text{ s}^{-1}$. Taking the theoretical value for $\Delta a = -1.4(3) a_B$ [44], with a_B being the Bohr radius, we note that the spin healing length $\xi_s = (8\pi n |\Delta a|)^{-1/2} = 2.5 \mu\text{m}$ is larger than the condensate radius $r_y = 1.6 \mu\text{m}$ along the imaging axis (\hat{y}). As in our previous work, we consider the condensate to be effectively two-dimensional with respect to spin dynamics in this study. For the condensates used in this experiment, the transition between the polar and ferromagnetic regime occurs at $q_0 = 2|c_2|\langle n \rangle = h \times 15 \text{ Hz}$ given the maximum \hat{y} -averaged condensate density $\langle n \rangle$.

The condensate is prepared in the $|m_z = 0\rangle$ state using rf pulses at a large magnetic field, as described in [11]. Following the preparation of the $|m_z = 0\rangle$ state, a 6 G/cm magnetic field gradient is applied to expel residual atoms in the $|m_z = \pm 1\rangle$ states from the trap[1]. This preparation takes place in a static 4 G field and with no microwave irradiation. The paramagnetic condensate is stable under this condition, since the field-induced quadratic shift is well above the transition, $q \gg q_0$.

The amplifier is “switched on” when the quadratic shift is rapidly quenched below the transition, into the ferromagnetic regime. The magnitude of the induced quadratic Zeeman shift is controlled using two fields: an applied bias magnetic field directed along the \hat{z} axis, provided by Helmholtz coils (Section 1.5.2); and a modulated magnetic field, provided by a linearly \hat{z} -polarized microwave field (Section 1.6). The bias magnetic field of magnitude B , induces a quadratic shift of $q_B/h = (70 \text{ Hz/G}^2)B^2$. The linearly polarized microwave field induces a quadratic shift [87]. Its magnitude is characterized by a Rabi frequency Ω (Section 1.5.3) and its detuning is given by $\delta/2\pi = \pm 35 \text{ kHz}$, measured from the $|F = 1, m_z = 0\rangle$ to $|F = 2, m_z = 0\rangle$ hyperfine transition. The applied microwave field induces a quadratic (AC) Zeeman shift of $q_\mu = -\hbar\Omega_R^2/4\delta$, which is carefully calibrated for this experiment (Section 4.4.2).

Prior to switching on the amplifier, the purified paramagnetic state is prepared in a field environment described by a static 4 G bias magnetic field and no microwave irradiation. The microwave field strength is then increased over 20 ms to a constant value, corresponding to a Rabi frequency in the range of $2\pi \times (0\text{--}1.5) \text{ ms}^{-1}$, to set q_μ . To switch on the amplifier, we rapidly ramp the magnetic field (over 5 ms) to a value of $B = 230 \text{ mG}$ (giving $q_B/h = 7.6 \text{ Hz}$). For separate repetitions of the experiment (for different values of q_μ), the quadratic Zeeman shift at the end of the ramp was thus brought to final values q_f/h between -2 and 16 Hz.

4.4.2 Calibration of the field-induced quadratic Zeeman shift

Due to the observed variation in the strength of the applied microwave field and bias magnetic field in the apparatus over the course of several days, they were calibrated prior to each experiment (Sections 1.5.2,1.6). The bias field was directly measured as part of the procedure to cancel inhomogeneities in the magnetic field environment (Section 1.5.2). In the quench experiment considered here, $g_F\mu_B B = 230 \text{ kHz} \pm 10 \text{ kHz}$ and $q_B/h = 7.6 \text{ Hz}$.

The contribution to the field-induced quadratic Zeeman shift from the modulated magnetic field, $q_\mu = -\hbar\Omega_R^2/4\delta$, was indirectly determined from a measurement of its characteristic Rabi frequency, Ω_R , and detuning, δ (Section 1.6). In addition, as a consistency check for our calibration of q_μ , we studied the spin-mixing amplifier as a function of q_μ at a few fixed values of q_B (*i.e.*, at a few bias fields). We verified that amplifier behavior depended upon q_μ through $q_f = q_\mu + q_B$, as expected.

First, the on-resonance Rabi frequency $\Omega_R \equiv \Omega_R(V)$ was measured as a function of its control setting, V (Fig. 1.8, Sec. 1.6). The resulting quadratic Zeeman shift, $q_f(V) = q_B + q_\mu(V)$, was determined for $|\delta| = 30$ MHz, and for two bias fields ($B = 190$ kHz and 235 kHz, such that $q_B = 5.2$ Hz and 7.9 Hz). In Fig. 4.3, we take the control setting to be $V \equiv V\delta/|\delta|$, to reflect the fact that applying q_μ may either increase or decrease q_f , depending upon the sign of δ .

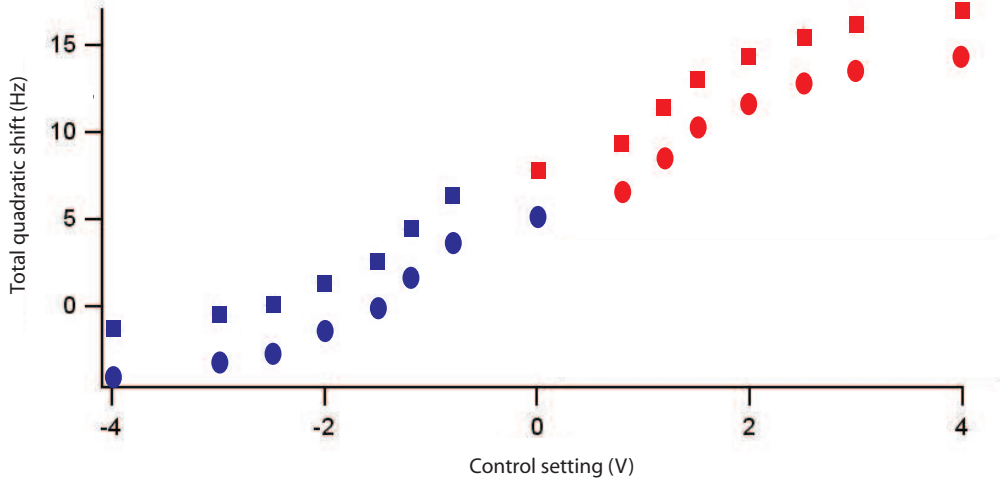


Figure 4.3: The total field-induced quadratic shift due to modulated and static magnetic fields, $q_f(V)$, as a function of the control setting for the applied microwave field, V . Here, $q_\mu(V) = -\Omega_R^2(V)/4\delta$ and $q_B = 70 \text{ Hz/G}^2 B^2$. The circles (squares) correspond to measurements performed at magnetic bias fields $B_z = 190(235)$ kHz, and microwave field detuning $|\delta| = 35$ kHz. The magnitude of the control setting reflects Ω^2 and the sign of the control setting reflects the sign of the microwave field detuning δ .

Next, the spin mixing amplifier was characterized as a function of $\Omega_R(V)$ at the two bias magnetic fields, holding $|\delta|$ constant. In Fig.4.4, the population of $m = \pm 1$ atoms generated by spin-mixing collisions, measured 110 ms after the quench, is shown as a function of q_f . As expected, spin mixing was suppressed as q_f was increased above the

transition at $q_0/h \approx 16$ Hz. Surprisingly, spin mixing was also reduced as q was lowered below roughly -2 Hz, and completely suppressed for q_f/h less than roughly -7 Hz.

At the two bias magnetic fields, the measured population of $m = \pm 1$ was found to exhibit the same dependence upon q_f/h , supporting the calibration of q_μ . In addition, the transverse magnetization profile of the condensate was directly imaged as a function of q_μ at the two magnetic fields. The qualitative variation of the condensate magnetization profile as a function of q_f , measured at the two bias fields, was found to be in good agreement.

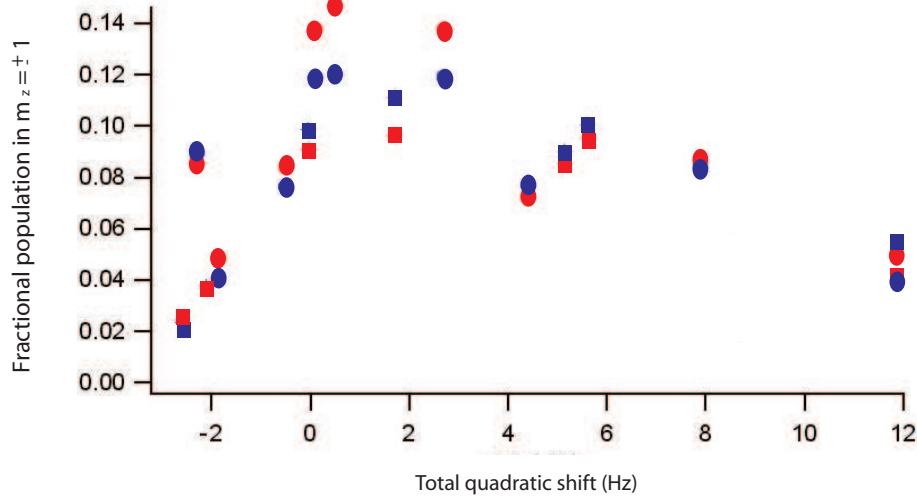


Figure 4.4: The fractional population in $m_z = \pm 1$, measured 110 ms after the quench, as a function of the final quadratic shift, q_f , at the end point of the quench. The squares (circles) correspond to measurements at magnetic bias fields $g_F\mu_B B_z = 190(235)$ kHz.

4.4.3 Characterizing the amplifier: the quench to a variable endpoint

Following the quench, the condensate is forced to find a ferromagnetic ground state, and does so locally, due to the conservation of the z -projection of its magnetization. We observe the condensate to spontaneously develop macroscopic transverse magnetization, saturating within about 110 ms to a pattern of spin domains, textures, vortices and domain walls [1]. As discussed, we interpret the observed symmetry broken domain structure as an amplified version of the initial seeding fluctuations.

To measure the transverse magnetization of the condensate, we made use of a sequence of non-destructive phase contrast images, as described in Chapter 2. After a specified evolution time, a 2-ms-long sequence of phase-contrast images was taken using 800-

ns-long pulses of circularly polarized light propagating along the \hat{y} direction. The transverse magnetization acquired by the condensate was detected by means of its Larmor precession about the uniform bias field, B_z . The amplitude and phase of this Larmor precession signal was extracted from the sequence of images and used to construct a spatially-resolved profile of the transverse magnetization density, $\tilde{M}_{x,y} = \tilde{n}F_{x,y}$, where \tilde{n} is the column number density [50, 12].

Representative images of the condensate transverse magnetization profile, $\tilde{M}_{x,y}$, for evolution times of 47, 87, and 127 ms following the quench, are shown in Fig. 4.5. For short evolution times ($t < 47$ ms), the measured transverse magnetization variance was smaller than, or on the order of, the photon-shot-noise-limited noise floor. In this case, the observed transverse magnetization profile was homogeneous and lacking in spatial features, indistinguishable from the initial $m_z = 0$ state. Following a longer evolution period, after the initial spin fluctuations had been amplified well above the noise floor, the observed transverse magnetization profile was characterized by a spatially inhomogeneous pattern of domains.

The formation of transversely magnetized domains was first observed at the center of the condensate, where the condensate density and hence the gain of the amplifier was greatest. At intermediate times following the quench ($t < 97$ ms), when the amplification of spin fluctuations had not yet saturated, significant shot to shot fluctuations in the observed condensate transverse magnetization profiles was observed. This may be attributed to the stochastic variation of the magnitude and spectrum of the initial spin fluctuations, as expected from a quantum mechanical description. This variation in the amplified magnetization pattern is evident in the condensate transverse magnetization profiles shown in Fig. 4.5, imaged at $t = 87$ ms following the quench. At this evolution time, magnetization fluctuations which were initially quantum-limited in magnitude would have been amplified by a gain of up to 30 dB. The spin-mixing amplifier can not run forever; eventually it runs out of gain. As the population of $m_z = 0$ atoms is depleted, the occupation of unstable modes increases and eventually saturates. This is reflected in the saturation of the transverse magnetization profile of the condensate at long evolution times. Representative images of $\tilde{M}_{x,y}$, such as those taken at $t = 127$ ms in Fig. 4.5, exemplify its eventual saturation: the condensate is characterized by significant transverse magnetization across its spatial extent. Shot-to-shot fluctuations of the transverse magnetization profiles were reduced for long evolution times, past the saturation of the amplifier ($t > 110$ ms). In addition to the

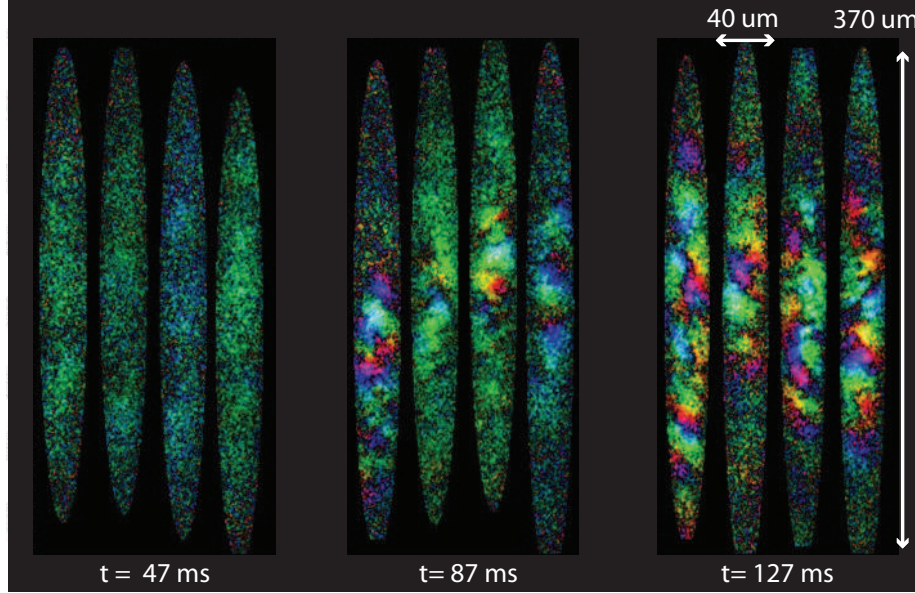


Figure 4.5: Representative images of the condensate transverse magnetization density, $\tilde{M}_{x,y}$, for the quench of a paramagnetic condensate to $q_f = 2$ Hz. At evolution times $t = 47, 87, 127$ ms, four examples of $\tilde{M}_{x,y}$ are shown in order to delineate the stochastic variation in the observed amplified spin fluctuations.

transverse magnetization, the longitudinal magnetization of the condensate was measured, but, consistent with prior observations, it remained small ($< 15\%$) throughout the evolution period (up to 300 ms).

By characterizing the transverse magnetization profile of the condensate following the quench to a variable final quadratic shift, q_f , we effectively probe the spectrum of instabilities of the spinor condensate, as presented in Section 4.1.1. Representative images of the saturated transverse magnetization profiles of spinor condensates, for a range of final quadratic Zeeman shifts, are shown in Figure 4.6. They confirm the aforementioned distinction between deep and shallow quenches. For the deep quench, characterized by $0 < q_f < 8$ Hz, the transverse magnetization profile is characterized by short-range features, specifically, by transversely magnetized domains on the order of 10 to 30 μm in size. As q_f is raised from 0 to 8 Hz, we observe the characteristic domain size to increase. Images of a central region of the condensate transverse magnetization profile, taken during the linear operation regime of the amplifier (Fig. 1, Appendix B), for $t = 87$ ms), confirm that the spatially averaged magnetization strength is roughly constant over $0 \leq q \leq 8$ Hz, reflecting the uniform gain of the amplifier. For the shallow quench, characterized by

$8 < q_f < 16$ Hz, the transverse magnetization profile is characterized by long-range features and is diminished in amplitude. Also evident in Fig. 1 of Appendix B, this trend reflects a diminishing gain as q_f is increased up to the transition point.

For $0 < q_f < \infty$, the experimental characterization of the condensate transverse magnetization profile is in good agreement with theoretical predictions. However, the results of the observed quench to negative values of q_f came as a surprise. For quenches to $q_f/h \leq -7$ Hz, the growth of magnetization was found to be greatly suppressed ($G(0)|_{t=160ms} \leq 10^{-2}$). It is possible that the domain formation observed at $0 < q < q_0$ is frustrated by incoherent magnons for the case of $q < 0$, which is a current subject of investigation.

Our characterization of the variation of the condensate magnetization profile with q_f , which reflects the *tunability* of the spectral gain profile of the spin-mixing amplifier, can be made more quantitative by studying the position-space correlations of the condensate magnetization.

4.4.4 Spatial magnetization correlations

A good probe of the amplifier's spectrum is provided by the condensate magnetization correlation function,

$$G(\delta\mathbf{r}) = \frac{\sum_{\mathbf{r}} \tilde{\mathbf{M}}(\mathbf{r} + \delta\mathbf{r}) \cdot \tilde{\mathbf{M}}(\mathbf{r})}{(g_F\mu_B)^2 \sum_{\mathbf{r}} \tilde{n}(\mathbf{r} + \delta\mathbf{r})\tilde{n}(\mathbf{r})}, \quad (4.38)$$

where \tilde{n} is the \hat{y} -integrated column density. Snapshots of the amplitude, phase, and spatial correlations of the transverse magnetization of a central region of the condensate are shown for a range of values of q_f (Fig. 4.6). A quantitative measure of the amplifier's spatial spectrum, and its tunability with q_f , is provided by the characteristic size of the spin domains, which we may extract from the correlation function. This characteristic domain size is taken as the distance from the origin at which the correlation function acquires its first minimum, measured in the direction of strongest correlations. On average, this direction corresponded to \hat{z} , but varied from shot-to-shot. Recent theoretical work which takes into account the asymmetric trap potential supports the observation that magnetization correlations are stronger along the long axis of the trapping potential, consistent with the experimental findings [45, 86].

The characteristic domain size was found to increase as q_f was raised (Fig. 2, Appendix B), in agreement with a quantum amplification theory. It was, however, measured

to be consistently larger than the predicted value according to this theory. One possible explanation for this discrepancy could be the presence of thermally generated populations of unstable modes at low spatial frequencies. Alternatively, these modes could be populated by spurious RF sources in the experiment apparatus, at a level below the sensitivity of experimental diagnostic techniques (Sec. 4.5).

Interestingly, once the pattern of domains formed at a given q_f , its characteristic size was observed to be relatively constant as a function of time. The temporal evolution of the average magnetization correlation function, determined from 8 repetitions of the experiment at $q_f = 2$ Hz, is shown in Figure 4.8. Here, the average magnetization correlations are clearly strongest along the \hat{z} axis, corresponding to the long axis of the trapping potential. In contrast, the magnetization profile is, on average, featureless in the \hat{x} direction. At long evolution times ($t > 150$ ms), the experimental findings are consistent with a slight increase in characteristic domain size, which may be related to coarsening behavior discussed in Ref. [42].

One may directly probe the spectral gain profile of the amplifier by making use of the spatial Fourier transform of the condensate transverse magnetization, given by $\tilde{\mathbf{M}}(\mathbf{k})$, where $\tilde{\mathbf{k}} = (k_x, k_z)$. In particular, the rate of growth of transverse magnetization may be taken as,

$$R(k) = \ln(P(k, t_2)/P(k, t_1))/(t_2 - t_1) \quad (4.39)$$

where $P(k, t) = |\tilde{\mathbf{M}}(\mathbf{k}, t)|^2$; $|k| = \sqrt{\vec{k} \cdot \vec{k}}$; and t_1 and t_2 correspond to two evolution times chosen during the linear regime of operation of the amplifier. For the same experimental data as above, and by making use of a central region of the condensate ($8 \mu\text{m} \times 32 \mu\text{m}$), $R(k)$ is shown in Figure 4.9. To establish a qualitative comparison with the theory of a homogeneous condensate, the predicted $R(k)$ is also shown for this case (taking the average value of \tilde{n} from the experiment and the theory value for Δa). In this comparison, the observed rate of structure formation is larger than expected at low spatial frequencies.

On account of its limited momentum resolution, the spatial Fourier transform of the condensate magnetization was only used for qualitative rather than quantitative comparisons with theory. The limited momentum resolution (due to the small x -dimension of the condensate) and the observed sensitivity to parameters of this analysis (such as the region size and location in the condensate) made this technique unreliable at a quantitative level. In a future implementation of the experiments in a large, isotropic condensate, this

tool may be more robust and better suited to quantitative studies.

Having characterized the spin-mixing amplifier, let us consider the source of its input signal. For this, as presented in Section 4.2.3, we have developed a quantum field description of the spin-mixing instability. To test the validity of this description, we compare the measured magnetization variance, $G(0)$, over the central region of the condensate after different intervals of amplification, to that predicted by the quantum amplification theory. In this section, we outline the calculation of $G(0)$ shown in Fig. 3 of Appendix B and summarize the result of its comparison to the quantum amplification theory.

In terms of the condensate magnetization, $\tilde{\mathbf{M}}(\mathbf{r})$, $G(0)$ is given by,

$$\begin{aligned} G(0) &= \frac{\sum_{\mathbf{r}} \tilde{\mathbf{M}}(\mathbf{r} + \delta\mathbf{r}) \cdot \tilde{\mathbf{M}}(\mathbf{r})}{(g_F\mu_B)^2 \sum_{\mathbf{r}} \tilde{n}(\mathbf{r})\tilde{n}(\mathbf{r})} \\ &= \frac{\langle |\tilde{\mathbf{M}}(\mathbf{r})|^2 \rangle}{(g_F\mu_B)^2 \langle \tilde{n}(\mathbf{r})^2 \rangle}, \end{aligned} \quad (4.40)$$

where the expectation value of $\tilde{\mathbf{M}}$ and \tilde{n} is taken over the central $16 \times 124 \mu\text{m}$ region of the condensate. Here we consider the determination of $G(0)$ from the experimental data. In so doing, we take a step back to the quantity that is measured in the experiment and used to determine $G(0)$: the amplitude of the Larmor precession signal at each position in the condensate, $A_{LP}(\mathbf{r})$ (Sec. 2.3.1). This quantity is proportional to both $\tilde{n}(\mathbf{r})$ and $|\tilde{\mathbf{M}}(\mathbf{r})|$. Were the measurement of $\langle A_{LP}(\mathbf{r})^2 \rangle$ noise-free, then we could simply determine $G(0)$ from normalizing the measured $\langle A_{LP}(\mathbf{r})^2 \rangle$ by the same quantity determined for a fully transversely magnetized cloud, $\langle A_{max,LP}(\mathbf{r})^2 \rangle$. However, an accurate analysis of $G(0)$ must take into account contributions from photon shot-noise and other noise sources.

In practise, $G(0)$ is determined from,

$$G(\delta\mathbf{0}) = \frac{(\langle A_{LP}(\mathbf{r})^2 \rangle - \langle \delta A_{ps}(\mathbf{r})^2 \rangle)}{(\langle A_{max,LP}(\mathbf{r})^2 \rangle - \langle \delta A_{ps}(\mathbf{r})^2 \rangle)}, \quad (4.41)$$

where $A_{LP}(\mathbf{r})$ is the measured precession signal at the position \mathbf{r} in the condensate; $A_{max,LP}(\mathbf{r})$ is the calculated precession signal for a transversely magnetized condensate for the same parameters (verified empirically); and $\langle \delta A_{ps}(\mathbf{r})^2 \rangle$ is the contribution to the measured magnetization variance due to photon shot-noise (determined from a numerical simulation and verified empirically).

Contribution to $G(0)$ from photon shot-noise: a numerical simulation

In determining $G(0)$, we must take into account the contribution to $\langle A_{LP}(\mathbf{r})^2 \rangle$ from photon shot-noise, which we determine by means of a numerical simulation that takes into account our analysis procedures. We verify that the photon shot-noise contribution, $\langle \delta A_{ps}(\mathbf{r})^2 \rangle$, determined from this simulation, agrees with the measured amplitude variance of experimental data dominated by photon shot-noise (as is the case for $t < 47$ ms). We also verify that $\langle \delta A_{ps}(\mathbf{r})^2 \rangle$ scales only weakly with the absolute precession amplitude and may be treated to be constant to a good approximation.

Here we outline a numerical simulation, in which we generate and then analyze artificial phase contrast images characterized by the condensate parameters and the imaging conditions of the experiment. Each of the generated sequences of phase contrast images is analogous to one iteration of the experiment. A sequence of phase contrast images is described by,

$$S(\mathbf{r}, j) = (1 + n(\mathbf{r})(C + Af \cos[\phi_j])N_{p,atom}(\mathbf{r})/N_{p,bright}(\mathbf{r})) \quad (4.42)$$

where \mathbf{r} is the position in the condensate; j is the frame number; $n(\mathbf{r})$ is the normalized Thomas Fermi profile describing the condensate density; C and A are the constant and amplitude contributions to the sinusoidally varying phase contrast signal for a transversely magnetized precessing condensate (Sec. 2.1); f is the normalized condensate magnetization; ϕ_j is the phase of precession per frame (which reflects the precession frequency); and $N_{p,atom}(\mathbf{r})$ and $N_{p,bright}(\mathbf{r})$ correspond to the number of photons per pixel in images of the condensate taken with and without the atoms, respectively.

Both $N_{p,atom}(\mathbf{r})$ and $N_{p,bright}(\mathbf{r})$ are Poissonian random variables. For each iteration of the simulation, they are determined from a Poissonian probability distribution characterized by $\langle N_p(\mathbf{r}) \rangle$, the average number of photons per pixel at \mathbf{r} in the experimental data. We are for the moment ignoring any spatial variation the fractional condensate magnetization f .

For each iteration of the simulation, we generate a new artificial sequence of phase contrast images $S(\mathbf{r}, j)$. We then determine its amplitude variance, $\langle A_{LP}(\mathbf{r})^2 \rangle$, by applying the identical analysis procedures as in our treatment of the experimental data. As shown in Fig.4.10, the average value for $\langle A_{LP}(\mathbf{r})^2 \rangle$ (taken over 10 iterations, choosing random precession frequencies) increases as a function of the peak precession amplitude, $A_{LP,max} =$

fA , as one would expect. Since the simulated value for the described amplitude variance (red circles) agrees with its theoretical value (blue triangles), the numerical procedures are not adding noise to the data analysis.

To determine the contribution to $\langle A_{LP}(\mathbf{r})^2 \rangle$ from photon shot-noise, we compare the value of $\langle A_{LP}(\mathbf{r})^2 \rangle$ calculated in two ways. First, we take into account fluctuations in the photon field by choosing values for $N_{p,atom}, N_{p,bright}$ from the described Poissonian distributions (red circles). Second, we ignore fluctuations in the photon field and simply take its average value, *i.e.*, $N_{p,atom}(\mathbf{r}) = N_{p,bright}(\mathbf{r}) = \langle N_p(\mathbf{r}) \rangle$ (green circles). The former result for the amplitude variance, which takes into account fluctuations in the photon field, is consistently higher than the latter result, which does not. Their difference corresponds to the contribution to the amplitude variance from photon shot-noise, $\langle \delta A_{ps}(\mathbf{r})^2 \rangle$ (green squares). It is approximately constant with respect to the precession amplitude. As shown in Fig. 4.11, it increases slightly with A_{LP} . Simulations which included an inhomogeneous magnetization, $f(\mathbf{r})$, (characteristic of the experimental data), for the same average value for the precession amplitude, yielded similar results for $\langle \delta A_{ps}(\mathbf{r})^2 \rangle$ which were within the error bars of the aforementioned simulation.

In evaluating $G(0)$ for the experimental data, we make use of Eq. 4.41 and the above result for $\langle \delta A_{ps}(\mathbf{r})^2 \rangle$, which in practise adds a small positive offset to the measured amplitude variance. The normalization factor for $G(0)$, corresponding to the amplitude variance of a fully transversely magnetized cloud, is determined empirically as well as theoretically. For the same initial conditions as the quench experiment, we prepared a transversely magnetized condensate and observed its Larmor precession after a given evolution time. Due to the loss of atoms from the trap, the measured amplitude variance decreased over time. The empirically determined amplitude variance as a function of evolution time is shown in Fig. 4.12 for a few repetitions of the experiment (open circles). Their average value (solid circles) compared well with the theoretically calculated amplitude variance for the pertinent condensate parameters and imaging settings (solid squares). At each evolution time, the condensate atom number was independently measured using an absorption image 2.5. The measured condensate number was used in the calculated amplitude variance.

4.4.5 Comparing our observations with a quantum amplification theory

Next we compare the measured magnetization variance with a quantum amplification theory. To compare our measurements to the quantum amplification theory, we performed numerical calculations of $G(0)|_t$, taking into account the inhomogeneous density profile, dipolar interactions, and quantum fluctuations of the initial state, as outlined in Ref. [45, 2]. From such simulations, we determined theoretical values for $G(0)|_t$ for several values of the scattering length difference Δa within the range of recent measurements [24, 88].

The measured magnetization variance, evaluated after an interval t of amplification, is shown in Fig. 3 of Appendix B. The value of $G(0)|_t$ is greater than the photon shot-noise floor for $t \gtrsim 40$ ms. We consider the linear-amplification theory to be applicable for $t \leq 90$ ms, and, following Ref.[42], perform a least-squares fit to a function of the form

$$G(0)|_t = G(0)|_{t_m} \times \sqrt{t/t_m} e^{(t-t_m)/\tau}, \quad (4.43)$$

where τ is the time constant characterizing the growth rate of the magnetization variance and we take $t_m = 77$ ms.

As shown in Figs. 4 of Appendix B, our data are consistent with the quantum-limited amplification of zero-point quantum fluctuations in the case that $|\Delta a|$ lies in the upper range of its reported values. Alternatively, under the assumption that the observed amplification of spin fluctuations is quantum limited, taking the best-fit value of $\tau = 12$ ms, the variance of initial spin fluctuations in our paramagnetic sample is measured to be roughly five times larger than that of purely quantum fluctuations.

4.5 Contributions from technical or thermal spin fluctuations

We investigated potential contributions from technical or thermal spin fluctuations to the experimentally probed spin fluctuations of our samples. To determine the quality of the initial state preparation, we varied the gradient strength, duration, and orientation. In addition, we varied the spin temperature and the kinetic temperature of our samples.

The initial $m = 0$ condensate was purified by applying a transient gradient pulse prior to the quench to expunge the system of any $m = \pm 1$ population and to set the spin

temperature to zero. We checked for a dependence of the time evolution of $G(0)$ upon a nonzero spin temperature by introducing a variable hold time, t_s between the purification pulse and magnetic field quench. We varied t_s up to 110 ms while keeping the total time for the experiment constant and found the time evolution for $G(0)$ to be in agreement within experimental error. This is shown in Figure 4.13 for the cases $t_s = 30, 100$ ms.

Similarly, we varied the strength of the purification pulse by increasing the transient gradient from 4 G/cm to 7 G/cm and found the measured time evolution of $G(0)$ to be unchanged within experimental error.

We confirmed that the trajectory of the experiment following the purification pulse was adiabatic by checking that a condensate prepared in the $m = -1$ state remained a pure state ($N_0 < 3 \times 10^3$) throughout the experimental sequence, and for evolution times up to 400 ms following the quench. Further, the time evolution of the magnetization was observed in the presence of a homogeneous magnetic field, where $dB_z/dz < 0.16$ mG/cm and $dB_z^2/dz^2 < 5.5$ mG/cm², and we confirmed that a condensate prepared in a transversely magnetized state, when observed after evolution time periods of up to 350 ms, underwent uniform Larmor precession. In addition to noise sources which drive atoms into $m = \pm 1$, we may also consider a source of technical noise which transforms the $m = 0$ condensate into a slightly ferromagnetic condensate at the start of the experiment. Given that q is small and that RF fields would therefore tend only to rotate the initial $m = 0$ state, we imagine this contribution to the initial fluctuations would be negligible.

Bound on $m = \pm 1$ atoms from absorption imaging

We determine an upper bound for the number of atoms in $m = \pm 1$ at short times after the quench given the resolution of our time of flight imaging. These atoms may contribute as an incoherent source to the magnetization. Given that this is the case, we can assign an upper bound to the magnetization signal $G(0)$ due to an incoherent population in $m = \pm 1$.

The measured transmission, $T = e^{-\sigma \tilde{n}} \cong 1 - \sigma \tilde{n}$, is close to unity for an image containing close to zero atoms and we bound the number of atoms ΔN which could be present in a blank region of an image. Here σ is the resonant cross section at $\lambda = 780$ nm and \tilde{n} is the two-dimensional density. Our bound on the atom number fluctuations is determined from the fluctuations in transmission, ΔT . We define $T_d = 1 - T$ and use the

fact that $\tilde{n} = T_d/\sigma$ to determine the atom number in a given region corresponding to the size of the condensate. Specifically, we sum \tilde{n} assigned to each pixel over the area occupied by the condensate in the image,

$$N_{atom} = \sum_i \tilde{n}_i \Delta x \Delta z \quad (4.44)$$

$$\begin{aligned} &= \sum_i \tilde{n}_i \left(\frac{L}{M} \right)^2 \\ &= \sum_i T_{d,i} \frac{1}{\sigma} \left(\frac{L}{M} \right)^2, \end{aligned} \quad (4.45)$$

where L is the size of the pixel, M is the magnification, and the sum is over the pixels labeled by i . The fluctuations in the total atom number is then given by,

$$\Delta N_{atom} = \frac{1}{\sigma} \left(\frac{L}{M} \right)^2 \sqrt{N_{pix}} \Delta T_d, \quad (4.46)$$

where we assume the transmission to be a random variable and the sum to be over a large number of pixels. The transmission is calculated from the ratio of the number of photons per pixel in an image taken with atoms, $N_{p,a}$, to the same quantity in second image taken without atoms, $N_{p,b}$. Let $T = N_{p,a}/N_{p,b}$. Assuming that the number of photons per pixel is large, then the average number of photons per pixel, λ is much greater than the fluctuations about that average, $\delta \sim \sqrt{\lambda}$. We can then write,

$$\frac{N_{p,a}}{N_{p,b}} = \frac{\lambda + \delta_a}{\lambda + \delta_b} \quad (4.47)$$

$$\begin{aligned} &= \frac{1 + \delta_a/\lambda}{1 + \delta_b/\lambda} \\ &\approx \frac{\delta_a - \delta_b}{\lambda} \end{aligned} \quad (4.48)$$

We see that T_d is given by $T_d = (\delta_b - \delta_a)/\lambda$, with average value zero. We assume the photon statistics for images a and b to be identical given that we are interested in the case with close to zero atoms in a , that is, we assume $\langle \delta_a^2 \rangle = \langle \delta_b^2 \rangle$ and $\langle \delta_a \rangle = \langle \delta_b \rangle$. The fluctuations in T_d are given by,

$$\Delta T_d = \sqrt{\langle T_d^2 \rangle} = \frac{2 \langle \delta_a^2 \rangle}{\lambda^2}. \quad (4.49)$$

For instance, suppose the fluctuations in the number of photons per pixel, δ_a , were determined solely by photon shot-noise according to Poissonian statistics. Then $\langle \delta_a^2 \rangle = \lambda$ and we determine the atom number fluctuations to be,

$$\Delta N_{atom} = \frac{1}{\sigma} \left(\frac{L}{M} \right)^2 \sqrt{N_{pix}} \sqrt{2/N_{phot}}. \quad (4.50)$$

For our TOF imaging conditions, $\sigma = 2.910^{-9} \text{ cm}^2$, $L = 13.410^{-4} \text{ cm}$, $M = 2.1$, $N_{pix} = 1250$, $N_{phot} = 2500$. This would yield a photon shot-noise limited value of $\Delta N_{atom} = 130$. Representative transmission fields measured in the experiment are characterized by slightly larger fluctuations, given by approximately $\Delta N_{atom} = 300$.

The Stern-Gerlach analysis of populations N_{\pm} in the $|m_z = \pm 1\rangle$ states just after the quench provides a bound for thermal contributions to the spin fluctuations in our samples. Using the above estimate, $N_{\pm} \leq 3 \times 10^2$ and assuming an incoherent admixture of Zeeman sublevels, the thermal contribution to $G(0)|_0$ is below $(2N_{\pm}/N_0) = 3 \times 10^{-4}$. We checked against technical noise that would induce extrinsic Zeeman transitions during the experiment, finding that a condensate starting in the $|m_z = -1\rangle$ state remained so for evolution times up to 400 ms following the quench.

These investigations suggest that our paramagnetic samples were prepared with a near-zero spin temperature. While we have done our best to carry out the experiment such that it is well described by a quantum amplification theory, we recognize that our samples correspond to non-zero temperature gases subject to constant heating and evaporation from the finite-depth optical trap that holds them. Previous work has shown that the non-condensed fraction of a gas may have a strong influence upon its spin dynamics [89]. To investigate this possibility, we compared the amplification of magnetization at kinetic temperatures of 50 and 85 nK, obtained for different optical trap depths. However, we observed no variation, but note that the condensate fraction was not substantially varied in this comparison.

In addition we checked that the magnetic field trajectories were adiabatic by observing that a pure $m_F = -1$ spin state remained so throughout the experimental sequence. The microwave field trajectories used were also observed to be adiabatic with respect to the $F = 1, m_z = 0$ state. At all stages of the experimental sequence, and out to long evo-

lution times following the quench, we verified that the $F = 2$ levels were not populated (at the level of the detection noise, $N_{atom,F=2} < 300$). To do so, we used resonant absorption images without repump, as previously discussed.

4.5.1 Possible role of $F = 2$ atoms

As discussed in Section 1.6, the applied microwave field serves to couple the $F = 1, F = 2$ ground state manifolds. By introducing this coupling, it is possible that the antiferromagnetic character of the $F=2$ manifold may be effectively mixed into the $F=1$ manifold.

One surprising observation made during the study of the quench to a variable final quadratic Zeeman shift, q_f , was the suppression of spin mixing for negative q_f . To discount the possibility that this observation was due to hyperfine mixing, we repeated the quench experiments for three different bias magnetic fields, giving three different values of q_B . These included $q_B/h = 8$ Hz (at $B = 250$ kHz), $q_B/h = 36$ Hz (500 kHz) and $q_B/h = 70$ Hz (700 kHz). At these magnetic field settings, we applied a microwave field with a constant detuning of 35 kHz from the hyperfine resonance, and studied spin mixing as a function of the total quadratic shift, q_f . In each case, spontaneous spin mixing was observed for small positive q_f , and was suppressed for a consistent negative value of q . If the conjecture that spin mixing was suppressed at negative q due to hyperfine mixing were correct, then the turn-off value of q would depend upon the applied microwave radiation, and would be smaller in magnitude when $|q_\mu|$ was larger. Since the observed turn-off value of q was consistent (± 2 Hz) for a range of q_B , this conjecture is not supported by the experiment. In addition, spin mixing was compared while varying q_B and holding q_μ constant; in this case, the admixing of hyperfine levels was constant. Spin mixing was maximized for the expected value of q_B (such that $q_f \approx 0$). While it may be possible to vary the scattering lengths a_0 and a_2 with the application of microwaves, the hyperfine mixing applied in these experiments was insufficient to observe this effect, and to significantly alter the results of the quench experiment.

4.6 Future investigations

The comparison between our experimental observations and a quantum amplification theory could be further constrained by an independent measure of the amplifier gain.

The theoretical value for the amplifier gain is uncertain as a result of the uncertainty in Δa . In a future study, one could empirically determine the gain of the amplifier by studying the amplification of a coherent seed at a given k using, *e.g.*, a spin modulation imprinted on the condensate wavefunction. This may be accomplished using a circularly-polarized Bragg grating, with a tunable periodicity. A coherent seed could also be added at $k = 0$, provided $q \neq 0$, by applying a rotation (RF pulse) to the spinor prior to the quench; however this characterization could be susceptible to technical noise at $k = 0$. In this work, where we characterize the amplifier by seeding it with broadband noise, we have confirmed that in the presence of an increased noise floor, the performance of the amplifier was in qualitative agreement with theory; however this noise floor was uncontrolled in magnitude due to technical limitations.

In a future study, it would be interesting to directly investigate the role of dipolar interactions in the quench experiment. Due to our choice of field alignment, the dipolar interactions played an insignificant role, slightly reducing the gain of the amplifier and shortening the characteristic domain size, each by less than ten percent. As discussed in Ref.[45], by aligning the magnetic field to the \hat{y} or \hat{x} axes and performing the quench experiment, one could enhance the role of dipolar interactions in the quench experiment and systematically vary their influence on the system dynamics.

4.7 Analysis of the time evolution of populated fluctuation modes

By mapping the system Hamiltonian onto that of a parametric amplifier we have established a connection between the physics of a spinor condensate and quantum optics. In this spirit, we further identify that processes of spontaneous and stimulated emission which populate the modes ϕ_x, ϕ_y , for which we have provided a clear physical interpretation. For this reason, we work with the polar basis set given by Equation 4.8.

We are interested in the growth of the population in the ϕ_x, ϕ_y modes following the quench from $q = \infty$. These modes are initially unpopulated and accumulate population (or fluctuations) due to spin mixing. Again, it is sufficient to study the time evolution of one mode, governed by

$$H_{s,k} = (\varepsilon_k + q + \tilde{c}_2(k))(\phi_{x,k}^\dagger \phi_{x,k}) - \frac{i\tilde{c}_2(k)}{2}((\phi_{x,k}^2 - \phi_{x,k}^{\dagger 2})) \quad (4.51)$$

$$\partial_t \phi_{x,k}^\dagger = -\frac{i}{\hbar}[H, \phi_{x,k}^\dagger] \quad (4.52)$$

where we absorb the atomic density n_0 into $\tilde{c}_2(k) \equiv \tilde{c}_2(k)n_0$, which is taken to be constant. For simplicity we drop the momentum (k) and polarization (x) index from now on. It is useful to introduce a few quantities, including the population, n , in the mode, ϕ ,

$$n = \phi^\dagger \phi \quad (4.53)$$

$$\rho = i(\phi^2 - \phi^{\dagger 2})$$

$$\sigma = (\phi^2 + \phi^{\dagger 2}). \quad (4.54)$$

We determine a system of differential equations to describe the evolution of these quantities (for convenience $\hbar = 1$),

$$\partial_t n = -\tilde{c}_2 \sigma \quad (4.55)$$

$$\partial_t \rho = -2(\varepsilon + q + \tilde{c}_2)\sigma$$

$$\partial_t \sigma = 2(\varepsilon + q + \tilde{c}_2)\rho - 4\tilde{c}_2 n + 2\tilde{c}_2 \quad (4.56)$$

We interpret the constant term in the time evolution for σ to reflect spontaneous emission into the mode ϕ , increasing its population n . Initially n can be identically zero; however, since $\partial_t \sigma$ is nonzero, σ and hence $\partial_t n$ become nonzero and the population n increases.

We next introduce re-scaled variables,

$$\tilde{n} = n + \frac{\tilde{c}_2^2/2}{(\varepsilon + q)(\varepsilon + q + 2\tilde{c}_2)} \quad (4.57)$$

$$\equiv n - n_0$$

$$\tilde{\rho} = \frac{\tilde{c}_2}{2(\varepsilon + q + \tilde{c}_2)}\rho$$

$$\tilde{\sigma} = \tilde{c}_2 \sigma,$$

$$(4.58)$$

which enable us to re-express the time evolution of the population in the described modes,

$$\begin{aligned}\partial_t^2 \tilde{n} &= -4((\varepsilon + q)(\varepsilon + q + 2\tilde{c}_2))\tilde{n} \\ &= 4\omega^2 \tilde{n} \\ \omega &= \sqrt{(\varepsilon + q)|\varepsilon + q + 2\tilde{c}_2|}\end{aligned}\tag{4.59}$$

and see that the population in the mode ϕ , in the linear regime, undergoes approximately exponential growth. For the initial condition corresponding to the $m_z = 0$ state, $n = 0$ and $\tilde{\sigma} = 0$ and we find,

$$n(t) = \frac{\tilde{c}_2^2}{\omega^2} \sinh^2(\omega t).\tag{4.60}$$

We have now solved for the time evolution of the population in the originally described modes ϕ_x and ϕ_y . We wish to determine an expression for the experimentally measured quantity, the squared transverse magnetization density $\langle f^\dagger f \rangle$, and connect its time evolution to the growth of population in these modes. We recall that the transverse magnetization F_\perp is given by,

$$\begin{aligned}F_\perp &= F_x + iF_y \\ &= \phi_+^\dagger \phi_0 + \phi_0^\dagger \phi_- \\ &= \sqrt{n}(\phi_+^\dagger + \phi_-),\end{aligned}\tag{4.61}$$

where in the last step we consider a linearized treatment about a coherent paramagnetic state. We make use of the definitions for ϕ_x, ϕ_y in Equation 4.8, and observe:

$$\begin{aligned}\phi_+^\dagger + \phi_- &= i\sqrt{i/2}((\phi_+^\dagger - \imath\phi_x) - \imath(\phi_y^\dagger - \imath\phi_y)) \\ &\equiv f_x - \imath f_y.\end{aligned}\tag{4.62}$$

$$(4.63)$$

where, in the last step, we implicitly define f_x, f_y , which may be interpreted as the transverse magnetization of the x, y polarization modes. We note $\langle f^\dagger f \rangle = \langle f_x^\dagger f_x \rangle + \langle f_y^\dagger f_y \rangle$. Since f_x, f_y are independent quantities, we can focus on the first term which describes the ϕ_x mode and we obtain, after some rearrangement:

$$\langle f_x^\dagger f_x \rangle = \frac{1}{2} \langle (\phi_+^\dagger - \imath\phi_x)(\phi_x + \imath\phi_+^\dagger) \rangle\tag{4.64}$$

$$= \frac{1}{2} + \frac{\tilde{c}_2}{|\varepsilon + q + 2\tilde{c}_2|} \sinh^2(\omega t).\tag{4.65}$$

The total transverse magnetization density is therefore given by,

$$\langle f^\dagger f \rangle = 1 + \frac{2\tilde{c}_2}{|\varepsilon + q + 2\tilde{c}_2|} \sinh^2(\omega t) \quad (4.66)$$

and agrees with the expression determined by Lamacraft [42].

Unlike the population in the modes ϕ_x, ϕ_y , the transverse magnetization density has a nonzero value at $t = 0$, which we often describe as the zero point fluctuations of the magnetization density. For a general spin-1 vector F , since its components F_i do not commute, it is always the case that $\langle F^\dagger F \rangle$ is *initially nonzero*, whether or not spin mixing is occurring.

The theoretical framework we have developed here is physically transparent because it establishes the fluctuating modes (the ϕ_x, ϕ_y modes) which are *initially zero* and whose population is specifically generated by spin mixing through processes akin to spontaneous and stimulated emission.

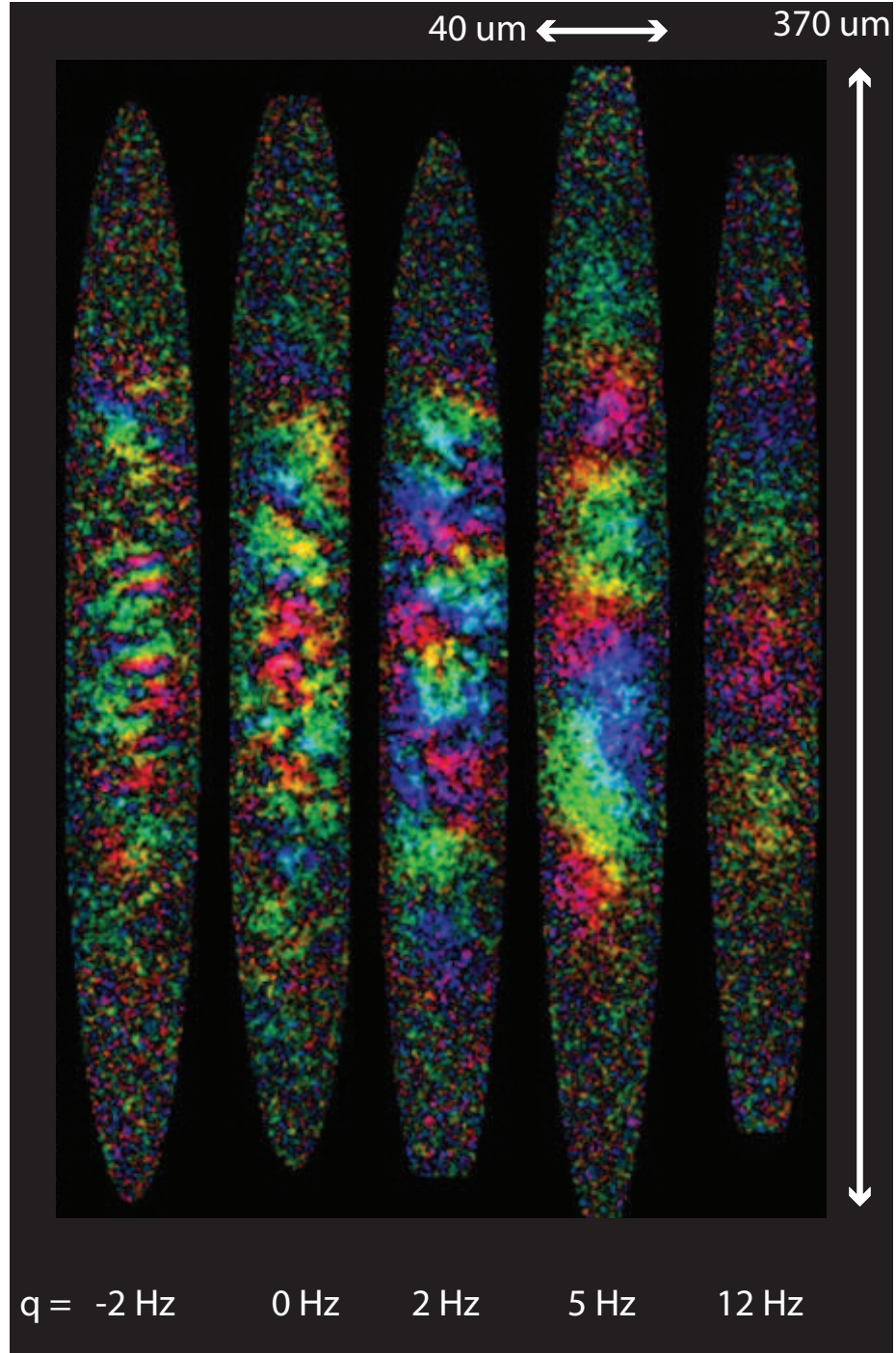


Figure 4.6: The saturated condensate transverse magnetization density as a function of the endpoint of the quench, q_f . For the deep quench, characterized by $0 < q_f < 8$ Hz, the transverse magnetization profile is characterized by short-range features, which increase with q_f . As q_f is raised from 8 to 16 Hz, long-range features are observed and the magnetization diminishes.

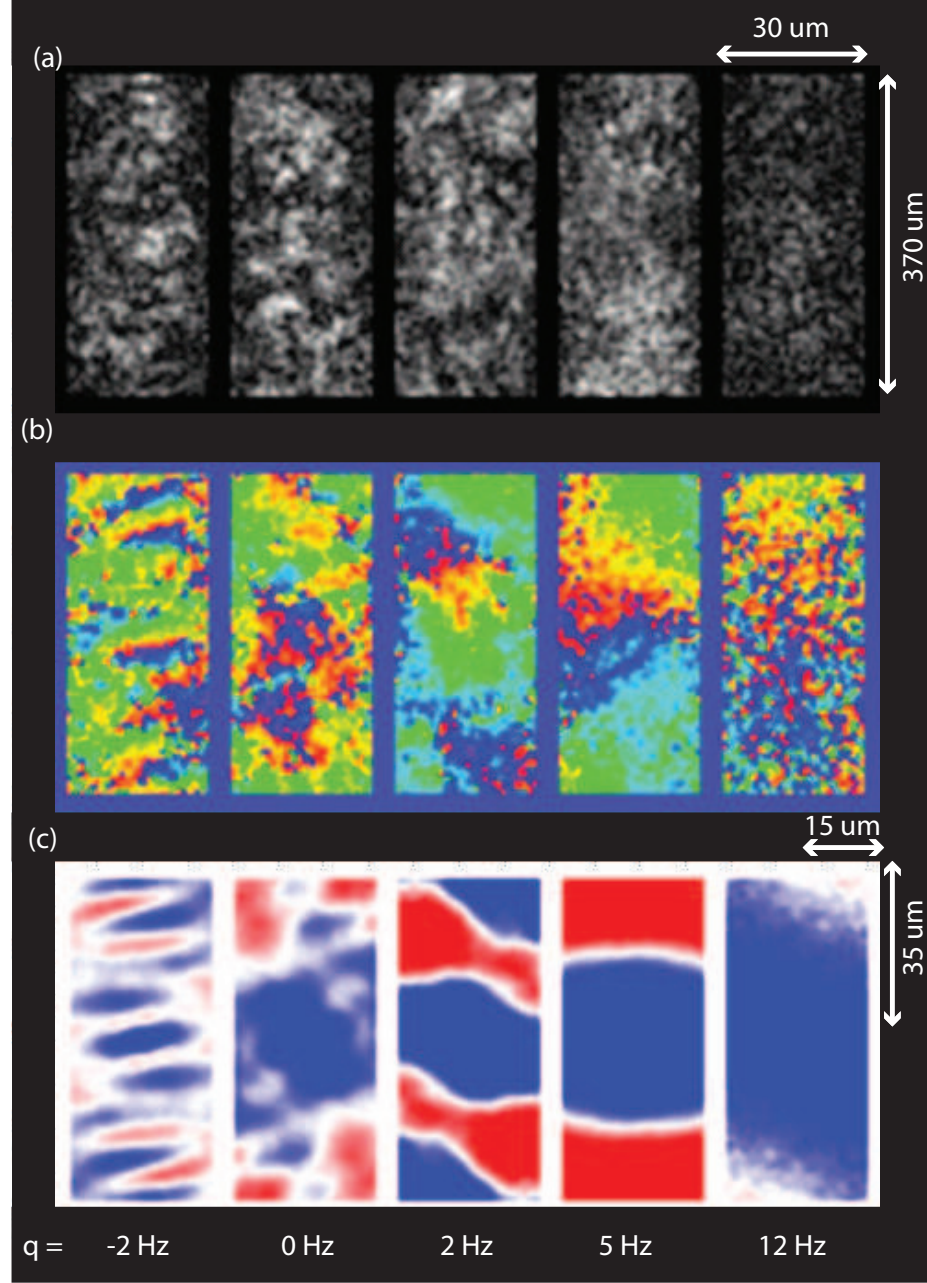


Figure 4.7: Snapshots of the amplitude, phase, and spatial correlations of the transverse magnetization of a central region of the condensate, for a range of values of q_f . The amplifier's spatial spectrum, and its tunability with q_f , is characterized using the magnetization correlations.

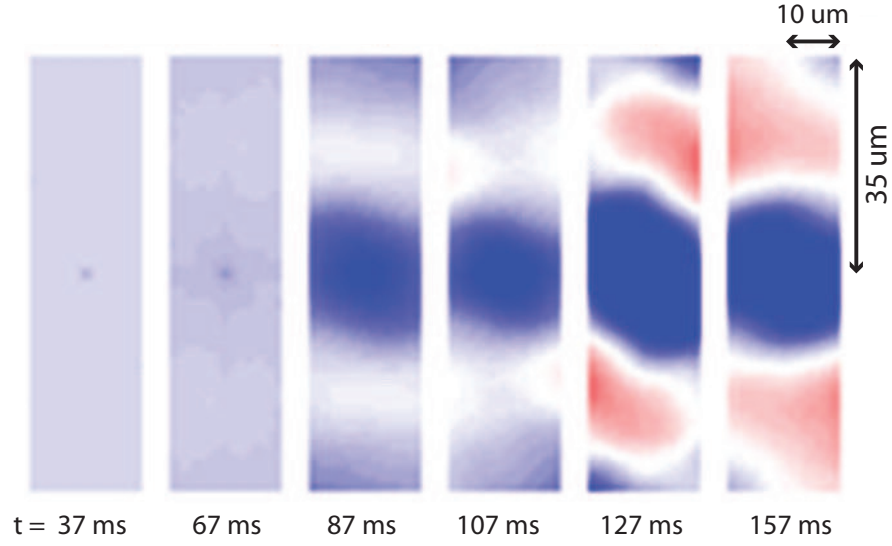


Figure 4.8: The temporal evolution of the magnetization correlation function for $q_f = 2$, averaged over 8 repetitions of the experiment. The characteristic feature size remains roughly constant over time.

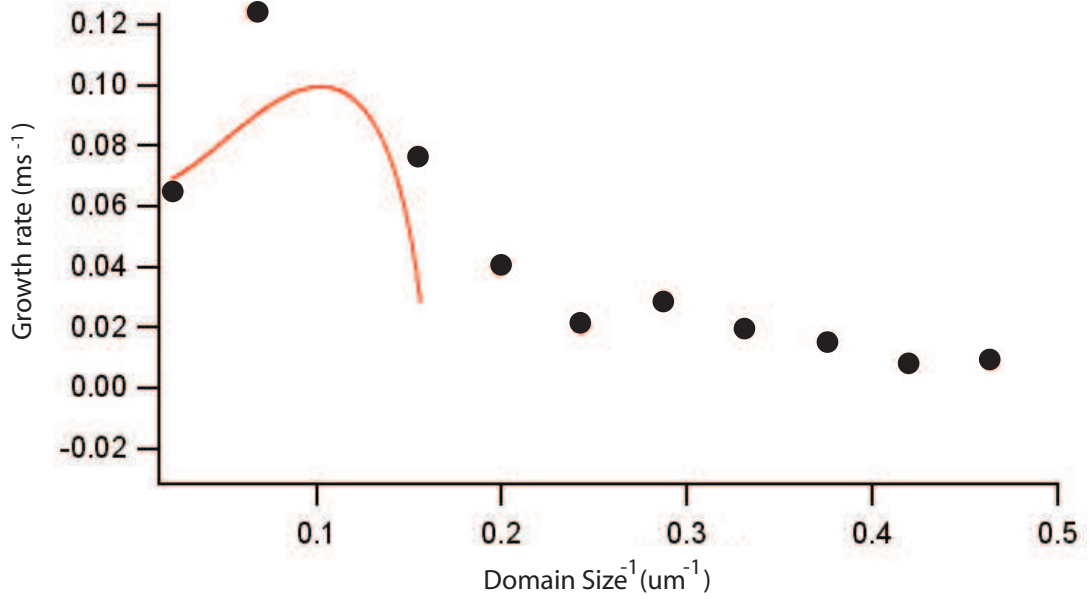


Figure 4.9: The power spectrum of the spatial Fourier transform of the condensate magnetization, as described in the text (circles). An approximate theory for a homogeneous condensate of the same average density as the experiment is shown in comparison (line).

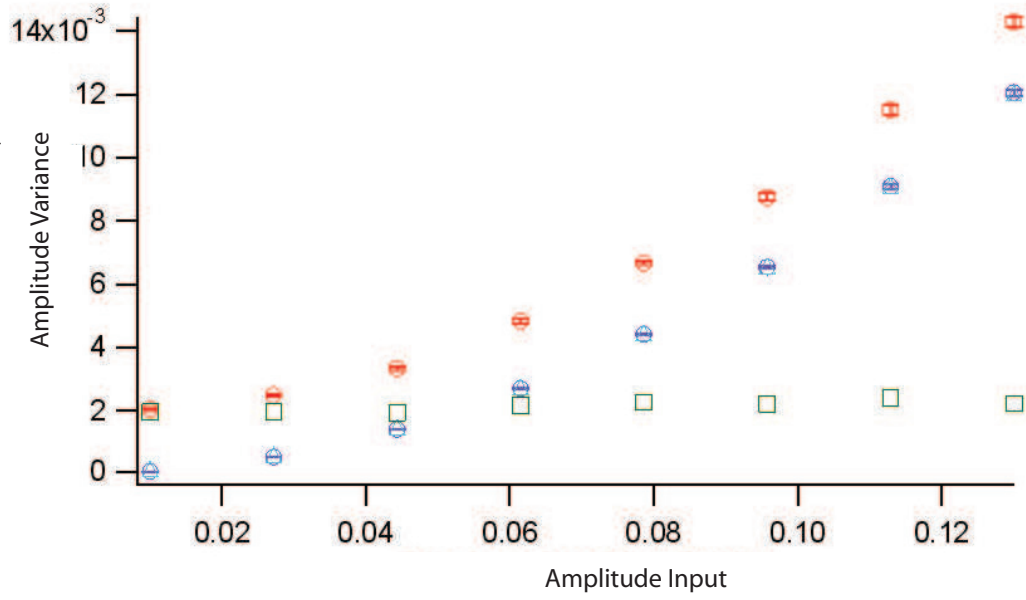


Figure 4.10: The amplitude variance $\langle A_{LP}(\mathbf{r})^2 \rangle$ increases as a function of the peak precession amplitude, $A_{LP,max} = fA$. The simulated amplitude variance averaged over ten repetitions (red circles) agrees with its theoretical value (blue triangles). It is systematically lower if we do not include fluctuations in the photon field (green circles) by an approximately constant offset (green squares).

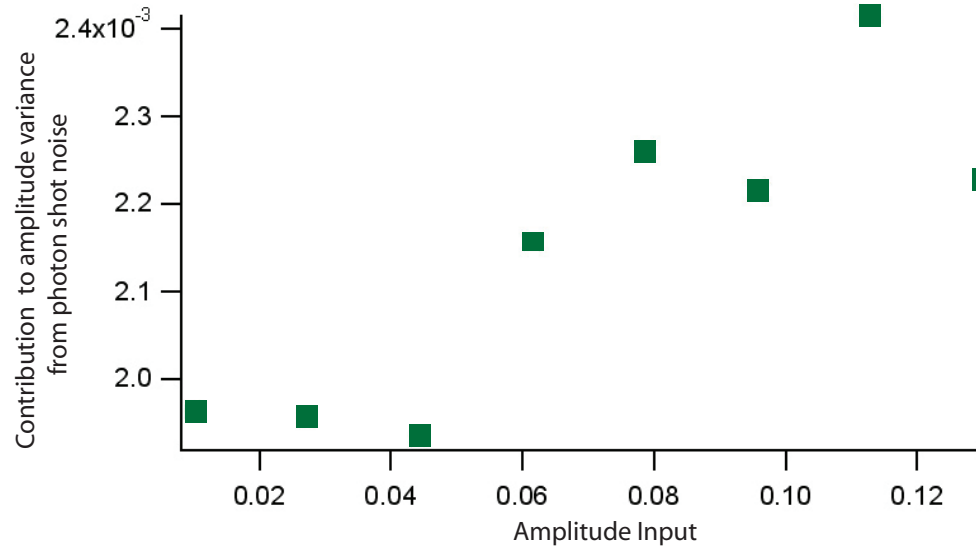


Figure 4.11: The boost in the measured variance of the precession amplitude which results from taking into account the fluctuations in the photon field, as compared to ignoring these fluctuations, in a numerical simulation. It is found to increase slightly with the average precession amplitude. It reflects the detection noise of our measurement of spin fluctuations and corresponds to photon shot-noise.

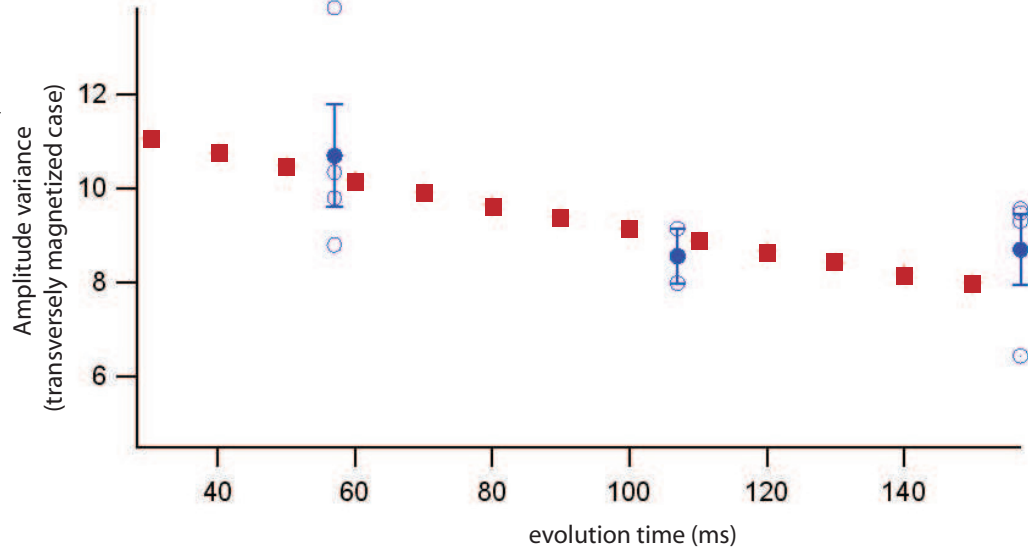


Figure 4.12: The amplitude variance of a fully transversely magnetized cloud, is determined empirically (circles) as well as theoretically (squares). Due to the loss of atoms from the trap, the measured amplitude variance decreased over time.

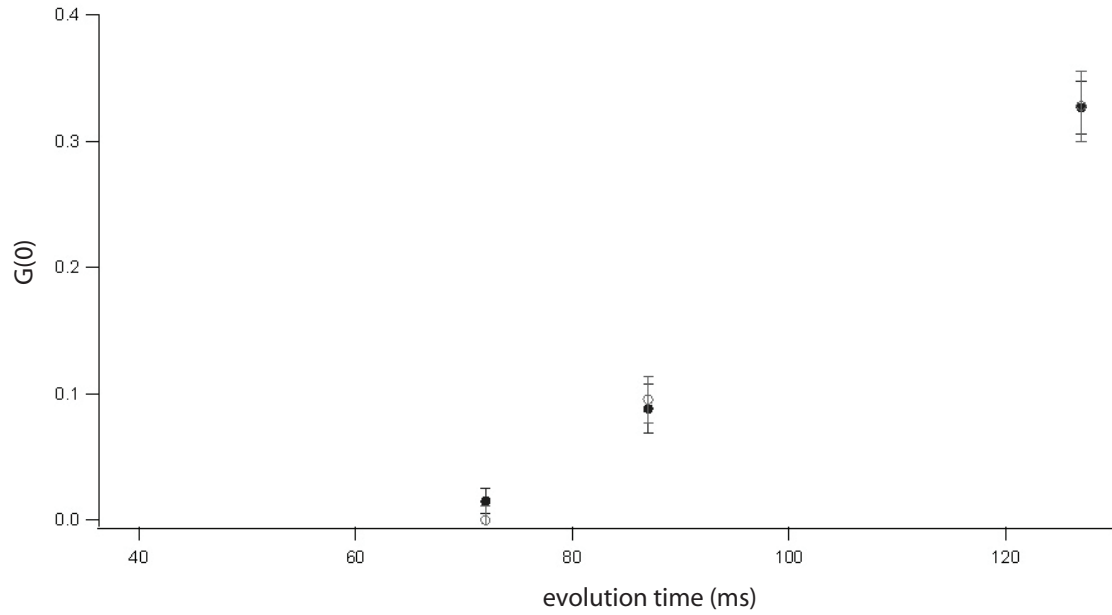


Figure 4.13: The time evolution of $G(0)$, with the introduction of a variable hold time, t_s between the purification pulse and magnetic field quench. For the two cases shown ($t_s = 30, 100$ ms), the time evolution for $G(0)$ is good agreement.

Chapter 6

Spinor Condensates as Dipolar Quantum Fluids

We study the evolution of spin textures in $F = 1$ ^{87}Rb Bose condensates. We find, much to our surprise, that a long wavelength spin helix dissolves spontaneously into short range spatially modulated patterns of spin domains [10]. Following extensive experimental tests, we are able to attribute the observed dissolution of helical spin textures to be a consequence of the dipole-dipole interactions inherent to the magnetized spinor gas. In this way, our characterization of $F = 1$ ^{87}Rb Bose condensates as dipolar magnetic fluids serves as a gateway toward a rich landscape of studies of quantum magnetism, featuring short and long range interactions of tunable relative magnitudes.

6.1 A puzzling observation

Our explorations of the effects of dipole-dipole interactions in spinor Bose condensates began with a peculiar observation made during an otherwise routine experimental procedure. As discussed in Section 1.3, the energetics and dynamics of spinor condensates are influenced by the magnitude, orientation, and spatial variation of the applied magnetic field. Prior to performing a given experiment, it was therefore necessary to reduce the magnetic field inhomogeneity present in our experimental apparatus. To determine the background field inhomogeneity, we allowed a transversely magnetized condensate to undergo Larmor precession in the presence of the background magnetic field for a given time period. By measuring the spatial variation of the accrued Larmor phase, we determined

the spatial variation of the background magnetic field. As discussed in Section 1.5.2, with the use of suitable electromagnets, we eventually succeeded in reducing the inhomogeneity of the magnetic field to a level of $\Delta B < 3 \mu\text{G}$ over the spatial extent of the condensate.

Prior to achieving this level of control over the background magnetic field, (for example, during our preparation for our study of the quantum quench of the spinor condensate presented in Ref. [1]), we observed the condensate magnetization to behave in an unexpected manner. Following an evolution period of roughly 200 ms in fairly homogeneous environment ($\Delta B < 15 \mu\text{G}$), we observed the condensate transverse magnetization profile to dissolve into a finely modulated pattern of magnetic domains. Returning to this puzzling observation, we systematically studied the evolution of helical textures in a spinor gas in order to investigate this behavior.

6.1.1 Why so puzzling?

Due to the small magnetic moment of the ^{87}Rb atom, the effect of dipole-dipole interactions in spinor condensates has previously been assumed to be negligible. The majority of the experimental characterization of $F = 1$ ^{87}Rb condensates has been limited by poor spatial resolution (as discussed in Section 1.2) and many of these studies have been carried out in a single-mode regime, imposed by a tight confinement potential [24, 26]. These observations have been well-described by a mean-field theory which neglects dipole-dipole interactions in the condensate.

A mean-field theory for the $F = 1$ ^{87}Rb condensate, neglecting dipole-dipole interactions, predicts the ground state of an $F = 1$ ^{87}Rb Bose condensate to be ferromagnetic at low magnetic fields (Section 1.3). Thus, one would expect a homogeneous transversely magnetized condensate to minimize the local contact interaction energy (Eq 1.6). Having prepared the condensate in such a state, one would not expect it to evolve into a finely modulated texture of magnetic domains, since this would correspond to a significant rise in kinetic energy.

6.1.2 A possible explanation: dipole-dipole interactions

Taking into account the effect of dipole-dipole interactions in a spinor condensate [103, 104], however, such a finely modulated magnetized state becomes comparable in energy to a uniformly magnetized state. While the kinetic energy of the former configuration is

raised due to its finely modulated spatial profile, the dipole-dipole interaction energy of this configuration is lowered.

To estimate the contribution from dipole-dipole interactions to the energy of the modulated magnetization profile, we model the system as a spin helix, taking

$$\mathbf{F} = \sin(\kappa z)\hat{x} + \cos(\kappa z)\hat{y}, \quad (6.1)$$

where $\kappa = \kappa\hat{z}$ is the wavevector of the helix. The transverse condensate magnetization density $M_{x,y} = g_F\mu_B\tilde{n}F_{x,y}$ generates a self-field along the axis of the helix, \hat{z} , of a magnitude $|B_s| \approx \mu_0|M| \approx \mu_0g_F\mu_Bn$. The difference in the total dipole-dipole energy between the finely modulated (large κ) and uniform ($\kappa = 0$) magnetization profiles is given by $\delta U_d \approx \mu_0g_F^2\mu_B^2n_0/2$. For simplicity, we have assumed a Gaussian transverse density profile for the condensate in this estimate. Taking $n_0 = 2.3 \times 10^{14} \text{ cm}^{-3}$ we find $U_d \sim h \times 5 \text{ Hz}$ per atom. The average kinetic energy cost, δE_k , of the observed modulated magnetization profile is of a similar magnitude. For example, assuming 50 % of the atoms to populate a mode characterized by a spatial modulation frequency $\kappa = 2\pi/10 \text{ } \mu\text{m}^{-1}$, $\delta E_k = (1/2)\hbar^2\kappa^2/4m = h \times 6 \text{ Hz}$ per atom.

The observation that $\delta U_d \approx \delta E_k$ certainly motivates the possibility that dipole-dipole interactions in $F = 1$ ^{87}Rb Bose condensates play a key role in understanding the observed dissolution of the condensate magnetization into finely modulated spin structures. To investigate this behavior further and confirm the role of dipole-dipole interactions in the spinor condensate, we have experimentally characterized the evolution of deliberately imposed helical spin textures.

6.2 Evolving helical spin textures in spinor condensates

In our studies of helical spin textures, we made use of optically trapped condensates of up to 2.3×10^6 ^{87}Rb atoms, initially prepared in the $m_z = -1$ state (described in Section 1.5.1). In this experiment, the optical dipole trap is characterized by trap frequencies $(\omega_x, \omega_y, \omega_z) = 2\pi \times (39, 440, 4.2) \text{ s}^{-1}$ and the condensate Thomas-Fermi radii are given by roughly $(r_x, r_y, r_z) = (17.6, 1.6, 165) \text{ } \mu\text{m}$. The spinor gas is considered to be two-dimensional with respect to spin dynamics since the Thomas-Fermi radius in the \hat{y} direction ($r_y = 1.8 \text{ } \mu\text{m}$) was less than the spin healing length, $\xi_s = (8\pi\Delta an_0)^{-1/2} = 2.4 \text{ } \mu\text{m}$, taking $n_0 = 2.3 \times 10^{14} \text{ cm}^{-3}$.

The spin helix was prepared using a series of two sequential operations. First, by applying a resonant $\pi/2$ pulse, the condensate magnetization was rotated transverse to the bias field, $\mathbf{B} = B_0\hat{z}$ (Sec 3.3.1). The transversely magnetized condensate was then free to Larmor precess about the \hat{z} axis at the precession frequency, $\omega_L = g_F\mu_B B_0/\hbar = 2\pi \times 115 \text{ s}^{-1}$. Second, a \hat{z} -directed magnetic field gradient dB_z/dz was applied for a duration $\tau_P = 5 - 8$ ms, using the axial gradient coils (described in Sec 1.5.2). Following this period of Larmor precession in the presence of a magnetic field gradient, the condensate magnetization was described by a helical spin texture,

$$\begin{aligned}\mathbf{F} &= \sin(\kappa z + \omega_L t)\hat{x} + \cos(\kappa z + \omega_L t)\hat{y} \\ \kappa &= (g_F\mu_B/\hbar)(dB_z/dz)\tau_P\hat{z}.\end{aligned}\tag{6.2}$$

For the remainder of this discussion, we will consider the condensate evolution in the frame co-rotating about the \hat{z} axis at the precession frequency, ω_L .

Helical spin textures with a pitch, $\lambda = 2\pi/\kappa$, ranging from 50 to 150 μm were prepared by varying the magnitude of the applied gradient $|dB_z/dz|$. The duration of the gradient pulse was chosen to be much shorter than the timescale characterizing the subsequent evolution of the spinor condensate. Following the application of the gradient pulse, the spin texture was free to evolve in the presence of a homogeneous magnetic field, to a level of $\delta B < 3 \mu\text{G}$ over the spatial extent of the condensate (Sec 1.5.2).

Following a given evolution period, a sequence of phase-contrast images was taken using 1.5- μs -long pulses of circularly polarized light propagating along the \hat{y} direction (described in Chapter 2). The condensate's transverse magnetization was detected by means of its Larmor precession about the uniform bias field, $B_0\hat{z}$. Portrayed in Figure 6.1 (a) and (b) are two such sequences of phase contrast images, which characterize the Larmor precession of a uniformly transversely magnetized state, and a helical spin texture, respectively.

The amplitude and phase of the Larmor precession signal were extracted from the sequence of images and used to construct a spatially-resolved profile of the transverse magnetization density, $\tilde{M}_{x,y} = (g_F\mu_B)\tilde{n}F_{x,y}$, where \tilde{n} is the column number density [50, 12]. As discussed in Section 2.3, a second $\pi/2$ pulse was applied following this imaging sequence to characterize the longitudinal component of the condensate magnetization.

The evolution of long-range helical textures revealed the condensate transverse magnetization profile, $\tilde{M}_{x,y}$, to develop short-range modulations, portrayed in Fig 6.2. The spontaneous formation of this pattern of magnetic domains, roughly 10 μm in size, was

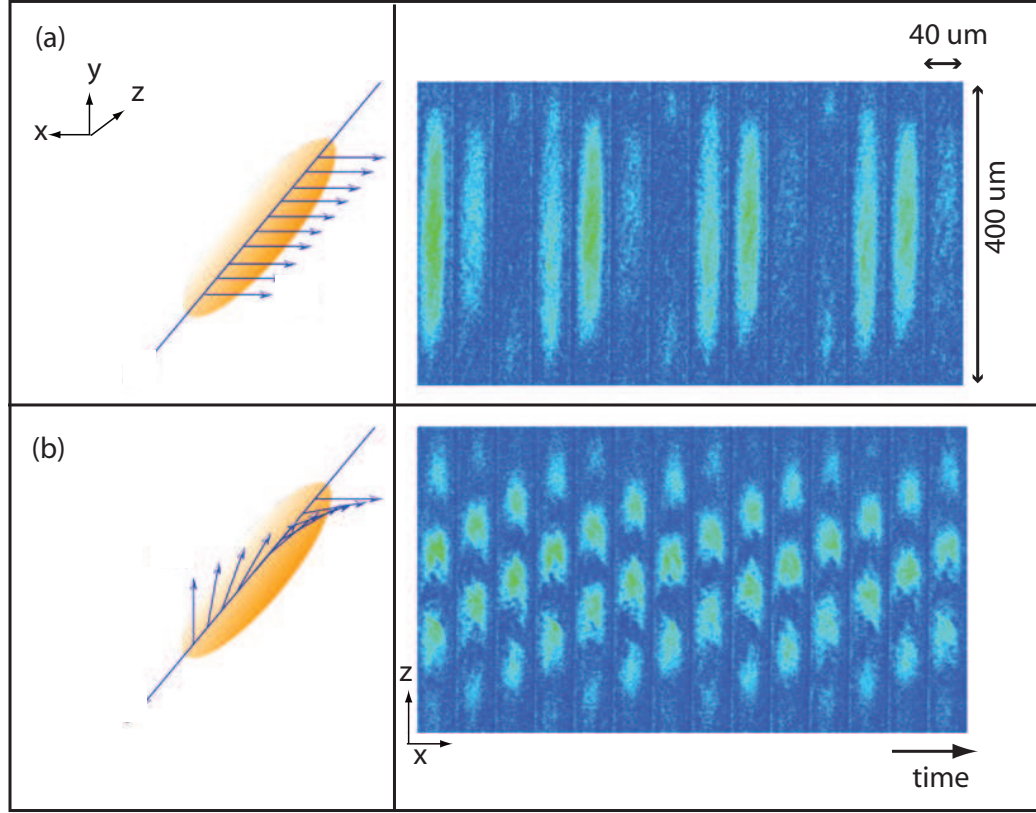


Figure 6.1: (Right) A sequence of phase contrast images characterizing the Larmor precession of a uniformly transversely magnetized condensate (a) and a helical spin texture imposed upon the condensate (b). (Left) An instantaneous snapshot of the condensate spin depicts its homogeneous or helical spatial profile.

observed for a wide range of spin helical textures ($\lambda < 2r_z$). Only for uniformly magnetized condensates characterized by $\lambda \gg 2r_z$ were these domains not observed, following evolution periods up to 300 ms.

For repeated iterations of the experiment, the spatial modulations in the condensate magnetization were observed to nucleate in different locations of the condensate. The sensitivity of the nucleation to the condensate density is reflected, in Fig 6.2, in the tendency for the nucleation to occur at one end of the condensate. Here, due to a slight astigmatism in the optical trap alignment, the condensate density was highest at one end of the condensate. Repeating the experiment using an optical trap which was not astigmatic, the domain pattern was observed to nucleate at random locations in the central region of the condensate. Following evolution periods up to 300 ms, this pattern of magnetized domains

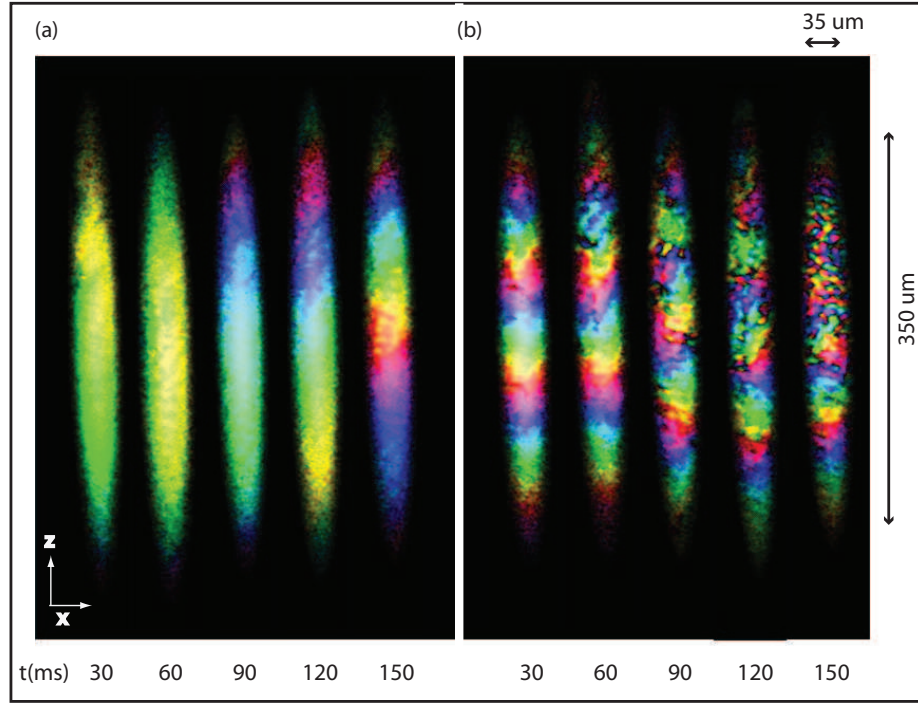


Figure 6.2: Long-range helical textures evolved into a finely modulated transverse magnetization profile $\tilde{M}_{x,y}$. Shown here, due to a slight astigmatism in the optical trap alignment, this pattern of magnetized domains was observed to nucleate most often at one end of the condensate.

extended across the entire condensate.

6.2.1 Quantifying short- and long-range magnetic order

To quantitatively describe the formation of this finely modulated spin texture, we make use of the spatial Fourier transform of the vector magnetization, $\tilde{\mathbf{M}}(k_x, k_z)$. The spectral power of the condensate magnetization, $|\tilde{\mathbf{M}}(k_x, k_z)|^2$, is shown for a $\lambda = 60 \mu\text{m}$ -pitch spin helix, following an evolution period of 250 ms. We find 50 % of the spectral weight to correspond to the long-range order of the initial helical texture. The aspect ratio of the central component of $|\tilde{\mathbf{M}}(k_x, k_z)|^2$ reflects the anisotropic condensate density profile. The remaining spectral weight is concentrated in regions corresponding to a discrete set of wavevectors. The magnitude of these wavevectors, given by $\kappa \sim 2\pi/10 \mu\text{m}^{-1}$, corresponds to the spatial frequency of the finely modulated magnetization pattern.

To characterize the dissolution of the spin helix, we temporally resolve the frac-

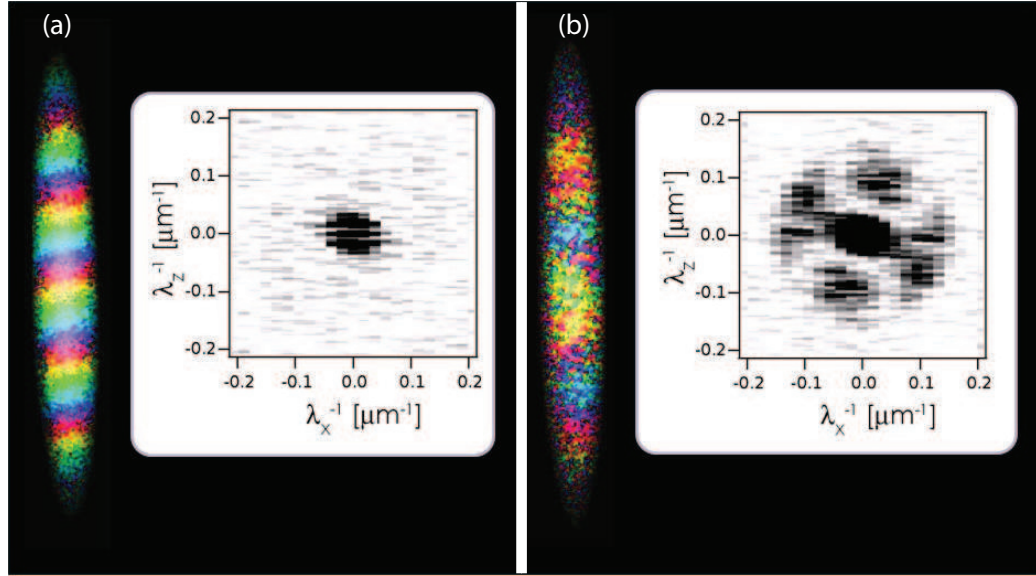


Figure 6.3: The power spectrum of the spatial Fourier transform of the vector magnetization $\tilde{\mathbf{M}}(k_x, k_z)$. The spectral weight of the initial spin helix is concentrated in a central region of k -space, reflecting its long-range order (a). Following the dissolution of the spin helix into a finely modulated magnetization pattern, the spectral weight of short-range features, characterized by modulation frequencies $\sim 2\pi/10 \mu\text{m}^{-1}$, is apparent [10].

tional spectral weight in the finely modulated spin structure. As depicted by Fig 6.4, this corresponds to the fractional spectral power in an annulus in Fourier space, providing a quantitative measure of the system's short range order. This annulus is bounded at small k by the initial long-range spin helix, and at large k by the resolution of our imaging system (Sec 2.2.2). Prior to normalizing the spectral weight contained in this region of Fourier space by the total spectral power, the contribution to each, due to imaging noise, was subtracted (described in Sec 4.4.4).

Accompanying the dissolution of the helical spin texture was an increase in the short-range order of the condensate magnetization, shown in Fig 6.4. Simultaneously, the long-range order of the condensate magnetization, corresponding to the fractional spectral weight in the spin helix, was observed to decrease. The total spectral power was roughly constant over the observed evolution period, reflecting the conservation of magnetization (in the transverse plane). Independent of the initial pitch of the helix, λ , the spectral weight of the short- and long-range magnetic order corresponded to roughly 50 %. The rate of growth of short-range structure increased with λ , as shown in the inset to Figure 6.4 and

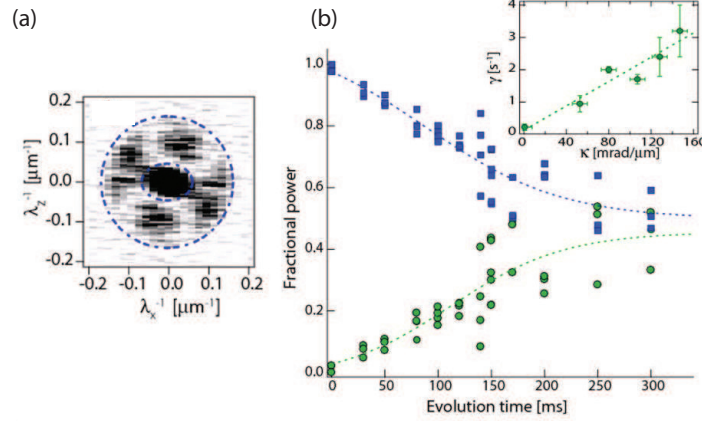


Figure 6.4: The short- and long-range magnetic order of the evolving spin texture are found to increase and decrease respectively, at a rate which depends upon the initial pitch of the helix (inset) [10].

Appendix C.

6.2.2 Manipulating dipole interactions

To investigate the role of magnetic dipole-dipole interactions in the observed dissolution of the helical spin textures, as suggested in Section 6.1.2, we applied a technique which geometrically averaged and hence effectively eliminated, dipole-dipole interactions in the spinor condensate. Described by Eq 1.11, the interaction between two magnetic dipoles, displaced by $\hat{\mathcal{R}}$ from one another, is proportional to $\mathbf{F}_1 \cdot \mathbf{F}_2 - 3(\hat{\mathcal{R}} \cdot \mathbf{F}_1)(\hat{\mathcal{R}} \cdot \mathbf{F}_2)$. By applying a rapid series of random rotations, common to \mathbf{F}_1 and \mathbf{F}_2 , the interaction could be effectively averaged to zero. For this cancelation to be robust, each rotation must be chosen at random from the three-dimensional group of rotations. This technique is a modification of the NMR technique of spin-flip narrowing [105].

To simultaneously study the evolution of the helical spin textures and remove the influence of dipole-dipole interactions, we applied a series of random rotations to the condensate's magnetization while it evolved. During the evolution period, we applied a rapid sequence of $\pi/2$ rf pulses to the Larmor precessing gas, spaced at random time intervals; this

resulted in a sequence of rotations of the condensate magnetization about random rotation axes.

For the dipole-canceling pulses to work, each three-dimensional rotation must be effected with equal likelihood. Following a variable period of Larmor precession of a uniformly-magnetized gas, during which this technique was applied, the \hat{z} projection of the condensate magnetization was determined. To check that the applied rotations were unbiased, the weight in each m_z state was shown to statistically averaged to 1/3 over many repetitions of this procedure. This was indeed the case when the sequence of rf pulses was applied with a mean rate of 1-2 kHz, the setting which was used in the above experiment. For higher and lower values of the average pulse frequency, the applied series of rotations no longer uniformly sampled the $S(3)$ group of rotations, remaining as a subject of future inquiry. The imperfection of this technique could be related to the diffusion of magnetization during the rf pulses.

The spontaneous dissolution of the helical spin texture was significantly suppressed when the dipole-cancellation pulses were applied throughout the evolution period (Fig 6.5). The detected spectral weight of the short-range magnetic order was not completely suppressed, however. Neglecting dipole interactions, the quantum spin fluctuations atop the transversely magnetized initial state are predicted to grow according to a spectrum of dynamical instabilities. Even in the absence of dipole-dipole interactions, a detectable spectral weight of short-range magnetic features is expected, although of a reduced magnitude [106, 107].

Since the application of the dipole-canceling pulses has the additional effect of canceling the quadratic Zeeman shift (q) induced by the magnetic field, these studies were performed at several values of q . For $0.8 < q < 4$ Hz, we observed no variation in the finely modulated magnetic phase.

6.2.3 Examining spin correlations

Complementing our characterization of condensate magnetization in Fourier space, we examine the spatial correlation function of the condensate magnetization (Eq 4.38),

$$G(\delta\mathbf{r}) = \frac{\sum_{\mathbf{r}} \tilde{\mathbf{M}}(\mathbf{r} + \delta\mathbf{r}) \cdot \tilde{\mathbf{M}}(\mathbf{r})}{(g_F\mu_B)^2 \sum_{\mathbf{r}} \tilde{n}(\mathbf{r} + \delta\mathbf{r})\tilde{n}(\mathbf{r})}. \quad (6.3)$$

Portrayed in Fig 6.6 and Appendix C, the modulated magnetization pattern exhibits short-range correlations in the \hat{z} and \hat{x} directions with a periodicity of roughly 10 μm . As

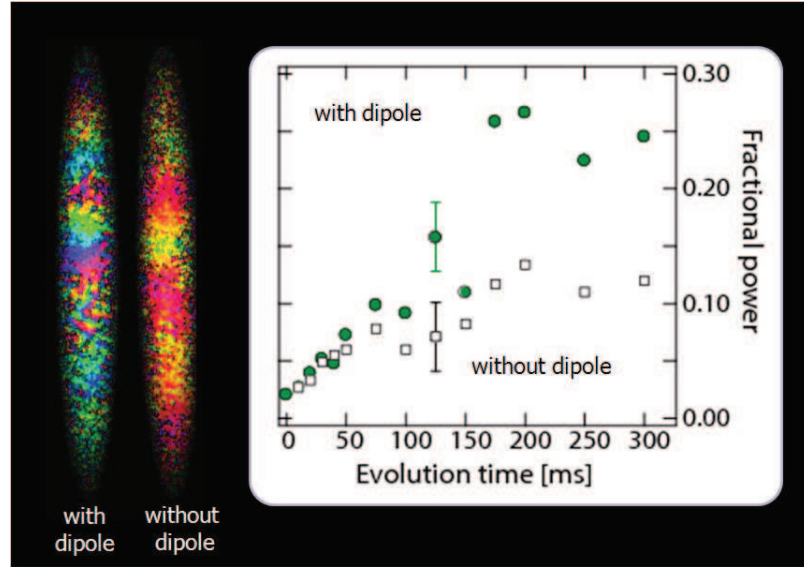


Figure 6.5: The evolution of the short-range order acquired by the condensate magnetization is characterized with and without the application of dipole-cancellation pulses. The initial helix pitch was $\lambda = 80 \mu\text{m}$ [10].

indicated by the width of the Fourier peaks, the correlations diminish over a few spacings of the lattice-like correlations. The six-fold structure in the spatial Fourier transform of the modulated phase is inherent to the lattice-like correlations in the condensate magnetization. The observed long-range order is thought to be mediated by dipole interactions, but has not been reproduced by a theoretical calculation.

Our experimental characterization of the evolution of helical spin textures in spinor condensates has revealed that dipole-dipole interactions play a significant role in the behavior of spinor gases. This is only one example of the experimental discoveries to be made by observing the dynamics of spinor condensates with high spatial resolution. Presently, we are investigating whether the equilibrium phase of this dipolar quantum fluid is described by a coherent magnetic lattice, providing an experimental platform for future studies of “spinor supersolids” [108, 109].

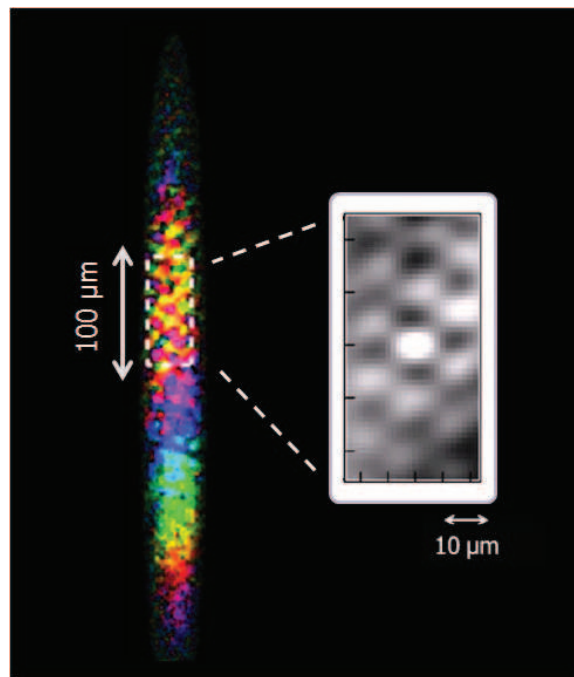


Figure 6.6: Correlations in the spatial correlation function of the condensate magnetization reveal magnetic order characterized by a spatial periodicity of roughly $10\ \mu\text{m}$.

Appendix A

High-Resolution Magnetometry with a Spinor Bose Einstein Condensate

High-Resolution Magnetometry with a Spinor Bose-Einstein Condensate

M. Vengalattore,¹ J. M. Higbie,¹ S. R. Leslie,¹ J. Guzman,¹ L. E. Sadler,¹ and D. M. Stamper-Kurn^{1,2}

¹Department of Physics, University of California, Berkeley California 94720, USA

²Materials Sciences Division, Lawrence Berkeley National Laboratory, Berkeley, California 94720, USA
(Received 15 December 2006; published 17 May 2007)

We demonstrate a precise magnetic microscope based on direct imaging of the Larmor precession of a ⁸⁷Rb spinor Bose-Einstein condensate. This magnetometer attains a field sensitivity of 8.3 pT/Hz^{1/2} over a measurement area of 120 μm², an improvement over the low-frequency field sensitivity of modern SQUID magnetometers. The achieved phase sensitivity is close to the atom shot-noise limit, estimated as 0.15 pT/Hz^{1/2} for a unity duty cycle measurement, suggesting the possibilities of spatially resolved spin-squeezed magnetometry. This magnetometer marks a significant application of degenerate atomic gases to metrology.

DOI: 10.1103/PhysRevLett.98.200801

PACS numbers: 07.55.Ge, 03.75.Mn

Precision magnetometers that map magnetic fields with high spatial resolution have been applied to studies of condensed matter systems [1], biomagnetic imaging [2], and tests of fundamental symmetries [3]. Many of these applications require the measurement of magnetic fields at low (<10 Hz) frequencies. Current technologies capable of micron-scale magnetic microscopy include superconducting quantum interference devices (SQUIDs), scanning Hall probe microscopes, magnetic force microscopes, and magneto-optical imaging techniques [4]. Of these, SQUIDs offer the highest sensitivity, demonstrated at 30 pT/Hz^{1/2} over a measurement area of around 100 μm² [5]. The low-frequency sensitivity of these devices is limited by (1/f) flicker noise of unknown origins [6].

Magnetic fields may also be sensed by detecting the Larmor precession of spin-polarized atomic gases. To date, atomic magnetometers have achieved field sensitivities of 0.5 fT/Hz^{1/2} over measurement volumes of 0.3 cm³ [7]. However, attaining high spatial resolution with a hot-vapor medium is precluded by rapid thermal diffusion of the atoms, restricting the minimum resolved length scale of these magnetometers to around 1 mm.

Trapped ultracold gases present an attractive medium for a variety of precision measurements due to their negligible Doppler broadening and long coherence times [8–10]. Spinor Bose gases, composed of atoms with a spin degree of freedom, are particularly well suited to magnetic microscopy. Unlike in hot-vapor atomic magnetometers, the suppression of thermal diffusion in a gas through Bose condensation enables precise measurements at high spatial resolution. Also, density-dependent collision shifts, which deleteriously affect other types of precision measurements using dense ultracold gases, do not affect Larmor precession due to the rotational invariance of interparticle interactions in a spinor gas [9,11].

Here, we perform precise magnetic microscopy with high two-dimensional spatial resolution using a ⁸⁷Rb $F = 1$ spinor Bose-Einstein condensate (BEC). In our magnetometer, longitudinally spin-polarized spinor condensates

are prepared in an optical trap. Larmor precession is induced using a rf pulse to tip the magnetization perpendicular to a bias field imposed along the axis of the condensate. The spins in each region of the condensate then precess at a rate that is proportional to the *local* magnetic field. After a variable integration time, the condensate is probed using magnetization-sensitive imaging to extract the local Larmor phase. The *difference* in this phase between various regions of the condensate reveals the spatial variation of the magnetic field.

The determination of the accrued Larmor phase of a coherent spin state, such as the transversely magnetized condensate, is subject to an uncertainty in the initial phase of $\delta\phi_a = 1/\sqrt{N}$ due to projection noise of measuring N atoms. This noise limits the field sensitivity over a measurement area A to $\delta B = (\hbar/g\mu_B)(1/\sqrt{\tau DT})(1/\sqrt{\tilde{n}A})$, where τ is the Zeeman coherence time and \tilde{n} the local column density of the gas. We assume the measurement is repeated over a total time T at a duty cycle D . The $A^{-1/2}$ scaling of field sensitivity with the measurement area for the atomic magnetometer may be compared with the area scaling for SQUID magnetometers. This scaling ranges between $A^{-3/4}$, for a fixed SQUID sensor coupled optimally to a variable pickup loop, and $A^{-5/8}$, for direct sensing with a SQUID optimized to operate at the quantum limit for the noise energy [12]. In either case, the atomic magnetometer outperforms SQUID magnetometers at small measurement areas (Fig. 1).

Optical detection of Larmor precession is limited also by photon shot noise. In this work, the Larmor precession phase is measured by repeated phase-contrast imaging of the condensate using circular polarized light [9]. For our probe detuning of $\Delta = 2\pi \times 500$ MHz below the $F = 1 \rightarrow F' = 2$ (D1) transition of ⁸⁷Rb, the phase-contrast signal can be written as $s \approx 1 + 2\tilde{n}\sigma_0(\gamma/2\Delta) \times [c_0 + c_1\langle F_y \rangle]$, where $\sigma_0 = 3\lambda^2/2\pi$ is the resonant cross section, γ is the natural linewidth, and F_y is the projection of the local atomic spin on the imaging axis \hat{y} , which is perpendicular to the field axis. The detuning-dependent

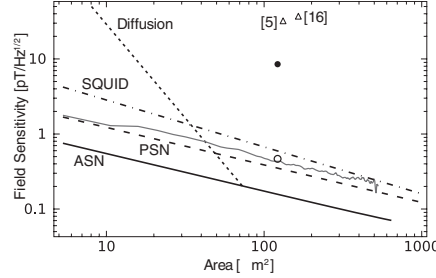


FIG. 1. Field sensitivity for repeated measurements using the spinor BEC magnetometer. Curves marked ASN (PSN) represent atom (photon) shot-noise limited sensitivities, assuming $\tau = 250$ ms, $D = 1$, and the atomic column density and probe light levels for our experiment. Diffusion of magnetization limits the sensitivity for a given length scale by imposing a limit on τ (short dashed line, assuming $D = 1$). The gray line indicates the measured spatial root Allan variance; the sensitivity demonstrated in measurements of an optically induced magnetic field (see text), assuming duty cycles of $D = 0.003$ (●) or $D = 1$ (○), is also shown. Results are compared both to the ideal sensitivity of a quantum-limited SQUID magnetometer (dot-dashed line) and to demonstrated low-frequency sensitivities [5,16] (Δ).

constants $c_0 = 0.118$ and $c_1 = 0.274$ describe the isotropic polarizability and optical activity, respectively. We neglect the effects of linear birefringence ($\propto F_y^2$). The Larmor precession phase is estimated by tracking the sinusoidal oscillation of the phase-contrast signal across the sequence of phase-contrast images. The photon shot-noise limited sensitivity of this estimate is then $\delta\phi_\gamma \approx \sqrt{(2/\eta N_p)[\sqrt{1 + \tilde{n}\sigma_0(\gamma/2\Delta)c_0/\tilde{n}\sigma_0(\gamma/2\Delta)c_1}]}$, limiting the field sensitivity to $\delta B = (\hbar/g\mu_B)(\delta\phi_\gamma/\sqrt{\tau DT})$. Here, η is the detection quantum efficiency and N_p is the total photon fluence, integrated across the multipulse imaging sequence, within the region of interest.

For our demonstration, spin-polarized ^{87}Rb condensates of up to 1.4×10^6 atoms were confined in a single-beam optical dipole trap characterized by trap frequencies $(\omega_x, \omega_y, \omega_z) = 2\pi(165, 440, 4.4) \text{ s}^{-1}$ [9]. The tight confinement along the imaging axis (condensate radius $r_y = 2.0 \mu\text{m}$) ensured that the condensate is effectively two dimensional with respect to spin dynamics. Next, we applied a $\sim 100 \mu\text{s}$ resonant rf pulse at 115 kHz to rotate the magnetization perpendicular to the \hat{z} axis. The sample was then allowed to Larmor precess in the presence of a 165(7) mG bias field aligned along its long axis (\hat{z}). A measurement integration time of 250 ms was chosen; at longer times, measurements were hampered by uncontrolled motion of the condensate along the weakly confining dimension (see below).

We operated our ultracold-atom magnetometer under two testing conditions. In one, we assessed the measure-

ment noise at short spatial length scales by measuring the long length-scale inhomogeneous background magnetic field in our apparatus. We applied a third-order polynomial fit to the measurements from each run of the magnetometer to account for this fluctuating background [13], and analyzed residuals from this fit to characterize experimentally the noise limits to our magnetometer.

In the second testing condition, we used the magnetometer to measure a deliberately applied, localized magnetic field. Such a field was simulated using a circularly polarized laser beam at a wavelength of 790 nm. The choice of wavelength and polarization ensured that this beam imposed a local optically induced Zeeman shift [14] on the trapped atoms [Fig. 2(a)]. The beam was aligned at an angle $\theta \sim 60^\circ$ to the direction of the bias field, incident and focused in the plane perpendicular to the imaging axis. The magnetic background for each run of the magnetometer was again determined by third-order polynomial fits, but using measurements from regions far from the localized field. The magnitude of the localized field was extracted from the residuals of this fit.

Measurements of this simulated field were affected by small center-of-mass oscillations of the condensate along its long axis. An oscillation with amplitude δz blurs the magnetic landscape and washes out features smaller than δz . Unable to eliminate this motion, we monitored the condensate position for each run of the magnetometer by a sequence of 4 images spaced at a quarter period of the

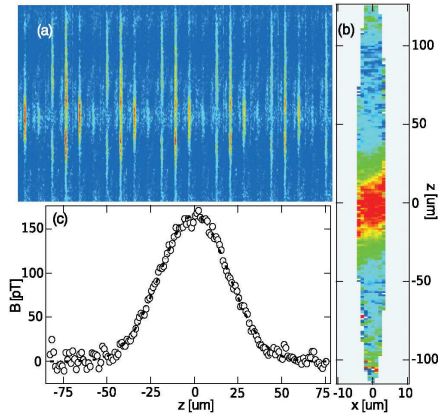


FIG. 2 (color). (a) A sequence of phase contrast images, taken at a strobe rate of 14 kHz, reveal Larmor precession as an aliased frame-to-frame oscillation of the signal. (b) The resulting 2D map of the magnetic field, obtained by a pixel-by-pixel estimation of the Larmor precession phase, reveals the optically induced local magnetic field near the condensate center. (c) The 1D phase profile precisely maps the applied field inhomogeneity with peak strength of 166.2 ± 1.2 pT.

axial trap frequency, taken prior to the Larmor imaging sequence. We discarded measurements in which the excursion was comparable to the extent of the localized field.

Two-dimensional maps of the magnetic field were obtained from a pixel-by-pixel analysis of the Larmor precession phase within the profile of the condensate [Fig. 2(b)]. The frame-to-frame variation of this signal showed the characteristic oscillations due to Larmor precession as well as an overall decay of the condensate number due to off-resonant scattering of probe light. This decay was taken into account in obtaining an unbiased estimate of the local Larmor phase. Our 2D approach was found to be susceptible to imaging aberrations, primarily in the narrow (\hat{x}) dimension of the gas.

More robust measurements were obtained by reducing measurements to a single resolved direction along the \hat{z} axis. For this, the aberrated signal profile in the \hat{x} direction was determined at each z coordinate in the images from averages over the multiple frames. The phase-contrast signal height in each image frame and at each z coordinate was then determined, effectively integrating the signal over \hat{x} . As before, the local Larmor phase was estimated by a least squares fit to the phase-contrast signal to obtain 1D phase profiles [Fig. 2(c)].

The demonstrated sensitivity of our magnetometer is shown in Fig. 1. The spatial root Allan variance [15] from the 1D data was determined for each of 15 runs of the magnetometer under the first testing conditions (background only) and then averaged. The measurement area is determined by accounting for the effective $5.3 \mu\text{m}$ length over which the aberrated signals are averaged in the \hat{x} direction. The observed noise level agrees closely with photon shot noise estimates and is ~ 3 times that due to atomic shot noise given the number of atoms in the corresponding areas. Excess noise for areas larger than about $20 \mu\text{m}^2$ was found to correlate with the local intensity of the probe light, an effect we attribute to probe-light induced shifts of the Larmor frequency during imaging. This noise can be reduced further by using a linearly polarized probe with a more homogenous intensity profile and by carefully aligning the magnetic bias field to be normal to the imaging axis.

Results from measurements under the second testing condition (background plus localized field) are shown in Fig. 3. Here, the strength of the applied field (peak value of Gaussian fits) was measured repeatedly at several powers of the field-inducing laser beam. From these measurements, a calibration between the laser power and the localized field strength was obtained. From the residual scatter in measurements of field with strengths up to 60 pT, we determine the rms sensitivity of our Larmor precession phase measurements as 1.0×10^{-2} rad over the $120 \mu\text{m}^2$ area under the Gaussian profile, corresponding to a single-shot field sensitivity of 0.9 pT. A marginally larger variance at higher fields points to the existence of small systematic effects, e.g., residual motion of the condensate or variations in the localized field strength.

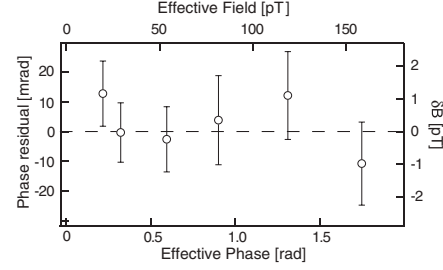


FIG. 3. Single-shot measurements of the localized magnetic field imposed by a laser beam focused to $\sigma = 24 \mu\text{m}$ rms width. Residuals are shown from a linear calibration fit of the field magnitude versus laser power. Error bars indicate standard deviations for 10 measurements per setting.

Under repeated operation, our magnetometer, with a low duty cycle of just $D = 3 \times 10^{-3}$, attains a field sensitivity of $8.3 \text{ pT/Hz}^{1/2}$, an improvement over that demonstrated for low-frequency ($< 10 \text{ Hz}$) field measurements with modern SQUID magnetometers [5,16]. Plausible extensions of current cold-atom experimental methods should enable duty cycles of order unity. At full duty cycle, our single-shot sensitivity would yield a field sensitivity of $0.5 \text{ pT/Hz}^{1/2}$.

In the photon shot-noise limit, the sensitivity of an atomic magnetometer increases with increasing probe fluence. While calculations based on linear Raman scattering rates indicated that reliable phase estimates could be obtained even at a fluence of $3400 \text{ photons}/\mu\text{m}^2$, it was found that light-induced decay of our imaging signal far exceeded these predictions. The discrepancy was attributed to superradiant Raman scattering of atoms into the $F = 2$ hyperfine states, in which atoms are no longer observed by our probe. To counter this problem, we reduced the superradiant gain by lowering the probe intensity and divided the probe light shone on each frame of the imaging sequence into four pulses, each of duration $2.2 \mu\text{s}$ and spaced by the Larmor period of $\sim 10 \mu\text{s}$. We also applied additional light during imaging that was resonant with the $F = 2 \rightarrow F' = 3$ (D2) transition so as to scatter light preferentially off the $F = 2$ atoms produced during superradiance and induce motional decoherence. Together, these strategies enabled a probe fluence of $750 \text{ photons}/\mu\text{m}^2$.

Our magnetometry medium, though Bose condensed, is still a gas in which atoms are free to move. Thus, in determining the phase shift accrued due to a local magnetic field, one must consider atomic motion due to both quantum-mechanical and classical effects. For instance, imposing a weak inhomogeneous field of characteristic length σ leads to quantum diffusive motion of the fluid. For times $\tau > \tau_Q = m\sigma^2/\hbar$, with m the atomic mass, the

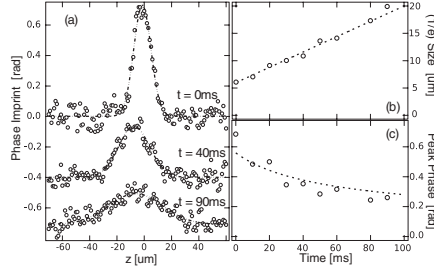


FIG. 4. Quantum evolution of an imprinted phase. (a) Cross sections of the phase imprint after free evolution times of $t = 0$, 40, and 90 ms. Traces are offset for clarity. (b) The $1/e$ width and (c) peak value of the imprinted phase are compared to (b) numerical simulations based on a noninteracting spinor gas and to (c) the expected scaling imposed by normalization of magnetization.

motion of the spinor gas will reduce the phase accrued due to Larmor precession. This evolution can be considered to be the quantum limit of thermal diffusion observed in NMR studies [17]. In our experiment, the condition $\tau = 250 \text{ ms} > \tau_Q$ is reached at length scales below $10 \mu\text{m}$ (Fig. 1). For integration times $\tau \ll \tau_Q$, effects of quantum diffusion require that phase measurements ϕ be corrected by an amount $\delta\phi/\phi \sim (\tau/\tau_Q)^4$.

An inhomogeneous magnetic field also exerts forces on magnetic dipoles. In the extreme case of static inhomogeneous fields with a Zeeman energy comparable to the chemical potential ($\sim 10^5$ times larger than those studied in this work), these classical forces can visibly modify the density distribution of the condensate [18]. In our case, these forces result in small corrections and limits to the accrued Larmor phase. The field strength B and a characteristic length σ for its variation define a classical time scale $\tau_C = \sqrt{m\sigma^2/\mu_B B}$, the time taken by an atom to move σ when accelerated by this field. For an integration time τ , this classical motion imposes a limit on the maximum detectable phase shift (when $\tau = \tau_C$) of $\phi_m \approx \tau_Q/\tau$. It should be noted that neither the diffusion of an imprinted phase nor the limitation on the dynamic range are fundamental; both can be eliminated by constraining atomic motion with suitable optical potentials.

To observe the dilution of magnetization due to atomic motion, we imposed a light-induced Zeeman shift localized to a $1/e$ width of $5.4 \mu\text{m}$ onto the transversely magnetized spinor condensate. Following a 5 ms exposure to the field-inducing laser beam, the condensate magnetization was allowed to evolve freely for variable time before being probed. During this evolution, the imprinted Larmor phase diminished in peak height and grew in extent, match-

ing well with calculations based on a noninteracting spinor gas in a localized field (Fig. 4).

In conclusion, we have demonstrated a spinor-BEC magnetometer, a powerful application of ultracold atoms to precision measurement of scientific and technological significance. Inasmuch as the Larmor precession phase represents the phase relations among BECs in several Zeeman states, this magnetometer can be regarded as a condensate interferometer with high temporal and spatial resolution. The single-shot phase sensitivity and shot-to-shot variations of 10 mrad achieved here represent an order of magnitude improvement over the performance of previous BEC interferometers [19].

The demonstrated phase sensitivity is close to the atom shot-noise limit. This augurs spin-squeezed magnetometry via continuous quantum nondemolition measurements of the condensate [20] and novel spatially and temporally resolved studies of spin-squeezed ensembles.

We thank D. Budker and J. Clarke for helpful discussions. This work was supported by the NSF and the David and Lucile Packard Foundation. S.R.L. acknowledges support from the NSERC.

- [1] C. C. Tsuei and J. R. Kirtley, *Rev. Mod. Phys.* **72**, 969 (2000).
- [2] K. Kobayashi and Y. Uchikawa, *IEEE Trans. Magn.* **39**, 3378 (2003).
- [3] L. R. Hunter, *Science* **252**, 73 (1991).
- [4] S. J. Bending, *Adv. Phys.* **48**, 449 (1999).
- [5] J. R. Kirtley *et al.*, *Appl. Phys. Lett.* **66**, 1138 (1995).
- [6] R. H. Koch *et al.*, *J. Low Temp. Phys.* **51**, 207 (1983).
- [7] I. K. Kominis *et al.*, *Nature (London)* **422**, 596 (2003).
- [8] P. Treutlein *et al.*, *Phys. Rev. Lett.* **92**, 203005 (2004).
- [9] J. M. Higbie *et al.*, *Phys. Rev. Lett.* **95**, 050401 (2005).
- [10] N. Davidson *et al.*, *Phys. Rev. Lett.* **74**, 1311 (1995).
- [11] T. L. Ho, *Phys. Rev. Lett.* **81**, 742 (1998); T. Ohmi and K. Machida, *J. Phys. Soc. Jpn.* **67**, 1822 (1998).
- [12] R. H. Koch *et al.*, *Appl. Phys. Lett.* **38**, 380 (1981).
- [13] Based on the geometry of the apparatus and the location of magnetic field sources, we estimate background field variations across the condensate due to fourth order and higher terms to be $\ll 1$ fT.
- [14] J. Dalibard and C. Cohen-Tannoudji, *J. Opt. Soc. Am. B* **6**, 2023 (1989).
- [15] The spatial Allan variance is similar to the commonly used temporal Allan variance [D. W. Allan, *Proc. IEEE* **54**, 221 (1966)], except that the data series (i.e., the magnetic field) is now a function of position rather than time.
- [16] T. S. Lee *et al.*, *Rev. Sci. Instrum.* **67**, 4208 (1996).
- [17] H. Carr and E. Purcell, *Phys. Rev.* **94**, 630 (1954).
- [18] S. Wildermuth *et al.*, *Nature (London)* **435**, 440 (2005).
- [19] S. Gupta *et al.*, *Phys. Rev. Lett.* **89**, 140401 (2002).
- [20] A. Kuzmich *et al.*, *Europhys. Lett.* **42**, 481 (1998); J. M. Geremia *et al.*, *Science* **304**, 270 (2004).

Appendix B

Amplification of Fluctuations in a Spinor Bose Einstein Condensate

LT11333

Amplification of Fluctuations in a Spinor Bose Einstein Condensate

S. R. Leslie^{1,*}, J. Guzman^{1,2}, M. Vengalattore¹, Jay D. Sau¹, Marvin L. Cohen^{1,2}, and D. M. Stamper-Kurn^{1,2}

¹*Department of Physics, University of California, Berkeley CA 94720*

²*Materials Sciences Division, Lawrence Berkeley National Laboratory, Berkeley, CA 94720*

(Dated: November 9, 2008)

Dynamical instabilities in a ^{87}Rb $F = 1$ spinor Bose-Einstein condensate are used as a parametric amplifier of quantum spin fluctuations. We demonstrate the spectrum of this amplifier to be tunable, in quantitative agreement with theory. We quantify the microscopic spin fluctuations of the initially paramagnetic condensate by applying this amplifier and measuring the resulting macroscopic magnetization. The variance of these fluctuations agrees with predictions of a beyond-mean-field theory. This spin amplifier is thus shown to be nearly quantum-limited at a gain as high as 30 dB.

Accompanied by a precise theoretical framework and prepared in a highly controlled manner, ultracold atomic systems serve as a platform for studies of quantum dynamics and many-body quantum phases, and as a potential resource for precise sensors. Among these systems, gaseous spinor Bose-Einstein condensates [1–5], in which atoms may explore all sub-levels of the hyperfine spin F , give access to interesting static and dynamical properties of a magnetic superfluid [6–9] and can serve as a medium for precise magnetometry [10].

Particularly interesting dynamics are associated with a quantum phase transition between a paramagnetic and ferromagnetic phase in an $F = 1$ spinor Bose-Einstein condensate [8]. This transition is crossed as the quadratic Zeeman energy term, of the form qF_z^2 , is tuned through a critical value $q = q_0$; here, F_z is the longitudinal (\hat{z} axis) projection of the dimensionless vector spin \mathbf{F} . This phase transition is accompanied by the onset of dynamical instabilities in a condensate prepared in the paramagnetic state, with macroscopic occupation of the $|m_z = 0\rangle$ state [11–13]. The instabilities cause transverse spin perturbations to grow, producing atoms into the $|m_z = \pm 1\rangle$ sublevels. In contradiction with the mean-field prediction that the paramagnetic state should remain stationary because it lacks fluctuations by which to seed the instability, experiments revealed the spontaneous magnetization of such condensates after they were quenched across the phase transition by a rapid change in q .

Here, we consider making use of dynamical instabilities in a quenched spinor condensate to realize a mode-by-mode, low-noise parametric amplifier of magnetization. Low-noise amplifiers have been developed in myriad physical systems to enable precision measurements and studies of quantum noise. For example, parametric amplifiers constructed with Josephson junctions have been used to measure weak microwave signals and to induce squeezing of microwave fields [14]. Similarly, quantum-limited amplification of spin excitations in spinor condensates could lead to the preparation of spin squeezed states, with applications toward metrology.

In this work, following studies of solid-state low-noise

amplifiers [14, 15, for example], we characterize the spin-mixing amplifier by seeding it with broadband noise and measuring precisely the spectrum of its output. We present two main results. First, we characterize the spectrum of the spin-mixing amplifier and demonstrate it to be tunable by varying the quadratic Zeeman shift. This spectrum compares well with a theoretical model that accounts for the inhomogeneous condensate density and for magnetic dipole interactions. Second, we measure precisely the transverse magnetization produced by this amplifier at various stages of amplification, up to a gain of 30 dB in the magnetization variance. Under the assumption that the system performs as a quantum-limited amplifier with the aforementioned spectral gain profile, this magnetization signal corresponds to the amplification of initial fluctuations with a variance slightly greater than that expected for zero-point fluctuations of the quantized spin excitation modes that become unstable.

Descriptions of the dynamics of initially paramagnetic spinor condensates [12, 13, 16–19] have focused on the effects of the quadratic Zeeman energy and of the spin-dependent contact interaction. The latter has the mean-field energy density $c_2 n(\mathbf{F})^2$, and, with $c_2 = 4\pi\hbar^2\Delta a/3m < 0$, favors a ferromagnetic state; here, $\Delta a = (a_2 - a_0)$ where $a_{F_{\text{tot}}}$ is the s -wave scattering length for collisions between particles of total spin F_{tot} and m is the atomic mass. Excitations of the uniform condensate include both the scalar density excitations and also two polarizations of spin excitations with a dispersion relation given as $E_s^2(\mathbf{k}) = (\varepsilon_k + q)(\varepsilon_k + q - q_0)$, where $\varepsilon_k = \hbar^2 k^2/2m$ and $q_0 = 2|c_2|n$. For $q > q_0$, spin excitations are gapped ($E_s^2 > 0$), and the paramagnetic condensate is stable. Below this critical value, the paramagnetic phase develops dynamical instabilities, defined by the condition $E_s^2 < 0$, that amplify transverse magnetization. The dispersion relation defines the spectrum of this amplification, yielding a wavevector-dependent time constant for exponential growth of the power in the unstable modes, $\tau = \hbar/2\sqrt{|E_s^2|}$.

The unstable regime is divided further into two regions. Near the critical point, reached by a “shallow” quench to $q_0/2 \leq q < q_0$, the fastest-growing instability occurs at zero wavevector, favoring the “light-cone” evolution of magnetization correlations at ever-longer range [12]. For a “deep” quench, with $q < q_0/2$, the instabilities reach

*Electronic address: sleslie@berkeley.edu

a maximum growth rate of $1/\tau = q_0/\hbar$. The non-zero wavevector of this dominant instability sets the size of magnetization domains produced following the quench.

Similar to previous work [8], we produce condensates of $N_0 = 2.0 \times 10^6$ ^{87}Rb atoms, with a peak density of $n = 2.6(1) \times 10^{14} \text{ cm}^{-3}$ and a kinetic temperature of $\simeq 50 \text{ nK}$, trapped in a linearly polarized optical dipole trap characterized by trap frequencies $(\omega_x, \omega_y, \omega_z) = 2\pi \times (39, 440, 4.2) \text{ s}^{-1}$. Taking $\Delta a = -1.4(3) a_B$ [20], with a_B being the Bohr radius, the spin healing length $\xi_s = (8\pi n |\Delta a|)^{-1/2} = 2.5 \mu\text{m}$ is larger than the condensate radius $r_y = 1.6 \mu\text{m}$ along the imaging axis (\hat{y}). Thus, the condensate is effectively two-dimensional with respect to spin dynamics. For this sample, $q_0 = 2|c_2|\langle n \rangle = \hbar \times 15 \text{ Hz}$ given the maximum \hat{y} -averaged condensate density $\langle n \rangle$.

The quadratic Zeeman shift arises from the application of both static and modulated magnetic fields. A constant field of magnitude B , directed along the long axis of the condensate, leads to a quadratic shift of $q_B/\hbar = (70 \text{ Hz/G}^2) B^2$. In addition, a linearly polarized microwave field [21], with Rabi frequency Ω and detuned by $\delta/2\pi = \pm 35 \text{ kHz}$ from the $|F=1, m_z=0\rangle$ to $|F=2, m_z=0\rangle$ hyperfine transition, induces a quadratic (AC) Zeeman shift of $q_\mu = -\hbar\Omega^2/4\delta$ [22].

The condensate is prepared in the $|m_z=0\rangle$ state using rf pulses followed by application of a 6 G/cm magnetic field gradient that expels atoms in the $|m_z=\pm 1\rangle$ states from the trap [8]. This preparation takes place in a static 4 G field and with no microwave irradiation, setting $q = q_B + q_\mu > q_0$ so that the paramagnetic condensate is stable. Next, we increase the microwave field strength to a constant value, corresponding to a Rabi frequency in the range of $2\pi \times (0 - 1.5) \text{ kHz}$, to set q_μ . To switch on the amplifier, we ramp the magnetic field over 5 ms to a value of $B = 230 \text{ mG}$ (giving $q_B/\hbar = 7.6 \text{ Hz}$). During separate repetitions of the experiment (for different values of q_μ), the quadratic Zeeman shift at the end of the ramp was thus brought to final values q_f/\hbar between -2 and 16 Hz .

Following the quench, the condensate spontaneously develops macroscopic transverse magnetization, saturating within about 110 ms to a pattern of spin domains, textures, vortices and domain walls [8]. Using a 2-ms -long sequence of phase-contrast images, we obtain a detailed map of the column-integrated magnetization \vec{M} at a given time after the quench [10]. The experiment is then repeated with a new sample.

The observed transverse magnetization profiles [23] of spinor condensates (Fig. 1) confirm the salient features predicted for the spin-mixing amplifier. The variation of the amplifier's spatial spectrum with q_f is reflected in the characteristic size of the spin domains, taken as the minimum distance from the origin at which the magnetization correlation function,

$$G(\delta\mathbf{r}) = \frac{\sum_{\mathbf{r}} \vec{M}(\mathbf{r} + \delta\mathbf{r}) \cdot \vec{M}(\mathbf{r})}{(g_F \mu_B)^2 \sum_{\mathbf{r}} \tilde{n}(\mathbf{r} + \delta\mathbf{r}) \tilde{n}(\mathbf{r})}, \quad (1)$$

acquires its first minimum; here $g_F \mu_B$ is the atomic mag-

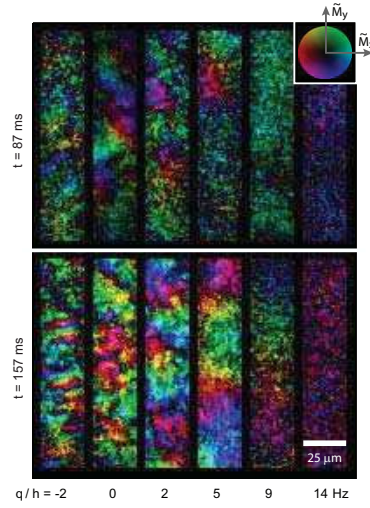


FIG. 1: Transverse magnetization produced near the condensate center after 87 ms (top) and 157 ms (bottom) of amplification at variable q_f . Magnetization orientation is indicated by hue and amplitude by brightness (color wheel shown). The characteristic spin domain size grows as q_f increases. The reduced signal strength for $q_f/\hbar \geq 9 \text{ Hz}$ reveals the diminished gain of the spin-mixing amplifier.

netic moment and \tilde{n} is the \hat{y} -integrated column density. This characteristic size increases with increasing q_f (Fig. 2). For $q_f/\hbar \geq 9 \text{ Hz}$, the magnetization features become long ranged, as predicted. An exact determination of their characteristic size then becomes limited by residual magnetic field inhomogeneities ($< 2 \mu\text{G}$).

The data also confirm the distinction between deep and shallow quenches. The spatially averaged magnetization strength during the amplification, quantified by $G(0)$ at $t = 87 \text{ ms}$ after the quench, is found to be constant for $0 < q_f/\hbar < 6 \text{ Hz}$, reflecting the gain of the amplifier being uniform over $0 \leq q \leq q_0/2$ [12]. For shallow quenches, with $q_f/\hbar \geq 7 \text{ Hz}$, the measured magnetization decreases, reflecting a diminishing gain as q_f increases up to the transition point.

While the above observations agree with theoretical predictions, we note the unexpected and unexplained outcome of quenches to negative values of q_f . That is, for quenches to $q_f/\hbar \leq -7 \text{ Hz}$, the growth of magnetization was greatly suppressed ($G(0)|_{t=160\text{ms}} \leq 10^{-2}$).

Having characterized the spin-mixing amplifier, let us consider the source of its input signal. For this, we develop a quantum field description of the spin-mixing instability [12, 19], working in the polar spin basis, where

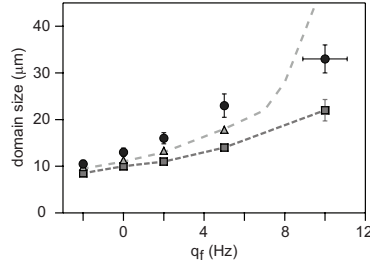


FIG. 2: Characteristic domain size after 87 ms of amplification at variable q_f . Data (circles) are averages over 5 experimental repetitions; error bars are statistical. Horizontal error bar reflects systematic uncertainty in q_f . Predictions based on numerical simulations for $|\Delta a| = 1.45 a_B$ [7] (squares) and $1.07 a_B$ [24] (triangles) are shown, with error bar reflecting systematic uncertainty in the atomic density.

$\hat{\phi}_{n,k}$ is the annihilation operator for atoms of wavevector k in the zero-eigenvalue states of $\mathbf{F} \cdot \mathbf{n}$. Treating a uniform condensate within the Bogoliubov approximation, one defines mode operators $\hat{b}_{n,k} = u\hat{\phi}_{n,k} + v\hat{\phi}_{n,-k}^\dagger$ for the two polarizations of transverse ($n \in \{x, y\}$) spin excitations. The portion of the spin-dependent Hamiltonian representing dynamic instabilities, H_{DI} , is then approximated as representing a set of parametric amplifiers:

$$H_{DI} = -\frac{i}{2} \sum_k [E_s(k)] (b_{x,k}^2 - b_{x,k}^{\dagger 2} + b_{y,k}^2 - b_{y,k}^{\dagger 2}). \quad (2)$$

The parametric amplifiers serve to squeeze the initial state in each spin excitation mode, amplifying one quadrature of $b_{n,k}$ and de-amplifying the other.

The above treatment may be recast in terms of spin fluctuations atop the paramagnetic state: fluctuations of the transverse spin, represented by the observables F_x and F_y , and fluctuations in the alignment of the spinor, represented by the components N_{yz} and N_{xz} of the spin quadrupole tensor. We identify the Bogoliubov operators defined above as linear combinations of these observables. Based on this identification, we draw two conclusions. First, an ideally prepared paramagnetic condensate is characterized by quantum fluctuations of the Bogoliubov modes. In the linear regime, fluctuations in $b_{x,k}$ ($b_{y,k}$) correspond to projection noise for the conjugate observables F_x (F_y) and N_{yz} (N_{xz}). Second, the dynamical instabilities lead to a coherent amplification of these initial shot-noise fluctuations. While in the present work we observe only the magnetization, in future work both quadratures of the spin-mixing amplifier may be measured using optical probes [25] or by using quadratic Zeeman shifts to rotate the spin quadrature axes.

To test the validity of this description, we evaluate $G(0)|_t$, the magnetization variance after an interval t of

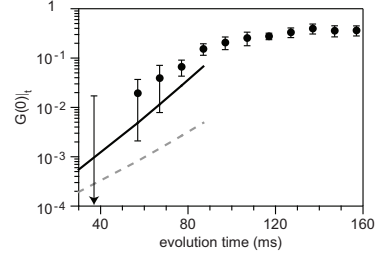


FIG. 3: Temporal evolution of the transverse magnetization variance $G(0)|_t$ at $q_f = 2$ Hz, evaluated over the central $16 \times 124 \mu\text{m}$ region of the condensate and averaging over 8 experimental repetitions; error bars are statistical. The contribution to $G(0)|_t$ from imaging noise was subtracted from the data. Predictions from numerical calculations for $|\Delta a| = 1.45 a_B$ and $1.07 a_B$ are shown as black and gray lines, respectively.

amplification, over the central region of the condensate. As shown in Fig. 3, $G(0)|_t$ rises above our detection noise floor for $t \gtrsim 40$ ms. We consider the linear-amplification theory to be applicable for $t \leq 90$ ms, and, following Ref. [12], perform a least-squares fit to a function of the form

$$G(0)|_t = G(0)|_{t_m} \times \sqrt{t/t_m} e^{(t-t_m)/\tau} \quad (3)$$

Here τ is the time constant characterizing the growth rate of the magnetization variance and $t_m = 77$ ms.

To compare our measurements to the amplifier theory outlined above, we performed numerical calculations of $G(0)|_t$, taking into account the inhomogeneous density profile, dipolar interactions, and quantum fluctuations of the initial state [26]. We simulate the condensate dynamics using the Truncated Wigner Approximation (TWA), i.e., we evolve classical spin fluctuations, whose initial variance is quantum-limited in magnitude, according to the Gross-Pitaevskii equation. This treatment is exact in the linear amplification regime, and also provides an approximate description of non-linear behaviour associated with depletion of the $|m=0\rangle$ population and with inter-mode coupling. To solve the Gross-Pitaevskii equation numerically we employ a 6th order Runge-Kutta method with a time and position-space resolution of $3.5 \mu\text{s}$ and $0.5 \mu\text{m}$ respectively. In contrast to the linear homogeneous case, which has been previously studied using momentum-space spin excitation modes [12, 13], the nonlinear inhomogeneous case requires the use of proper position-space modes. Our calculations show the rate of growth of magnetization fluctuations to be smaller than that indicated by the maximum condensate density, owing to the inhomogeneous density profile of the trapped gas. The asymmetric trap potential also causes the calculated magnetization correlations to be stronger along the long axis of the trapping potential [27], a tendency that

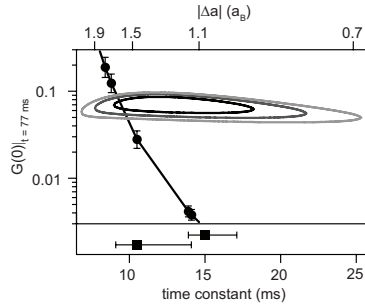


FIG. 4: The magnetization variance $G(0)|_{t_m}$ at $t_m = 77$ ms and exponential time constant τ of the amplifier, obtained by fitting data in Fig. 3 corresponding to $57 \leq t \leq 87$ ms, are indicated by contours of the 1, 2, and 3 σ confidence regions using a χ^2 test. Predictions from numerical calculations of the quantum amplification theory, assuming different values of $|\Delta a|$, are shown (circles and interpolating line). Error bars reflect systematic uncertainty in q_f and in the condensate density. Time constants corresponding to reported values for $|\Delta a|$ are indicated at bottom.

is supported by our observations (Fig. 1). For our experimental settings, the calculation indicates that dipolar interactions serve to increase slightly the time-constant and decrease the length scale which characterize the formation of transversely magnetized domains in the condensate.

From such simulations, we determined theoretical values for $G(0)|_t$ for several values of the scattering length difference Δa within the range of recent measurements [7, 24]. As shown in Figs. 3 and 4, our data are consistent with the quantum-limited amplification of zero-point quantum fluctuations in the case that $|\Delta a|$ lies in the upper range of its reported values. Alternatively, under the assumption that the observed amplification of spin fluctuations is quantum limited, taking the best-fit value of $\tau = 12$ ms, the variance of initial spin fluctuations in our paramagnetic sample is measured to be roughly five times larger than that of purely quantum fluctuations.

We performed several investigations to identify possible technical or thermal contributions to the spin fluctuations of our samples. A bound on such noise was obtained by performing a Stern-Gerlach analysis of populations N_{\pm} in the $|m_z = \pm 1\rangle$ states just after the quench. Our measurements were found to be insensitive to variations in the gradient strength, duration, and orientation used during the initial state preparation, and also to the delay (varied between 0 and 110 ms) between this preparation and the initiation of the spin amplifier. Obtaining $N_{\pm} \leq 3 \times 10^2$ and assuming an incoherent admixture of Zeeman sublevels, the thermal contribution to $G(0)|_0$ is below $(2N_{\pm}/N_0) = 3 \times 10^{-4}$. We checked also for techni-

cal noise that would induce extrinsic Zeeman transitions during the experiment. For the experimental conditions used for the measurements reported here, we found that a condensate starting in the $|m_z = -1\rangle$ state remained so for evolution times up to 400 ms following the quench, confirming the absence of noise-induced spin flips. For comparison, we also performed tests of the spin-mixing amplifier under experimental conditions in which noise-induced flips were indeed observed. Under these noisier conditions, the increased spin fluctuations input to the spin-mixing amplifier indeed yielded stronger magnetization outputs at early times following the quench.

Altogether, these results suggest that the state-purified paramagnetic samples were prepared with a near-zero spin temperature. Nevertheless, it remains uncertain whether the zero-temperature amplifier theory should remain accurate out to a gain in the magnetization variance as high as 30 dB, in a non-zero temperature gas subject to constant heating and evaporation from the finite-depth optical trap. Indeed, previous work showed a strong influence of the non-condensed gas on spin dynamics in a two-component gaseous mixture [28]. We examined the role of thermal effects by comparing the amplification of magnetization at kinetic temperatures of 50 and 85 nK, obtained for different optical trap depths. We observed no variation, but note that the condensate fraction was not substantially varied in this comparison.

As indicated by the experimental uncertainties presented in Fig. 4, the comparison between a quantum amplification theory and experimental observations could be further constrained by an independent measure of the amplifier gain. The theoretical value for the amplifier gain is uncertain as a result of the uncertainty in Δa . In a future study, one could empirically determine the gain of the amplifier by studying the amplification of a coherent seed at a given k , e.g. a finite k spin modulation produced by Raman scattering or a $k = 0$ seed produced by tipping the condensate spinor before the quench to $q \neq 0$.

In conclusion, we have demonstrated the use of the spinor condensate as an amplifier of magnetization. Two tests of the amplifier have been performed simultaneously. First, assuming the input to the amplifier to have a white spatial spectrum and an initial variance consistent with quantum noise, we measure the tunable spatial spectrum and gain of the amplifier and find good agreement with predictions of a quantum linear amplification theory. Second, assuming the amplifier to be described well by our theory, we find the magnitude and spatial distribution of magnetization fluctuations in the initial paramagnetic sample to be consistent with quantum noise. This demonstration of a low-noise spin amplifier holds promise for a host of applications and for future studies of quantum magnetism.

Moreover, by performing rapid quenches of paramagnetic condensates to variable q_f , we characterize the variation of the spin-mixing instability spectrum as one approaches the critical value of the quadratic shift, q_0 , from

below. As discussed in several theoretical works, the nature of this variation determines the dynamical scaling behaviour expected for variable-rate quenches across a phase transition between paramagnetic and ferromagnetic states [12, 13, 16, 17]. The observation that paramagnetic gases are prepared with near quantum-limited spin fluctuations supports the possibility of quantitative investigations of quantum phase transitions with spinor gases.

We acknowledge insightful discussions with J. Moore and S. Mukerjee and experimental assistance from C. Smallwood. This work was supported by the NSF, the David and Lucile Packard Foundation, DARPA's OLE Program. Partial personnel and equipment support was provided by the LDRD Program of LBNL under the Dept. of Energy Contract No. DE-AC02-05CH11231. S.R.L. acknowledges support from the NSERC.

-
- [1] T.-L. Ho, Phys. Rev. Lett. **81**, 742 (1998).
 - [2] T. Ohmi and K. Machida, J. Phys. Soc. Jpn. **67**, 1822 (1998).
 - [3] J. Stenger et al., Nature **396**, 345 (1998).
 - [4] H. Schmaljohann et al., Phys. Rev. Lett. **92**, 040402 (2004).
 - [5] M.-S. Chang et al., Phys. Rev. Lett. **92**, 140403 (2004).
 - [6] H.-J. Miesner et al., Phys. Rev. Lett. **82**, 2228 (1999).
 - [7] M.-S. Chang et al., Nature Physics **1**, 111 (2005).
 - [8] L. Sadler et al., Nature **443**, 312 (2006).
 - [9] M. Vengalattore, S.R. Leslie, J. Guzman, and D.M. Stamper-Kurn, Phys. Rev. Lett. **100**, 170403 (2008).
 - [10] M. Vengalattore et al., Phys. Rev. Lett. **98**, 200801 (2007).
 - [11] W. Zhang et al., Phys. Rev. Lett. **95**, 180403 (2005).
 - [12] A. Lamacraft, Phys. Rev. Lett. **98**, 160404 (2007).
 - [13] H. Saito, Y. Kawaguchi, and M. Ueda, Phys. Rev. A **75**, 013621 (2007).
 - [14] R. Movshovich et al., Phys. Rev. Lett. **65**, 1419 (1990).
 - [15] M. Mück, J. B. Kycia, and J. Clarke, App. Phys. Lett. **78**, 967 (2001).
 - [16] B. Damski and W. H. Zurek, Phys. Rev. Lett. **99**, 130402 (2007).
 - [17] M. Uhlmann, R. Schutzhold, and U. R. Fischer, Phys. Rev. Lett. **99**, 120407 (2007).
 - [18] H. Saito and M. Ueda, Phys. Rev. A **72**, 023610 (2005).
 - [19] G. I. Mias, N. R. Cooper, and S. M. Girvin, Phys. Rev. A **77**, 023616 (2008).
 - [20] E. van Kempen et al., Phys. Rev. Lett. **88**, 093201 (2002).
 - [21] F. Gerbier et al., Phys. Rev. A **73**, 041602(R) (2006).
 - [22] By comparing experiments with similar q_f but variable q_{μ} , the admixing of hyperfine levels produced by the applied microwave field was found not to influence the dynamics of the $F = 1$ gas.
 - [23] We measure also the longitudinal magnetization of the condensate, but find that it remains small ($< 15\%$ of the maximum magnetization).
 - [24] A. Widera et al., New Journal of Physics **8**, 152 (2006).
 - [25] I. Carusotto and E. J. Mueller, J. Phys. B **37**, S115 (2004).
 - [26] J.D. Sau et al., to be published.
 - [27] M. Baraban et al., arXiv:0807.1280.
 - [28] J. M. McGuirk, D. M. Harber, H. J. Lewandowski, and E. A. Cornell, Phys. Rev. Lett. **91**, 150402 (2003).

Appendix C

Spontaneously Modulated Spin Textures in a Dipolar Spinor Bose-Einstein Condensate

Spontaneously Modulated Spin Textures in a Dipolar Spinor Bose-Einstein Condensate

M. Vengalattore,¹ S.R. Leslie,¹ J. Guzman,¹ and D.M. Stamper-Kurn^{1,2}

¹Department of Physics, University of California, Berkeley, California 94720, USA

²Materials Sciences Division, Lawrence Berkeley National Laboratory, Berkeley, California 94720, USA
(Received 25 December 2007; revised manuscript received 18 February 2008; published 1 May 2008)

Helical spin textures in a ^{87}Rb $F = 1$ spinor Bose-Einstein condensate are found to decay spontaneously toward a spatially modulated structure of spin domains. The formation of this modulated phase is ascribed to magnetic dipolar interactions that energetically favor the short-wavelength domains over the long-wavelength spin helix. The reduction of dipolar interactions by a sequence of rf pulses results in a suppression of the modulated phase, thereby confirming the role of dipolar interactions in this process. This study demonstrates the significance of magnetic dipole interactions in degenerate ^{87}Rb $F = 1$ spinor gases.

DOI: 10.1103/PhysRevLett.100.170403

PACS numbers: 05.30.Jp, 03.75.Mn, 75.45.+j, 75.50.Mm

In a wide range of materials, the competition between short- and long-range interactions leads to a rich landscape of spatially modulated phases arising both in equilibrium and as instabilities in nonequilibrated systems [1,2]. In classically ordered systems such as magnetic thin films [3] and ferrofluids [4], short-range ferromagnetic interactions are commonly frustrated by the long-range, anisotropic magnetic dipolar interaction, rendering homogeneously magnetized systems intrinsically unstable to various morphologies of magnetic domains [5]. Long-range interactions are also key ingredients in many models of strongly correlated electronic systems [6] and frustrated quantum magnets [7].

In light of their relevance in materials science, strong dipole interactions have been discussed as an important tool for studies of many-body physics using quantum gases of atoms and molecules, offering the means for quantum computation [8], simulations of quantum magnetism [9] and the realization of supersolid or crystalline phases [10,11]. However, in most ultracold atomic gases, the magnetic dipolar interaction is dwarfed by the contact (s -wave) interaction. Hence, experimental efforts to attain dipolar quantum gases have focused on nonalkali atoms, notably ^{52}Cr with its large magnetic moment [12], and on polar molecules [13].

In this Letter, we demonstrate that magnetic dipole interactions play a critical role in the behavior of a quantum degenerate $F = 1$ spinor Bose gas of ^{87}Rb . In this quantum fluid, s -wave collisions yield both a spin-independent and a spin-dependent contact interaction [14,15], with strengths proportional to $\bar{a} = (2a_2 + a_0)/3$ and $\Delta a = (a_2 - a_0)/3$, respectively, where the scattering length a_F describes collisions between particles of total spin F . In ^{87}Rb , with $a_0(a_2) = 5.39(5.31)$ nm, the spin-dependent contact interaction is far weaker than the spin-independent one; nevertheless, it is a critical determinant of the magnetic properties of degenerate $F = 1$ ^{87}Rb gases [16–18]. The magnetic dipole interaction strength may be parameterized similarly by a length $a_d = \mu_0 g_F^2 \mu_B^2 m / (12\pi\hbar^2)$, where μ_0 is the permeability of vacuum, $g_F =$

$1/2$ the gyromagnetic ratio, μ_B the Bohr magneton and m the atomic mass [19]. Given $a_d/\Delta a = 0.4$, the $F = 1$ spinor Bose gas of ^{87}Rb is an essentially dipolar quantum fluid [20].

In our study, the influence of dipolar interactions on the spinor gas is evidenced by the spontaneous dissolution of deliberately imposed long-wavelength helical spin textures, in favor of a finely modulated pattern of spin domains. We ascribe the emergence of this modulated phase to the magnetic dipole energy that disfavors the homogeneously magnetized state and drives the fluid toward short-wavelength spin textures. To test this ascription, we reexamine the behavior of spin helices in condensates in which the dipolar interaction is tempered using a rapid sequence of rf pulses. The suppression of the modulated phase observed in this case confirms the crucial role of dipolar interactions.

For this work, spin-polarized ^{87}Rb condensates of up to $2.3(1) \times 10^6$ atoms in the $|F = 1, m_F = -1\rangle$ hyperfine state and at a kinetic temperature of $T \approx 50$ nK were confined in a single-beam optical dipole trap characterized by trap frequencies $(\omega_x, \omega_y, \omega_z) = 2\pi(39, 440, 4.2)$ s $^{-1}$. The Thomas-Fermi condensate radius in the \hat{y} (vertical) direction ($r_y = 1.8$ μm) was less than the spin healing length $\xi_S = (8\pi\Delta a n_0)^{-1/2} = 2.4$ μm , where $n_0 = 2.3 \times 10^{14}$ cm $^{-3}$ is the peak density of the condensate. This yields a spinor gas that is effectively two-dimensional with regard to spin dynamics.

The condensate was transversely magnetized by applying a $\pi/2$ rf pulse in the presence of an ambient magnetic field of $B_0 = 165(5)$ mG aligned to the \hat{z} axis. Stray magnetic gradients (curvatures) were canceled to less than 0.14 mG/cm (4.3 mG/cm 2). A helical spin texture was then prepared by applying a transient magnetic field gradient dB_z/dz for a period $\tau_p = 5$ –8 ms. Larmor precession of the atomic spins in this inhomogeneous field resulted in a spatial spin texture with a local dimensionless spin of $\mathbf{F} = \cos(\kappa z + \omega_L t)\hat{x} + \sin(\kappa z + \omega_L t)\hat{y}$, where $\vec{\kappa} = (g_F \mu_B / \hbar)(dB_z/dz)\tau_p \hat{z}$ is the helix wave vector. The

fast time variation at the $\omega_L/2\pi \approx 115$ kHz Larmor precession frequency will be henceforth ignored by considering the spin at a particular instant in this rapid evolution. The helix pitch $\lambda = 2\pi/\kappa$ ranged between 50 and 150 μm . Given $\lambda \gg \xi_S$, the kinetic energy per atom in this spin texture, $E_\kappa = \hbar^2 \kappa^2 / 4m$, was always negligible compared to the ferromagnetic contact-interaction energy [21].

The helical spin texture was then allowed to evolve in a homogenous magnetic field for a variable time before the vector magnetization was measured using a sequence of nondestructive phase contrast images. Because of Larmor precession, a sequence of images taken with circularly polarized light propagating along the \hat{y} direction can be analyzed to determine the column-integrated magnetization perpendicular to the ambient field [22,23], with vector components $\vec{M}_{x,y} = (g_F \mu_B) \bar{n} F_{x,y}$, where \bar{n} the column number density. Subsequent to this imaging sequence, a $\pi/2$ pulse was applied to rotate the longitudinal spin F_z into the transverse spin plane, and a second sequence of images was obtained. A least-squares algorithm comparing data from the two imaging sequences allowed the longitudinal magnetization M_z to be determined [24].

The evolution of helical textures is portrayed in Fig. 1. While uniform spin textures ($\lambda \gg 2r_z$) remain homogeneous for long times, helical textures ($\lambda < 2r_z$) spontaneously develop short-wavelength modulations of the magnetization. This modulated phase is characterized by spin domains with typical dimensions of ≈ 10 μm , much smaller than the pitch of the imprinted helix, with the magnetization varying sharply between adjacent domains.

To quantify this behavior, we considered the power spectrum of the spatial Fourier transform of the vector magnetization, $|\vec{M}(k_x, k_z)|^2$, where (k_x, k_z) is the spatial wave vector in the image plane. This spectrum was found to consist of two distinct components: a central component that quantifies the long-range order of the helical texture,

and a second concentration of spectral power at a discrete set of wave vectors of magnitude $k_{\text{mod}} \approx 2\pi/(10 \mu\text{m})$ representing the short-range order of the final modulated texture. After subtracting out the background representing image noise, we divided spatial Fourier space into regions indicated in Fig. 2 and defined the integrated spectral power in the central region (annular region) as the parameterization of long-range (short-range) spatial order in the quantum fluid.

The formation of the spontaneously modulated texture is reflected in the reduction of the long-range order parameter and the concomitant rise of the short-range order parameter (Fig. 3). During this process, the total spectral power was found to be roughly constant indicating that the bulk of the quantum fluid remains fully magnetized even as the long-range order is reduced. Further, the longitudinal magnetization M_z was found to be much smaller than $M_{x,y}$ throughout this process. The growth rate γ of the short-range order parameter determined from such data was found to rise monotonically with the wave vector κ of the initial helical texture. While the long-range order was found to decrease after sufficiently long evolution times even in condensates prepared with nearly uniform magnetization, we note that stray magnetic field inhomogeneities of ~ 5 μG across the axial length of the condensate would by themselves produce a helical winding across the condensate over a period of 300 ms, constraining our ability to test the stability of homogenous spin textures.

Another measure of the spontaneous short-range modulation in the condensate is the appearance of polar-core spin vortices throughout the gas. Such vortices were identified as in Ref. [18] by a net winding of the transverse magnetization along a closed two-dimensional path of nonzero magnetization in the imaged gas. The number of identified spin vortices was roughly proportional to the short-range order parameter, with no vortices identified in the initially prepared spin helix and up to 6 vortices/

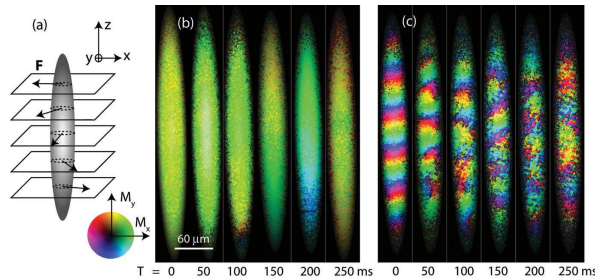


FIG. 1 (color). Spontaneous dissolution of helical textures in a quantum degenerate ^{87}Rb spinor Bose gas. A transient magnetic field gradient is used to prepare transversely magnetized (b) uniform or (a),(c) helical magnetization textures. The transverse magnetization column density after a variable time T of free evolution is shown in the imaged x - z plane, with orientation indicated by hue and amplitude by brightness (color wheel shown). (b) A uniform texture remains homogeneous for long evolution times, while (c) a helical texture with pitch $\lambda = 60$ μm dissolves over ~ 200 ms, evolving into a sharply spatially modulated texture.

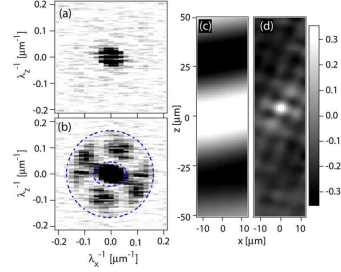


FIG. 2 (color online). Power spectrum of the spatial Fourier transform and the two-point correlation function $G(x, z)$ for the initial spin helix (a),(c) and the spontaneously modulated phase (b),(d). These data are derived from the same image sequence shown in Fig. 1(c). The images (a),(c) correspond to an evolution time $T = 0$ ms while (b),(d) correspond to an evolution time $T = 250$ ms. The short-range spatial order is defined as the integrated spectral power in the annular region shown in (b).

image identified in the strongly modulated texture produced after free evolution. In each instance, the number of vortices with positive and negative charge was found to be approximately equal.

A striking feature in the evolution of spin textures is the significant rise in the kinetic energy of the condensed atoms, reaching a value of $\hbar^2 k_{\text{mod}}^2 / 8m = \hbar \times 6$ Hz per atom given that roughly half the spectral weight of the texture's magnetization is at the wave vector k_{mod} . One expects the total energy per atom in the condensate to be constant during this evolution, or even to diminish through the transfer of energy to the noncondensed portion of the

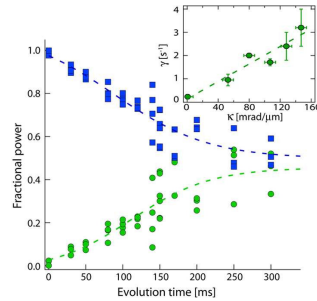


FIG. 3 (color online). Growth of the spontaneously modulated phase (●) coincides with a reduction in the integrated energy in the low spatial frequency region (■). The data shown correspond to an initial helical pitch of $60 \mu\text{m}$. Inset: The initial growth rate γ of the modulated phase as a function of the helix wave vector. These were extracted from linear fits of the short-range order parameter at short evolution times.

gas. Yet, in examining the energy of the initially prepared spin helix, we find the local contact-interaction energy is minimized, the quadratic Zeeman energy is just $q/2 = \hbar \times 1$ Hz at the ambient magnetic field, and the kinetic energy of the spin helix is just $E_k < \hbar \times 0.5$ Hz for a helix pitch of $\lambda > 50 \mu\text{m}$.

This apparent energetic deficit of the spin helix state can be accounted for by the magnetic dipole interaction. The on-axis magnetic field produced by a spin helix in an infinite axial column of gas with a Gaussian transverse density profile can be simply calculated. From this calculation, we estimate that a gas with uniform transverse magnetization possesses an excess of $E_d = \mu_0 g_F^2 \mu_B^2 n_0 / 2 \sim \hbar \times 5$ Hz compared to the energy of a tightly wound helix, a figure that is close to the excess kinetic energy of the finely modulated texture.

To confirm the role of magnetic dipolar interactions in the evolution of these spin textures, we employed a modification of the NMR technique of spin-flip narrowing [25] to eliminate effectively the dipolar interactions. The interaction energy of two magnetic dipoles separated by the displacement vector \mathbf{r} is proportional to $\mathbf{F}_1 \cdot \mathbf{F}_2 - 3(\hat{\mathbf{r}} \cdot \mathbf{F}_1)(\hat{\mathbf{r}} \cdot \mathbf{F}_2)$. If both dipoles experience rapid, common spin rotations that evenly sample the entire $SO(3)$ group of rotations, the interaction energy will average to zero regardless of the relative orientations of the spin vectors $\mathbf{F}_{1,2}$ and of the displacement vector \mathbf{r} . We note that such spin rotations also annul the quadratic Zeeman shift. However, since the nature of the spontaneously modulated phase was observed to be unchanged as q was varied over a factor of 5 ($0.8 < q/\hbar < 4$ Hz), we suggest this annulment is inconsequential.

Experimentally, after the initial spin texture had been prepared as before, we effected such spin rotations by applying a rapid sequence of $\pi/2$ rf pulses to the Larmor precessing atoms at random intervals, and thus, along random rotation axes, at a mean rate of 1–2 kHz. We confirmed that such a sequence of $\pi/2$ pulses led to an uniform sampling of the rotation group and that each pulse was spatially homogenous across the extent of the condensate. The spin helix was allowed to evolve under the constant action of these dipole-cancellation pulses until the pulses ceased and the sample was imaged as described earlier. In this case, the short-range order parameter grew at a similar rate at early evolution times, but reached a lower plateau at late times, demonstrating a suppression of the modulated phase (Fig. 4). The reduction of the excess kinetic energy of the final spin texture in the spin-rotation-averaged sample supports our identification of the dipole energy as its source.

To account for the residual (but weakened) appearance of short-length scale features in the power spectra [Fig. 4(b)], we note that this technique of spin-flip narrowing is most effective in the case of static dipoles. It is possible that motion of the gas, either coherent or thermal, prevents the $\pi/2$ pulse train from completely eliminating

Spontaneously Modulated Spin Textures in a Dipolar Spinor Bose-Einstein Condensate

M. Vengalattore,¹ S.R. Leslie,¹ J. Guzman,¹ and D.M. Stamper-Kurn^{1,2}¹Department of Physics, University of California, Berkeley, California 94720, USA²Materials Sciences Division, Lawrence Berkeley National Laboratory, Berkeley, California 94720, USA
(Received 25 December 2007; revised manuscript received 18 February 2008; published 1 May 2008)

Helical spin textures in a ^{87}Rb $F = 1$ spinor Bose-Einstein condensate are found to decay spontaneously toward a spatially modulated structure of spin domains. The formation of this modulated phase is ascribed to magnetic dipolar interactions that energetically favor the short-wavelength domains over the long-wavelength spin helix. The reduction of dipolar interactions by a sequence of rf pulses results in a suppression of the modulated phase, thereby confirming the role of dipolar interactions in this process. This study demonstrates the significance of magnetic dipole interactions in degenerate ^{87}Rb $F = 1$ spinor gases.

DOI: 10.1103/PhysRevLett.100.170403

PACS numbers: 05.30.Jp, 03.75.Mn, 75.45.+j, 75.50.Mm

In a wide range of materials, the competition between short- and long-range interactions leads to a rich landscape of spatially modulated phases arising both in equilibrium and as instabilities in nonequilibrated systems [1,2]. In classically ordered systems such as magnetic thin films [3] and ferrofluids [4], short-range ferromagnetic interactions are commonly frustrated by the long-range, anisotropic magnetic dipolar interaction, rendering homogeneously magnetized systems intrinsically unstable to various morphologies of magnetic domains [5]. Long-range interactions are also key ingredients in many models of strongly correlated electronic systems [6] and frustrated quantum magnets [7].

In light of their relevance in materials science, strong dipole interactions have been discussed as an important tool for studies of many-body physics using quantum gases of atoms and molecules, offering the means for quantum computation [8], simulations of quantum magnetism [9] and the realization of supersolid or crystalline phases [10,11]. However, in most ultracold atomic gases, the magnetic dipolar interaction is dwarfed by the contact (s -wave) interaction. Hence, experimental efforts to attain dipolar quantum gases have focused on nonalkali atoms, notably ^{52}Cr with its large magnetic moment [12], and on polar molecules [13].

In this Letter, we demonstrate that magnetic dipole interactions play a critical role in the behavior of a quantum degenerate $F = 1$ spinor Bose gas of ^{87}Rb . In this quantum fluid, s -wave collisions yield both a spin-independent and a spin-dependent contact interaction [14,15], with strengths proportional to $\bar{a} = (2a_2 + a_0)/3$ and $\Delta a = (a_2 - a_0)/3$, respectively, where the scattering length a_F describes collisions between particles of total spin F . In ^{87}Rb , with $a_0(a_2) = 5.39(5.31)$ nm, the spin-dependent contact interaction is far weaker than the spin-independent one; nevertheless, it is a critical determinant of the magnetic properties of degenerate $F = 1$ ^{87}Rb gases [16–18]. The magnetic dipole interaction strength may be parameterized similarly by a length $a_d = \mu_0 g_F^2 \mu_B^2 m / (12\pi\hbar^2)$, where μ_0 is the permeability of vacuum, $g_F =$

$1/2$ the gyromagnetic ratio, μ_B the Bohr magneton and m the atomic mass [19]. Given $a_d/\Delta a = 0.4$, the $F = 1$ spinor Bose gas of ^{87}Rb is an essentially dipolar quantum fluid [20].

In our study, the influence of dipolar interactions on the spinor gas is evidenced by the spontaneous dissolution of deliberately imposed long-wavelength helical spin textures, in favor of a finely modulated pattern of spin domains. We ascribe the emergence of this modulated phase to the magnetic dipole energy that disfavors the homogeneously magnetized state and drives the fluid toward short-wavelength spin textures. To test this ascription, we reexamine the behavior of spin helices in condensates in which the dipolar interaction is tempered using a rapid sequence of rf pulses. The suppression of the modulated phase observed in this case confirms the crucial role of dipolar interactions.

For this work, spin-polarized ^{87}Rb condensates of up to $2.3(1) \times 10^6$ atoms in the $|F = 1, m_F = -1\rangle$ hyperfine state and at a kinetic temperature of $T \approx 50$ nK were confined in a single-beam optical dipole trap characterized by trap frequencies $(\omega_x, \omega_y, \omega_z) = 2\pi(39, 440, 4.2)$ s $^{-1}$. The Thomas-Fermi condensate radius in the \hat{y} (vertical) direction ($r_y = 1.8$ μm) was less than the spin healing length $\xi_S = (8\pi\Delta a n_0)^{-1/2} = 2.4$ μm , where $n_0 = 2.3 \times 10^{14}$ cm $^{-3}$ is the peak density of the condensate. This yields a spinor gas that is effectively two-dimensional with regard to spin dynamics.

The condensate was transversely magnetized by applying a $\pi/2$ rf pulse in the presence of an ambient magnetic field of $B_0 = 165(5)$ mG aligned to the \hat{z} axis. Stray magnetic gradients (curvatures) were canceled to less than 0.14 mG/cm (4.3 mG/cm 2). A helical spin texture was then prepared by applying a transient magnetic field gradient dB_z/dz for a period $\tau_p = 5$ –8 ms. Larmor precession of the atomic spins in this inhomogeneous field resulted in a spatial spin texture with a local dimensionless spin of $\mathbf{F} = \cos(\kappa z + \omega_L t)\hat{x} + \sin(\kappa z + \omega_L t)\hat{y}$, where $\vec{\kappa} = (g_F \mu_B / \hbar)(dB_z/dz)\tau_p \hat{z}$ is the helix wave vector. The

Appendix D

Transmission spectrum of an optical cavity containing N atoms

PHYSICAL REVIEW A **69**, 043805 (2004)**Transmission spectrum of an optical cavity containing N atoms**Sabrina Leslie,^{1,2} Neil Shenvi,² Kenneth R. Brown,² Dan M. Stamper-Kurn,¹ and K. Birgitta Whaley²¹*Department of Physics, University of California, Berkeley, California 94720, USA*²*Department of Chemistry and Kenneth S. Pitzer Center for Theoretical Chemistry, University of California, Berkeley, California 94720, USA*

(Received 24 October 2003; published 6 April 2004)

The transmission spectrum of a high-finesse optical cavity containing an arbitrary number of trapped atoms is presented in the zero-temperature, low saturation limit. We take spatial and motional effects into account and show that in the limit of strong coupling, the important spectral features can be determined for an arbitrary number of atoms, N . We also show that these results have important ramifications in limiting our ability to determine the number of atoms in the cavity.

DOI: 10.1103/PhysRevA.69.043805

PACS number(s): 42.50.Pq

I. INTRODUCTION

Cavity quantum electrodynamics (CQED) in the strong-coupling regime holds great interest for experimentalists and theorists for many reasons [1–3]. From an applied perspective, CQED provides precise tools for the fabrication of devices which generate useful output states of light, as exemplified by the single-photon source [4–6], the N -photon source [7], and the optical phase gate [8]. Conversely, CQED effects transform the high-finesse cavity into a sensitive optical detector of objects which are in the cavity field. Viewed simply, standard optical microscopy is made more sensitive by having a probe beam pass through the sample multiple times and by efficiently collecting scattered light. In the weak-coupling regime, this has allowed for nanometer-resolution measurements of the positions of a trapped ion [9,10]. In the strong-coupling regime, the presence and position of single atoms can be detected with high sensitivity by monitoring the transmission [11,12], phase shift [13], or spatial mode [14] of probe light sent through the cavity.

In this paper, we consider using strong-coupling CQED effects to precisely count the number of atoms trapped inside a high-finesse optical microcavity. The principle for such detection is straightforward: the presence of atoms in the cavity field splits and shifts the cavity transmission resonance. A precise N -atom counter could be used to prepare the atoms-cavity system for generation of optical Fock states of large photon number [7], or to study ultracold gaseous atomic systems [15] in which atom number fluctuations are important, such as number-squeezed [16] and spin-squeezed [17–19] systems.

A crucial issue to address in considering such a CQED device is the role of the spatial distribution of atoms and their motion in the cavity field. An N -atom counter (or any CQED device) would be understood trivially if the N atoms to be counted were held at known, fixed positions in the cavity field. This is a central motivation for the integration of CQED with extremely strong traps for neutral atoms [20,21] or ions [9,10]. The Tavis-Cummings model [22], which applies to this case, predicts that the transmission spectrum of a cavity containing N identically coupled (with strength g), resonant atoms will be shifted from the empty cavity resonance by a frequency $g\sqrt{N}$ at low light levels. Atoms in a

cavity can then be counted by measuring the frequency shift of the maximum cavity transmission and distinguishing the transmission spectrum of N atoms from that of $N+1$ atoms in the cavity. However, to assess the potential for precise CQED-aided probing of a many-body atomic system, we consider here the possibility that atoms are confined at length scales comparable to or indeed larger than the optical wavelength.

In this paper, we characterize the influence of cavity mode spatial dependence and atomic motion on the transmission spectrum for an arbitrary number of atoms in the limit of low temperature, low light intensity, and low atomic recoil energy. The impact of atomic motion on CQED has been addressed theoretically in previous work [23–26], although attention has focused primarily on the simpler problem of a single atom in the cavity field. We show that when spatial dependence is included, the intrinsic limits on atom counting change significantly. The organization of this paper is as follows. In Sec. II we introduce the system Hamiltonian, define our notation, and derive an explicit expression for the intrinsic transmission function. In Sec. III, we introduce the method of moments, and use this method to calculate the shape of the intrinsic transmission function. Conclusions and implications for atom counting are presented in Sec. IV.

II. TRANSMISSION

Let us consider the Hamiltonian for N identical two-level atoms in a harmonic potential inside an optical cavity which admits a single standing-wave mode of light. We consider atomic motion and the spatial variation of the cavity mode only along the cavity axis, assuming that the atoms are confined tightly with respect to the cavity mode waist in the other two dimensions. The Hamiltonian for this system is

$$H = \hbar\omega_c a^\dagger a + \sum_{i=1}^N \hbar\omega_a |e_i\rangle\langle e_i| + H_0 + V, \quad (1)$$

where ω_c is the frequency of the cavity mode and $a(a^\dagger)$ is the annihilation (creation) operator for the cavity field. The motional Hamiltonian $H_0 = \sum_i H_{0,i}$ is a sum over single-atom Hamiltonians $H_{0,i} = p_i^2/2m + m\omega_0^2 x_i^2/2$, where m is the atomic

mass and ω_0 the harmonic trap frequency. The atomic ground and excited internal states, $|g\rangle$ and $|e\rangle$, respectively, are separated by energy $\hbar\omega_a$. The dipole interaction with the light field $V = \sum_i V_i$ is a sum over interactions with the dipole moment of each atom $V_i = \hbar g \cos(kx_i)(|e_i\rangle\langle g_i|a + |g_i\rangle\langle e_i|a^\dagger)$, where g is the vacuum Rabi splitting, which depends on the atomic dipole moment and the volume of the cavity mode. In this paper we assume the cavity mode frequency to be in exact resonance with the atomic transition frequency, $\omega_c = \omega_a$.

Since the Hamiltonian [Eq. (1)] commutes with the total excitation operator, $n_T = a^\dagger a + \sum_i |e_i\rangle\langle e_i|$, the eigenspectrum of H breaks up into manifolds labeled by their total excitation number. In this work, we are concerned with excitation spectra of the atoms-cavity system at the limit of low light intensity, and we therefore restrict our treatment to the lowest two manifolds, with $n_T = \{0, 1\}$.

We consider here the excitation spectra from the ground state (motional and internal) of the atoms-cavity system. This represents the simplest system that can be treated analytically and provides a basis for more realistic treatments of the initial state. In practice, scattering of a few photons or finite temperatures would excite the system to a higher motional state. These effects can be minimized experimentally by working at low light intensity (highest signal to noise per spontaneously emitted photon) and low temperature. The initial state $|\Psi_0\rangle$ is given simply as a product of motional and internal states, $|\Psi_0\rangle = |\Phi_0\rangle \otimes |0_c; g_1, g_2, \dots, g_N\rangle$. In the uncoupled internal-state notation, the 0_c symbol indicates there are zero photons in the cavity and the g_i symbol indicates that atom i is in the ground state. The motional state $|\Phi_0\rangle = \prod_{i=1}^N |\phi_0(x_i)\rangle$ is a product of single-atom ground states of the harmonic trap.

Let us calculate the low light intensity transmission spectrum of the cavity. We assume that the system is pumped by a near-resonant linearly coupled driving field such that the cavity excitation Hamiltonian is $H_I = E(a^\dagger e^{-i\omega t} + a e^{i\omega t})$, where E is the product of the external driving electric-field strength and the transmissivity of the input cavity mirror and ω is the driving frequency. To determine the cavity transmission spectrum, we determine the excitation rate to atoms-cavity states in the $n_T = 1$ manifold from the initial ground state. The atoms-cavity eigenstates decay either by cavity emission, with the transmitted optical power proportional to $\kappa\langle N_c \rangle$, where κ is the cavity decay rate and $N_c = a^\dagger a$ is the intracavity photon number operator, or by other processes (spontaneous emission, losses at the mirrors, etc.) at the phenomenological rate constant γ . Neglecting the width of the transmission spectrum caused by cavity and atomic decay ($\kappa, \gamma \rightarrow 0$), we use Fermi's golden rule to obtain the transmission spectrum $I(\omega)$:

$$\begin{aligned} I(\omega) &= \sum_{j, n_T=1} |\langle \Psi_j | a^\dagger | \Psi_0 \rangle|^2 \delta(\omega_j - \omega_0 - \omega) \\ &= \sum_{j, n_T=1} |\langle \Psi_j | \Psi_0 \rangle|^2 \delta(\omega_j - \omega_0 - \omega), \end{aligned} \quad (2)$$

where $|\Psi_0\rangle = a^\dagger |\Psi_0\rangle$. In the summation over all atoms-cavity eigenstates, we make the simplification that only states with

$n_T = 1$ need be included since only these states are coupled to the ground state by a single excitation. To simplify notation, we make this implicit assumption throughout the remainder of this paper. We denote by $I(\omega)$ the "intrinsic transmission spectrum." In the limit of $\kappa, \gamma \rightarrow 0$ this is composed of δ functions in frequency, while an experimentally observed transmission spectrum would be convolved by nonzero linewidths.

To proceed further, we introduce the basis states $\{|0\rangle; |i\rangle\}$ which span the space of *internal states* in the $n_T = 1$ manifold. The state $|0\rangle = |1_c; g_0, g_1, \dots, g_N\rangle$ has one cavity photon and all atoms in their ground state. The state $|i\rangle = |0_c; g_0, g_1, \dots, e_i, \dots, g_N\rangle$ is the state in which the cavity field is empty, while a single atom (atom i) is in the excited state. Restricted to the $n_T = 1$ manifold, the Hamiltonian [Eq. (1)] is written as $H = H_0 + V_{n_T=1}$, where

$$V_{n_T=1} = \sum_i \hbar g \cos(kx_i) \otimes (|i\rangle\langle 0| + |0\rangle\langle i|). \quad (3)$$

To gain intuition regarding the behavior of the system, let us define the operator $V(\mathbf{x})$ as the optical potential operator $V_{n_T=1}$ for which the position operators are replaced by definite positions \mathbf{x} . In the $(N+1)$ -dimensional space of internal states for the $n_T = 1$ manifold, the operator $V(\mathbf{x})$ has two non-zero eigenvalues, $\pm \hbar g \chi(\mathbf{x}) = \pm \hbar g \sqrt{\sum_i \cos^2 kx_i}$ with corresponding eigenstates

$$|D_\pm(\mathbf{x})\rangle = \frac{1}{\sqrt{2}} \left(|0\rangle \pm \frac{1}{\chi(\mathbf{x})} \sum_i \cos kx_i |i\rangle \right). \quad (4)$$

We will refer to the $|D_-(\mathbf{x})\rangle$ and $|D_+(\mathbf{x})\rangle$ eigenstates of the potential matrix as the red and blue internal states, respectively, in reference to their energies being red or blue detuned from the empty cavity resonance. The remaining $N-1$ eigenvalues of the optical potential matrix are null valued. These correspond to dark states having no overlap with the excited cavity internal state, $|0\rangle$, and which, therefore, cannot be excited by the cavity excitation interaction H_I . Note that $\langle N_c \rangle = 1/2\langle 0|$ for all bright (dark) states, hence the cavity transmission spectrum is equivalent to the excitation spectrum in this treatment. We can now write the optical potential operator $V_{n_T=1}$ as

$$\begin{aligned} V_{n_T=1} &= g \int d\mathbf{x} \chi(\mathbf{x}) |\mathbf{x}\rangle\langle \mathbf{x}| \otimes (|D_+(\mathbf{x})\rangle\langle D_+(\mathbf{x})| \\ &\quad - |D_-(\mathbf{x})\rangle\langle D_-(\mathbf{x})|). \end{aligned} \quad (5)$$

We also note that the initial state $|\Psi_0\rangle$ can be written as a superposition of bright states,

$$|\Psi_0\rangle = \frac{1}{\sqrt{2}} (|\phi_+(\mathbf{x}) \otimes D_-(\mathbf{x})\rangle + |\phi_-(\mathbf{x}) \otimes D_+(\mathbf{x})\rangle). \quad (6)$$

Our treatment allows us to recover easily results of the Tavis-Cummings model [22] in which a collection of fixed two-level atoms are coupled to a single-mode cavity with fixed, identical dipole coupling. Considering $V(\mathbf{x}_0)$ with all atoms at the origin $[\mathbf{x}_0 = (0, 0, \dots, 0)]$, we find a spectrum

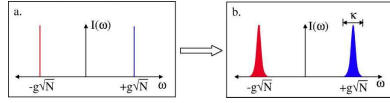


FIG. 1. (a) Intrinsic transmission spectrum of atoms-cavity system neglecting spatial dependence of potential and atomic motion. (b) Transmission spectrum of spatially independent case including cavity decay.

composed of δ functions at $\pm g\sqrt{N}$ [see Fig. 1(a)] corresponding to the two bright states $|D_{\pm}(\mathbf{x}_0)\rangle$. The clear dependence of the frequency of peak transmission on the integer number of atoms in the cavity provides the background for a basic, transmission-based atom-counting scheme. “Extrinsic” line broadening, due to cavity decay and other losses, will smear out these sharp transmission peaks [see Fig. 1(b)], and will determine the maximum number of atoms that can be counted at the single-atom level by discriminating between the transmission spectra for N and $N+1$ atoms. For the remainder of the paper, we focus on intrinsic limitations to atom counting, i.e., those due to atomic localization and motion.

III. METHOD OF MOMENTS

To analyze the transmission characteristics of the atoms-cavity system in the presence of spatial dependence and atomic motion, we shall assume that the key features of the spatially independent limit discussed above are maintained (Fig. 2). Specifically, the transmission spectrum will still be described by two sidebands, one red shifted and one blue shifted from the empty cavity resonance by some frequency on the order of g . In determining the cavity transmission $I(\omega)$, we may thus divide the bright excited states $\{|\Psi_j\rangle\}$ of the $n_T=1$ manifold into red $\{|\Psi_{j,-}\rangle\}$ and blue $\{|\Psi_{j,+}\rangle\}$ states. From these red and blue states, we determine the transmission line shapes $L_-(\omega)$ and $L_+(\omega)$ of the red and blue sidebands, respectively.

The validity of this approach is made more exact by the following considerations. We have already obtained the locally defined internal-state eigenbasis for the $n_T=1$ manifold as eigenstates of the operator $V(\mathbf{x})$, namely, the states $|D_{\pm}(\mathbf{x})\rangle$ and the remaining $N-1$ dark states. Let $\hat{U}(\mathbf{x})$ be the rotation operator which connects the uncoupled internal states $\{|0\rangle, |1\rangle, \dots, |N\rangle\}$ to the eigenstates of $V(\mathbf{x})$ at a particular set of coordinates \mathbf{x} (the “coupled internal-state basis”). Now, consider applying this local choice of “gauge” everywhere in

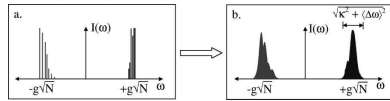


FIG. 2. (a) Intrinsic transmission spectrum of atoms-cavity system including spatial dependence of potential and atomic motion. (b) Corresponding transmission spectrum including cavity decay.

the system. Since the dipole interaction operator V is diagonalized in the coupled internal-state basis, it is convenient to examine the full Hamiltonian H in this basis. Defining the spatially dependent rotation operator $\hat{U} = \int d\mathbf{x} |\mathbf{x}\rangle \langle \mathbf{x}| \hat{U}(\mathbf{x})$, we therefore consider the transformed Hamiltonian $H' = \hat{U} H \hat{U}^\dagger$.

Returning to Eq. (1), the only portion of the Hamiltonian H which does not commute with the operator \hat{U} is the kinetic energy. Considering the transformation of the momentum operator for atom i ,

$$\hat{U} p_i \hat{U}^\dagger = p_i + \frac{\hbar}{i} \hat{U} \frac{d}{dx_i} \hat{U}^\dagger = p_i + A_i \quad (7)$$

the transformed Hamiltonian H' can be expressed as $H' = H_{ad} + \Delta H$, where

$$H_{ad} = \sum_i \left(\frac{p_i^2}{2m} \otimes \mathcal{I} + \frac{1}{2} m \omega_0^2 x_i^2 \otimes \mathcal{I} \right) + \hbar g \chi(\mathbf{x}) |D_+\rangle \langle D_+| - |D_-\rangle \langle D_-|, \quad (8)$$

$$\Delta H = \frac{1}{2m} \sum_i (p_i A_i + A_i p_i + A_i^2). \quad (9)$$

The operator H_{ad} describes the behavior of atoms which adiabatically follow the coupled internal-state basis while moving through the spatially varying cavity field and ΔH represents the kinetic energy associated with this local gauge definition.

We assume we are working in the limit of small atomic recoil energy, i.e., $\hbar g \gg \hbar^2 k^2 / 2m$, and therefore treat ΔH as a perturbation and expand the eigenvalues and eigenstates of H' as

$$E_{j,\pm} = E_{j,\pm}^{(0)} + E_{j,\pm}^{(1)} + \dots, \quad (10)$$

$$|\Psi_{j,\pm}\rangle = |\Psi_{j,\pm}^{(0)}\rangle + |\Psi_{j,\pm}^{(1)}\rangle + \dots \quad (11)$$

We define projection operators onto the red and blue and dark internal states, Π_-, Π_+, Π_d , respectively, with the explicit forms

$$\Pi_{\pm} = \int d\mathbf{x} |\mathbf{x}\rangle \langle \mathbf{x}| \otimes |D_{\pm}(\mathbf{x})\rangle \langle D_{\pm}(\mathbf{x})|. \quad (12)$$

These projection operators commute with H_{ad} . Hence the bright eigenstates of H_{ad} , which are simultaneous eigenstates of Π_{\pm} and Π_d , can be written as

$$|\Psi_{j,\pm}^{(0)}\rangle = |\phi_{j,\pm}^{(0)}\rangle \otimes |D_{\pm}\rangle = \int d\mathbf{x} \phi_{j,\pm}^{(0)}(\mathbf{x}) |\mathbf{x}\rangle \otimes |D_{\pm}(\mathbf{x})\rangle. \quad (13)$$

We now assign an eigenstate, $|\Psi_j\rangle$, of H' to the red or blue sideband if its zeroth-order component $|\Psi_j^{(0)}\rangle$ belongs, respectively, to the $|D_-\rangle$ or $|D_+\rangle$ manifold. We can therefore define the sideband transmission spectra $I_{\pm}(\omega)$ as the separate contributions of red/blue sideband states to the total transmission spectra [see Eq. (2)]:

$$I_{\pm}(\omega) \propto \sum_j |\langle \Psi_{j,\pm} | \Psi \rangle|^2 \delta(\omega_{j,\pm} - \omega_0 - \omega). \quad (14)$$

Determining the exact form of $I_{\pm}(\omega)$ is equivalent to solving for all the eigenvalues $\hbar\omega_{j,\pm}$ of the full Hamiltonian. This is a difficult problem, particularly as the number of atoms in the cavity increases. In practice, given the potential extrinsic line-broadening effects which may preclude the resolution of individual spectral lines, it may suffice to simply characterize the main features of the transmission spectra. As we show below, general expressions for the various moments of the spectral line can be obtained readily as a perturbation expansion in ΔH . These moments allow one to assess the feasibility of precisely counting the number of atoms contained in the high-finesse cavity based on the transmission spectrum.

In general, we evaluate averages $\langle \omega_{\pm}^n \rangle$ weighted by the transmission spectral distributions $I_{\pm}(\omega)$. We make use of the straightforward identification (for notational clarity, shown here explicitly for the case of the blue sideband)

$$\hbar\langle \omega_+ \rangle = \frac{\hbar \int d\omega I_+(\omega) \omega}{\int d\omega I_+(\omega)} \quad (15)$$

$$= \frac{\sum_j E_{j,+} \langle \Psi_j | \Psi_{j,+} \rangle \langle \Psi_{j,+} | \Psi \rangle}{\sum_j \langle \Psi_j | \Psi_{j,+} \rangle \langle \Psi_{j,+} | \Psi \rangle} \quad (16)$$

$$= \frac{\sum_j E_{j,+} \langle \Psi_j | (\Pi_+ + \Pi_-) | \Psi_{j,+} \rangle \langle \Psi_{j,+} | (\Pi_+ + \Pi_-) | \Psi \rangle}{\sum_j \langle \Psi_j | (\Pi_+ + \Pi_-) | \Psi_{j,+} \rangle \langle \Psi_{j,+} | (\Pi_+ + \Pi_-) | \Psi \rangle}, \quad (17)$$

where we have made use of the facts that $\Pi_+ + \Pi_- + \Pi_d = I$ and $\Pi_d | \Psi \rangle = 0$. To zeroth order, Eq. (15) becomes

$$\hbar\langle \omega_+ \rangle^{(0)} = \frac{\sum_j E_{j,+}^{(0)} \langle \Psi_j | \Psi_{j,+}^{(0)} \rangle \langle \Psi_{j,+}^{(0)} | \Psi \rangle}{\sum_j \langle \Psi_j | \Psi_{j,+}^{(0)} \rangle \langle \Psi_{j,+}^{(0)} | \Psi \rangle} = 2 \langle \Psi_j | \Pi_+ H_{ad} \Pi_+ | \Psi \rangle. \quad (18)$$

The first-order correction to this result is given by,

$$\begin{aligned} \hbar\langle \omega_+ \rangle^{(1)} = & 2(\langle \Psi_j | \Pi_+ \Delta H \Pi_+ | \Psi \rangle + \langle \Psi_j | \Pi_- \sum_j E_{j,+}^{(0)} \langle \Psi_j^{(1)} | \Psi_{j,+}^{(0)} \rangle \langle \Psi_{j,+}^{(0)} | \Pi_+ | \Psi \rangle + \langle \Psi_j | \Pi_+ \sum_j E_{j,+}^{(0)} \langle \Psi_j^{(0)} | \Psi_{j,+}^{(1)} \rangle \langle \Psi_{j,+}^{(1)} | \Pi_- | \Psi \rangle) \\ & - 4 \langle \Psi_j | \Pi_+ H_{ad} \Pi_+ | \Psi \rangle (\langle \Psi_j | \Pi_- \sum_j \langle \Psi_j^{(1)} | \Psi_{j,+}^{(0)} \rangle \langle \Psi_{j,+}^{(0)} | \Pi_+ | \Psi \rangle + \langle \Psi_j | \Pi_+ \sum_j \langle \Psi_j^{(0)} | \Psi_{j,+}^{(1)} \rangle \langle \Psi_{j,+}^{(1)} | \Pi_- | \Psi \rangle). \end{aligned} \quad (19)$$

To evaluate the sums over the first-order corrections to the eigenstates, $|\Psi_j^{(1)}\rangle$, we approximate the energy denominator in the first-order perturbation correction as the difference between the average energies of the red and blue sidebands,

$$\begin{aligned} & \langle \Psi_j | \Pi_- \sum_j |\Psi_j^{(1)}\rangle \langle \Psi_{j,+}^{(0)} | \Pi_+ | \Psi \rangle \\ &= \langle \Psi_j | \sum_j \sum_k \frac{|\Psi_k^{(0)}\rangle \langle \Psi_k^{(0)} | \Delta H | \Psi_{j,+}^{(0)} \rangle}{\hbar\omega_{j,+}^{(0)} - \hbar\omega_{k,-}^{(0)}} \langle \Psi_{j,+}^{(0)} | \Pi_+ | \Psi \rangle, \end{aligned} \quad (20)$$

$$\approx \frac{1}{\langle \hbar\omega_+^{(0)} \rangle - \langle \hbar\omega_-^{(0)} \rangle} \langle \Psi_j | \Pi_- \Delta H \Pi_+ | \Psi \rangle. \quad (21)$$

It is valid to approximate the denominator by the difference between the average energies of the red and blue sidebands when the eigenstates in the different sidebands are well separated in energy. In the exceptional case in which ω_0 is sufficiently large, some states in the $|D_+(\mathbf{x})\rangle$ (red) manifold may have high motional contributions to their energy which cause their energy to be comparable with states in the $|D_-(\mathbf{x})\rangle$ (blue) manifold. However such states will have negligible overlap with the initial state and therefore should not contribute to Eq. (20). Using this approximation, we can evaluate Eq. (15) to first order in the perturbation, yielding

$$\begin{aligned} \hbar\langle \omega_+ \rangle = & 2 \langle \Pi_+ H \Pi_+ \rangle + \frac{1}{\langle \hbar\omega_+^{(0)} \rangle - \langle \hbar\omega_-^{(0)} \rangle} (4 \langle \Pi_+ H_{ad} \Delta H \Pi_- \rangle \\ & - 8 \langle \Pi_+ H_{ad} \Pi_+ \rangle \langle \Pi_- \Delta H \Pi_+ \rangle), \end{aligned} \quad (22)$$

where all expectation values are calculated over the initial

state $|\Psi_I\rangle$. We can also calculate the second moment of the distribution using the same technique. To first-order, we obtain

$$\begin{aligned} \hbar^2 \langle \omega_+^2 \rangle &= 2 \langle \Pi_+ (H_{ad}^2 + \Delta H H_{ad} + H_{ad} \Delta H) \Pi_+ \rangle \\ &+ \frac{1}{\langle \hbar \omega_+^{(0)} \rangle - \langle \hbar \omega_-^{(0)} \rangle} (4 \langle \Pi_+ H_{ad}^2 \Delta H \Pi_- \rangle \\ &- 8 \langle \Pi_+ H_{ad}^2 \Pi_+ \rangle \langle \Pi_- \Delta H \Pi_+ \rangle). \end{aligned} \quad (23)$$

In order to evaluate these expressions, we must calculate expectation values of the form $\Pi^\pm H_{ad}^k \Delta H^l \Pi^\pm$ over the initial state $|\Psi_I\rangle$. To simplify matters, we note that we can act with the projection operators on the initial state $|\Psi_I\rangle$, which is equivalent to operating in the $|D_\pm\rangle$ internal-state basis. Since H_{ad} is diagonal in the $|D_\pm\rangle$ basis, and $\phi_I(\mathbf{x})$ is the N -dimensional harmonic-oscillator ground state, it is straightforward to obtain

$$H_{ad} \phi_I(\mathbf{x}) |D_\pm\rangle = [E_0 \pm \hbar g \chi(\mathbf{x})] \phi_I(\mathbf{x}) |D_\pm\rangle. \quad (24)$$

Using the definition in Eq. (9), we find that the $|D_\pm\rangle$ matrix elements of ΔH are given by the matrix

$$\Delta H = \frac{\hbar^2 k^2 \zeta(\mathbf{x})}{4m} \otimes \begin{pmatrix} 1 & -1 \\ -1 & 1 \end{pmatrix}, \quad (25)$$

where we have defined

$$\zeta(\mathbf{x}) = -\frac{N-1}{\chi^2} + 1 - \sum_{i=1}^N \frac{\cos^4(kx_i)}{\chi^4}. \quad (26)$$

Combining Eqs. (22) and (23) with Eqs. (24) and (25), we obtain to first order in ΔH ,

$$\begin{aligned} \hbar \langle \omega_+ \rangle - E_0 &= \hbar g \langle \chi \rangle + \frac{1}{2} \frac{\hbar^2 k^2}{2m} \langle \zeta \rangle + \frac{1}{2} \frac{\hbar^2 k^2}{2m} \frac{1}{\langle \chi \rangle} \\ &\times (-\langle \zeta \chi \rangle + \langle \zeta \rangle \langle \chi \rangle), \end{aligned} \quad (27)$$

$$\begin{aligned} \hbar^2 (\langle \omega_+^2 \rangle - \langle \omega_+ \rangle^2) &= \hbar^2 g^2 (\langle \chi^2 \rangle - \langle \chi \rangle^2) + \hbar g \frac{\hbar^2 k^2}{2m} \left(\frac{1}{\langle \chi \rangle} (\langle \zeta \chi^2 \rangle \right. \\ &\left. + \langle \zeta \rangle \langle \chi^2 \rangle) - 2 \langle \zeta \rangle \langle \chi \rangle \right). \end{aligned} \quad (28)$$

Here all expectation values are taken over the spatial state $\phi_I(\mathbf{x})$. Although the function $\phi_I(\mathbf{x})$ is simply the product of N harmonic-oscillator ground states, the presence of various powers of $\chi(\mathbf{x})$ and $\zeta(\mathbf{x})$ in the above expectation values makes their analytic evaluation very difficult for arbitrary N . To determine the dependence of these integrals on atom number N , one may expand the integrand as a Taylor series in χ^2 , leading to approximate analytic solutions for the integral as a series in $1/N$. After some tedious algebra, we find the average positions of the red- and blue-transmission sidebands to be

$$\begin{aligned} \hbar \langle \omega_\pm \rangle - E_0 &= \pm \hbar g \sqrt{N} \sqrt{\frac{1+\epsilon}{2}} \left(1 - \frac{1}{N} \frac{(1-\epsilon)^2}{16} \right) \\ &- \frac{\hbar^2 k^2}{2m} \left(\frac{1-\epsilon}{2(1+\epsilon)} \right) + O\left(\frac{1}{N}\right). \end{aligned} \quad (29)$$

Here we quantify the relative length scales of the initial harmonic trap as compared to the optical interaction potential through the parameter $\epsilon = \exp(-k^2 \sigma^2)$, which is related to the Lamb-Dicke parameter η by $\sqrt{2} \eta = k \sigma$ and $\sigma = \sqrt{\hbar/m\omega_0}$. Note that we recover the zeroth-order result that the sideband expectation value scales as $\sqrt{N}g$.

Next, we obtain an expression for the width of the red and blue sidebands by evaluating the second moment of the sidebands. Expanding Eq. (28) as a series in $1/N$, we obtain

$$\begin{aligned} \hbar^2 (\langle \omega_\pm^2 \rangle - \langle \omega_\pm \rangle^2) &= \frac{1}{16} \hbar^2 g^2 (1-\epsilon)^2 (1+\epsilon) \\ &\pm \hbar g \frac{\hbar^2 k^2}{2m} \frac{1}{4\sqrt{N}\sqrt{2(1+\epsilon)}} \\ &\times (1-\epsilon)^2 (3+\epsilon) + O\left(\frac{1}{N}\right). \end{aligned} \quad (30)$$

To gain some physical insight into these results, we consider two important regimes: the tight- and loose-trap regimes. These different regimes are reflected in the corresponding values of the parameter ϵ , which tends towards 1 in the extreme tight-trap limit and to 0 in the extreme loose-trap limit. In the tight regime, the length scale of the trapping potential is much smaller than the wavelength of the light, i.e., $k\sigma \ll 1$. This is equivalent to the Lamb-Dicke regime and is applicable to current experiments for trapped ions in cavities [9,10], or for neutral atoms held in deep optical potentials [20]. In the loose-trap regime, $k\sigma \gg 1$ and atoms in the ground state of the harmonic-oscillator potential are spread out over a distance comparable to the optical wavelength. As atoms in this regime sample broadly the cavity field, one expects, and indeed finds, a significant inhomogeneous broadening of the atoms-cavity resonance.

In the extreme loose-trap limit ($\epsilon \rightarrow 0$), we find

$$\langle \omega_\pm \rangle - E_0/\hbar = \pm g \sqrt{\frac{N}{2}} \left(1 - \frac{1}{16N} \right) + \frac{1}{2} \frac{\hbar k^2}{2m} + O\left(\frac{1}{N}\right), \quad (31)$$

$$\langle (\Delta \omega_\pm)^2 \rangle = \frac{1}{8} g^2 \pm g \frac{\hbar k^2}{2m} \frac{3}{4\sqrt{2N}} + O\left(\frac{1}{N}\right). \quad (32)$$

In the loose-trap limit, the center of the red sideband is now located at $g\sqrt{N}/2$ instead of at $g\sqrt{N}$ as we obtained for the spatially independent case. This difference is due to the spatial dependence of the standing mode; the atoms no longer always feel the full strength of the potential, but are sometimes located at nodes of the potential. We also see that the sidebands have an intrinsic width of $\approx g/\sqrt{8}$. This width will play an important part in limiting our

ability to count the number of atoms in the cavity in the limit of a loose trap.

Considering the tight-trap limit, we expand in the small parameter $k\sigma$ and obtain

$$\langle\omega_{\pm}\rangle - E_0/\hbar = \pm g\sqrt{N}\left(1 - \frac{1}{4}k^2\sigma^2\right) - \frac{1}{4}\frac{\hbar k^2}{2m}k^2\sigma^2 + O(k^4\sigma^4), \quad (33)$$

$$\langle(\Delta\omega_{\pm})^2\rangle = \frac{1}{8}g^2k^4\sigma^4 \pm g\frac{\hbar k^2}{2m}\frac{1}{2\sqrt{N}}k^4\sigma^4 + O(k^6\sigma^6). \quad (34)$$

In the limit $k\sigma \rightarrow 0$, the atoms are confined to the origin and we recover the Tavis-Cummings result discussed earlier, wherein the transmission sidebands are δ functions at $\pm g\sqrt{N}$ away from the empty cavity resonance. As the tightness of the trap decreases, the atoms begin to experience the weaker regions of the optical potential and the centers of the sidebands move towards the origin. In addition, the sidebands develop an intrinsic variance which scales as $k^4\sigma^4$.

An important feature of both regimes is the intrinsic linewidth of both the red and blue sidebands [see Fig. 2(a)]. This linewidth has a magnitude of approximately $g\sqrt{(1-\epsilon)}/8$ when the vacuum Rabi splitting is much larger than the atomic recoil energy, i.e., $g \gg \hbar k^2/2m$. It is unrelated to linewidth due to cavity decay or spontaneous emission which we have not addressed here and results purely from the spatial dependence of the atom-cavity coupling. Thus, it will provide an intrinsic limit to our ability to count N atoms, regardless of the quality of the cavity that is used. Our expression for the intrinsic linewidth also highlights an asymmetry between the red and blue sidebands. To first order, increasing the atomic recoil energy *reduces* the linewidth of the red sideband but increases the linewidth of the blue sideband. Consequently probing the red sideband of the atoms-cavity system rather than the blue sideband would facilitate counting atoms. In addition, these results suggest that the ability to tune both the atomic recoil energy $\hbar k^2/2m$ and the coupling strength g (this can be done, for instance, using CQED on Raman transitions) would be beneficial. We attribute the asymmetry between the sidebands to the different effective potentials seen by states within the red and blue sidebands. A detailed analysis of this aspect will be provided in a future publication.

IV. CONCLUSIONS

We have found that the transmission spectrum of the cavity containing N atoms trapped initially in the ground state of a harmonic potential will consist of distinct transmission sidebands which are red and blue detuned from the bare-cavity resonance, when the vacuum Rabi splitting dominates the atomic recoil energy. Analytic expressions for the first and second moments of the transmission sidebands were derived, and evaluated in the limits of tight and loose initial confinement. These expressions include terms containing the vacuum Rabi splitting $\hbar g$ and the recoil energy $\hbar^2 k^2/2m$. The former can be regarded as line shifts and broadenings obtained by quantifying inhomogeneous broadening under a

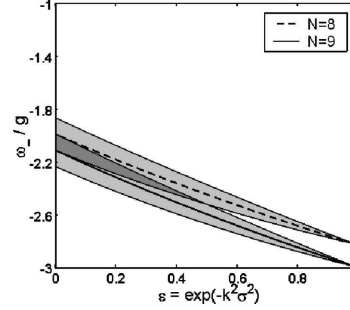


FIG. 3. Plot of $\langle\omega_{\pm}\rangle$ as a function of the trap tightness $\epsilon = \exp(-k^2\sigma^2)$ for $N=8$ and $N=9$ and small ratio of atomic recoil energy to vacuum Rabi splitting, $\hbar k^2/2mg=0.01$. The shaded regions indicate the intrinsic width of the red sideband, $\pm\sqrt{\langle(\Delta\omega_{\pm})^2\rangle}/2$. In the tight-trap limit, $N=8$ and $N=9$ can be distinguished. In the loose-trap limit, the intrinsic width of the spectra render determination of atom number difficult.

local-density approximation, i.e., treating the initial atomic state as a statistical distribution of infinitely massive atoms. The latter quantifies residual effects of atomic motion, in essence quantifying effects of Doppler shifts and line broadenings. We surmise that this understanding of our results should allow them to be applied directly to a finite-temperature sample, characterized by some thermal size (leading to inhomogeneous broadening) and velocity (leading to Doppler effects).

These results can be applied to assess the potential for precisely counting the number of atoms trapped in a high-finesse optical cavity through measuring the transmission of probe light, analogous to the work of Hood *et al.* [11] and Münstermann *et al.* [11,12] for single-atom detection. To set the limits of our counting capability, we assume that atoms are detected through measuring the position of the mean of the red sideband. In order to reliably distinguish between N and $N+1$ atoms in the cavity, the difference between the means for N and $N+1$ atoms must be greater than the width of our peaks, i.e., $|\langle\omega_{\pm}(N)\rangle - \langle\omega_{\pm}(N+1)\rangle| > \Delta\omega_{\pm}$ (see Fig. 3). Let us consider that, in addition to the intrinsic broadening derived in this paper, there exists an extrinsic width κ' due to the finite cavity finesse and other broadening mechanisms. Evaluated in the limit $g \gg \hbar k^2/2m$ and assuming large N ,

$$\langle\omega_{\pm}(N)\rangle - \langle\omega_{\pm}(N+1)\rangle \approx g\sqrt{\frac{1+\epsilon}{8N}}. \quad (35)$$

We thus obtain an atom counting limit of

$$N_{\max} \approx \frac{1+\epsilon}{8\frac{\kappa'^2}{g^2} + \frac{1}{2}(1-\epsilon)^2(1+\epsilon)}, \quad (36)$$

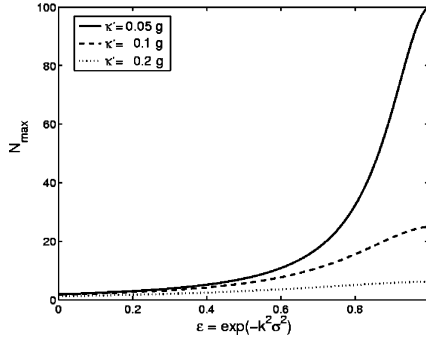


FIG. 4. Maximum limit N_{max} on atom counting as a function of trap tightness $\epsilon = \exp(-k^2 \sigma^2)$ for several values of the decay parameter κ' . $\epsilon \rightarrow 0$ corresponds to the loose-trap limit while $\epsilon \rightarrow 1$ corresponds to the tight-trap limit. Notice that for the infinitely tight trap, atom counting is limited only by κ' .

where we have assumed that the intrinsic and extrinsic widths add in quadrature. This atom counting limit ranges from $N_{max} = g^2/4\kappa'^2$ in the tight-trap limit to $N_{max} = 1/(1/2 + 8\kappa'^2/g^2)$ in the loose-trap limit. Figure 4 shows N_{max} as a function of ϵ for various values of κ' . In general, atom counting will be limited by extrinsic linewidth when $16\kappa'^2 > g^2(1-\epsilon)^2$ and by intrinsic linewidth when $16\kappa'^2 < g^2(1-\epsilon)^2$.

These results demonstrate that atom counting using the transmission spectrum is best accomplished within the tight-trap limit. Certainly, in the loose-trap limit, atom counting will be rendered difficult as the intrinsic linewidth of the sidebands is increased. However, several questions regarding the feasibility of atom-counting experiments remain. First,

although atom counting by a straightforward measurement of the intensity of the transmitted light may be difficult, it is possible that the phase of the transmitted light may be less affected by motional effects [13]. Dynamical measurements (possibly using quantum feedback techniques) might also yield higher counting limits. Second, atomic cooling techniques could be used in the loose-trap limit to cool the atoms into the wells of the optical potential, thereby decreasing the observed linewidth [27–30]. In addition, cavity-cooling-based detection would naturally stabilize the problems of heating atoms during the measurement of their number. Finally, the state dependence of spontaneous emission has not yet been taken into account. Although the loose-trap regime leads to an intrinsic linewidth which limits atom counting, it may also suppress the extrinsic linewidth as a result of contributions from superluminescence. On the other hand, in the Lamb-Dicke limit, the atoms are all highly localized, which could lead to enhanced spontaneous emission due to cooperative effects. Future work will investigate alternative methods of atom counting and will explore complementary techniques of reducing the intrinsic linewidth in atom-cavity transmission spectra.

ACKNOWLEDGEMENTS

We thank Po-Chung Chen for a critical reading of the manuscript. S.L. thanks NSERC and The Department of Physics of the University of California, Berkeley, for financial support. N.S. thanks the University of California, Berkeley, for financial support. The work of K.R.B. was supported by the Fannie and John Hertz Foundation. The work of D.M.S.K. was supported by the National Science Foundation under Grant No. 0130414, the Sloan Foundation, the David and Lucile Packard Foundation, and the University of California. K.B.W. thanks the Miller Foundation for basic research. The authors' effort was sponsored by the Defense Advanced Research Projects Agency (DARPA) and Air Force Laboratory, Air Force Materiel Command, USAF, under Contract No. F30602-01-2-0524.

- [1] *Cavity Quantum Electrodynamics*, edited by P. Berman (Academic Press, Boston, 1994).
- [2] H. Kimble, *Phys. Scr.*, T **76**, 127 (1998).
- [3] J. Raimond, M. Brune, and S. Haroche, *Rev. Mod. Phys.* **73**, 565 (2001).
- [4] C. Law and H. Kimble, *J. Mod. Opt.* **44**, 2067 (1997).
- [5] A. Kuhn *et al.*, *Appl. Phys. B: Lasers Opt.* **B69**, 373 (1997).
- [6] A. Kuhn, M. Hennrich, and G. Rempe, *Phys. Rev. Lett.* **89**, 067901 (2002).
- [7] K. R. Brown *et al.*, *Phys. Rev. A* **67**, 043818 (2003).
- [8] Q. Turchette *et al.*, *Phys. Rev. Lett.* **75**, 4710 (1995).
- [9] G. Guthohrlein *et al.*, *Nature (London)* **414**, 49 (2002).
- [10] A. Mundt *et al.*, *Phys. Rev. Lett.* **89**, 103001 (2002).
- [11] C. Hood *et al.*, *Science* **287**, 1447 (2000).
- [12] P. Münstermann *et al.*, *Phys. Rev. Lett.* **82**, 3791 (1999).
- [13] H. Mabuchi, J. Ye, and H. Kimble, *Appl. Phys. B: Lasers Opt.* **68**, 1095 (1999).
- [14] P. Horak *et al.*, *Phys. Rev. Lett.* **88**, 043601 (2002).
- [15] P. Horak and H. Ritsch, *Phys. Rev. A* **63**, 023603 (2001).
- [16] C. Orzel *et al.*, *Science* **291**, 2386 (2001).
- [17] D. Wineland *et al.*, *Phys. Rev. A* **46**, R6797 (1992).
- [18] J. Hald *et al.*, *Phys. Rev. Lett.* **83**, 1319 (2000).
- [19] A. Kuzmich, L. Mandel, and N. P. Bigelow, *Phys. Rev. Lett.* **85**, 1594 (2000).
- [20] J. Ye, D. W. Vernooy, and H. J. Kimble, *Phys. Rev. Lett.* **83**, 4987 (1999).
- [21] J. McKeever *et al.*, *Phys. Rev. Lett.* **90**, 133602 (2003).
- [22] M. Tavis and F. Cummings, *Phys. Rev.* **170**, 379 (1968).
- [23] W. Ren and H. J. Carmichael, *Phys. Rev. A* **51**, 752 (1995).
- [24] D. W. Vernooy and H. J. Kimble, *Phys. Rev. A* **56**, 4287 (1997).
- [25] A. Doherty *et al.*, *Phys. Rev. A* **56**, 833 (1997).

LESLIE *et al.*

PHYSICAL REVIEW A **69**, 043805 (2004)

- [26] T. Fischer *et al.*, New J. Phys. **3**, 11 (2001).
- [27] V. Vuletic and S. Chu, Phys. Rev. Lett. **84**, 3787 (2000).
- [28] G. Hechenblaikner, M. Gangl, P. Horak, and H. Ritsch, Phys. Rev. A **58**, 3030 (1998).
- [29] S. J. van Enk, J. McKeever, H. J. Kimble, and J. Ye, Phys. Rev. A **64**, 013407 (2001).
- [30] V. Vuletic, H. W. Chan, and A. T. Black, Phys. Rev. A **64**, 033405 (2001).

Bibliography

- [1] L.E. Sadler et al. *Nature*, 443:312, 2006.
- [2] S.R. Leslie, J. Guzman, M. Vengalattore, and D.M. Stamper-Kurn. *to be published*, 2008.
- [3] T.Lahaye et. al. *Nature*, 448:672 (2007).
- [4] J.Doyle et. al. *Eur.Phys. J D*, 31:149 (2004).
- [5] A. Micheli, G.K. Brennan and P. Zoller *Nature Physics*, 2:341 (2006).
- [6] T.Garel and S.Doniach *Phys. Rev. B*, 26:325 (1982).
- [7] S. Odenbach, ed. *Ferrofluids: magnetically controllable fluids and their applications*, vol. 594 of *Lecture Notes in Physics* (Springer, New York, 2002).
- [8] E. Dagotto *Science*, 309:257 (2005).
- [9] U. Schollwöck et al., eds. *Quantum Magnetism*, vol. 465 of *Lecture Notes in Physics* (Springer, Berlin, 2004).
- [10] M. Vengalattore, S.R. Leslie, J. Guzman, and D.M. Stamper-Kurn. *Phys. Rev. Lett.*, 100:170403, 2008.
- [11] J.M. Higbie. Ph.D., U.C. Berkeley, 2005.
- [12] M. Vengalattore et al. *Phys. Rev. Lett.*, 98(20):200801, 2007.
- [13] S.R. Leslie, J.D. Sau, M.L. Cohen, and D.M. Stamper-Kurn. *to be published*.
- [14] L.E. Sadler. Ph.D., U.C. Berkeley, 2006.

- [15] S. Sydoriak, E. Grilly, and E. Hammel *Phys. Rev.*, 75:303, 1949.
- [16] C.J. Myatt et al. *Opt. Lett.*, 21:290, 1996.
- [17] D.M. Stamper-Kurn et al. *Phys. Rev. Lett.*, 80:2027, 1998.
- [18] J. Stenger et al. *Nature*, 396:345, 1998.
- [19] D.M. Stamper-Kurn et al. *Phys. Rev. Lett.*, 83:661, 1999.
- [20] H.J. Miesner et al. *Phys. Rev. Lett.*, 82:2229, 1999.
- [21] M.S. Chang et al. *Phys. Rev. Lett.*, 92:140403, 2004.
- [22] H. Schmaljohann et al. *Phys. Rev. Lett.*, 92:040402, 2004.
- [23] T. Kuwamoto et al. *Phys. Rev. A*, 69:063604, 2004.
- [24] M.-S. Chang et al. *Nature Physics*, 1:111, 2005.
- [25] W. Zhang et al. *Phys. Rev. A*, 72:031602, 2005.
- [26] A. Widera et al. *Phys. Rev. Lett.*, 95(19):190405, 2005.
- [27] T.-L. Ho. *Phys. Rev. Lett.*, 81:742, 1998.
- [28] S.-K. Yip. *Phys. Rev. Lett.*, 83(23):4677, 1999.
- [29] T. Isoshima et al. *J. Phys. Soc. Jpn.*, 70:1604, 2000.
- [30] U. A. Khawaja and H. Stoof *Nature*, 411(6840):918, 2001.
- [31] T. Mizushima et al. *Phys. Rev. Lett.*, 89(3):030401, 2002.
- [32] N. P. Robins et al. *Phys. Rev. A*, 64(2):021601, 2001.
- [33] H. Saito and M. Ueda. *Phys. Rev. A*, 72(2):023610, 2005.
- [34] W. Zhang et al. *Phys. Rev. Lett.*, 95(18):180403, 2005.
- [35] J. Kronjager et al. *Phys. Rev. Lett.*, 97(11):110404, 2006.
- [36] C. K. Kaw et al. *Phys. Rev. Lett.*, 81(24):5257, 1998.

- [37] K. Gross et al. *Phys. Rev. A*, 66:033603, 2002.
- [38] A. M. Rey et al. *Phys. Rev. Lett.*, 99:140601, 2001.
- [39] I. Bloch, J. Dalibard and M. Lewenstein *Rev. Mod. Phys.*, 80:885, 2008.
- [40] L.-M. Duan, J. I. Cirac, and P. Zoller *Phys. Rev. A*, 65:033619, 2002.
- [41] T. Ohmi and K. Machida. *J. Phys. Soc. Jpn.*, 67:1822, 1998.
- [42] A. Lamacraft. *Phys. Rev. Lett.*, 98(16):160404, 2007.
- [43] D.M. Stamper-Kurn. Ph.d., Massachusetts Institute of Technology, 2000.
- [44] E.G.M. van Kempen et al. *Phys. Rev. Lett.*, 88:093201, 2002.
- [45] J.D. Sau, S.R. Leslie, D.M. Stamper-Kurn and M.L. Cohen. *to be published*.
- [46] S. Bize et al. *Europhys. Lett.*, 45:558, 1999.
- [47] S. Chandrasekhar. *Liquid Crystals*, Second Edition, Cambridge University Press, Cambridge (1992).
- [48] I.C. and E.J. Mueller. *J. Phys. B*, 37:S115, 2004.
- [49] F. Zernicke. *Mont. Not. Roy. Astro. Soc.*, 94:0377, 1933.
- [50] J.M. Higbie et al. *Phys. Rev. Lett.*, 95:050401, 2005.
- [51] M.R. Matthews et al. *Phys. Rev. Lett.*, 83:3358, 1999.
- [52] T.P. Purdy Ph.D., U.C. Berkeley, to be published.
- [53] L.R. Hunter. *Science*, 252:73, 1991.
- [54] C. C. Tsuei and J.R. Kirtley. *Rev. Mod. Phys.*, 72:969, 2000.
- [55] K. Kobayashi and Y. Uchikawa. *IEEE Trans. Mag.*, 39:3378, 2003.
- [56] S. J. Bending. *Adv. Phys.*, 48:449, 1999.
- [57] J. R. Kirtley, et al. *App. Phys. Lett.*, 66(9):1138, 1995.
- [58] Koch et al. *J. Low Temp. Phys.*, 51:207, 1983.

- [59] I.K. Kominis, T.W. Kornack, J.C. Allred, and M.V. Romalis. *Nature*, 422:596, 2003.
- [60] P. Treutlein et al. *Phys. Rev. Lett.*, 92:203005, 2004.
- [61] G. B. Jo et al. *Phys. Rev. Lett.*, 98(3):030407, 2007.
- [62] D. M. Harber et al. *Phys. Rev. A*, 72:033610, 2005.
- [63] G. K. Campbell et al. *Phys. Rev. Lett.*, 94:170403, 2005.
- [64] S. Gupta et al. *Phys. Rev. Lett.*, 89:140401, 2002.
- [65] D. M. Harber et al. *Phys. Rev. A*, 66:053616, 2002.
- [66] C. Fertig et al. *Phys. Rev. Lett.*, 85:1622, 2000.
- [67] M. D. Barrett et al. *Phys. Rev. Lett.*, 87:010404, 2001.
- [68] R. H. Koch, D. J. Van Harlingen, and J. Clarke. *App. Phys. Lett.*, 38(5):380–382, 1981.
- [69] T. S. Lee, E. D., and J. Clarke. *Rev. Sci. Instrum.*, 67(12):4208–4215, 1996.
- [70] D. Budker et al. *Phys. Rev.*, 85:2088, 2000.
- [71] J. Dalibard and C. Cohen-Tannoudji. *J. Opt. Sci. Am. B*, 6:2023, 1989.
- [72] H.Y. Carr and E.M. Purcell. *Phys. Rev.*, 94:630, 1954.
- [73] B. Damski and W. H. Zurek. *Phys. Rev. Lett.*, 99(13):130402, 2007.
- [74] M. Uhlmann, R. Schutzhold, and U. R. Fischer. *Phys. Rev. Lett.*, 99(12):120407, 2007.
- [75] H. Saito, Y. Kawaguchi, and M. Ueda. *Phys. Rev. A*, 75(1):013621, 2007.
- [76] G. I. Mias, N. R. Cooper, and S. M. Girvin. *Phys. Rev. A*, 77(2):023616, 2008.
- [77] J. Mur-Petit et al. *Phys. Rev. A*, 73(1):13629–1–6, 2006.
- [78] H. Pu et al. *Phys. Rev. A*, 60(2):1463, 1999.
- [79] R. Movshovich et al. *Phys. Rev. Lett.*, 65(12):1419, 1990.
- [80] O. Arcizet et al. *Nature*, 444:71, 2006.

- [81] A. Schliesser et al. *Phys. Rev. Lett.*, 27:243905, 2006.
- [82] D. Rugar et al. *Nature*, 430:329, 2004.
- [83] A. Abramovici et al. *Science*, 256:325, 2006.
- [84] D.F. Walls and G.J. Milburn. Springer, New York, 1994.
- [85] M. Mück, J. B. Kycia, and J. Clarke. *App. Phys. Lett.*, 78(7):967–969, 2001.
- [86] M. Baraban et al. *arXiv:0807.1280*.
- [87] F. Gerbier et al. *Phys. Rev. A*, 73(4):041602, 2006.
- [88] A. Widera et al. *New Journal of Physics*, 8:152, 2006.
- [89] J. M. McGuirk, D. M. Harber, H. J. Lewandowski, and E. A. Cornell. *Phys. Rev. Lett.*, 91(15):150402, 2003.
- [90] J. Esteve et al. *arXiv*, 0810.0600, 2008.
- [91] J. Appel et al. *arXiv*, 0810.3545, 2008.
- [92] I. Teper et al. *arXiv*, 0807.4762, 2008.
- [93] M. Auzinsh et al. *Phys. Rev. Lett.*, 93(17):173002 – 173005, 2004.
- [94] F. Gerbier et al. *Phys. Rev. Lett.*, 96(9):090401 – 090404, 2006.
- [95] I. B. and K. Mølmer. *Phys. Rev. A*, 66(4):043811, 2002.
- [96] C. Orzel et al. *Science*, 291:2386, 2001.
- [97] A. Sorensen, J.I. Cirac, P. Zoller, L.M. Duan *Phys. Rev. Lett.*, 85(19):3991 – 3994, 2000.
- [98] J. Hald, J.L. Sorensen, C. Schori, and E.S. Polzik. *Phys. Rev. Lett.*, 83(7):1319, 2000.
- [99] Q.A. Turchette et al. *Phys. Rev. A*, 58:4056, 1998.
- [100] D.J. Wineland et al. *Phys. Rev. A*, 46:R6797, 1992.
- [101] M. Kitagawa and M. Ueda. *Phys. Rev. A*, 47(6):5138–5143, 1993.

- [102] A. Andre and M.D. Lukin. *Phys. Rev. A*, 65:053819, 2002.
- [103] L. Santos, G. Shlyapnikov and M. Lewenstein *Phys. Rev. Lett.*, 90:250403, 2003.
- [104] S. Yi and H. Pu *Phys. Rev. Lett.*, 97:020401, 2006.
- [105] C. Slichter. *Principles of Magnetic Resonance*, (Springer, New York, 1978).
- [106] A. Lamacraft *Phys. Rev. A*, 77:063622, 2008.
- [107] R.W. Cheng, V. Gritsev, D.M. Stamper-Kurn, and E. Demler. *Phys. Rev. Lett.*, 100:180404, 2008.
- [108] K. Goral, L. Santos and M. Lewenstein *Phys. Rev. Lett.*, 88:170406, 2002.
- [109] H.P. Buchter et al. *Phys. Rev. Lett.*, 98:060404, 2007.